Novel Analytical Hydrodynamic Modeling for Evaluating and Optimizing Alluvial Recharge

Principles, Model Approaches and Their Application for Water Resources Assessment in an Arid Region

DISSERTATION

by Dipl.-Hydrol. Andy Philipp
born May 20th, 1981 in Zwickau

In partial fulfillment of the requirements for obtaining the degree of
Doctor rerum naturalium (Dr. rer. nat.)

Submitted to the Faculty of Environmental Sciences,
Technische Universität Dresden,
March 13th, 2013

Examination location and date:
Dresden, July 17th, 2013

Reviewers:
em. Prof. Dr.-Ing. habil. Gerd H. Schmitz, TU Dresden
Prof. Dr. Harald Kunstmann, Universität Augsburg
Dr. habil. Johannes Cullmann, UNESCO IHP/HWRP Secretariat, Koblenz

"It needs categorically to be reaffirmed
that the continuum mechanics of a fluid
innocent of electric current
has as vital and exciting a present and future
as any other branch of physical science."

Sir James Lighthill

Declaration of the Author

I hereby confirm that this copy is identical to the original dissertation with the title

Novel Analytical Hydrodynamic Modeling
for Evaluating and Optimizing Alluvial Recharge

Principles, Model Approaches and Their Application for
Water Resources Assessment in an Arid Region

(Andy Philipp)

Dresden, October 1st, 2013

Preface

This thesis essentially comprises three research papers on analytical zero-inertia modeling of free surface flows and model application under conditions which are characteristic for arid areas. These papers were, or are going to be, published in the American Society of Civil Engineers' Journal of Hydraulic Engineering.[1] A copy of the papers can be found in the Appendix B. For this reason, wider parts of the text and a not insubstantial number of figures and tables were adopted from the aforementioned publications without any or with only slight modifications. The aim of this thesis is to present the content of all three papers in a concise and consistent manner. Hence, some nomenclature used herein differs from that which is used in the papers. Although passing a thorough peer review process, a very small—but not necessarily negligible—amount of reproduction errors were found in the published papers, mainly in equations. In case of any doubt, this thesis represents the corrected version of these mistakes. Furthermore, this thesis is written in American English in order to maintain consistency with the aforementioned publications.

I am very thankful to everyone who directly or indirectly made a contribution to this work. First and foremost, I want to express my deeply-felt gratitude to my supervisor Prof. Gerd Schmitz for his guidance and ongoing support during the years. Gerd Schmitz generously reviewed this thesis and also acted as an author or co-author for a number of publications I was involved in, including Philipp et al. (2010). I am also very grateful to Prof. Rudolf Liedl (TU Dresden) who delivered the theoretical background of the analytical flow models presented herein, as well as helped as a mathematician during various stages of model development. Rudolf Liedl also co-authored two of the three papers which contributed to this thesis (Philipp et al., 2010 and Philipp et al., 2012).

I am obliged to Dr. Johannes Cullmann (German IHP/HWRP) for always being such a diligent supporter, patron, and friend of mine, as well to Dr. Thomas "Eddy" Wöhling (WESS Tübingen) and Prof. Harald Kunstmann (Universität Augsburg) for helping me in so many ways. Moreover, Johannes Cullmann and Harald Kunstmann both took care of reviewing this thesis. It should also be mentioned that Eddy Wöhling acted as a co-author for Philipp et al. (2012).

My colleagues, Dr. Michael Wagner, Dr. Sabine Seidel, Dr. Thomas Krauße, Dr. Peter Stange, Sebastian Kloß, Ruben Müller, Dr. Niels Schütze, and Dr. Franz Lennartz are acknowledged for always being willing to help me with the problems I was having regarding this work. In particular, I thank Dr. Jens Grundmann for co-authoring Philipp and Grundmann (2013) and Stefan Werisch for going through the manuscript.

[1] Philipp et al. (2010), Philipp et al. (2012), and Philipp and Grundmann (2013).

Special appreciation is given to my old friend, band mate, and computer expert, Ludwig Schmutzler, who always showed a keen interest in hydrology and inspired this thesis in many ways. Additionally, I would like to thank Prof. Bernhard Schmid (TU Wien), Prof. Axel Bronstert (Universität Potsdam), Prof. Rao S. Govindaraju (Purdue University), and Dr.-Ing. Gerhard Haimerl for having provided data and/or computer codes, helpful for my work.

A number of graduate and undergraduate students have contributed to this work, including Matthias Zink, Stefanie Schurig, Markus Giese, Achim Six, Sandra Hirschfeld, and Diana Spieler. Some of the material which was later able to be used for this thesis was obtained by Farnush Ghasempour, who was a PhD candidate at the institute but regrettably passed away in the year 2005 before being able to finish his work.

My very special appreciation goes to my wife, Marie, and our son, Anton, for their love, support, patience, and participation during the ups and downs of this PhD process. Finally, I want to thank my parents, Monika and Horst, as well as my parents-in-law, Sabine and Peter, for their backup concerning many aspects of everyday life.

Abstract

This thesis presents a novel analytical solution strategy for the zero-inertia (ZI) equations of free surface flow. These equations are utilized herein for routing flood flow in open channels and for simulating excess rainfall runoff on overland planes. The novel solution approach is shown to be both accurate and robust, especially under the complicated and intricate conditions of infiltrating flow on initially dry river beds or soils, e.g., as present in arid and semiarid areas. This is underlain by comparing modeling results of the novel analytical procedure with those of validated numerical solutions. Furthermore, it is shown that the analytical ZI model can deliver a process-oriented portrayal of runoff concentration in the flood-generating parts of the catchment.

Subsequently, the novel analytical ZI model is applied for a real-world water management problem in the Sultanate of Oman, Arabian Peninsula. Within an integrated flash flood routing model—which is also presented in this thesis—the novel analytical routing approach helps in accurately matching the dynamics of advancing and infiltrating ephemeral river flow, established as a consequence of release from a groundwater recharge dam. The integrated modeling system houses the aforementioned analytical downstream model and tailor-made, state-of-the-art modeling components to portray the upstream flow processes, dam operation (including evaporation), and spillway release flow. The proposed modeling system can aid in rendering a realistic image of transient transmission losses and dependent flow dynamics. This is of extremely high importance for water resources assessment, as well as for optimizing recharge dam operation strategies in order to maximize downstream transmission losses and, thus, groundwater recharge.

Contents

List of Figures

List of Tables

List of Algorithms

List of Symbols and Acronyms

Capital Latin Symbols (I)

A	Wetted cross-sectional area	$[\mathrm{L}^2]$
$\tilde{A}$	Wetted cross-sectional area related to $\tilde{h}$, $\tilde{B}$, $\tilde{P}$, or $\tilde{R}$	$[\mathrm{L}^2]$
A_0	Wetted cross-sectional area at upper boundary	$[\mathrm{L}^2]$
A_c	Culvert inlet area	$[\mathrm{L}^2]$
A_r	Water table area of a reservoir	$[\mathrm{L}^2]$
B	Flow width	[L]
$\tilde{B}$	Flow width related to $\tilde{h}$, $\tilde{A}$, $\tilde{P}$, or $\tilde{R}$	[L]
C	Courant number	[−]
D^-	Backward difference quotient	[ ]
D^+	Forward difference quotient	[ ]
D^c	Central difference quotient	[ ]
D_c	Culvert diameter	[L]
E	Evaporation volume	$[\mathrm{L}^3\mathrm{T}^{-1}]$
E_G	Evaporation equivalent of global radiation	$[\mathrm{LT}^{-1}]$
F	Froude number	[−]
G	Global radiation	$[\mathrm{ML}^2\mathrm{T}^{-3}\mathrm{L}^{-2}]$
H_{c_m}	Inlet axis elevation of culvert m	[L]
H_s	Elevation of the spillway crest	[L]
I	Cumulative infiltration	$[\mathrm{L}^3]$
I_act	Actual infiltration rate	$[\mathrm{L}^3\mathrm{T}^{-1}]$
K	Roughness coefficient	$[\mathrm{L}^{1-\beta}\mathrm{T}^{-1}]$
K_St	Strickler roughness coefficient	$[\mathrm{L}^{1-\frac{2}{3}}\mathrm{T}^{-1}]$
K_C	Chézy roughness coefficient	$[\mathrm{L}^{1-\frac{1}{2}}\mathrm{T}^{-1}]$
L	Distance between two channel cross sections	[L]
L_0	Length of a flow element	[L]
L_s	Length of the spillway	[L]
M	Number of culverts	[−]
N	Number of observation locations along x	[−]
O	Number of flow observations	[−]
P	Wetted perimeter	[L]
P_0	Wetted perimeter at the upper boundary	[L]
$\tilde{P}$	Wetted perimeter related to $\tilde{h}$, $\tilde{A}$, $\tilde{B}$, or $\tilde{R}$	[L]

Capital Latin Symbols (II)

Q	Total discharge or discharge per unit width	$[\mathrm{L}^3\mathrm{T}^{-1}]$ or $[\mathrm{L}^2\mathrm{T}^{-1}]$
Q_0	Upper boundary inflow	$[\mathrm{L}^3\mathrm{T}^{-1}]$ or $[\mathrm{L}^2\mathrm{T}^{-1}]$
Q_{in}	Reservoir inflow	$[\mathrm{L}^3\mathrm{T}^{-1}]$
Q_{out}	Total reservoir outflow	$[\mathrm{L}^3\mathrm{T}^{-1}]$
$Q_{\mathrm{out}_{c_m}}$	Outflow through culvert m	$[\mathrm{L}^3\mathrm{T}^{-1}]$
$Q_{\mathrm{out}_{\mathrm{s}}}$	Outflow over the spillway	$[\mathrm{L}^3\mathrm{T}^{-1}]$
Q_{obs}	Observed flow	$[\mathrm{L}^3\mathrm{T}^{-1}]$
$\overline{Q_{\mathrm{obs}}}$	Mean value of observed flow	$[\mathrm{L}^3\mathrm{T}^{-1}]$
Q_{sim}	Simulated flow	$[\mathrm{L}^3\mathrm{T}^{-1}]$
R	Hydraulic radius	[L]
R_0	Hydraulic radius at the upper boundary	[L]
$\tilde{R}$	Hydraulic radius related to $\tilde{h}$, $\tilde{A}$, $\tilde{B}$, or $\tilde{P}$	[L]
S_0	Bottom slope	[–]
S_{f}	Friction slope	[–]
T	Temperature	[Θ]
V	Reservoir storage volume	$[\mathrm{L}^3]$
W	Reservoir water level	[L]

Lower Case Latin Symbols (I)

a	Cross-sectional shape parameter	[–]
c	Wave celerity	$[\mathrm{LT}^{-1}]$
$\hat{c}$	Maximum wave celerity	$[\mathrm{LT}^{-1}]$
c_{b}	Backward characteristic curve gradient	$[\mathrm{LT}^{-1}]$
c_{f}	Forward characteristic curve gradient	$[\mathrm{LT}^{-1}]$
c_κ	Kinematic wave celerity	$[\mathrm{LT}^{-1}]$
e	Actual water vapor pressure	$[\mathrm{ML}^{-1}\mathrm{T}^{-2}]$
e_0	Saturated water vapor pressure	$[\mathrm{ML}^{-1}\mathrm{T}^{-2}]$
f	An arbitrary function	[ ]
g	Acceleration due to Earth's gravity	$[\mathrm{LT}^{-2}]$
h	Water depth	[L]
h_0	Water depth at upper boundary	[L]
$\overline{h}$	Mean water depth over t_{e}	[L]
$\tilde{h}$	Water depth related to $\tilde{A}$, $\tilde{B}$, $\tilde{P}$, or $\tilde{R}$	[L]
h_{n}	Normal flow depth	[L]
h_{r}	Reference water depth related to w_{r}	[L]
i	Integer index in space direction	[–]
j	Integer index in time direction	[–]
k	Iteration index	[–]

Lower Case Latin Symbols (II)

k_a	Empirical Kostiakov-Lewis coefficient	$[-]$
k_c	Steady infiltration rate	$[\mathrm{LT}^{-1}]$
k_k	Empirical Kostiakov-Lewis coefficient	$[\mathrm{LT}^{-k_\mathrm{a}}]$
l	Arc length of a continuous function	[L]
m	Culvert index	$[-]$
n	Index of observation nodes	$[-]$
p_1	Cross-sectional parameter	$[\mathrm{L}^{1-2p_2}]$
p_2	Cross-sectional parameter	$[-]$
p_3	Cross-sectional parameter	$[\mathrm{L}^{1-2p_4}]$
p_4	Cross-sectional parameter	$[-]$
q	Volumetric loss or yield rate per unit area	$[\mathrm{LT}^{-1}]$
q^ϕ	Volumetric loss rate per unit length	$[\mathrm{L}^2\mathrm{T}^{-1}]$
q_0^ϕ	Volumetric loss rate per unit length at upper boundary	$[\mathrm{L}^2\mathrm{T}^{-1}]$
q_inf	Volumetric infiltration rate per unit area	$[\mathrm{LT}^{-1}]$
q_rain	Volumetric rainfall rate per unit area	$[\mathrm{LT}^{-1}]$
q_max	Maximum lateral inflow per unit surface area	$[\mathrm{LT}^{-1}]$
$r_{A,t}$	Relaxation parameter for the calculation of $A_{0,n}$ or t_n	$[-]$
s	Gradient of the saturated water vapor pressure curve	$[\mathrm{ML}^{-1}\mathrm{T}^{-1}\Theta^{-1}]$
t	Time	[T]
t_d	Travel time from upstream to downstream section	[T]
t_e	Duration of a flow event	[T]
t_end	End time of simulation	[T]
t_n	Arrival time at n	[T]
t_u	Time related to a specific upstream inflow	[T]
$t_\mathrm{arr}^\mathrm{ref}$	Reference arrival time	[T]
$t_\mathrm{arr}^\mathrm{var}$	Arrival time for varied process parameters	[T]
u	Flow velocity	$[\mathrm{LT}^{-1}]$
$\overline{u}$	Mean flow velocity over t_e	$[\mathrm{LT}^{-1}]$
u_0	Flow velocity at the upper boundary	$[\mathrm{LT}^{-1}]$
u_tip	Velocity at the advancing flow tip	$[\mathrm{LT}^{-1}]$
v	Wind function	$[\mathrm{LT}^{-1}]$
w	Wind speed	$[\mathrm{LT}^{-1}]$
w_r	Half the channel width at h_r	[L]
x	Longitudinal space coordinate	[L]
x_0	Location of the upper boundary	[L]
x_end	Location of the lower end of the spatial domain	[L]
x_n	Location of an observation point n	[L]
x_tip	Position of the advancing flow tip	[L]
y	Space coordinate perpendicular to the flow direction	[L]
z	Vertical coordinate positive upwards	[L]
z_0	Dynamic roughness length	[L]
z_w	Elevation of wind speed measurement	[L]

Greek Symbols

α_c	Culvert discharge coefficient	$[-]$
α_s	Spillway discharge coefficient	$[-]$
β	Exponent of the flow formula	$[-]$
γ	Psychrometric constant	$[\mathrm{ML^{-1}T^{-1}\Theta^{-1}}]$
δ	Factor of the kinematic wave model	$[\mathrm{TL^{-1}}]$
ε	Iteration precision criterion	$[-]$
η	Kinematic wave cross-sectional coefficient	$[-]$
θ	Implicit weighting factor of the Preissmann scheme	$[-]$
ι	Radiation conversion factor	$[\mathrm{ML^2T^{-3}L^{-2}}]$
κ	Kinematic wave number	$[-]$
λ	Abbreviation for the expression $2p_4\beta + p_2$	$[-]$
μ	Factor of the kinematic wave model	$[\mathrm{L^{-2}}]$
ν	An arbitrary continuous and differentiable function	$[\ ]$
ξ	Integration variable in space	$[\mathrm{L}]$
ρ_0	A momentum-representative term	$[\mathrm{L}^{2\beta}]$
σ	Upper limit for the increase rate of advance times	$[-]$
ς	Maximum tolerable number of iterations	$[-]$
τ	Infiltration opportunity time	$[\mathrm{T}]$
ψ_n	An abbreviation for a mathematical expression at n	$[\mathrm{L}^{1-2p_2}\mathrm{L}^{-(1-2p_4)}]$
ω_n	An abbreviation for a mathematical expression at n	$[-]$
Γ	Substitution variable for $p_1(x)^{\frac{\lambda}{p_2}}A^{\lambda}$	$[\mathrm{L}^{2p_2}]$
Φ	Proxy for the function of a dependent flow variable	$[\ ]$
Ω	An arbitrary domain in $\mathbb{R}^n$	$[\ ]$

Other Nomenclature

$\mathfrak{a}, ..., \mathfrak{g}$	Arbitrary functions of two variables	$[\ ]$
$\mathrm{A}, ..., \mathrm{E}$	Discrete points in the (x,t) plane	$[\ ]$
Δt	Temporal discretization step	$[\mathrm{T}]$
Δx	Spatial discretization step	$[\mathrm{L}]$
ICC	Iteration convergence criterion	$[-]$
NSE	Nash-Sutcliffe model efficiency coefficient	$[-]$
$\mathcal{O}$	Landau symbol	$[\ ]$
RD	Region of dependence	$[\ ]$
RI	Region of influence	$[\ ]$
RMS	Residual mean squares of profile functions	$[\mathrm{L}]$
RMSE	Root-mean-square error of the flow	$[\mathrm{L^3T^{-1}}]$

Dimensions

[L]	Length
[M]	Mass
[T]	Time
[Θ]	Thermodynamic temperature
[−]	Dimensionless
[ ]	Not further specified

Acronyms

ASCE	American Society of Civil Engineers
ASTER	Advanced Spaceborne Thermal Emission and Reflection Radiometer
CFL condition	Courant-Friedrichs-Lewy condition
CPU	Central processing unit
DEM	Digital elevation model
FORTRAN	Formula Translating System; a family of programming languages
GIS	Geographic information system
(n)HD model	(Numerical) full hydrodynamic model
HEC-RAS	Hydrologic Engineering Centers River Analysis System
KINEROS	Kinematic Runoff and Erosion Model
(n)KW model	(Numerical) kinematic wave model
MAF	Ministry of Agriculture and Fisheries
MATLAB	Matrix Laboratory; a programming language
MENA	Middle East and North Africa
MRMEWR	Ministry of Regional Municipalities, Environment and Water Resources
ODE	Ordinary differential equation
PDE	Partial differential equation
PMF	Probable maximum flood
PMP	Probable maximum precipitation
SCS	Soil Conservation Service of the United States Department of Agriculture
UNEP	United Nations Environment Programme
UNESCO	United Nations Educational, Scientific and Cultural Organization
UTC	Universal Time Coordinated
WMO	World Meteorological Organization
(a/n)ZI model	(Analytical/numerical) zero-inertia model

Chapter 1

Introduction

Arid and semiarid areas make up more than one third of global land area (UNEP, 1997). Many arid and semiarid regions[1] face a rapid population growth and, therefore, an increasing water demand. Groundwater is almost the only renewable freshwater resource and is used to a high degree in the Middle East and North Africa (MENA) countries. Projections of the World Bank (The World Bank, 2007) say that available water resources for the MENA region will *decrease* from 1,100 m^3 to 550 m^3 per year and per head over the next 40 years. A recent study by Voss et al. (2013) evaluates freshwater storage trends in the north-central Middle East (transboundary Tigris and Euphrates basins) using observations from the Gravity Recovery and Climate Experiment (GRACE) satellite mission. The study shows that total groundwater resources in the 753,960 km^2 investigation area decreased by 121.1 mm (17.3 $mm \cdot a^{-1}$) from January 2003 to December 2009, mainly attributable to withdrawals for irrigation purposes.

In some MENA areas, such as the Al Batinah Region in Oman, groundwater withdrawal exceeds natural replenishment even more strongly, which leads to falling groundwater levels of locally up to 2,000 $mm \cdot a^{-1}$ (Haimerl, 2004). Besides the improvement of water use efficiency, increasing groundwater recharge is of very high importance for a more sustainable water resources management in arid regions (Kowsar, 1996; Battashi and Rashid, 1998; Bouwer, 2002). Therefore, as the basis of a sound management and for recharge-improving measures, e.g., groundwater recharge dams, the magnitude and spatiotemporal dynamics of groundwater recharge need to be estimated.

Lerner et al. (1990) classified groundwater recharge into *direct recharge*, *indirect recharge*, and *localized recharge*. Direct recharge is the direct vertical movement of water through the soil into the groundwater (percolation), localized recharge is recharge due to spatially limited concentrations of surface water, and, finally, indirect recharge is the infiltration and percolation from watercourses. Especially in arid areas, the scarcity of data and the extreme variability and spottiness of rainfall[2] renders the estimation of groundwater recharge a rather cumbersome bundle of problems. It is feasible, to not only limit the term "direct recharge" to recharge at a specific point, but also include

[1] In this work, the term "arid" comprises arid and hyperarid climates. Usually, an aridity index is used to distinguish different degrees of aridity, e.g., hyperarid, arid, and semiarid. A number of aridity indices are available from the literature where in general precipitation and potential evaporation are related, but other variables, such as radiation or temperature, may also be supplemented. An aridity index of 0.5 marks the boundary of humid and (semi)arid climate, whereas an aridity index of < 0.05 usually indicates hyperarid climate conditions.

[2] Spotty, convective storm cells with a diameter of some to 20 kilometers were reported to cause local, highly concentrated rainfall events in (semi)arid regions of the USA (Arizona), Israel, and Oman (Renard and Keppel, 1966; Sharon, 1972; Fisher, 1994).

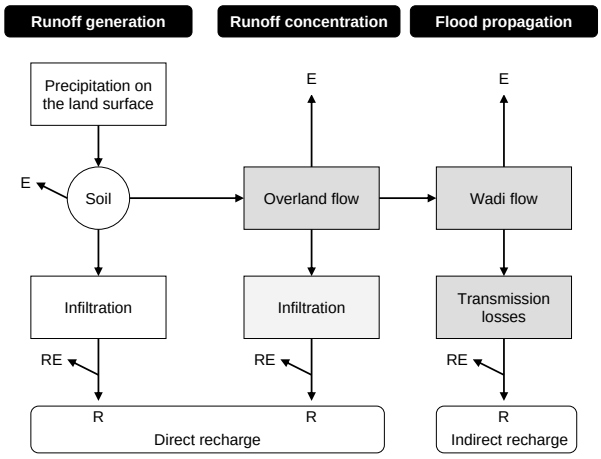

Figure 1.1: Overview of recharge processes in (semi)arid areas, modified according to Lerner (1997) and de Vries and Simmers (2002). E: Evaporation; RE: re-evaporation; R: groundwater recharge. The processes in the gray boxes are addressed in this work. Infiltration from overland flow is not directly addressed herein, but is considered in model development. The corresponding box is, therefore, filled in with a lighter gray.

the recharge emerging from smaller-scale infiltrating overland flow processes. Figure 1.1 shows this classification of surface flow and recharge processes. Eventually, groundwater recharge is driven by the rainfall–runoff phenomena, which are usually subdivided into three phases, namely runoff generation, runoff concentration, and flood propagation (cf. Fig. 1.1).

1.1 The Role of Ephemeral River Flow for Groundwater Recharge

Runoff in ephemeral riverbeds is a common phenomenon in many dryland regions. The riverbeds (or wadis) are dry throughout most of the year due to intermittent rainfall regimes and the absence of a continuously flowing water source. Especially in arid regions, convective rainstorms can lead to torrential downpours and, consequently, pronounced runoff events, called *flash floods*. Such events typically show a rapidly rising water level and are often associated with considerable sediment transport processes. Moreover, a flash flood surging down a channel may form a "wall of water", which is connected with highly turbulent flow and discontinuities in the hydraulic process variables, e.g., flow depth, velocity, and discharge (cf. Fig. 1.2). This surging tendency of an advancing flash flood wave can be amplified by an initially dry channel bed, causing typically high initial infiltration losses.

Since there is no direct connection between ephemeral river flow and groundwater, a certain amount of runoff infiltrates through the permeable riverbeds. This infiltration is often very noticeable and the phenomenon is referred to as *transmission loss*, although the water is not lost and can recharge the groundwater (Sorman and Abdulrazzak, 1993; Shentsis and Rosenthal, 2003; Goodrich et al., 2004). Transmission losses cause a recession of event-specific flow volumes and discharges along the watercourse, which can be seen from flow data obtained at a series of gauges, as shown, for example, in Table 1.1.

Figure 1.2: Advancing front of a seasonal flash flood wave in an ephemeral river in Southern Utah, USA. Shot on 08/08/2010 at Wahweap Creek, hours after heavy rain hit the drainage basin. Wahweap Creek is a western tributary to Lake Powell. Footage courtesy of David O. Rankin.

Table 1.1: Effects of transmission losses on flow volume and peak discharge for a flood event in Walnut Gulch, Arizona, United States. Data taken from Renard and Keppel (1966).

Catchment area (km^2)	Volume of flood ($10^3\,m^3$)	Peak discharge ($m^3 \cdot s^{-1}$)
95	92.3	41.9
114	79.9	27.2
149	40.1	15.6

Some authors, e.g., Rushton (1997), define transmission losses as *potential indirect groundwater recharge*, whereas actual recharge is potential recharge minus the amount of water which has infiltrated but does not contribute to the groundwater. Haimerl (2004) lists typical magnitudes and values of hydrological processes in Northern Oman (Table 1.2). Although this information only bears an assumptive character, it becomes clear that foremost infiltration opportunity times and the wetted infiltrating channel area both control transmission losses and, therefore, indirect groundwater recharge.

The interdependence of transmission losses and ephemeral river flow is strongly nonlinear. An increasing flow rate causes an acceleration of flow advance. This leads to an increase of the wetted channel area and, therefore, transmission losses, which in turn lower the flow rate, flow volumes, and—finally—decelerate the flow advance. At the same time, infiltration rates might change. Figure 1.3 exemplarily shows the spatiotemporal development of hydraulic parameters and infiltration rates for wadi flow under transmission losses, simulated with the modeling system developed herein.[1] Changes in the inflow rate cause changes in the other dependent hydraulic process parameters (e.g., water depth, wetted cross-sectional area, etc.) and, consequently, total infiltration. Additionally, infiltration rates change over time, which introduces further nonlinearity. Special attention should be drawn to the nonlinear recession trajectory of the flow domain (cf.,

[1] Simulation results are shown for a hypothetical flood event for Wadi Bani Kharus between Al Abyadh gauging station and the Sea of Oman (cf. Section 7.2.1). The incorporated Kostiakov-Lewis infiltration model was parametrized with realistic values but not on the basis of observed transmission losses.

Table 1.2: Typical scales and values of hydrological processes in Oman's ephemeral rivers, modified according to Haimerl (2004).

Process or parameter	Typical scale	Typical value
Precipitation		
Precipitation rate	$10^{-6}\,\mathrm{m \cdot s^{-1}}$	$100\,\mathrm{mm \cdot d^{-1}}$
Catchment area	$10^{8}\,\mathrm{m^2}$	$1{,}500\,\mathrm{km^2}$
Duration	$10^{3}\,\mathrm{s}$	6 h
Precipitation volume	$10^{6}\,\mathrm{m^3}$	$37.6 \cdot 10^{6}\,\mathrm{m^3}$ †
Surface runoff		
Flow velocity	$10^{0}\,\mathrm{m \cdot s^{-1}}$	$3\,\mathrm{m \cdot s^{-1}}$
Wetted cross-sectional area	$10^{2}\,\mathrm{m^2}$	$150\,\mathrm{m^2}$
Duration	$10^{3}\,\mathrm{s}$	12 h
Flow volume	$10^{6}\,\mathrm{m^3}$	$19.4 \cdot 10^{6}\,\mathrm{m^3}$ †
Infiltration		
Infiltration rate	$10^{-5}\,\mathrm{m \cdot s^{-1}}$	$2{,}000\,\mathrm{mm \cdot d^{-1}}$
Wetted channel area	$10^{6}\,\mathrm{m^2}$	$15\,\mathrm{km^2}$
Duration	$10^{3}\,\mathrm{s}$	12 h
Infiltration volume	$10^{6}\,\mathrm{m^3}$	$15 \cdot 10^{6}\,\mathrm{m^3}$ †
Evaporation from surface flow		
Evaporation rate	$10^{-8}\,\mathrm{m \cdot s^{-1}}$	$5\,\mathrm{mm \cdot d^{-1}}$
Wetted channel area	$10^{6}\,\mathrm{m^2}$	$15\,\mathrm{km^2}$
Duration	$10^{3}\,\mathrm{s}$	12 h
Evaporation volume	$10^{4}\,\mathrm{m^3}$	$0.0375 \cdot 10^{6}\,\mathrm{m^3}$ †

†Values are volumes which were calculated from typical values of rate, area, and duration of the considered processes (volume = rate · area · duration).

e.g., lower left subplot of Fig. 1.3b), where wadi infiltration leads foremost to a recession of the downstream end of the flow domain.[1]

It can be further seen from Fig. 1.3 that, although the advance of the flow domain is comparably dynamic (ca. 12 h, until recession begins), the main amount of transmission losses occurs under weak process dynamics (lower right subplot of Fig. 1.3). However, the initial advance of the infiltrating flow domain strongly controls the available infiltrating channel area and, therefore, final infiltration volumes. Such intricate and strongly nonlinear dynamics should be taken into account for the assessment of indirect groundwater recharge. Clearly, sound groundwater management is only possible with an exact and event-related simulation of transmission losses and interlinked surface flow.

1.2 A General Overview of Methods for Estimating Groundwater Recharge with the Focus on Indirect Recharge

A vast number of techniques and methods for estimating direct and indirect groundwater recharge are available from the literature. A very profound review of related studies can be found in Lerner et al. (1990) and Scanlon and Healy (2002). These authors distinguish (a) surface-water based techniques; (b) unsaturated-zone techniques; and (c) saturated-zone techniques.

[1] According to the classification of Walker and Humpherys (1983), this effect is termed "front-end recession".

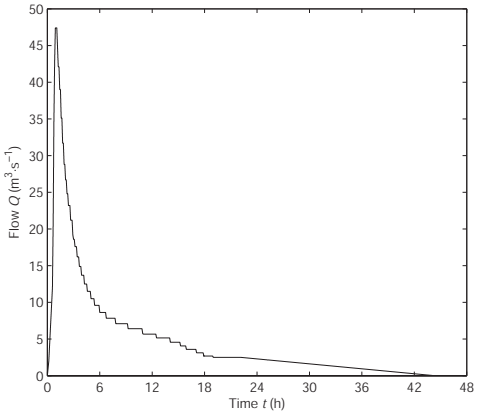

(a) The hypothetical inflow hydrograph at $x = 0\,\text{m}$.

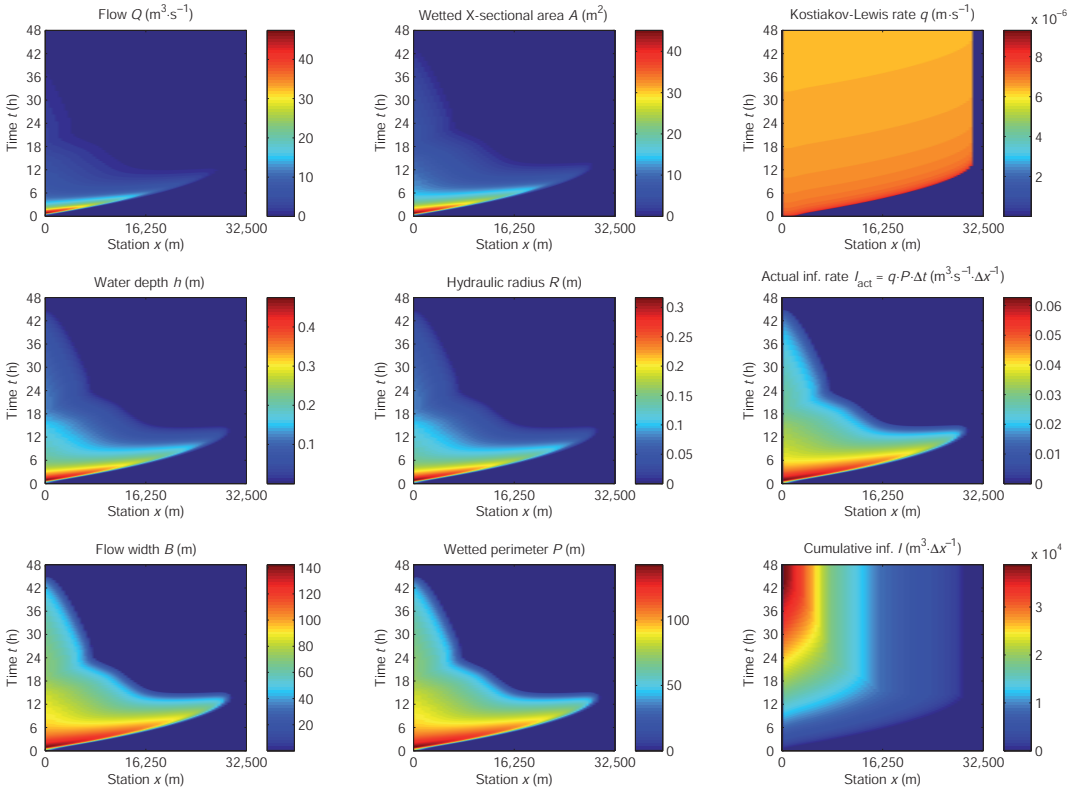

(b) Simulated highly nonlinear spatiotemporal process dynamics for a 32.5 km wadi reach over 48 h (spatial resolution $\Delta x = 50\,\text{m}$).

Figure 1.3: Simulated dynamics of wadi flow under transmission losses. An inflow hydrograph (a) is routed along a nonprismatic channel. The several plots (b) show the spatiotemporal evolution of flow, wetted cross-sectional area, infiltration rate, water depth, hydraulic radius, actual infiltration rate, flow width, wetted perimeter, and cumulative infiltration.

Surface-water based techniques and unsaturated-zone techniques estimate potential recharge, whereas groundwater methods provide estimates of actual recharge. The available methodology ranges from physical techniques, e.g., water budgeting and direct measurement of seepage (with infiltrometers), over miscellaneous tracer methods, to the application of process models[1] for the portrayal of surface and subsurface flows. Table 1.3 gives a comprehensive overview of the discussed studies with respect to their applicability for estimating indirect recharge. To maintain brevity, further references can be found in Scanlon and Healy (2002).

Not all methods referred to are applicable for an event-based and spatially/temporally distributed estimation of transmission losses, which is a precondition for a sound assessment of indirect recharge from wadi flow under the influence of groundwater recharge dams. Specific conditions which impede the use of certain techniques are set in italic font in Table 1.3. It becomes clear that the applicability of a great number of the listed recharge estimation methods for transmission loss assessment is questionable, attributable to the specifics of the arid scoping area of the present study: No baseflow is present, rainfall data are scarce and highly uncertain, and the groundwater flow is highly unsteady due to intense groundwater pumping. Furthermore, a number of methods only deliver point estimates of recharge, where, at the same time, sophisticated data, e.g., soil hydraulic properties or water content and matrix potential measurements, need to be supplemented. Additionally, several methods, e.g., all tracer methods, cannot be applied on an event-related time scale.

As seen from Table 1.3, surface-water based techniques seem to generally be more appropriate for transmission loss modeling than unsaturated-zone and saturated-zone methods. Referring to surface-water techniques, physical techniques and tracer studies expose only a limited applicability for transmission loss estimation under the problem-specific conditions present in arid and semiarid areas. Therefore, a *hydrologic* or *hydrodynamic routing approach* seems to offer the most suitable option for the estimation of ephemeral channel recharge if gauging and channel morphology data are obtainable, which is mostly the case. Numerous surface-water oriented studies related to arid and semiarid transmission loss estimation are discussed in more detail in Chapter 2.

1.3 A Closer Look at Artificial Groundwater Augmentation Techniques and the Involved Processes

The shortage of groundwater can be a major restricting factor for socio-economic development (The World Bank, 2007). Basically, two options arise in order to stop—or at least decelerate—a progressive groundwater depletion: (a) curtail groundwater extraction; and (b) artificially increase groundwater recharge. As already outlined, the improvement of water-use efficiency definitely holds the highest potential in facing an increasing water shortage. Complementarily, the application of methods known as *artificial groundwater recharge* can help to relieve the situation. According to Todd (1959), artificial groundwater recharge is usually defined as "the practice of increasing by artificial means the amount of water that enters a ground-water reservoir." Hence, any artificial system or scheme which increases natural recharge is an artificial recharge system.

Following this definition, artificial groundwater recharge systems have been known for hundreds of years, e.g., in Iran, India, Israel, and Spain (Garoussi, 1999). The employed methods are

[1] Herein, the terms "process model", "process-oriented model", and "physically-based model" are used synonymously.

Table 1.3: Overview of methods for estimating indirect groundwater recharge with respect to transmission loss (TL) estimation (according to Scanlon and Healy, 2002).

Technique		Method	Suited for TL estim.?	Temporal scale	Spatial scale	Accuracy	Remarks
Surface-water techniques	Physical techniques	Channel water budget	Limited	Event	Reach	Depending on flow data quality	*Only integral results for reach*
		Seepage meters (Infiltrometers)	Limited	Event–days	Point	Depending on number of sampling sites	*Not applicable during a flow event*
		Baseflow discharge	No	Months–years	Point	–	*No baseflow under arid conditions*
	Tracers	Heat as tracer	Limited	Event–years	Point	*Depending on accuracy of unsat. zone model*	Requires inverse numerical modeling
		Isotopes (e.g., $^{18}O, ^{2}H$)	No	Years–decades	Catchment	–	*Delivers no recharge rates*
	Process modeling	Watershed modeling	Limited	Day–years	Catchment	*Limited by rain data uncertainties*	High data demand
		Flow routing (hydrologic/ hydrodynamic)	Yes	Event	Point–reach	Accurate, if sufficient data are available	Gauging and morphological data required
Unsaturated-zone techniques	Physical techniques	Lysimeters	No	Years	Point	–	*Not suited for recharge estimation*
		Zero flux plane concept	Limited	Event–years	Point	*Depending on data quality; point estimate*	High data demand (water content and matrix potential)
		Darcy's law	Limited	Event–years	Point–Area	Depending on quality of conductivity field	*Recharge set equal to hydraulic conductivity*
	Tracers	Applied tracers (e.g., dyes, bromide)	Limited	Months-years	Point	*Point estimate*	Applicable for recharge rates $> 200\,\mathrm{mm \cdot a^{-1}}$
		Historical tracers (e.g., ^{3}H)	Limited	Years	Catchment	Depending on magnitude of tracer signal	*For recharge rates* $10–50\,\mathrm{mm \cdot a^{-1}}$
		Environmental tracers (e.g., Cl)	Limited	Months-years	Point	*Point estimate*	For recharge rates $< 100\,\mathrm{mm \cdot a^{-1}}$
	Process modeling	Richards' equation	Limited	Event–years	Point–Area	*Depending on data situation and macropore effects*	High data demand (soil hydraulic characteristics)
Saturated-zone techniques	Physical techniques	Water table fluctuation	Limited	Years	Catchment	Uncertainty of pumping data?	*Pumping rates need to be estimated*
		Darcy's law	Limited	Years–decades	Catchment	Depending on quality of conductivity field	*Method assumes no water extraction*
	Tracers	Historical tracers (e.g., $^{3}H/^{3}He$)	Limited	Months–years	Catchment	Depending on magnitude of tracer signal	*Recharge rates estimated only via age gradient*
		Environmental tracers (e.g., Cl)	Limited	Years	Point	*Point estimate*	–
	Process modeling	Groundwater flow models	Limited	Years	Catchment	Uncertainty of pumping data?	*Pumping rates need to be estimated*

generally classified into *direct methods* and *indirect methods*. Direct methods comprise (a) direct surface recharge; (b) direct subsurface recharge; and (c) combined direct methods (UNEP, 1998). Whereas direct subsurface recharge techniques aim towards a direct injection of water into the aquifer via wells, direct surface methods include techniques such as spreading basins, recharge pits and shafts, ditches, and recharge dams. Indirect methods artificially induce infiltration from hydraulically connected water bodies onto the land surface by lowering groundwater levels with pumping equipment. Further literature on various groundwater recharge projects can be found in Bouwer (2002) and Haimerl (2004), for example.

An efficient method for improving natural recharge from ephemeral rivers is the construction of *groundwater recharge dams*. In the last decades, several recharge dams have been erected on the northern coastal plain of Oman in order to promote recharge of the coastal aquifer system and to minimize freshwater losses to the sea (MRMEWR, 2007). Such dams span the wadi beds, retain flood flow, and support a decelerated release of water, typically over several days, which leads to higher infiltration opportunity times in the downstream wadi sections. Thus, recharge dams have to be distinguished from structures such as sand dams, where recharge occurs beneath the dam structure itself (Quilis et al., 2009). Furthermore, recharge dams prevent clogging of the downstream channel reaches by retaining sediment load. The dams decrease runoff dynamics significantly, since release rates—typically established by culvert release—are low compared with peak inflow rates. Therefore, simulating the runoff behavior in ephemeral channels under the influence of recharge dams requires the consideration of different types of runoff dynamics upstream and downstream of the dam, particularly for the possibly weak dynamics in the downstream reaches where standing wave effects can occur under small, though persistent, quasisteady release rates.

Figure 1.4 shows a schematic section of Oman's coastal plain with a recharge dam, located in a wadi bed. Groundwater extraction led to a dropping of the original groundwater table and the groundwater–saltwater interface shifted inland towards the zone of groundwater extraction. Infiltration below the dam leads to a recharge of groundwater which counteracts the groundwater drop. However, groundwater uptake is by far not equalized by artificially improved groundwater recharge, which lets groundwater tables drop further.

The hydrologic dimensioning of a recharge dam requires the determination of the design storage capacity, the spillway design flood, and the culvert design. The design storage capacity is usually related to an inflow volume of a certain probability, as well as to a return period. Typically, a return period of 15 to 30 years is chosen. The spillway design flood is estimated depending on a specific risk category in which the dam falls. Such risk categories are, for example, defined by the International Commission on Large Dams (ICOLD). For Oman's recharge dams, the design flood is mostly related to a return period of 10,000 years, or 0.5 times the probable maximum flood (PMF)[1], depending on what delivers the higher value (MAF, 1992). The dimensioning of the culvert outlets is generally carried out in a much less sophisticated way. To prevent malaria infestation[2], the outlets are designed so that they are capable of emptying the reservoir in 12 to 14 days at most by request of the health authorities in Oman (MAF, 1989). This approach should

[1] The PMF concept relates the probable maximum precipitation (PMP) via a rainfall–runoff simulation to a specific flood flow (the probable maximum flood). PMP is defined by WMO (1986) as "[...] the greatest depth of precipitation for a given duration meteorologically possible for a given size storm area at a particular location at a particular time of the year, with no allowance made for long-term climatic trends".

[2] For breeding, mosquitoes lay eggs which are potentially infected with plasmodium protists in open water bodies. The larvae need at least 14 days for maturing.

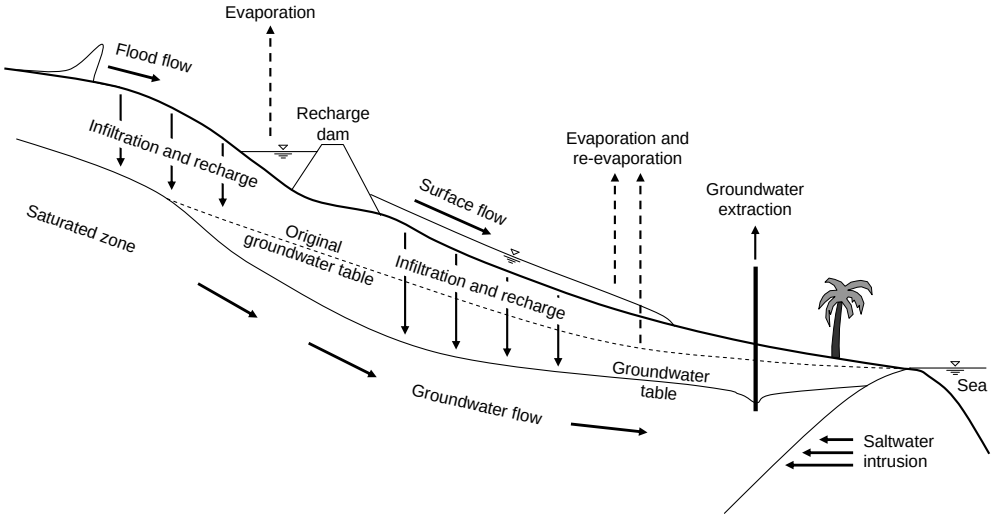

Figure 1.4: Groundwater recharge processes in ephemeral channels downstream of recharge dams.

be supplemented with a hydrodynamic investigation. Assuming a certain downstream wadi reach with appropriate infiltration characteristics, the question arises of what is a suitable outlet design for efficiently utilizing the available wadi reach length for groundwater recharge without causing losses, e.g., to the sea. The same applies for an optimal operation of the culverts with respect to a preferably high downstream infiltration quota.

Up to this point of the present thesis, vertical processes leading to groundwater recharge have been distinguished into surface flow, infiltration (or transmission losses), and recharge processes. A more detailed view of the involved processes, their influencing parameters, and suitable process models for their simulation is given in Fig. 1.5. The relevant processes which control groundwater recharge are surface flow, infiltration, evaporation and re-evaporation, percolation and water vapor transport in the unsaturated zone, as well as groundwater flow. Transmission losses (or potential indirect recharge, according to Section 1.1) are controlled by the interplay of surface flow, infiltration, and evaporation, which are further subsumed as *surface processes* (denoted with a dashed box in Fig. 1.5). These surface processes are subsequently discussed in more detail. It will get clear that, compared to channel infiltration and dam evaporation, direct evaporation from wadi flow is small to negligible (Menk, 1998). Hence, the scope of the recharge-influencing processes investigated in this study is set to interlinked surface flow and infiltration (solid box in Fig. 1.5).

Surface Flow: According to the nomenclature used in hydraulics textbooks, such as Chow (1959) or Subramanya (2009), ephemeral river flow can be generally classified as gradually-varied nonuniform (i.e., $\frac{\partial u}{\partial x} \neq 0$) and unsteady (i.e., $\frac{\partial u}{\partial t} \neq 0$) flow in a nonprismatic channel. When aiming at a process-based description of infiltration through a permeable bed, it is most important to quantify the dynamics of the wetted channel area. In contrast to perennial rivers, two characteristics of ephemeral river flow render hydrodynamics rather complex: (a) attributable to infiltration (and evaporation), the flow loses mass *and* a certain amount of momentum, and (b) a typically pronounced (i.e., surging) flow occurs over initially dry beds and transmission losses weaken process dynamics,

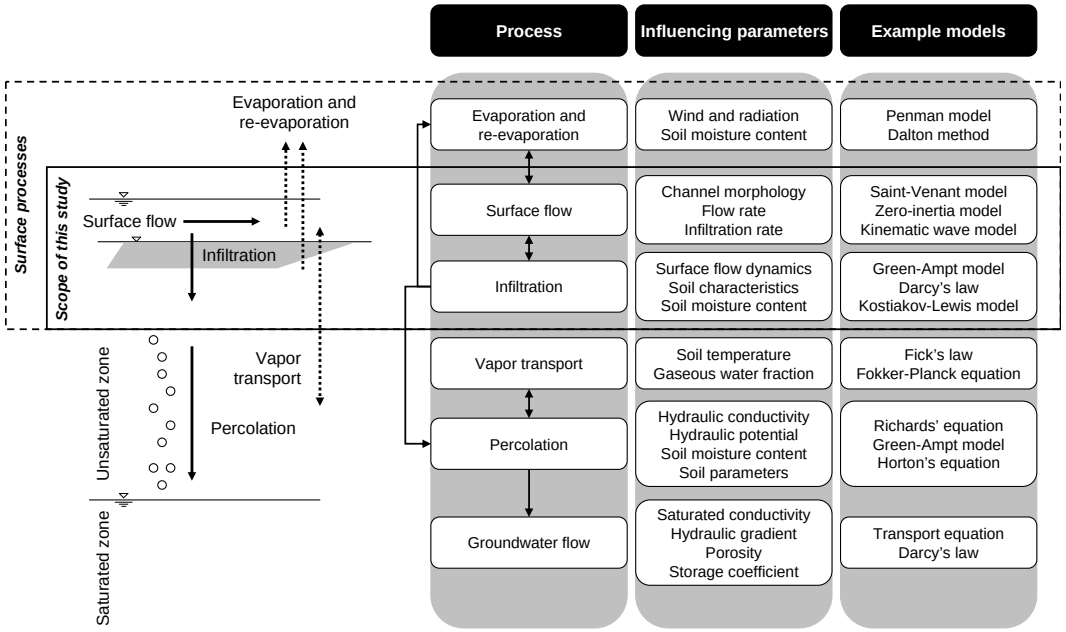

Figure 1.5: Involved processes, parameters, and mathematical process models for groundwater recharge estimation. Modified according to Haimerl (2004).

especially downstream of recharge dams. These findings establish two cardinal demands posed for a sound process description: (a) accounting for losses of mass and—if necessary—momentum in the process description, and (b) encountering the shortcomings of common numerical solution strategies for handling a dry-channel initial condition and significant infiltration losses (Schmitz, 1989; Garcia-Navarro et al., 1999). This thesis presents a modeling framework which is able to meet the aforementioned specific demands of ephemeral river routing.

Infiltration: Infiltration from free surface flow causes losses which either contribute to groundwater recharge or re-evaporate into the atmosphere. Infiltration appears at the interface of the surface and the subsurface. Water moving further downward through the porous soil matrix, driven by the gravitational force (and, to a certain degree, the matrix potential), establishes percolation and, consequently, recharge. A certain amount of soil water can be held by the capillary forces of the soil matrix against gravitation. This water may be transferred further downward with the next infiltration event, move upwards again due to capillary rise, or be transported as water vapor. Under matrix flow conditions, infiltration rates are dependent on the initial soil moisture, the soil hydraulic characteristics, and the upper boundary condition, e.g., given as the pressure head which results from the depth of ponding surface water. Assuming the depth of the groundwater table is significantly larger than the ponding water depth[1], an application of Darcy's law shows that the water depth at the upper soil layer is negligible with respect to initial infiltration rates as, shown by Bouwer (1982), for example. In turn, the groundwater level does not impact infiltration rates and, therefore, initial infiltration equals the hydraulic conductivity of the unsaturated zone under conditions found, e.g., in Oman (Bouwer, 2002). However, infiltration rates typically decrease

[1] Which means, e.g., twenty times or more.

Table 1.4: Typical values of the hydraulic conductivity for various soils. Taken from Bouwer (1999).

Soil type	Hydraulic conductivity ($mm \cdot d^{-1}$)
Clays	< 100
Loams	200
Sandy loams	300
Loamy sands	500
Fine sands	1,000
Medium sands	5,000
Coarse Sands	10,000

over time due to a decrease in the driving pressure-head gradient, attributable to the downward movement of the wetting front.

For the coarse upper layers of the thick, unsaturated alluvial soils found in wadi beds, the matrix gradient does not strongly differ from zero and the initial vertical water movement is mainly, but not solely, a consequence of gravitation (Scanlon and Healy, 2002). Moreover, as already discussed, the influence of a transient hydrostatic pressure head on wadi infiltration is assumed to be small (Bouwer, 1982; Haimerl, 2004).[1] Furthermore, infiltration on permeable alluvial material is also driven by macropore flow processes (Beven and Germann, 1982; Wood et al., 1997). Together with the limited data situation in arid areas, the applicability of matrix flow models (i.e., models based on Richards' equation) for the quantification of infiltration is often precluded. The present study, therefore, incorporates an empirical Kostiakov-Lewis model for predicting wadi infiltration (cf. Section 6.1.1.1), whereas the novel modeling approaches developed herein are not restricted to a specific procedure for the quantification of infiltration losses. The Kostiakov-Lewis model offers a reliable performance in predicting infiltration rates on various dryland soils, which was shown, e.g., by Zolfaghari et al. (2012) who fitted seven empirical infiltration models to field data of (semi)arid regions in Iran, where the Kostiakov-Lewis approach performed best. Bouwer (1999) gives estimates of the unsaturated hydraulic conductivity—and, therefore, potential infiltration rates, as outlined above—for various soils (Table 1.4). For the alluvium covering the beds of Oman's coastal wadis, values of some hundred to some thousand millimeters per day are typical (Haimerl, 2004), which is confirmed by the infiltrometry data used for this thesis, presented in Chapter 7.2.1.

Evaporation and Re-Evaporation: Event-related direct evaporation from wadi flow is negligible. Infiltrometry tests for Oman showed infiltration rates of some hundreds to thousands of millimeters per day for the wadi bed alluvium (e.g., MAF, 1990), whereas typical potential evaporation is 5 to $10\,mm \cdot d^{-1}$ (Fisher, 1994). In contrast, case studies, e.g., of Strobl and Haimerl (1999), have estimated reservoir evaporation from Omani recharge dams to be some per cent up to 20 % of total retained flow volumes. Therefore, dam evaporation is regarded in this study with respect to a sound assessment of the dam water balance and potential downstream recharge. The quantification of re-evaporation of infiltrated water from wetted alluvial topsoils in an Omani wadi,

[1] If the matrix gradient and the hydrostatic surface potential are neglected, the driving total head gradient is equal to unity which is often referred to as unit-gradient assumption (Scanlon and Healy, 2002). Consequently, infiltration rates will be constant under these conditions. However, such a constant-rate approach might be questionable for transmission loss modeling since infiltration experiments (e.g., Haimerl, 2004; Zolfaghari et al., 2012) often show a noticeable temporal decline of infiltration rates. This is especially the case if finer material can be found between coarser fractions of the alluvium, which is generally the rule rather than the exception in arid areas.

located in the Al Batinah Region, was comprehensively investigated by Haimerl (2004). Although re-evaporation can consume a significant amount of transmission losses and, therefore, reduce groundwater recharge (cf. Fig. 1.1), the cited study essentially found by means of field and model experiments that re-evaporation losses are very small (8 to 16 $mm \cdot a^{-1}$) if recharge occurs during temporarily isolated events, which is generally the rule rather than the exception for Northern Oman. Re-evaporation is, therefore, not considered in the modeling approaches developed herein.

1.4 The Role of Overland Flow for Flash Flood Formation

Overland flow on hillslopes is the driving process of runoff concentration and, therefore, flood formation in semiarid and arid areas during flood-prone hydro-meteorological situations. Flow on the surface is affected by topography and micro relief of the catchment, positive and negative mass (and minor momentum) contributions attributable to precipitation and infiltration, antecedent wetness conditions, erosion and deposition of soil material, and water supervening from upper parts of the catchment. The preceding listing illustrates the complex character of surface flow processes and renders their closed, physically-based description nearly impossible, since the relevant processes are strongly interconnected as well as highly nonlinear, and available data for such an ambitious process modeling will always be lacking for real meso-scale catchments in (semi)arid areas.

The concept of *sheet flow* is commonly used to tackle the aforementioned problems when aiming at a process-oriented modeling of surface flow. This means that the flowing water on the surface is considered to be a somehow virtual, moving water body (or sheet of water), traveling down a characteristically rough slope without considering the real flow conditions in rills and small channels. Nevertheless, only the average characteristics of the water movement are portrayed this way. For the one-dimensional case, there are only a few studies (e.g., Tayfur and Kavvas, 1998) that try to overcome the simplifications of the sheet flow concept towards a more realistic representation of rill flow, which of course results in a mostly unrealistically high data demand. The same applies for two-dimensional approaches (e.g., Howes et al., 2006; Liu et al., 2004), which are not only restricted by the sheet flow assumption, but also demand highly-resolved information on surface and subsurface characteristics, as well as topography.

Moreover, uncertain rainfall data might not justify the application of process-oriented models for the simulation of runoff concentration. Especially for drylands, conceptual approaches, such as more or less lumped nonlinear (leaky) storage models, or even empirical relationships between spatially-averaged rainfall and gauged ephemeral runoff, can deliver comparably good results under the rainfall uncertainties typical for arid areas (McIntyre et al., 2007; Al-Qurashi, 2008; Al-Rawas, 2009). Nevertheless, future developments in Oman encourage the hope for better rainfall prediction from rainfall radars, spaceborne data (e.g., emerging from the Tropical Rainfall Measuring Mission, Kummerow et al., 1998), and short-term numerical weather predictions, e.g., in order to issue a reliable flash flood warning (Grabs, 2012). Under such conditions, only a distributed and physically-based modeling approach is able to fully exploit a highly resolved precipitation forecast.

1.5 Objectives of the Thesis

Tooth (2000) provides a remarkably comprehensive review on the state of the art in recent dryland river research, wherein the author outlines a strong demand for a better assessment of transmission

losses. During the past two decades, a vast number of studies were published on interacting surface–subsurface processes on the land surface and in river channels, which can be seen strikingly from the references given in Stanley and Jones (2000), Sophocleous (2002), Morita and Yen (2002), Wöhling et al. (2004a), and Wöhling and Schmitz (2007). Sophocleous (2002) stated that the main obstacle for a proper assessment of surface–subsurface processes is the limited understanding of near-channel and in-channel water exchange processes, which would be the key for a more sophisticated assessment and management of water resources. The author further calls upon research on the spatiotemporal dynamics of groundwater recharge processes from open channels. The study concludes that these efforts demand a physically-based description of flow dynamics.

This thesis essentially develops three *process-oriented*, i.e., physically-based modeling components, bundled within an *integrated system*, which further contributes to an integrated water resources management (IWRM) toolbox for Oman's Batinah Region (Grundmann et al., 2012). The central element of the integrated modeling system is a hydrodynamic free surface flow model which aims at overcoming the hydrological problem to adequately mimic the propagation of a waterfront on an initially dry soil, strongly influenced by infiltration. This is, e.g., required for the description of transient, indirect groundwater recharge resulting from infiltrating flow in ephemeral channels, influenced by the operation of groundwater recharge dams. Besides the highly nonlinear interplay of surface flow and infiltration downstream of a recharge dam, the modeling system needs to consider the effects of dam operation and upstream hydrodynamics to predict the dam inflow. Thus, upstream hydrodynamics and dam operation are also each portrayed with a physically-based modeling component within the integrated system.

As a corollary of the intended process-orientated approach, the incorporated model components have to be coupled in a reasonable manner. This demands a flow-boundary-based coupling of surface flow and a simultaneous inclusion of transmission losses in the governing process equations. Special attention has to be drawn on the sound (i.e., stable[1] and accurate[2]) portrayal of advancing dam release flow in an initially dry channel (cf. Section 1.1), which is challenging for common numerical solution procedures applied to the governing equations. To cope with the aforementioned demands, a novel analytical solution procedure of the flow equations is proposed. It is further shown that the proposed analytical approach can also provide a robust and reliable description of overland flow processes under infiltration.

1.6 Structure of the Work

This thesis is divided in nine chapters, the first three of which follow a hierarchical structure. Figure 1.6 provides a representation of the structure of the thesis.

Chapter 2 delivers the state of the art of surface-water based and process-oriented modeling of transmission losses in ephemeral channels on the basis of a comprehensive *review of the literature*. Furthermore, the chapter reviews studies on *overland flow modeling* with hydrodynamic approaches, which also unveils a need for improvements.

Chapter 3 presents the *theoretical background* of common hydrodynamic process models for open channel and overland flow modeling.

[1] The term "stability" is defined in Section 4.2.1.

[2] With respect to mass conservation and with respect to matching observed flow dynamics.

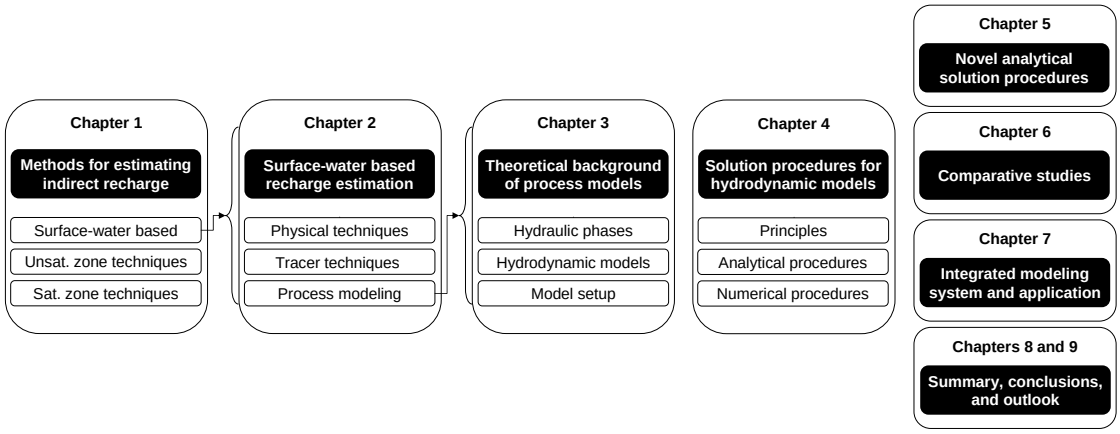

Figure 1.6: Representation of the structure of the thesis.

Chapter 4 covers the *theory of numerical and analytical solution procedures* for the hydrodynamic models and their *applicability* under the governing process characteristics. The *need for innovation* is outlined by means of an intercomparison of available modeling approaches with respect to the specifics of the scoping area of this study.

Chapter 5 presents a *novel analytical solution theory* of the zero-inertia simplifications of the full hydrodynamic process description, which is able to fully satisfy the specific demands of *routing advancing and infiltrating dam release flow*. Based on the same theory, an analytical *overland flow* model is derived which employs the sheet flow analogon of surface flow.

Chapter 6 carries out a *comparison of the proposed analytical models with generally accepted approaches* in order to prove the accurateness and applicability of the novel analytical modeling concepts.

Chapter 7 shows the inclusion of the analytical zero-inertia approach within the frame of a novel *integrated wadi flow and dam simulation model* for the assessment of indirect groundwater recharge resulting from recharge dam operation for a study area in Northern Oman.

Chapter 8 *summarizes* the main findings of this thesis and draws *conclusions*.

Chapter 9 delivers an *outlook* on issues requiring further research.

Chapter 2

Literature Review

The literature review carried out for this thesis defines the state of the art of surface-water based estimation of groundwater recharge from wadi channels. It will become clear that only a process-oriented modeling concept can provide rigorous and accurate insight into the involved intricate flow phenomena. Further effort is made to outline the demands and limits of overland flow modeling in arid areas, where it is shown that infiltrating channel flow and overland flow can be modeled with the same concepts but, on the other hand, can both involve inconveniences when solving the governing flow equations by means of numerical procedures.

2.1 Review of Surface-Water Based Studies on the Estimation of Indirect Groundwater Recharge from Ephemeral Channels

As discussed previously, surface-water based process-modeling techniques hold the highest potential for the estimation of indirect groundwater recharge from infiltrating ephemeral channel flow. A number of studies which carried out surface-water based analyses of indirect recharge in (semi)arid areas are available from the literature. Table 2.1 concisely shows information on the methodology applied in various publications. The selection attempts to cover all relevant papers of the recent years in order to deliver an overview of the state of the art of indirect recharge estimation, where a focus is set on physical and process-oriented methods (cf. Table 1.3). Typically, for all reviewed studies, the potential indirect recharge is estimated by considering the event-based transmission losses in an infiltrating wadi reach. All studies which are shown in Table 2.1 focus on the estimation of transmission losses in dryland areas, comprising the Southwestern United States (Walnut Gulch Experimental Watershed at Tombstone, Arizona), the Arabian Peninsula (Saudi Arabia, Oman), Egypt, India, Namibia, Israel, as well as semiarid areas in Australia and Brazil.

Besides flood propagation under transmission losses, roughly half of the publications (11/24) also address runoff generation and runoff concentration processes. If considered, runoff generation is modeled with approaches ranging from empirical regression methods (McIntyre et al., 2007; Al-Rawas, 2009), over the empirical SCS curve number method (e.g., Sorman and Abdulrazzak, 1993; Saber et al., 2009), to semi-distributed and distributed water balance modeling (e.g., Costelloe et al., 2003; Goodrich et al., 2004). Runoff concentration is described with methods ranging from

Table 2.1: Overview of selected literature on surface-water based (physical and process-oriented) estimation of indirect recharge in (semi)arid areas.

Reference	Portrayed R–R processes	Region	RG/RC model components	RG/RC model resolution	FP approach	FP model	TL model
Walters (1990)	FP	USA, KSA	–	–	EM	GGC	REG
Sorman and Abdulrazzak (1993)	RG, RC, FP	KSA	SCS, TRAN	SD	EM	GGC	REG
Sharma and Murthy (1994)	FP	IND	–	–	EM	GGC	REG
Hughes and Sami (1994)	RG, RC, FP	–	WB, STO	SD	HL	STO	KL
Sharma and Murthy (1995)	FP	IND	–	–	HL	STO	REG
Sharma and Murthy (1996)	FP	IND	–	–	HL	STO	LRA
El-Hames and Richards (1998)	RG, RC, FP	KSA	WB, KW	SD	DY	HD	RE
Dunkerley and Brown (1999)	FP	AUS	–	–	EM	GGC	REG
Shentsis et al. (1999)	FP	IL	–	–	EM	GGC	REG
Lange et al. (1999)	RC, FP	IL	REC	SD	HL	MCM	CRA
Gheith and Sultan (2000)	RG, RC, FP	ET	SCS, UH	SD	EM	LAG	REG
Shentsis and Rosenthal (2003)	FP	IL	–	–	EM	GGC	REG
Chapman (2003)	FP	AUS	–	–	HL	STO	CRA, EXP, SMD
Costelloe et al. (2003)	RG, RC, FP	AUS	WB, STO	DS	HL	STO	REG
Goodrich et al. (2004)†	RG, RC, FP	USA	WB, KW	SD	DY	KW	CWB
Haimerl (2004)	FP	OM	–	–	DY	MS	RE
Lange (2005)	FP	NAM	–	–	HL	MCM	–††
Mudd (2006)	FP	USA	–	–	DY	HD	RE
McIntyre et al. (2007)	RG, RC, FP	OM	REG	SD	EM	GGC	REG
Al-Qurashi et al. (2008)	RG, RC, FP	OM	WB, KW	SD	DY	KW	CWB
Al-Rawas (2009)	RG, RC, FP	OM	REG	SD	EM	GGC	REG
Morin et al. (2009)	FP	NAM	–	–	DY	KW	CRA
Saber et al. (2009)	RG, RC, FP	OM, KSA, ET	SCS, KW	DS	DY	KW	REG
Costa et al. (2012)	FP	BR, USA	–	–	DY	KW	GA

With R–R: rainfall–runoff; RG: runoff generation; RC: runoff concentration; FP: flood propagation; TL: transmission loss; USA: United States; KSA: Saudi-Arabia; IND: India; AUS: Australia; IL: Israel; ET: Egypt; NAM: Namibia; OM: Oman; BR: Brazil; SCS: SCS method; TRAN: runoff translation function; WB: water balance; STO: (non)linear storage model; KW: kinematic wave hydrodynamic model; REC: rainfall excess convolution; UH: unit hydrograph; SD: semi-distributed; DS: distributed; EM: empirical; HL: hydrologic; DY: hydrodynamic; GGC: gauge to gauge correlation; HD: full hydrodynamic model; MCM: Muskingum-Cunge method; LAG: empirical lag time formula; MS: Manning-Strickler approach; REG: regression model; KL: Kostiakov-Lewis model; LRA: "leaky reservoir" approach; RE: Richards' equation; CRA: constant rate; EXP: exponential decline; SMD: dependent on soil moisture deficit; CWB: via remainder term of channel water balance; GA: Green-Ampt infiltration model.

†The study reviews different recharge estimation methods. Only process-oriented methods are regarded for this table.

††Transmission losses were excluded from modeling and derived by comparing modeled to observed hydrographs.

simple translation functions (Sorman and Abdulrazzak, 1993), over rainfall excess convolution with empirical catchment response functions (Lange et al., 1999) and the unit hydrograph method[1] (Gheith and Sultan, 2000), to conceptual storage models (Hughes and Sami, 1994; Costelloe et al., 2003), and hydrodynamic overland flow models (e.g., El-Hames and Richards, 1998; Saber et al., 2009).

Nevertheless, only three of the 24 reviewed studies explicitly assess losses during runoff concentration (cf. Fig. 1.1), e.g., by employing a spatially distributed modeling approach (Costelloe et al., 2003; Saber et al., 2009). Hence, a cell-wise consideration of precipitation, rainfall excess, and infiltration delivers potential direct recharge during the overland passage. Another possibility for assessing the direct recharge from overland flow is to include a loss term in the overland flow equations, as proposed, e.g., by El-Hames and Richards (1998). Especially regarding runoff generation and concentration, it should be emphasized again that, although a comprehensive modeling of rainfall–runoff processes in arid areas is a noble goal, the lacking quality and extreme variability of rainfall data introduces potentially tremendous uncertainties (Fisher, 1994; Wheater, 2002; McIntyre et al., 2007; Al-Rawas and Valeo, 2009).

For the estimation of indirect recharge, the ephemeral channel flow and the dependent transmission losses need to be regarded. According to Table 1.3, the channel processes are modeled with routing approaches[2], or by using simpler empirical models, such as gauge to gauge correlation (e.g., applied by Shentsis et al., 1999; Shentsis and Rosenthal, 2003) or empirical lag time formulas (Gheith and Sultan, 2000). Routing methods can be grouped into hydrologic (conceptual) and hydrodynamic (physically-based) approaches.[3] Typical hydrologic routing models are (non)linear storage-routing models of a river reach (e.g., Hughes and Sami, 1994; Sharma and Murthy, 1996) or the Muskingum-Cunge method (Lange et al., 1999; Lange, 2005). Hydrodynamic approaches are based on the solution of the full hydrodynamic flow equations or their simplifications (cf. Chapter 3) and were applied, e.g., by El-Hames and Richards (1998), Goodrich et al. (2004), Morin et al. (2009), and Costa et al. (2012). For the reviewed 24 papers, empirical, hydrologic, and hydrodynamic models are used similarly frequently for the simulation of flood propagation (empirical: 9/24; hydrologic: 7/24; hydrodynamic: 8/24).

Simple empirical gauge to gauge correlations deliver only integral values of recharge within a reach between two considered flow gauges. For deriving a spatially distributed information of transmission losses along the channel, many authors applied regression models (e.g., Sharma and Murthy, 1995; Dunkerley and Brown, 1999; Saber et al., 2009) which essentially relate occurring losses to channel reach length or discharge. Other authors, such as Lange et al. (1999) used constant loss rates together with hydrologic routing approaches, such as the Muskingum-Cunge method. Sharma and Murthy (1996) modified a conceptual storage-based routing model with leaky reservoirs, i.e., a constant or storage-dependent amount of water is lost along the channel.

[1] Strictly speaking, the unit hydrograph method also performs a convolution of (excess) rainfall with a hypothetical unit response (i.e., the unit hydrograph).

[2] Fread (1993): "Flow routing is a mathematical procedure for predicting the changing magnitude, speed, and shape of a flood wave as a function of time (i.e., the flow hydrograph) [...]"

[3] More precisely, there is a hydrologic and a hydraulic path to derive routing methods. The hydrologic approach towards a routing method is to account for the translation and retention of water in virtual storages along a flowpath. The hydraulic approach considers the forces affecting the movement of a representative body of water. Therefore, formal similarities or even physical adequateness may exist between hydrologic and hydraulic (i.e., hydrodynamic) models. For instance, the linear kinematic wave model (cf. Appendix 4.3) is a different form of the Muskingum-Cunge method (Cunge et al., 1980), and vice versa.

Morin et al. (2009) also applied constant loss rates together with a hydrodynamic routing model, which was based on the kinematic wave simplifications of the Saint-Venant equations (cf. Section 3.2.3). As later shown in this thesis, this constant-rate approach is questionable for modeling highly dynamic and infiltrating events. Flow observations show that the rising hydrograph of flash flood events may steepen while the flood wave travels downstream, which is reported, for example, by Sharma and Murthy (1994), Sharma and Murthy (1995), and Lange (2005). This behavior is not singularly an intrinsic corollary of the pronounced hydrodynamics, but also a result of intense initial losses at the wetting wave front. Field studies which quantify the temporal evolution of infiltration rates after wetting (e.g., Haimerl, 2004) support these findings.

Chapman (2003) presented a methodology to model the impact of recharge on streamflow recession. The study employs a nonlinear storage routing model in order to validate the applicability of several assumptions regarding indirect recharge: (a) The recharge is constant; (b) the recharge has an exponential decline; and (c) the recharge is dependent on the vadose zone moisture deficit and the dependency is expressed by a semi-empirical function. Although only a small number of the regarded 28 catchments featured (semi)arid conditions, the work strongly supports the conclusion that recharge is of *transient* nature. This finding is essentially no surprise since the main influencing factors of transmission loss formation, namely infiltration rates, the wetted infiltrating area, infiltration opportunity times, and soil moisture, are transient.

A way of including transient infiltration during a flow event is the application of infiltration formulas. Most commonly for this approach, the Kostiakov-Lewis formula is used (e.g., Hughes and Sami, 1994). If sufficient infiltrometry data are available for parametrization, the Kostiakov-Lewis model can deliver reliable estimates of infiltration through the permeable channel bed, which is later shown in this thesis. In contrast, conceptual infiltration models, such as the Green-Ampt model (e.g., Costa et al., 2012), or process-oriented approaches, such as Richards' equation (e.g., El-Hames and Richards, 1998; Haimerl, 2004; Mudd, 2006), can be applied, which raises the demand for specific soil data, e.g., porosity, conductivity, and water content.

Costa et al. (2012) developed a process-oriented model for assessing in-channel transmission losses for both hydraulically connected and disconnected streams, considering a possible transition between the two. Surface flow dynamics were modeled with a kinematic wave approach and infiltration was described with the Green-Ampt model. The authors point out that the application of the Green-Amp model under hydraulically disconnected conditions (which is the rule rather than the exception in arid areas) usually precludes an analytical solution of the infiltration model, which might exacerbate the coupling of surface flow and infiltration. Moreover, the authors explicitly state that their approach does not focus on the prediction of in-channel flow dynamics, especially under hydraulically disconnected conditions. Consequently, their model showed a rather poor performance regarding the agreement of simulated and observed hydrographs in an arid catchment in the Southwestern United States (Walnut Gulch Experimental Watershed).

Mudd (2006) coupled a full hydrodynamic surface flow model with a Richards model to quantify transmission losses. Although the study aims at flash flood modeling in ephemeral channels, no real-world application was performed. Nevertheless, the numerical analyses carried out in the study strongly demand the inclusion of losses in the mass balance *and* the momentum equation of the incorporated hydrodynamic model for advancing-flow conditions under high transmission losses. Furthermore, the author showed a way to circumvent numerical inconveniences when modeling

flow with steep, shock-like gradients over initially dry channel beds by applying a shock-capturing technique.

Regarding the degree of process orientation, one of the most rigorous investigations was carried out by El-Hames and Richards (1998) who coupled a full hydrodynamic flow model with Richards' equation and applied the system for predicting flow hydrographs and transmission losses in Saudi Arabian wadis. Furthermore, the authors included a semi-distributed catchment model with a process-oriented overland flow component, which considers a loss term in the continuity equation of the incorporated kinematic wave model. The modeled hydrographs were mostly in good agreement with observed ones, even though the application of a matrix flow model (i.e., Richards' equation) is problematic for alluvial bed material. Moreover, the authors report of singularity problems when applying common numerical solution schemes (e.g., finite difference methods) to the flow equations for overland and channel flow under dry-channel initial conditions. These numerical inconveniences are stronger for steeper gradients of the flow variables (e.g., water depth) and/or weakening process dynamics, as they would occur as a consequence of progressive significant infiltration, for example.

Haimerl (2004) is the only author of the listing in Table 2.1 who tried by means of process modeling to assess transmission losses influenced by artificial groundwater recharge dams. However, in his study, the hydrodynamics downstream of an Omani dam were only described with an assumptive steady Manning-Strickler approach, which essentially delivered a value for the flow duration and a "theoretical flow length", both of highly assumptive character. Nevertheless, the study was focused on infiltrometry experiments and their numerical validation and, therefore, gives sound insight into the governing infiltration processes.

Summing up, the development of a suitable modeling system for ephemeral flow under the control of a groundwater recharge dam needs to satisfy the following demands, which have not yet been fulfilled by any available approach at the same time. The model should:

- ▷ regard the governing hydrodynamics of the infiltrating flow (i.e., apply a process-oriented approach);
- ▷ include transmission losses in the mass *and* the momentum balance, where necessary (e.g., for advancing flow influenced by strong transmission losses);
- ▷ account for a transient development of infiltration after the initial wetting; and
- ▷ circumvent numerical issues and singularity problems when modeling advancing free-boundary flow on an initially dry channel bed under weakening process dynamics.

Especially the last point of the above listing strongly motivates the application of an *analytical solution strategy* for the governing model equations. Analytical solutions for open channel flow models are available for the Saint-Venant equations (e.g., Chalfen and Niemiec, 1986; Wang et al., 2002; Chung and Kang, 2004) and their simplifications, namely the zero-inertia equations (e.g., Schmitz et al., 2002; Fan and Li, 2004) and the kinematic wave model (e.g., Henderson, 1966; Singh, 1996). However, most of the aforementioned approaches introduce assumptions which make them inapplicable under the outlined problem-specific conditions. The problems for deriving an analytical hydrodynamic model which is universally applicable are discussed in more detail in Chapter 4. Consecutively, Chapter 5 presents a novel analytical open channel flow model which satisfies the afore-listed demands of flow routing under transmission losses in ephemeral channels.

2.2 Review of Literature on Process-Oriented Overland Flow Modeling

In arid areas, overland flow is the predominant runoff component during the phase of runoff concentration, which calls for a process-oriented description (Dunne and Aubry, 1986; Kirkby, 1988). Apart from the very limited knowledge of the process-influencing topography previously discussed in this work, rainfall and infiltration establish significant source/loss terms which should be regarded in a physically reasonable manner. Besides using empirical approaches, simple volume balance models, or conceptual (storage-type) models, overland flow is, therefore, mostly simulated with hydrodynamic models.

Basically, the same flow models as those for open channel flow can be applied for simulating overland flow. The governing equations are either used in a one-dimensional form—which, consequently, implies the sheet flow analogon (cf. Section 1.4)—or within the frame of a two-dimensional analysis. The latter approach does not assume a fixed flow network, which renders a two-dimensional model more suited for erosion studies. When aiming at a one-dimensional model, there are two ways for reducing the two-dimensional flow problem[1] to one spatial dimension: (a) The model elements are defined in a way that they yield a cascade of one-dimensional flow elements (e.g., Schmid, 1990; Bronstert and Plate, 1997; Bronstert, 1999), or—which is more assumptive—single planes are used for a lumped representation of the land surface, e.g., as inherent to the widely known KINEROS model family (Smith et al., 1995), and (b) a routing algorithm is used to determine a single outflow direction for each flow element[2], which is a common method in distributed (i.e., cell-wise) one-dimensional overland flow modeling (e.g., Howes et al., 2006; Saber et al., 2009).

Hydrodynamic overland flow modeling incorporates the Saint-Venant equations or their simplifications, namely, the zero-inertia and the kinematic wave approximation (cf. Sections 3.2.2 and 3.2.3). Despite the fact that the kinematic wave approach for overland flow modeling has been extensively studied (e.g., by Henderson and Wooding, 1964; Ross et al., 1979; Hjelmfelt, 1981; Hjelmfelt, 1984; Govindaraju et al., 1992; Jaber and Mohtar, 2003; Liu et al., 2004) and a great number of researchers (e.g., Woolhiser and Liggett, 1967; Zhang and Cundy, 1989; Esteves et al., 2000) have investigated the usability of one-dimensional and two-dimensional full hydrodynamic Saint-Venant models for this task, far less has been reported on the validity, limits, and applicability of the zero-inertia or diffusion wave approximation (which some authors consider synonymous, while some others do not[3]).

Morris and Woolhiser (1980) first used the zero-inertia simplification of the full Saint-Venant equations for overland flow modeling. They showed that the often assumed validity of the kinematic wave approximation can be harmed under highly subcritical flow conditions (e.g., on a flat and/or

[1] In fact, turbulent flow is variable in all three spatial dimensions. Typically, two-dimensional hydrodynamic model approaches neglect the process variability in one direction by introducing a depth averaging of the variables (cf. Section 3.2).

[2] A widespread algorithm for deriving a one-dimensional flow network is the one proposed by Tarboton (1997). The paper further lists comprehensive references to other flow-network algorithms.

[3] Yen and Tsai (2001) outline the differences between the often synonymously used terms "diffusion wave approximation" and "zero-inertia approximation". They state that the term "diffusion wave approximation" includes the class of zero-inertia waves but is not limited to it. The technique most often used—to neglect the convective and local acceleration terms of the full dynamic process description (cf. Section 3.2)—should be termed "zero-inertia approximation" according to the authors. On the other hand, numerous authors (e.g., Govindaraju et al., 1988; Singh, 1996) call the aforementioned neglecting of terms "diffusion wave approximation". In this thesis, the term "zero-inertia approximation" is used.

very rough terrain). Daluz Vieira (1983) compared 150 simulations on the basis of the Saint-Venant equations with those obtained by the kinematic wave and the zero-inertia approximation for a range of flow conditions, rendered by various Froude numbers[1] and kinematic wave numbers[2]. Their study shows the wide applicability and validness of the zero-inertia approximation for Froude numbers smaller than 0.5 and kinematic wave numbers greater than 20. As Morris and Woolhiser (1980), Govindaraju et al. (1988) showed that for Froude numbers < 0.5 and low kinematic wave numbers, the kinematic wave approximation may fail.

The governing process equations are most often solved numerically. Compared to open channel flow, surface roughness strongly impacts the overland flow, which can cause problems when applying standard numerical solution procedures to the flow equations. Many authors report of serious problems, like attenuation errors, phase errors, and discretization errors, e.g., Wasantha Lal (1998), Singh (2002), Jaber and Mohtar (2003), and Tsai and Yang (2005), to name only a few. Moreover, the variability of surface topography lies within the same order of magnitude as the overland flow depth, which poses further obstacles for numerical solution schemes (Zhang and Cundy, 1989). To circumvent such problems, there is a vital demand for an analytical treatment of the overland flow models.

Henderson and Wooding (1964) developed analytical solutions of the KW model. Baiamonte and Agnese (2010) presented an analytical solution considering Green-Ampt infiltration, based on the characteristic equations of the KW model (cf. Section 4.1). Mizumura (2006) also applied the method of characteristics to the KW equations for time-varying excess rainfall rates. By postulating a sinusoidal rainfall function and by expressing discharge per unit width using a simple parabolic model, the author was able to derive a closed-form analytical solution which performed quite well with respect to observed data. Mizumura and Ito (2011a) compared the results of their former model with solutions obtained from a numerical KW model, which again yielded reasonable results. With the same strategy, Mizumura and Ito (2011b) expanded their analytical model to accommodate for moving rainstorms of a constant direction and velocity by shifting the incorporated sinusoidal rainfall functions in time. The results were again in good agreement with numerical solutions and reasonably predicted observed overland flows.

However, research on analytical solutions of the zero-inertia equations for overland flow problems remains limited. Govindaraju et al. (1988) proposed an analytical solution of the zero-inertia problem for steep slopes under invariant rainfall conditions. Such a steep-slope assumption allows to apply a zero-depth gradient boundary condition (cf. Section 3.3). This methodology—like in the case of the research presented herein—leads to nonlinear equations that can be solved by means of numerical or analytical methods and can deliver a solution for the rising as well as the recession hydrograph. Govindaraju et al. (1990) and Govindaraju et al. (1992) expanded the aforementioned

[1] The Froude number is used to discriminate supercritical and subcritical flows by relating the mass transport velocity u [LT^{-1}] to wave celerity $c = \sqrt{gh}$ [LT^{-1}]:

$$F = \frac{u}{c}$$

with g: acceleration due to Earth's gravity [LT^{-2}] and h: water depth [L]. If $F < 1$, the flow is called subcritical, if $F > 1$, it is called supercritical. The water depth corresponding to $F = 1$ is called critical depth.

[2] According to Singh (1994), "The kinematic wave number reflects the effect of bed slope, channel length, normal flow depth, and Froude number". First proposed by Woolhiser and Liggett (1967), the dimensionless kinematic wave number for a flow element is defined by

$$\kappa = \frac{S_0 L_0}{h_\mathrm{n} F^2}$$

where S_0: general slope of the flow element [−]; L_0: length of the flow element [L]; and h_n: normal flow depth [L].

concepts to an approximate analytical solution for space-time-varying rainfall input and lateral inflow for one-dimensional and two-dimensional cases.

Furthermore, the literature shows no evidence of an exact analytical solution of the zero-inertia equations for milder slopes, where the realistic portrayal of the lower flow boundary is important, as well as under arbitrarily time-varying (i.e., unsteady) rainfall. A number of authors introduced and expanded upon a free boundary formulation of the zero-inertia problem, introduced by Schmitz and Seus (1987), who proposed an exact—not only an approximate—analytical solution to the problem. The developed models already performed well for a wide range of model applications, e.g., border and furrow irrigation (Schmitz, 1989; Schmitz and Seus, 1990; Schmitz and Seus, 1992), coupled one-dimensional surface–two-dimensional subsurface flow (Wöhling et al., 2004b; Wöhling, 2005; Wöhling et al., 2006; Wöhling and Schmitz (2007); Wöhling and Mailhol, 2007), and surge flow in prismatic and non-prismatic channels over initially dry beds (Schmitz et al., 2002).

As for open channel flow modeling, although analytical solutions of the full hydrodynamic model for overland flow phenomena are available, such solutions are often derived under restricting conditions, e.g., constant rainfall rates (e.g., Singh, 1996) or strongly simplified depth-discharge relationships (e.g., Wang et al., 2002). Such restrictions might consume the advantages of the more detailed process description of the full hydrodynamic model, compared to the kinematic wave or zero-inertia model. However, analytical solutions of the flow models are important for benchmarking numerical solution methods (cf. Section 4.3). In this thesis, a novel analytical solution strategy for the zero-inertia model is developed, not only for open channel flow in Section 5.1, but also for setting up an accurate analytical overland flow model, which is outlined in Section 5.2.

2.3 Summary

The literature indicates foremost that an assessment of indirect recharge from infiltrating ephemeral river flow should be rooted in a sound and physically-based (i.e., hydrodynamic) description of the flow processes. Attributable to potentially high transmission losses, process variables can span a wide range of magnitudes under changing dynamics. It was briefly discussed that such conditions can counteract the application of typical numerical solution procedures for the governing flow equations. Chapter 4 reviews and discusses the applicable solution procedures for the flow models in more depth after the hydrodynamic theory is presented in the following Chapter 3. Consequently, in Chapter 5, this thesis presents an analytical zero-inertia model for advancing surge flow in initially dry non-prismatic channels with a significant effect of infiltration on the mass and momentum balance, as well as under potentially weak process dynamics. One further objective of this thesis is the development and testing of an exact analytical solution of the zero-inertia equations for runoff phenomena on hillslopes under time-varying rainfall.

Chapter 3

Principles of Physically-Based Modeling of Infiltrating Free Surface Flows

This chapter presents the basic theoretical background of hydrodynamic flow routing in ephemeral channels. Moreover, the presented approaches can be applied for any kind of free surface flows, i.e., also for overland flow modeling. The dynamics of an infiltrating flow event are first discussed with regard to different governing conditions, for example, for furrow irrigation or infiltrating wadi flow. Consecutively, coming from the full hydrodynamic shallow-water equations for the one-dimensional case (the Saint-Venant equations), the zero-inertia and kinematic wave approximations are discussed. The physically-based models are then extended in order to account for losses or inflows and, consecutively, the consideration of two-dimensional flow geometries in a one-dimensional model is outlined. The chapter closes with a discussion on the applicability of the hydrodynamic modeling approaches under the specific conditions of ephemeral river routing and overland flow routing. The discussion is supplemented with a brief outline of the kinematic shock phenomenon, which can play a role, particularly for flash flood events.

3.1 Hydraulic Phases of an Infiltrating Flow Event

In furrow irrigation modeling (Walker and Humpherys, 1983; Wöhling, 2005), an infiltrating flow event on a permeable bed can be divided in four phases, namely, the *advance phase*, *storage phase*, *depletion phase*, and *recession phase* (Fig. 3.1a). Flow advance starts if there is an inflow into the furrow and persists until the flow reaches the lower end of the furrow. More water is applied during the storage phase which ends when the inflow is decreased. The depletion phase begins when water moves further down the furrow as the water depth at the inlet decreases. If the inflow ceases, the recession phase begins, which lasts until all water has infiltrated or left the furrow at the lowermost end.

Furrow irrigation is mostly carried out by applying surges of water, i.e., the inlet is opened, the inflow rapidly reaches a quasiconstant value, and is then swiftly cut off after a certain time. Together with the comparably short length of an irrigation furrow, this methodology usually leads

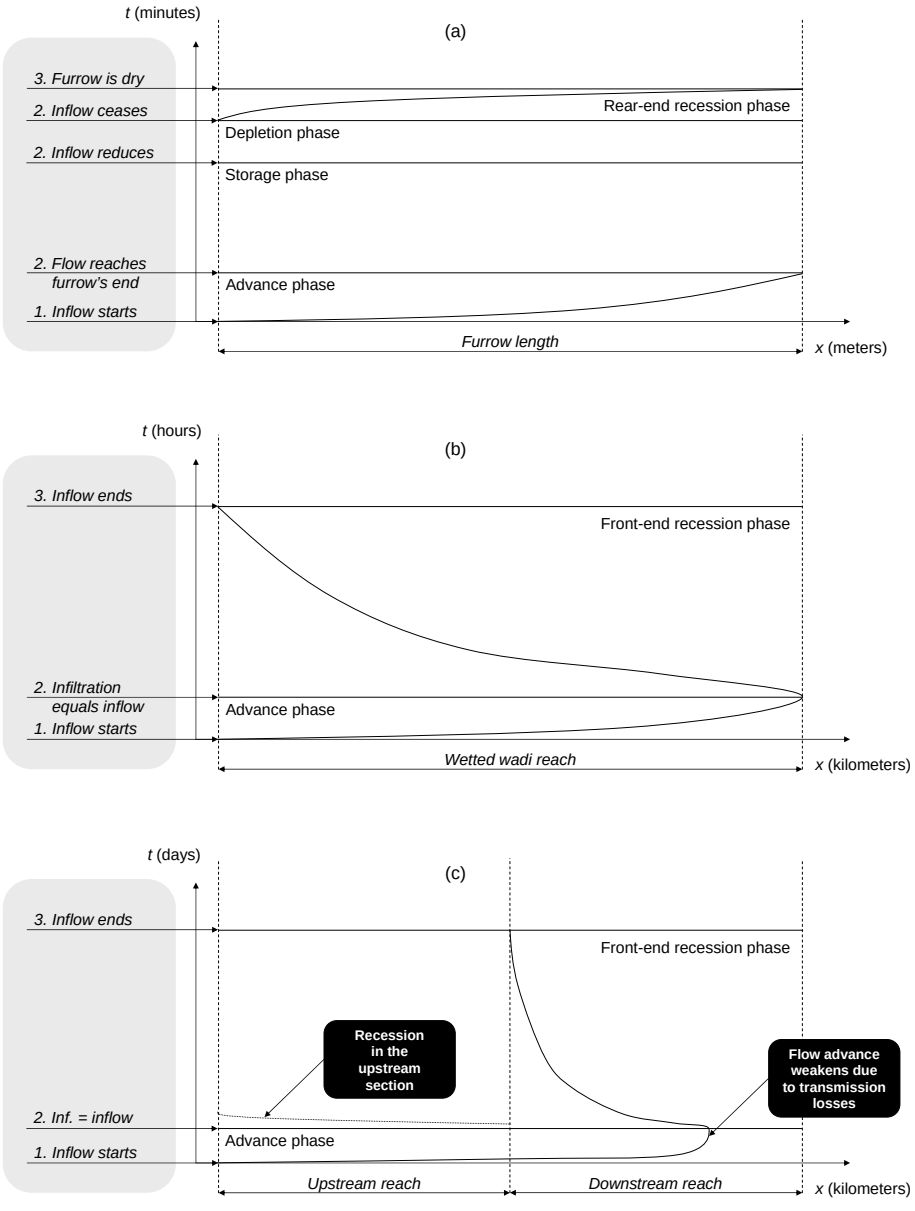

Figure 3.1: Hydraulic phases of a flow event (a) in a field furrow; (b) in a natural wadi channel; and (c) downstream of a recharge dam.

Table 3.1: Main properties of the flow upstream and downstream of a recharge dam under normal operational conditions (no spillway operation).

	Upstream reach	Downstream Reach
Event duration	Hours	Days
Process dynamics	Pronounced	Typically weak
Gradients of the dependent variables	Steep	Smoothed
Typical flow rates ($m^3 \cdot s^{-1}$)	10^2	10^0–10^1
Transmission loss quotas	Low–intermediate	Intermediate–high
Initial wadi bed state	Dry	Dry

to a rear-end recession, which means that upper portions of the furrow fall dry when the body of water in the furrow still moves downwards. If infiltration is pronounced and/or furrow slope is mild, a *front-end recession* can occur when the inflow reduces, leading to a ceasing flow, beginning from the wave tip and moving in the upstream direction (Walker and Humpherys, 1983). Nevertheless, this front-end recession is of minor interest in furrow irrigation theory and modeling.

Compared to wadi flow, furrow irrigation events are of a short duration; the inflow is cut off relatively fast, and flow lengths are limited. In contrast, the natural flood inflow to a wadi reach is highly transient, with a steep rising limb of the hydrograph and a comparably mild recession (cf. Fig. 1.3a). This leads to a fast advance of the flow and an extended recession phase, mainly established by front-end recession (Fig. 3.1b). Typically during recession, inflow rates and, therefore, flow momentum are small. Assuming a free lower boundary and a limited inflow volume, the flow advance coercively ends if total infiltration exceeds the flow rate, which may be the case a certain time *after* the inflow peak has entered the wadi. The recession phase directly follows the advance phase. Although front-end recession is assumed to be dominant, *rear-end recession* can occur as well, which would be observable as a decline in the wetting and traveling flow domain from the lower *and* the upper end. Moreover, certain constellations of inflow dynamics, infiltration properties, and wadi morphology could even lead to a dispartment of one infiltrating flow domains into two or more.

Figure 3.1c shows the advance and recession dynamics in a natural wadi, influenced by dam operation for an event significantly smaller than the design flood; in other words, all water infiltrates in the reach downstream of the dam, and the outflow of the dam is not influenced by spillway operation. Dam operation leads to a weakening of process dynamics downstream of the dam and the flow event may be prolonged from some hours in the upstream reach to some days in the downstream reach. Maximum dam outflow and the maximum extent of the infiltrating flow domain more or less coincide[1] and the downstream advance finally ceases during a prolonged dam release. Nevertheless, infiltration and the connected loss of mass and momentum also impact the advance dynamics of the downstream flow domain in a transient and nonlinear manner. Hence, a *hydrodynamic* modeling concept with included infiltration losses is envisaged for the simulation of wadi flow under dam operation to estimate potential recharge. Finally, Table 3.1 summarizes main properties of the flow upstream and downstream of a recharge dam.

[1] More precisely, the point in time where recession starts is not directly dependent on the transit of an inflow peak, but on the relationship of inflow rates and infiltration. The distinction between flow advance and flow recession cannot, therefore, be provided a priori.

3.2 Hydrodynamic Models

Unsteady, nonuniform free surface flow can be described by the *full hydrodynamic wave* (HD) equations, reflecting the conservation laws of mass and momentum. Usually, the dependent variables of the equations (e.g., flow velocity, flow area, etc.) are averaged over the water depth.[1] For the one-dimensional case[2], the governing equations are referred to as Saint-Venant equations (de Saint-Venant, 1871; Eagleson, 1970), named after J. C. de Saint-Venant. Keeping the pressure-gradient and momentum-source/sink term, but neglecting the inertia and acceleration terms in the momentum equation of the Saint-Venant model, leads to the *zero-inertia wave* (ZI) approximation (Hayami, 1951). The *kinematic wave* (KW) model, reported on thoroughly in the classical paper by Lighthill and Whitham (1955), neglects all of the aforementioned terms, which implies that friction slope is parallel to bottom slope.

All three flow models are mathematically expressed as a system of two equations, where one (KW) or two (HD, ZI) are partial differential equations (PDEs), representing continuity (conservation of mass) and conservation of momentum. Such a system describes an initial-boundary-value problem. This means that the solution functions of the PDEs[3] are dependent on the initial values of the considered process variables[4] at a specific point in time for all points in space (expressed in the initial condition, cf. Section 3.3), as well as the temporal evolution of the process variables, given at specific points in space (boundary conditions, cf. Section 3.3). The solution of the PDEs is, therefore, only valid for a certain domain in both the spatial and temporal dimension, spanned by the initial and boundary conditions.

3.2.1 The Saint-Venant Equations (Full Hydrodynamic Model)

Assuming no lateral losses or inflows to the flow domain, the continuity and momentum equations of the one-dimensional full hydrodynamic (Saint-Venant) model read

$$\frac{\partial A}{\partial t} + \frac{\partial Q}{\partial x} = 0 \tag{3.1}$$

$$\frac{\partial h}{\partial x} = S_0 - S_\mathrm{f} - \frac{u}{g}\frac{\partial u}{\partial x} - \frac{1}{g}\frac{\partial u}{\partial t} \tag{3.2}$$

where t: time [T]; x: longitudinal space coordinate [L]; $A(x,t)$: wetted cross-sectional area [L^2]; $Q(x,t)$: discharge [$\mathrm{L}^3\mathrm{T}^{-1}$]; $h(x,t)$: water depth [L]; S_0: bottom slope [−]; S_f: friction slope [−]; $u(x,t)$: flow velocity [LT^{-1}]; and g: acceleration due to Earth's gravity [LT^{-2}].

The Saint-Venant model is widely used for modeling unsteady, nonuniform free surface flows. Equations (3.1) and (3.2) form a system of quasilinear first-order partial differential equations of the hyperbolic type[5]. However, coming from the more general Navier-Stokes equations (Tenman,

[1] This simplification is usually referred to as shallow water approximation.

[2] This means an additional averaging over the flow width.

[3] For example, discharge and water depth as a function of the independent variables space and time.

[4] Flow velocity and wetted cross-sectional area, as well as water depth, respectively.

[5] Given is a PDE for a function $\nu(x,t)$ of two variables. Such an equation has the general form

$$\mathfrak{a}\nu_{xx} + 2\mathfrak{b}\nu_{xt} + \mathfrak{c}\nu_{tt} + \mathfrak{d}\nu_x + \mathfrak{e}\nu_t + \mathfrak{f}\nu + \mathfrak{g} = 0$$

and the coefficients $\mathfrak{a} = \mathfrak{a}(x,t), ..., \mathfrak{g} = \mathfrak{g}(x,t)$ are functions of two variables. The PDE is called elliptic if $\mathfrak{ac} - \mathfrak{b}^2 > 0$, parabolic for $\mathfrak{ac} - \mathfrak{b}^2 = 0$, and hyperbolic if $\mathfrak{ac} - \mathfrak{b}^2 < 0$.

1977), it is important to review the assumptions made for the derivation of Eqs. (3.1) and (3.2), since these assumptions constrain the model validness to specific flow phenomena:

- ▷ Acceleration of the fluid in the vertical direction is neglected; the vertical pressure gradient is approximated by a hydrostatic pressure distribution[1];
- ▷ the flow is assumed to be one-dimensional; all dependent variables are averaged over the width and depth of the flow;
- ▷ bottom slope is small, such that $\sin(S_0) \approx S_0$;
- ▷ the flowing liquid (water) is assumed to be incompressible; and
- ▷ the considered fluid is a Eulerian fluid, i.e., the flow exposes no or only low inner friction (viscosity). Friction slope is not dependent on flow type, turbulence, or sediment load. The relationship between friction and the hydraulic variables is expressed with a flow formula (e.g., the Manning-Strickler formula).

Especially the last assumption might restrict the validness of the Saint-Venant model applied for heavily sediment-laden flows as occurring in ephemeral rivers, which is discussed in the closing section of this thesis. Nevertheless, the listed restrictions do not endanger the model's applicability for a wide range of flow processes on natural surfaces, as present in numerous hydraulic and hydrologic problems.

3.2.2 Zero-Inertia Approximation

As stated before, simplifications of the Saint-Venant equations only address the momentum equation (3.2). The continuity equation (3.1) remains unchanged for all discussed modeling concepts (HD, ZI, KW). The diffusion wave or zero-inertia approximation neglects the inertia and acceleration terms of Eq. (3.2), yielding

$$\frac{\partial h}{\partial x} = S_0 - S_\mathrm{f} \tag{3.3}$$

In contrast to the full hydrodynamic model, Eqs. (3.1) and (3.3) now form a parabolic system. The ZI momentum equation cannot account for pronounced, unsteady, and nonuniform flow phenomena, since the governing terms are neglected. Nevertheless, a certain degree of nonuniformity is preserved in the momentum balance through the possible distinction of bed and friction slope. The model is an adequate substitute for the full hydrodynamic model if the acceleration and inertia terms are negligible (cf. Section 3.7.1). The portrayal of backwater effects is possible with the ZI model.

3.2.3 Kinematic Wave Approximation

The kinematic wave approximation additionally neglects the $\frac{\partial h}{\partial x}$ pressure-gradient term in Eq. (3.3). Hence, bottom and friction slope can be assumed parallel, which yields the momentum equation of the kinematic wave model as

$$0 = S_0 - S_\mathrm{f} \tag{3.4}$$

[1] Strictly speaking, this precludes a physically meaningful, closed-form representation of turbulence.

In turn, together with the continuity equation, this yields a biunique relationship of discharge and stage (rating curve). Furthermore, any rating curve—expressed, e.g., by a steady and uniform flow equation like Manning-Strickler[1], Chézy, or Darcy-Weisbach—which is coupled to the continuity equation (3.1) is referred to as a kinematic wave model. As applies for the Saint-Venant model, the system of Eqs. (3.1) and (3.4) is of the hyperbolic type.

3.2.4 Other Simplifications of the Full Hydrodynamic Model

Two other simplifications of the full dynamic momentum equation are physically reasonable (Ponce and Simons, 1977). The *steady dynamic wave* neglects the unsteady $\frac{1}{g}\frac{\partial u}{\partial t}$ term of the full dynamic model. If the influence of the bottom slope is insignificant (e.g., for great water depths[2] or for zero-slope conditions), the $S_0 - S_\mathrm{f}$ term can be omitted, leading to a process description applicable for a *gravity wave*. These two special cases of flow models are not further regarded in this thesis.

3.3 Initial and Boundary Conditions

Mathematically, the presented hydrodynamic models belong to the class of initial-boundary value problems, i.e., the governing equations deliver unique solution functions only for a specified initial state and for a defined evolution of process variables at the model boundaries over time. These two entities are called *initial condition* and *boundary condition*. The initial condition comprises the values of all dependent variables for the whole solution domain at a fixed point in time. From that state, the process evolves in a positive temporal direction, constrained by the boundary conditions.

An inflow or stage hydrograph is typically considered as an upper boundary condition, and a stage–discharge relationship is implemented at the lower model domain. Most often, a steady stage–discharge relationship is used as a lower boundary condition by assuming the flow is leaving the model domain at normal depth, i.e., friction slope equals bottom slope and water surface slope[3]. This approach leads to a neglecting of unsteady flow characteristics that may be inherent to the upstream inflow.[4] For subcritical flow regimes, such an assumptive lower boundary condition can influence the upstream results and attenuate their unsteady information.

The afore-discussed philosophy of implementing an upper and a lower boundary condition at two specific points in space is referred to as a *two-point boundary condition*. Especially for flow over initially dry surfaces, the lower boundary can be treated as a *moving lower boundary condition*, depicting the location of the interface between a dry and a wetted section of the model domain.[5] On the one hand, the formulation of such a boundary condition is straightforward since the process variables can be set to zero. On the other hand, the actual problem is the determination of the location of the moving lower boundary condition, which can be quite demanding.

[1] Corresponding to its authors Gaspar Gauckler, Robert Manning, and Albert Strickler, the formula is sometimes referred to as Gauckler-Manning-Strickler formula.

[2] For water depths, that are great in relation to wave length.

[3] This implies that the depth gradient is zero at the lower boundary, i.e., $\frac{\partial h}{\partial x} = 0$. Therefore, such a boundary condition is also referred to as zero-depth gradient boundary condition.

[4] A neglecting of unsteady flow characteristics can also be a corollary of a simplified process description. The parallelism of friction slope, bottom slope, and water surface slope is inherent to the kinematic wave model. Vice versa, a normal-depth lower boundary condition, therefore, establishes no further simplification of the KW model.

[5] If rear-end recession occurs (cf. Section 3.1), a moving boundary condition could also be implemented for the upper end of the model domain.

Typically, the flow equations are solved at discrete points in space and time. For weak process dynamics, such as those typically connected with infiltrating flows, the determination of the moving boundary location might be very cumbersome and connected with modeling issues in terms of stability problems, mass balance errors, and an erratic representation of process dynamics (cf. Wöhling, 2005). Nevertheless, circumventing a moving boundary condition by assuming a spatially fixed two-point boundary condition introduces other errors. As discussed in more detail in the subsequent chapter, the solution procedures for the flow equations may fail for a two-point boundary condition with parts of the model domain being dry. This can be addressed by changing the dry-channel initial condition to a minimum-flow condition, which indeed helps to obtain a stable solution, but again introduces errors attributable to an unrealistic characterization of the flow process. Yielding a stable and accurate solution for advancing flows under weak process dynamics is, therefore, a major goal of this work.

3.4 Relating Friction and Flow Properties

In the absence of a friction law for unsteady flows, velocity, channel roughness, channel geometry, and friction slope are commonly related using a steady flow formula of the type

$$u = K R^{\beta} S_{\mathrm{f}}^{\frac{1}{2}} \tag{3.5}$$

where K: roughness coefficient [$\mathrm{L}^{1-\beta}\mathrm{T}^{-1}$]; R: hydraulic radius [L]; β: exponent of the flow formula [$-$] (e.g., $\beta = \frac{2}{3}$ for the Manning-Strickler equation; Strickler, 1923). Eq. (3.5) can easily be rearranged for S_{f} and inserted into the desired momentum equation, e.g., Eq. (3.2), (3.3), or (3.4):

$$S_{\mathrm{f}} = \frac{u^2}{K^2 R^{2\beta}} \tag{3.6}$$

It should be made clear that such a friction law is only valid for the particular case of a steady and uniform flow.[1] Strictly speaking, neither S_{f} nor K are known, in fact they have to be estimated using a series of observed hydrologic flow conditions (stage and/or discharge) along the model domain, i.e., K is considered as an *effective process parameter*. However, it is beyond controversy that K is *not invariant* to a changing water depth. Moreover, K changes with variations in sediment load, which particularly applies for ephemeral streams (e.g., Nomicos, 1956; Vanoni and Brooks, 1957; Martin-Vide et al., 1999).

3.5 Accounting for Losses or Gains

A loss or gain of water (e.g., resulting from river confluence, rainfall on a surface, or infiltration through the riverbed or into the soil) leads to a modification of the flow's mass balance and can—additionally—alter the momentum balance significantly. For instance, flow in an ephemeral river can be strongly impacted by infiltration, such that the loss of mass *and* momentum should be regarded in flow modeling. On the other hand, rainfall on a surface can lead to a significant

[1] Although specific transformations may allow the application for steady and nonuniform conditions, e.g., shown by Schmitz (1981).

increase of flowing water over time and space, although the rate of change of flow momentum is insignificant, looking at a fixed point in space.

The continuity equation (3.1) can be straightforwardly supplemented by a term representing the volumetric rate of loss/gain to the flow:

$$\frac{\partial A}{\partial t} + \frac{\partial Q}{\partial x} = -q^{\phi} \tag{3.7}$$

where $q^{\phi}(x,t)$: rate of positive/negative mass contribution attributable to rainfall or infiltration per unit length [$\mathrm{L^2T^{-1}}$]. For Eq. (3.7), a negative q^{ϕ} accounts for losses, and vice versa.

Furthermore, the momentum equation can be extended by a term accounting for the loss or gain of momentum. For example, the momentum equation of the Saint-Venant model, which is extended in this way, reads

$$\frac{\partial h}{\partial x} = S_0 - S_\mathrm{f} - \frac{u}{g}\frac{\partial u}{\partial x} - \frac{1}{g}\frac{\partial u}{\partial t} + \frac{q^{\phi}u}{gA} \tag{3.8}$$

where the adding of a positive $\frac{q^{\phi}u}{gA}$ term means a loss of momentum in terms of a steepening of the water depth gradient $\frac{\partial h}{\partial x}$. In general, these modifications can be applied disregarding the specific flow model. The gain/loss rate q^{ϕ} can be quantified a priori (e.g., as observed rainfall) or included via a functional relationship (e.g., via an infiltration model). The dependent variables of the flow might influence q^{ϕ}, and vice versa. For instance, higher flow rates in a permeable channel lead to a greater wetted area which increases infiltration. In turn, increased infiltration consumes mass and momentum, which then lowers flow rates. This requires a specific strategy to *couple the surface flow and the infiltration model*, e.g., alternating iterative coupling (cf. Sections 5.1.7 and 7.1.1.1).

Up to this point, the hydraulic variables have been given in a dimension to yield the total flow [$\mathrm{L^3T^{-1}}$]. Alternatively, the the hydraulic variables can be expressed for a unit width of the flow domain, which is feasible for overland flow modeling. In this case, Q is yielded as specific flow for a unit width [$\mathrm{L^2T^{-1}}$] which particularly requires the yield/loss rate to be given as a volumetric rate per unit area [$\mathrm{LT^{-1}}$]. In this work, the yield/loss rate per unit area is labeled as q, whereas the use of q^{ϕ} indicates the rate given per unit length [$\mathrm{L^2T^{-1}}$]. In both cases, the same nomenclature for the discharge Q is used, whereas the dimension of Q (either [$\mathrm{L^3T^{-1}}$] or [$\mathrm{L^2T^{-1}}$]) differs depending on whether the flow equations are expressed for a unit width or the whole cross-sectional area.

3.6 Including Arbitrary Cross-Sectional Geometries

Although the discussed one-dimensional modeling concepts average the considered process variables for each cross section, it is inevitable to take into account the influence of different cross-sectional geometries on the flow. Therefore, a one-dimensional description of the underlying two-dimensional cross-sectional geometry is needed. To obtain unique and characteristic information of the geometry, at least two functional relationships have to be used. For instance, the wetted cross-sectional area A and the hydraulic radius R are expressed in terms of the water depth h (Fig. 3.2 illustrates the used notation):

$$\tilde{A}(x,h) = \int_0^{\tilde{B}(x,h)} \tilde{h}(x,y)\mathrm{d}y \tag{3.9}$$

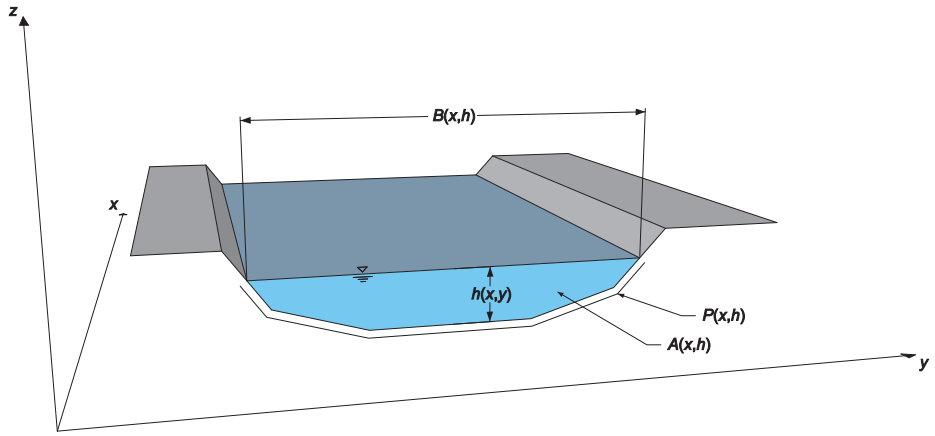

Figure 3.2: Illustration of a cross-sectional profile with notation.

$$\tilde{R}(x,h) = \frac{\tilde{A}(x,h)}{\tilde{P}(x,h)} = \frac{\int_0^{\tilde{B}(x,h)} \tilde{h}(x,y)\mathrm{d}y}{\int_0^{\tilde{B}(x,h)} \sqrt{1+\tilde{h}'(x,y)^2}\,\mathrm{d}y} \tag{3.10}$$

where x: longitudinal space coordinate [L], y: space coordinate perpendicular to the flow at a specific channel location x [L]; z: vertical coordinate positive upwards [L]; $\tilde{h}(x,y)$: depth of water reaching the cross-sectional coordinate (x,y) [L]; $\tilde{A}(x,h)$: wetted cross-sectional area as a function of water depth $h(x,t)$ [L^2]; $\tilde{B}(x,h)$: flow width in the channel as a function of water depth $h(x,t)$ [L]; $\tilde{R}(x,h)$: hydraulic radius as a function of water depth $h(x,t)$ [L]; and $\tilde{P}(x,y)$: the wetted cross-sectional perimeter [L]. For formal reasons, the profile-specific functions $\tilde{h}$, $\tilde{A}$, $\tilde{B}$, $\tilde{R}$, and $\tilde{P}$ are distinguished from the spatiotemporal functions of the dependent variables $h(x,t)$, $A(x,t)$, $B(x,t)$, $R(x,t)$, and $P(x,t)$.

The denominator of the right-hand side of Eq. 3.10 contains a first-order derivative of $\tilde{h}(x,y)$ with respect to y. This expression emerges from the integral arc length l [L] of the function $f(y)$ in an interval $[y_1,...,y_2]$, given by

$$l = \int_{y_1}^{y_2} \sqrt{1+f'(y)^2}\mathrm{d}y \tag{3.11}$$

Assuming that the considered cross section is very wide (flow width is much greater than water depth), the wetted perimeter P can be set equal to the flow width B and, therefore, the hydraulic radius R equals the water depth h.[1]

Another practice is expressing the water depth and the hydraulic radius in terms of the wetted cross-sectional area, i.e., obtaining $\tilde{h}(x,A)$ and $\tilde{R}(x,A)$, which can be achieved by employing the inverse function of $\tilde{A}(x,h)$ and mapping $\tilde{R}(x,h)$ on $\tilde{R}(x,A)$. When carrying out the required integrations numerically on discrete increments—which is feasible since information on cross-sectional geometry is usually available as discrete coordinate pairs of y and z—a simple lookup table can be used to map $\tilde{h}$, $\tilde{A}$, and $\tilde{R}$ onto each other. Generally, the profile functions have to be biunique,

[1] This practice is mostly referred to as wide channel assumption.

which forbids discontinuities in the morphological data, e.g., caused by bank overboard sections with a horizontal bottom. Hence, it is indicated to remove discontinuities from the empirical profile functions or to fit continuous analytical functions to the empirical profile functions. This is done for the flow models derived and applied herein, where power laws are used for the approximation of the two profile functions (cf. Section 5.1.2).

3.7 Discussion of the Reviewed Flow Models

The full hydrodynamic model poses the most rigorous concept for modeling one-dimensional flow phenomena which maintains the highest generality for its application. Nevertheless, three aspects may motivate using simplifications of the full dynamic model, rather than the full Saint-Venant equations itself: (a) A numerical solution (cf. Section 4.2) of the zero-inertia and the kinematic wave model consumes less time and memory since terms of the Saint-Venant equations are neglected; (b) the numerical solution of parabolic PDEs (ZI model) is less prone to numerical inconveniences, compared to hyperbolic equations (e.g., the Saint-Venant equations); and (c) the simplified models are better accessible for analytical solutions (cf. Section 4.3). Therefore, it is important to prove the feasibility and validity of the discussed flow model simplifications for the processes regarded herein.

3.7.1 Discussion of the Hydrodynamic Modeling Approaches in the Light of Flow Modeling in Ephemeral Rivers

The afore-presented hydrodynamic models (full hydrodynamic, zero-inertia, and kinematic wave) combine the same continuity equation (3.1) with a more or less sophisticated momentum equation, which can be expressed in the form[1]

$$\underbrace{\underbrace{\underbrace{S_\mathrm{f} = S_0}_{\mathrm{KW}} - \frac{\partial h}{\partial x}}_{\mathrm{ZI}} - \frac{u}{g}\frac{\partial u}{\partial x} - \frac{1}{g}\frac{\partial u}{\partial t}}_{\mathrm{HD}}$$

Apart from the simplifications made for the development of the Saint-Venant model (cf. Section 3.2.1), neglecting specific terms of the HD momentum equation further constricts the validity and applicability of the resulting hydrodynamic models (ZI or HD model). It is subsequently discussed under which flow conditions one of the aforementioned simplifications is justifiable. This should finally be reflected by the structure of a modeling system, intended for the simulation of ephemeral channel flow under transmission losses and influenced by recharge dam operation (cf. Section 7.1).

Under the zero-inertia simplifications, the change of velocity with distance and the change of velocity with time (expressed by the so-called inertia terms) are neglected. Thus, the momentum equation holds no terms significant for nonuniform (i.e., $\frac{\partial u}{\partial x} \neq 0$) and unsteady (i.e., $\frac{\partial u}{\partial t} \neq 0$) flow conditions, and changes in the kinetic energy of the flow due to local or convective accelerations[2] are not regarded. Nevertheless, the conservation of the pressure-gradient term $\frac{\partial h}{\partial x}$ accounts for a

[1] For brevity, a $\frac{q^{\phi} u}{gA}$ term to account for the loss or gain of momentum is omitted.

[2] Which implies acceleration or deceleration.

Table 3.2: Impact of model simplifications on the validity of hydrodynamic models.

	Kinematic	Zero-inertia	Full hydrodynamic
Advection	yes	yes	yes
Attenuation	no	yes	yes
Backwater effects	no	yes	yes
Acceleration and deceleration	no	no	yes

potential divergence of water surface and bottom slope, which lets the zero-inertia model account for backwater effects and wave attenuation due to dispersion.

Neglecting the inertia terms and the pressure-gradient term (usually referred to as secondary terms) of the dynamic wave model leads to a balance between gravitational and frictional forces and, consequently, the full hydrodynamic momentum equation reduces to the kinematic wave momentum equation, $S_\mathrm{f} = S_0$. The consequences of model simplifications on the representation of specific flow phenomena are briefly summarized in Table 3.2. It becomes clear that, compared to the full hydrodynamic model, the KW model cannot account for wave attenuation, backwater effects, or wave acceleration, whereas the ZI model is not able to cover wave acceleration.

Assuming a sufficiently large bottom slope (> 0.001, according to Ponce, 1991), an order of magnitude reasoning of Eq. (3.2) reveals that the gradient $\frac{\partial h}{\partial x}$ is much smaller than S_0 or S_f. Taking typical values of an Omani wadi upstream of a recharge dam (cf. Table 1.2: flow velocity $3\,\mathrm{m}\cdot\mathrm{s}^{-1}$; wetted cross-sectional area $150\,\mathrm{m}^2$; flood duration 12 h) and assuming a wetted reach length of 15,000 m[1], a wetted channel width of 150 m, a channel slope of 0.008, and a ratio of hydrograph rise time to recession time of 1 : 2, the following values of the gradients in the full hydrodynamic momentum equation (3.2) can be calculated:

$$\begin{array}{cccc} S_0; & \frac{\partial h}{\partial x}; & \frac{u}{g}\frac{\partial u}{\partial x}; & \frac{1}{g}\frac{\partial u}{\partial t} \\ 8.0\cdot 10^{-3}; & 6.7\cdot 10^{-5}; & 6.1\cdot 10^{-5}; & 2.1\cdot 10^{-5} \end{array}$$

where the secondary terms are two orders of magnitude smaller than the channel slope. Miller (1984) reports the following values for a moderately steep alluvial river

$$\begin{array}{cccc} S_0; & \frac{\partial h}{\partial x}; & \frac{u}{g}\frac{\partial u}{\partial x}; & \frac{1}{g}\frac{\partial u}{\partial t} \\ 4.9\cdot 10^{-3}; & 9.5\cdot 10^{-6}; & 4.7\cdot 10^{-5}; & 9.5\cdot 10^{-6} \end{array}$$

where the values for the pressure-gradient term and the local acceleration term are even three orders of magnitude smaller than S_0. Hence, neglecting secondary terms seems feasible under the present hydraulic conditions (which confirms the rule of thumb given by Ponce, 1991), and the kinematic wave model (which neglects the secondary terms) poses a valid approach for routing pronounced flood flow in a sufficiently sloping wadi channel reach, as found upstream of the dams regarded in this study.

Specific for the scoping area of this study (cf. Section 7.2.1), flow resulting from dam culvert release occurs on somewhat milder slopes around 0.002, and under lower flow velocities, compared to the upstream reach with slopes around 0.008. This leads to a further decreasing impact of the inertia terms on the momentum balance and the flow can be assumed to be highly subcritical. Nevertheless, flow widths decrease disproportionately to flow depths and the flow might infiltrate

[1] Which means, the distance between zero-flow conditions and the occurrence location of the given typical values.

along a limited wadi reach length, which *increases* the downstream value of the pressure-gradient term.

Moreover, especially at the downstream end of an advancing and infiltrating flow domain, the change in the water surface elevation along the spatial direction might be significant and should, therefore, be regarded in the governing hydrodynamic approach via the $\frac{\partial h}{\partial x}$ term. Furthermore, heavy infiltration—as particularly present at the advancing downstream end of the flow domain—does consume mass *and* momentum of the flow. A sound portrayal of the spatiotemporal dynamics of flow advance is, therefore, essential for an accurate simulation of transmission loss dynamics. For these reasons, the advancing and infiltrating flow for slopes greater than 0.001 should be modeled by employing the zero-inertia model, which further regards the loss of momentum attributable to infiltration via a $\frac{q^{\phi}u}{gA}$ term in the momentum equation. This leads to an extension of the ZI momentum equation in the form

$$S_{\mathrm{f}} = S_0 - \frac{\partial h}{\partial x} + \frac{q^{\phi}u}{gA} \tag{3.12}$$

Infiltration leads further to a decrease of flow volume and, therefore, water depth, which is implicitly regarded via the pressure-gradient term.

When the advance of the flow domain ceases, the surficial flow volume is continually depleted by infiltration. At this time, sustained infiltration and the downward movement of the water body already led to a rectification of the water surface profile and a low advance velocity of the flow domain is the consequence. Therefore, the $\frac{\partial h}{\partial x}$ term and the other secondary momentum terms can be neglected, which allows the application of the kinematic wave approximations for modeling the quasisteady receding flow. The concept of modeling flow recession with steady or quasisteady approaches is often applied in irrigation engineering (cf. Wöhling, 2005). Of course, the consumption of mass is still accounted for using a continuity equation in the form of Eq. (3.7), which applies for all routing models applied herein.

A rare condition of recharge dam operation is established by spillway operation. Depending on the specific design of the spillway, spillway release can cause flow rates in the order of magnitude of dam inflow rates. Considering the dynamic character of spillway release flow and a minor wave dispersion tendency, the kinematic wave model seems feasible to act again as a robust modeling approach to simulate spillway release flow, given that channel slope is sufficiently greater than 0.001, which is always the case for the envisaged study area.

3.7.2 A Suitable Hydrodynamic Model for Overland Flow

Most often, overland flow processes are modeled with the kinematic wave approach (cf. Section 2.2). Neglecting the inertia terms of the full hydrodynamic model (i.e., applying the zero-inertia approximations) is justified by the generally low flow velocities associated with overland flow. More questionable is the often practiced neglecting of the pressure-gradient term. As already mentioned in Section 2.2, the validity of the kinematic wave approximation can be negatively affected under specific flow conditions (Morris and Woolhiser, 1980; Daluz Vieira, 1983; Govindaraju et al., 1988). Related to numerous numerical experiments, Singh (1996) proposes a criterion to check for the applicability of the kinematic wave simplifications for overland flow modeling:

$$\frac{t_{\mathrm{e}} S_0 \overline{u}}{\overline{h}} \overset{!}{\geq} 171 \tag{3.13}$$

where t_e: duration of the flow event; S_0: surface slope; $\overline{u}$: flow velocity, averaged over t_e; $\overline{h}$: water depth, averaged over t_e.

It can be seen that decreasing flow velocities and increasing flow depths (e.g., resulting from increased roughness) lead to lower values of the criterion. The same applies for a decreased surface slope. This means, the flatter and the rougher the surface, the higher the chance the KW assumptions may fail. To maintain the generality of an envisaged overland flow model, the zero-inertia approximations should, therefore, be used, which is regarded for the analytical overland flow model developed in Section 5.2.

3.7.3 On the Portrayal of Shocks with the Kinematic Wave Model

The advection of the kinematic wave is solely a corollary of gravitation (expressed by the channel slope, and the surface slope, respectively). When traveling along a topographic gradient, the kinematic wave undergoes a change in shape which is attributable to the nonlinear influence of friction on the flow. In contrast, the peak flow value of a kinematic wave does not attenuate since wave attenuation is evoked by the interplay of friction and the pressure-gradient term (zero-inertia wave) or of friction and the acceleration terms (full hydrodynamic wave), as shown by Ponce et al. (1978) and Ponce (1982). Furthermore, due to neglecting the pressure-gradient terms of the dynamic wave, the kinematic wave cannot translate a propagation of momentum in the upstream direction (which would occur under subcritical flow conditions) and cannot, therefore, be applied under backwater conditions (cf. Table 3.2).

In Appendix A.4, it is shown that the celerity of a kinematic wave is only dependent on water depth.[1] Thus, points of a wave profile having a larger water depth are propagated faster than more shallow sections of the wave. Together with the property of neglected dispersion[2], and assuming a sufficiently long flowpath, this can lead to the formation of a surge or a so-called *kinematic shock* (Lighthill and Whitham, 1955). Of course, the potential formation of a shock is also included in the full hydrodynamic wave and the zero-inertia wave models. Nevertheless, the presence of secondary terms (pressure-gradient term and acceleration terms) leads to wave dispersion and attenuation, which counteracts shock formation. Consequently, the kinematic wave is *per se* prone to shock formation, whereas for the full hydrodynamic or the zero-inertia model, the secondary terms of their respective momentum equation prevent, or at least delay, the formation of a surge.

Although there is an ongoing controversy about the existence of kinematic shocks in nature[3], flood waves in ephemeral rivers may tend to steepen, as seen from the literature review in Section 2.1, provided that wave gradients are initially steep and channel slope is sufficiently high. Therefore, the intrinsic wave steepening tendency of the kinematic wave concept poses—additionally to the motivation given in Section 3.7.1—a further argument for choosing the KW model for flash flood routing on pronounced slopes.

[1] Assuming no lateral inflows and a prismatic cross-sectional geometry.

[2] Hence, the wave does not subside.

[3] Which is not further commented on this work. Further reading on the formation and properties of kinematic shocks can be found, e.g., in Ponce and Windingland (1985), Singh (1996), and Singh (2002).

3.8 Summary

Hydrodynamic models allow for a realistic simulation of free surface flow processes. Full hydrodynamic models establish the most rigorous modeling approach. Compared to their simplifications (ZI and KW models), HD models are mathematically complex and their numerical solution is costly and may be afflicted with inconveniences. Regarding the specific character of the considered flow phenomena, the application of simplified models is indicated in order to reduce the complexity of the governing equations. Furthermore, the ZI and KW models are better accessible for analytical solutions. Concerning the envisaged modeling system for ephemeral river flow under recharge dam control, it was shown that the KW model is feasible for portraying pronounced wadi flow and the ZI approach is needed for a sound description of advancing wadi flow under weak process dynamics and intense infiltration, as well as overland flow.

Chapter 4

Solution Procedures for the Reviewed Flow Models

All presented flow models comprise partial differential equations. In most cases, PDEs are numerically solved, although analytical solutions might be available for distinct or simplified process conditions. For their practical applicability, the equations need to be integrated, which is most often carried out by means of numerical analysis. On the other hand, analytical solution procedures of the flow equations are of importance as they can deliver reliable solutions for evaluating the quality of numerical results. Moreover, numerical approaches are prone to failure for complicated and intricate process dynamics, e.g., as associated with infiltrating runoff on initially dry surfaces.

According to Press et al. (1992) and Munz and Westermann (2012), the physically-based description of hydrodynamic phenomena and their subsequent numerical (i.e., approximate) solution introduces three classes of errors:

- ▷ *Model errors*, which are a consequence of neglecting parts of the governing natural process behavior in the mathematical model (i.e., by depth-integrating the hydraulic variables in order to obtain the Saint-Venant equations);
- ▷ *approximation errors* (or consistency errors), which emerge if the mathematical model is not solved exactly but, for example, at a finite number of points under certain approximations (e.g., considering the differential quotients of the underlying mathematical model to be linear); and
- ▷ *truncation errors*, which result from the fact that a computer which is used for numerical computations cannot hold an infinite number of digits, which in turn delimits the precision of each calculation and, therefore, introduces errors.

Whereas numerical solutions incorporate errors from all three aforementioned sources, analytical solutions are only prone to model errors, which are, moreover, an issue of mathematical modeling and not associated with the specific solution procedures for the governing flow models.

This chapter opens with some fundamental ideas on the solution of PDEs on the basis of the method of characteristics, which allows a qualitative insight into the governing PDEs and their potential approximate solution. Subsequently, the principles of relevant numerical and analytical solution procedures for the hydrodynamic equations are discussed. The chapter closes with a

discussion of the reviewed approaches in the light of flow modeling in ephemeral rivers under the influence of groundwater recharge dams. It is concluded that the modeling of advancing and infiltrating wadi flow demands an analytical modeling concept. It is also discussed that hydrodynamic overland flow modeling benefits from the incorporation of an analytical solution procedure for the governing equations. This establishes a need for innovation with respect to finding appropriate analytical solution methods of the regarded process models.

4.1 Method of Characteristics

The method of characteristics was already used prior to the age of digital computers for the solution of partial differential equations, associated with unsteady flow phenomena (e.g., Massau, 1889). Abbott (1979) gives a sound introduction to the method's application in technical hydraulics. The method can only be applied for solving quasilinear first-order PDEs of the hyperbolic type, like the Saint-Venant and the kinematic wave equations. At first, the system of PDEs is simplified in a mathematically exact manner. This essentially comprises a coordinate transformation that affects the original PDEs in such a way that the derivatives of the solution functions are related to the directions of a set of two inclined and skewed or straight coordinate curves. These curves are called forward and backward characteristics or characteristic curves (c_f and c_b in Fig. 4.1). The transformation implies that along these characteristics, an original PDE becomes an ordinary differential equation (ODE), called characteristic equation.

Once such an ODE is found, it can be solved with common solution procedures[1] along one direction of the characteristic curves, and the result can then be transformed back into the solution domain of the original PDE. An important property of the characteristic curves is that curves of one set (of forward or backward characteristics) do not intersect, and that each characteristic of each set intersects with another characteristic of the other set in at no more than one point (P in Fig. 4.1).

One way of solving the characteristic ordinary differential equations is the application of a finite difference approximation (cf. Section 4.2.1). By replacing the derivatives in the characteristic equations with difference quotients (i.e., introducing a spatial and temporal discretization with the step size Δx and Δt), one obtains difference equations, representative for the nodes that are established by the intersecting characteristics (Fig. 4.1). This way, the function values at point 3 can be calculated using the values at points 1 and 2. Therefore, it is important to assure that the solution functions at point P are only dependent on the initial values, located at the abscissa between points A and B. The same applies for all virtual points within the region of dependence RD of $\overline{\mathrm{AB}}$. In turn, the solution at point P influences only the solutions within the region of influence RI.

Due to the fact that only the initially known values of $\overline{\mathrm{AB}}$ are used for the calculation of values of RD[2], the gradient of the characteristics, c_f and c_b, and the employed spatial discretization step Δx determine an upper limit for the time step Δt of an applied numerical solution scheme. Under

[1] Which can be numerical approximations, e.g., by applying finite differences (cf. Section 4.2.2), or analytical methods (cf. Section 4.3).

[2] Which means that the method of characteristics can be classified as an explicit procedure (cf. Section 4.2.2).

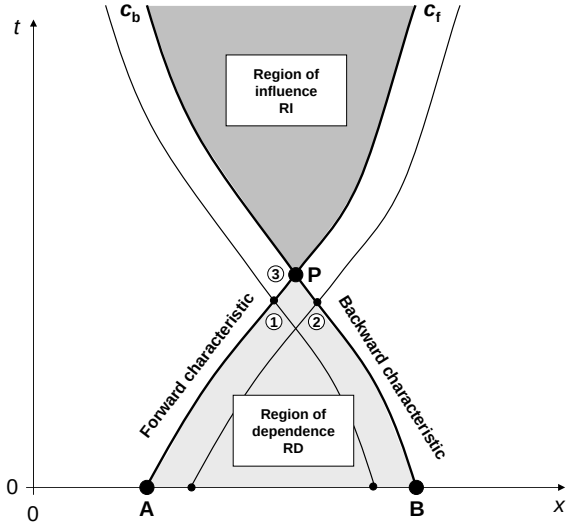

Figure 4.1: Forward/backward characteristics and regions of dependence/influence of the underlying PDE.

these restrictions, the Courant-Friedrichs-Lewy (CFL) condition (Courant et al., 1928) is a necessary condition for a stable (and thus convergent)[1] solution. The CFL condition reads

$$\frac{\Delta x}{\max(c_{\mathrm{f,b}})} \overset{!}{\geq} \Delta t \tag{4.1}$$

The gradient of the characteristic curves ($\frac{\partial x}{\partial t}$) is a measure for the maximum propagation velocity of the considered process. Physically, this is the maximum of the flow velocity u and of the wave celerity $c = \sqrt{gh}$, which are not necessarily orientated in the same direction. Defining this maximum propagation velocity as $\hat{c} = \max(u \pm c)$, one obtains the definition of the *Courant number* C from Eq. (4.1) to

$$\mathrm{C} = \hat{c}\frac{\Delta t}{\Delta x} \tag{4.2}$$

From Eqs. (4.1) and (4.2), it can be directly seen that the temporal and spatial domain should be discretized[2] with respect to $\hat{c}$, such that $\mathrm{C} \leq 1$. Furthermore, it is clear that the spatial and temporal resolution of a discretization scheme are *not independent* of each other. Heuristically, C is a measure for the number of cells of the numerical grid which are passed by the flow within one time step.

4.2 Numerical Solution Procedures

With the strong advancement of digital computers during and after the Second World War, numerical analysis and numerical algorithms rapidly evolved. A wide range of scientific computing problems

[1] The terms "stability" and "convergence" are defined in Section 4.2.1.

[2] A comprehensive explanation of "discretization" is given in Section 4.2.1.

was discussed and solved by applied mathematicians and engineers, such as three-body problems in spaceflight, structural analysis, and fluid dynamics. During the decades, computational fluid dynamics spawned numerous methods for the numerical treatment of a large variety of flow problems, ranging from one-dimensional open channel flow of water to three-dimensional flow of compressible fluids, or multiphase systems with complex material and energetic interactions. O'Brien et al. (1951) and Stoker (1957) were among the first to present a numerical finite difference solution of the Saint-Venant equations.

Generally, depending on the structure of the flow equations, an appropriate solution procedure has to be chosen, i.e., the results should, as close as possible, match the exact but unknown solution of the governing model equations under a preferably low computational effort. A great number of numerical methods for the solution of PDEs are available. The approaches can be roughly grouped into three classes: *finite difference methods*, *finite element methods*, and *finite volume methods*. For this work, a finite difference method is applied in case a numerical solution of the governing flow equations is desired. Finite difference methods are preferred for one-dimensional problems (Press et al., 1992).[1] Both the finite element and the finite volume methods are not considered for this study. Finite difference methods have been extensively reported on (for an overview see, e.g., Press et al., 1992) and a great number of modifications of the technique are available.

4.2.1 Introduction to Finite Difference Methods

The basic idea of all finite difference methods is to replace the partial derivatives of the model equations with linear finite difference quotients, yielding linear difference equations. These difference equations can be solved in order to obtain a solution of the original PDEs. As for all numerical techniques, such a solution delivers only an *approximate* result at predefined points in space and time, and, consequently, introduces errors. The decomposition of the continuous solution domain into a pattern of nodes for which the solution is obtained is called *discretization*: The modeling domain—spanned by the independent variables of, e.g., space and time, and housing the solution functions of the PDE (e.g., flow rate $Q = f(x,t)$, water depth $h = f(x,t)$, etc.)—is divided into discrete time steps of Δt and space steps of Δx. Assuming the governing PDEs to be continuous and differentiable, the introduced difference operators will converge against the replaced differential operators for small values of Δt and Δx, and, therefore, the approximate finite difference solution will converge against the analytical (but often unknown) solution of the model equations.

In this context, the underlying mathematical theory (e.g., Richtmyer and Morton, 1967) demands the fulfillment of three properties: *consistency*, *stability*, and *convergence*. Assuming that the applied discretization intervals will tend uniformly[2] to zero, it is claimed that (cf. Liedl, 1991):

- ▷ the difference equations resemble the analytical model equations (consistency);
- ▷ the solution of the difference equations remains bounded and the bound must not be dependent on the discretization step size (stability); and

[1] Of course, finite element and finite volume methods are valuable, almost indispensable tools for water resources research and management. Their strength lies in the flexible adaption of model topology to reality, which is important if a two-dimensional or three-dimensional process modeling is intended. On the other hand, the required mathematical background is more sophisticated than for finite difference procedures. For one-dimensional investigations, the advantages of finite element and finite volume methods are often outweighed by the simple and straightforward applicability of finite differences.

[2] Which means under invariance of $\frac{\Delta t}{\Delta x}$.

▷ the approximate solution functions of the difference equations converge against the solution functions of the governing model equations (convergence).

Based on the evident fact that the replacement of the differential quotients by well-posed difference quotients leads to consistency (cf. Liedl, 1991), the Lax equivalence theorem (Lax and Richtmyer, 1956) states that for *linear* PDEs with *constant* coefficients, stability is a necessary and sufficient condition for convergence. Although an exact definition of stability depends on the context[1], it generally states that a numerical solution procedure (or algorithm) applied for a PDE is insusceptible to small errors in the driving data. It further says that perturbations that would decay in the underlying analytical model do not grow in the numerical simulation, but rather decay over time. In turn, this means that approximation errors and truncation errors do not affect the quality of the result.

For *nonlinear* equations, e.g., the Saint-Venant equations, consistency and stability are necessary *but not sufficient* conditions for convergence, which renders the Lax equivalence theorem not directly applicable. The proof of convergence of a specific numerical procedure is, therefore, often carried out by employing linearized model equations, leading to constant coefficients. This case is covered by a complete theory (Richtmyer and Morton, 1967) which also implicates the Lax equivalence theorem. Therefore, the theory states that under the aforementioned conditions, convergence can be deduced from stability. The latter evokes a great importance for the practical use of finite difference approximations: Indirectly proving convergence by proving stability is much less arduous than searching for a direct proof. Especially for strongly nonlinear PDEs (e.g., Richards' equation), an exact proof is possible in the fewest cases (Liedl, 1991). However, convergence proofs of numerical procedures for the solution of the unaltered quasilinear Saint-Venant equations are available (e.g., Edenhofer and Schmitz, 1981).

4.2.2 Mathematical Principles of Finite Difference Methods

The first-order temporal partial derivative of an unknown function $\nu(x,t)$ should be given by

$$\frac{\partial \nu}{\partial t}(t) \qquad t \in \Omega \tag{4.3}$$

where $\Omega \subset \mathbb{R}^n$ is a spatiotemporal domain with a piecewise smooth boundary. The differential operator is replaced by a difference quotient:

$$\frac{\partial \nu}{\partial t}(t) \approx \frac{\Delta \nu}{\Delta t} \tag{4.4}$$

For a specific time t, $\Delta\nu$ can be evaluated looking in different "directions" of t, i.e., "forward" and "backward". This way, three possible variants of the difference quotient read

$$D^- = \frac{\Delta \nu}{\Delta t} = \frac{\nu(t) - \nu(t - \Delta t)}{\Delta t} + \mathcal{O}(\Delta t) \tag{4.5}$$

$$D^+ = \frac{\Delta \nu}{\Delta t} = \frac{\nu(t + \Delta t) - \nu(t)}{\Delta t} + \mathcal{O}(\Delta t) \tag{4.6}$$

$$D^c = \frac{\Delta \nu}{\Delta t} = \frac{\nu(t + \Delta t) - \nu(t - \Delta t)}{2\Delta t} + \mathcal{O}(\Delta t^2) \tag{4.7}$$

[1] Whether the governing equations are linear or nonlinear, for example.

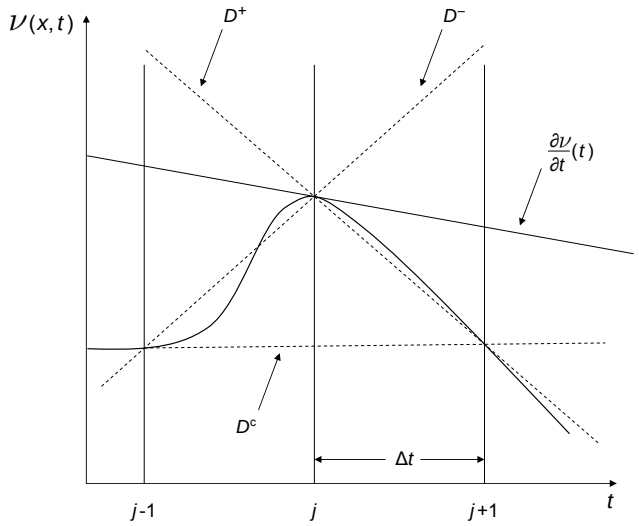

Figure 4.2: Approximation of the derivative $\frac{\partial \nu}{\partial t}$ in $t = j$ by means of difference quotients.

where D^- is called *backward difference quotient*, D^+ *forward difference quotient*, D^c *central difference quotient*, and $\mathcal{O}$ is the Landau symbol.

Figure 4.2 provides a representation of the approximation of the derivative $\frac{\partial \nu}{\partial t}(t)$ (i.e., the tangent of the function ν in $t = j$) by the various difference quotients (i.e., secants of ν through $j-1$ and j, j and $j+1$, and $j-1$ and $j+1$, respectively). It can easily be shown that for $\Delta t \to 0$, all three quotients converge against the partial derivative $\frac{\partial \nu}{\partial t}(t)$. Thus, for a sufficiently small Δt, one should obtain a good approximation of the partial derivative using one of the aforementioned difference quotients. The same can be applied for the spatial derivatives of ν, i.e., $\frac{\partial \nu}{\partial x}(x)$.

When approximating differential quotients with finite differences, it is of interest how fast the approximation error approaches zero for decreasing discretization step sizes of Δt and Δx, respectively. This change of the error is characterized by the *order of consistency*, which can be expressed using the big O notation with the Landau symbol $\mathcal{O}$ (Bachmann, 1894). By applying a Taylor series expansion to Eqs. (4.5) through (4.7), it can be shown that the backward and forward quotients exhibit a consistency order of $\mathcal{O}(\Delta t)$ and the central difference quotient of $\mathcal{O}(\Delta t^2)$. Essentially, this means that the error decreases quadratically with decreasing step size for central differences, but only linearly for forward or backward differences. The same applies for a spatial discretization, i.e., $\frac{\partial \nu}{\partial x}(x) \approx \frac{\Delta \nu}{\Delta x}$.

The discretization of the solution domain for a spatiotemporal problem may be oriented to an equidistant grid, leading to equidistant nodes in space and time (with constant values for Δx and Δt) for which the finite difference equations are evaluated (cf. Fig. 4.3). This procedure yields a pointwise approximation of the governing PDEs. Hence, the solution can be obtained by solving a system of equations, holding finite difference equations for each spatiotemporal node. The system of equations is determined by the initial and boundary conditions, establishing values for nodes of a cut in the temporal dimension, e.g., for $(\forall i, j-1)$ (initial condition), and in the spatial dimension, e.g., for $(i-1, \forall j)$ (boundary condition), respectively.

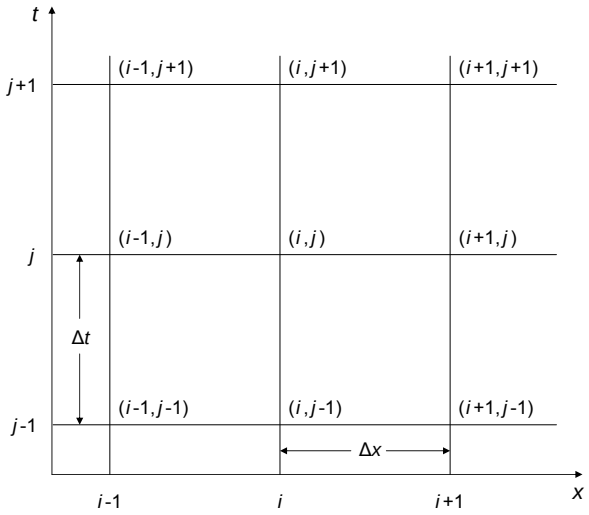

Figure 4.3: Solution domain of the governing equations and discretization grid (modified according to MacArthur and DeVries, 1993).

If the numerical solution is obtained using backward differences, the solution of the difference equations for one specific point in the solution domain can be expressed as a function of already know solutions. In this case, the solution scheme is called *explicit*. Appendix A.1 exemplarily shows the derivation of an explicit first-order finite difference scheme (Euler method) for the kinematic wave model, related to the nomenclature of Fig. 4.3.

In contrast, both the central and the forward difference quotient involve the terms $\nu(t+\Delta t)$ and $\nu(x+\Delta x)$, respectively, which are a priori unknown for the given initial and boundary conditions. Nevertheless—depending on the physical character of the modeled processes—it could be indicated to use central or forward differences, rather than backward differences. In this case, the difference equations for every spatiotemporal node hold initially unknown values, and their system has to be solved simultaneously. A numerical scheme to solve such a system is called *implicit*. Appendix A.3 exemplarily presents the widely-used implicit Preissmann scheme. Due to the nonlinearity[1] of the emerging algebraic[2] equations, the required simultaneous solution is mostly based upon iteration, e.g., provided by a fixed-point scheme or the Newton-Raphson method (Ypma, 1995).

To obtain stability (and, therefore, convergence), explicit schemes have to satisfy the CFL condition; they are conditionally stable (cf. Section 4.1, Eq. (4.1)). As a corollary of the definitions (4.5) to (4.7), explicit and implicit schemes are equivalent for a sufficiently small discretization of the space and time dimension. A major advantage of implicit schemes is—although the iteration means higher computational demand—that the discretization required for a convergent solution can be much coarser than for explicit methods because the stability of the solution is not liable to the CFL condition. This usually leads to a better performance of implicit methods with respect to available computation time and memory.

[1] Nonlinearity is not a feature introduced by the applied numerical solution procedure but is inherent to the governing hydrodynamic equations!

[2] According to Cunge et al. (1980), explicit schemes do not lead to a system of algebraic equations, since the solution for each point can be computed separately.

Furthermore, not only adjacent temporal nodes have to be taken into account for the formulation of difference quotients to replace the temporal derivatives. Nodes located further away, e.g., $(i, j-2)$, are also applicable. In such a case, one speaks of a multi-step scheme. Another possibility is to use intermediate values with single-step schemes (e.g., half steps, as used for the second-order Runge-Kutta scheme, cf. Appendix A.2) in order to obtain a higher order method.

The difference of multi-step and single-step schemes with intermediate values is that the former use and keep the information from previous steps throughout the numerical solution, whereas the latter discard the previous information before turning to the next calculation step. Compared with first-order single-step methods, single-step methods with intermediate values and multi-step schemes tend to possess better stability and, therefore, convergence properties. Nevertheless, the selection of suitable difference quotients and a solution scheme (i.e., implicit or explicit) strongly depends on the class and character of the investigated problem, which is discussed in Section 4.4.

4.3 Analytical Solution Procedures

Considering the flexibility and universality of numerical flow models, the question arises: Why are analytical solutions of the governing equations needed? Arguments that are given in the literature are: (a) Straightforward model applicability since only physically-based parameters are needed; (b) the sensitivity and influence of single parameters can often be directly seen from the computation formulas; (c) the data situation omits the application of numerical methods; (d) there are no numerical inconveniences (e.g., emerging from approximation and truncation errors); (e) analytical models can be coupled on an analytical basis; and (f) the analytical solution can serve as a reference for numerical models, e.g., to quantify the influence of different numerical methods on the quality of the solution.[1]

A direct solution of the flow model equations discussed herein is not possible for the general case. However, there are ways towards an analytical solution of the PDEs. If no direct integration is possible, strategies to analytically solve the model equations are: to reduce the occurring PDEs to ODEs (e.g., by finding characteristic curves, cf. Section 4.1) and, consecutively, apply suitable classical analytical solution methods[2], or to apply integral transforms.[3] Certain assumptions may be, therefore, necessary to obtain an analytical solution of the governing PDEs. These assumptions address (a) the boundary and initial conditions; (b) cross-sectional geometry; and (c) the way the dependent variables are related, e.g., depending on a chosen stage–discharge relationship. For illustration, Appendix A.4 shows an analytical solution of the kinematic wave model by obtaining characteristic solutions and applying a direct integration under the restriction of a very wide rectangular channel geometry (wide channel assumption).

Based on the literature research carried out for this thesis (cf. Chapter 2), a number of analytical solutions for overland and open channel flow were found, foremost for the kinematic wave and the

[1] Especially considering the last point, (f), it is important to distinguish between the terms "analytical solution" and "exact solution". An exact solution is a valid solution of the analytical model equations and can only be obtained by applying analytical solution methods, whereas every numerical procedure would introduce errors. The term "analytical solution" is somewhat more general since it only states that the desired solution is obtained by using analytical calculus. For instance, applying a series approximation to the governing equations can deliver an analytical solution procedure but will not produce an exact solution of the initial PDEs. Nevertheless, the terms "analytical solution" and "exact solution" are used synonymously in this thesis.

[2] As direct integration, separation of variables, or change of variables.

[3] The given statements refer to linear or quasilinear PDEs.

zero-inertia approximation of the full hydrodynamic model. Attributable to the more complicated structure of the governing equations, analytical solutions of the full hydrodynamic model were found less frequently. Common for all approaches is the introduction of assumptions from the above listing (a–c). Table 4.1 shows literature which incorporates analytical solutions for the KW, ZI, and HD flow models. The investigated flow processes range from overland flow resulting from rainfall excess (with or without upper inflow and/or infiltration), over flow in irrigation borders and furrows, to flow in prismatic and nonprismatic open channels (again with or without lateral inflow, but no infiltration).

As already mentioned, one way for obtaining an analytical solution of the governing equations is to simplify the boundary conditions. This can be achieved, for instance, by introducing assumptions regarding the lower boundary, e.g., applying a zero-depth gradient (i.e., $\frac{\partial h}{\partial x} = 0$) lower boundary condition (e.g., Govindaraju et al., 1990; Govindaraju et al., 1992). Furthermore, various sources and sinks of mass and momentum are imaginable to influence the discussed flow phenomena. More precisely, the flow domain can be charged by flow through the upper boundary and/or lateral inflows (i.e., through river inflow, overland inflows, or gains from rainfall) and, on the other hand, the flow may lose mass and momentum, e.g., attributable to infiltration on permeable surfaces. These source/sink processes are often strongly simplified in the regarded modeling approaches (i.e., neglected, assumed to be stationary, or described with simplified analytical approaches) in order to obtain an analytical expression of the flow equations (e.g., Henderson and Wooding, 1964; Govindaraju et al., 1988; Mizumura, 2006).

Another popular simplification in order to obtain an analytical solution procedure is to assume regular prismatic cross-sectional geometries (e.g., rectangular cross sections), which is justifiable for flow over a plane, i.e., overland flow and flow in an irrigation border (Schmitz, 1989; Schmitz and Seus, 1990) or, e.g., in a regular irrigation furrow (Schmitz and Seus, 1992), but may be questionable for natural river channels with irregular cross sections and a potentially pronounced change in channel geometry along the flowpath. By assuming prismatic or very wide geometries, it is likely possible to apply the method of characteristics and directly integrate the resulting ODEs (e.g., Henderson, 1966; Chalfen and Niemiec, 1986; Singh, 1996; for the basic methodology, cf. Appendix A.4).

A more comprehensive approach to include cross-sectional geometries was proposed by Schmitz et al. (2002) who described the nonprismatic geometry of a natural river with spatially changing analytical profile functions, based on a flexibly adaptable power law. The concept of their analytical zero-inertia solution further connects flow properties to a momentum-representative cross section, which is placed at the upper domain boundary. Furthermore, their solution assumes a free-moving lower boundary condition, which renders the model favorable for predicting advancing surge flow. The restriction of their approach is that strongly falling upper boundary conditions are not covered by the assumptions which were made in model development.

Familiar with the ideas of Schmitz et al. (2002), Wöhling et al. (2004b) and Wöhling (2005) presented a quite rigorous analytical furrow irrigation model which is able to account for unsteady inflows and unsteady infiltration losses. Although the model was applied for prismatic furrow geometries, the approach is basically able to include nonprismatic cross-sectional profiles, utilizing the respective concepts of Schmitz et al. (2002). Being generally well-suited for simulating *advancing* flow under infiltration, again it needs to be stated that the proposed analytical ZI model cannot account for strongly falling hydrographs and zero-advance conditions. This directs the approach to

Table 4.1: Overview of selected studies presenting analytical solution methods for the hydrodynamic models.

Reference	Model class	Flow process	Cross sections	Lateral inflow/ rainfall	Infil- tration	Upper inflow	Solution approach
Henderson and Wooding (1964)	KW	O	WCA	S	–	–	MOC, DI
Henderson (1966)	KW	C	P	–	–	US	MOC, DI
Singh (1996)	KW	C	P	–	–	US	MOC, DI
Mizumura (2006)	KW	O	WCA	US	–	–	MOC, DI
Baiamonte and Agnese (2010)	KW	O	WCA	US	US	–	MOC, DI
Mizumura and Ito (2011a)	KW	O	WCA	US	–	–	MOC, DI
Mizumura and Ito (2011b)	KW	O	WCA	US	–	–	MOC, DI
Govindaraju et al. (1988)	ZI	O	WCA	S	–	–	ASS†
Schmitz (1989)	ZI	B	P	–	US	US	MRXS, DI
Govindaraju et al. (1990)	ZI	O	WCA	US	–	–	ASS†
Schmitz and Seus (1990)	ZI	B	P	–	US	US	MRXS, DI
Govindaraju et al. (1992)	ZI	O	WCA	US	–	–	ASS†
Schmitz and Seus (1992)	ZI	F	P	–	US	US	MRXS, DI
Schmitz et al. (2002)	ZI	C	NP	–	–	US	MRXS, DI
Fan and Li (2004)	ZI	C	P	US	–	S	IT
Wöhling et al. (2004b)	ZI	F	P	–	US	US	MRXS, DI
Wöhling (2005)	ZI	F	P	–	US	US	MRXS, DI
Chalfen and Niemiec (1986)	HD	C	P	–	–	US	MOC, DI
Singh (1996)	HD	O	WCA	S	–	–	MOC, DI
Wang et al. (2002)	HD††	O	WCA	US	–	S	MOC, DI
Chung and Kang (2004)	HD	C	P	–	–	US	IT

With KW: kinematic wave model; ZI: zero-inertia model; HD: full hydrodynamic model (based on the Saint-Venant equations); O: overland flow; C: river channel flow; B: flow in irrigation borders; F: flow in irrigation furrows; WCA: wide channel assumption; P: prismatic cross sections; NP: nonprismatic cross sections; S: steady; US: unsteady; MOC: method of characteristics; DI: direct integration; ASS: approximate Taylor series solution; MRXS: momentum-representative cross section; IT: integral transform.

†Although the proposed solution delivers an analytical procedure for the flow computations, the result is not an exact one, corresponding to the governing flow equations, but an approximate solution.

††The introduced, strongly simplified depth-discharge relationship renders the model equivalent to a KW model.

the application for modeling advancing dam culvert release (cf. Section 3.7.1). However, Wöhling (2005) accounted for the other phases of a flow event (cf. Section 3.1) by using simplified (i.e., steady and volume-balance approaches) yet still analytical concepts that turned out to be reasonable under the problem-specific conditions of furrow irrigation.

In summary, the listing in Table 4.1 supports the finding that inevitably none of the available analytical solutions retains the generality of the governing flow model PDEs. Therefore, although the results obtained by an analytical model are at best exact solutions, their validity is constituted by the restrictions which were made during the mathematical development of the analytical model. Nevertheless, as discussed initially in this section, analytical solutions are of high importance for simulating processes where numerical solution schemes are prone to failure or introduce unacceptable errors, e.g., associated with surge flow modeling in initially dry channels under significant losses, or overland flow modeling.

4.4 Discussion of the Reviewed Solution Procedures in the Light of Flow Modeling in Ephemeral Rivers

As shown in Section 3.1, wadi flow under dam operation features a wide range of magnitudes and process dynamics, which should be regarded in model development. The flow in the wadi reaches upstream of a dam is characterized by potentially steep gradients and pronounced process dynamics. Employing finite differences (cf. Section 4.2.1) offers an appropriate and well-proven method for solving such initial-boundary-value problems in one spatial dimension (i.e., the afore-presented one-dimensional hydrodynamic models).

When choosing a certain finite difference scheme, two decisions have to be made: First, appropriate difference quotients have to be selected. Second, one has to choose between an explicit or an implicit formulation of the finite difference equations. The following criteria—which might be contradictory to some extent—should be balanced by a suitable numerical integration scheme:

- ▷ The algorithm should be efficient with regard to the available computational resources;
- ▷ exhibit a suitable convergence behavior;
- ▷ yield accurate results, i.e., so that numerical errors have a negligible influence on mass balance and dynamics of the considered process; and
- ▷ allow for straightforward implementation, testing, and application.

The use of a higher-order scheme proposes a reduction of the approximation errors and, therefore, yields a better convergence behavior of the solution scheme, which is additionally conditioned by the chosen spatial and temporal discretization of the solution domain. Additionally, higher-order schemes tend to introduce less numerical dispersion[1], which might facilitate an accurate simulation of steep gradients, e.g., associated with flash floods. On the other hand, higher-order schemes demand more computational resources. According to Press et al. (1992), a second-order or third-order scheme, therefore, seems to offer a balance of improved convergence, tolerable numerical dispersion, and computational efficiency. Despite the fact that implicit finite difference schemes feature greater numerical stability and comparably intermediate computational demand, an explicit scheme should be chosen for a kinematic wave routing model which is intended for the upstream reach of the dam and spillway release flow (cf. Section 3.7.1). Explicit schemes introduce less numerical dispersion and are, therefore, more suited for highly dynamic, shock-prone flows, as present in sewer networks (Duchesne et al., 2001), associated with dam-break problems (e.g., Delis and Skeels, 1998; Garcia-Navarro et al., 1999), or—as applies to this work—flash flood routing (e.g., Mudd, 2006).

Most important for a sound description of indirect recharge influenced by dam operation is the accurate and robust process modeling of the advancing, discontinuous culvert release flow in the downstream wadi sections. Trying to employ numerical schemes to solve the governing equations is prone to fail for two reasons: (a) The water surface curvature at the tip of the advancing and

[1] Numerical dispersion is a corollary of the approximations inherent to a numerical solution scheme and causes a smoothing of gradients due to averaging physical values in space and time. This adds some dispersion (and, therefore, wave attenuation) to the solution, which is then added to physical dispersion, represented in the momentum equations of the full hydrodynamic and the zero-inertia model. In contrast, the kinematic wave momentum equation neglects physical dispersion.

infiltrating flow domain is infinitely steep, which causes gradients that cannot be appropriately resolved by a numerical scheme which approximates gradients over space and/or time. Hence, convergence problems can occur which leads to errors at best, and to nonconvergence of the applied scheme, at worst. (b) The advance dynamics can become very weak, as the lower moving boundary of the flow domain is associated with only a discrete position of the incorporated discretization grid. This yields errors in the mass balance and restrains a correct simulation of advance dynamics.

A popular strategy to circumvent such shortcomings caused by a numerical solution is the introduction of a nonzero initial flow in the channel, e.g., applied by Mudd (2006) and Morin et al. (2009). For comparably high flow rates and low infiltration quotas (as in the wadi sections upstream of a recharge dam), this assumption causes no greater errors. This looks differently for the high infiltration quotas associated with dam release flow in the downstream reaches, where an accurate simulation of the growing extents of the infiltrating flow domain is desired. A lot of research has tried to challenge equivalent problems, emerging from process-oriented modeling of infiltrating flow in furrows or borders. Besides the already mentioned nonzero initial flow assumption, literature shows various approaches trying to cope with the complicated portrayal of discontinuous hydrodynamics of an advancing wave tip.

When trying to avoid an assumptive nonzero initial flow, the process has to be regarded as a moving-boundary problem. The shape and the dynamics of the downwards moving tip of the (typically infiltrating) flow domain have to be portrayed. A possibility of facing the inconvenient modeling of the wave tip is the simplification of the flow process to a basic volume consideration and the assumption of an arbitrary water surface shape, mostly represented by a parabola (e.g., Kincaid, 1970; Schmitz et al., 1985). Capturing the moving interface between the dry and the wetted channel with numerical means leads to further errors. For high infiltration quotas, the wave advance slows down significantly, which makes an adaption of the spatial or temporal discretization inevitable. For instance, Strelkoff and Katopodes (1977) used a computation grid with a constant time step. The spatial discretization is adapted to the distance the wave tip travels within each fixed time step. For a decelerating wave, the spatial discretization is refined, which increases the required computational effort.

Alternatively, the space step can be kept constant and the time step is adapted to wave advance dynamics (e.g., Rayej and Wallender, 1985). Since the decelerating wave travels decreasing distances within a constant time, the time step can be coarsened in case of a constant space step. Nevertheless, if the time step is altered disregarding the spatial resolution, the underlying numerical scheme is susceptible to harm the Courant criterion, which is why the aforementioned authors applied implicit solution schemes. Moreover, changes in the relation of the time and space step produce changes in numerical dispersion, which might not correspond to the physical character of the flow.

4.5 Summary and Conclusions

Summing up, numerical procedures are generally suited to solve the governing equations of the flow models discussed herein for a wide range of conditions. Special attention has to be drawn to the dynamics of the considered processes, which span a wide range for wadi flow in the upstream and downstream reaches of a recharge dam. The upstream processes and the spillway release flow are very pronounced and the hydrographs reflect an intrinsic steepening tendency of the flow. Hence, an explicit finite difference scheme is proposed for the numerical solution of the governing kinematic

wave model, where the KW model was selected on the basis given in Section 3.7.1. Moreover, to balance convergence behavior, numerical dispersion, and computational demands, a second-order solution scheme is proposed.

In contrast, the numerical solution of the flow equations in case of advancing and infiltrating flow caused by dam culvert release is prone to considerable errors and shortcomings and, therefore, an analytical procedure is indicated. The same applies for overland flow modeling. It was discussed in Sections 3.7.1 and 3.7.2 that the ZI model poses a feasible approach for portraying such advancing, gradually varied flows. As shown in Section 4.3, analytical solutions of the ZI model that account for initially dry channel conditions via a moving lower boundary condition are available for prismatic and nonprismatic geometries (Schmitz, 1989; Schmitz and Seus, 1990; Schmitz and Seus, 1992; Schmitz et al., 2002; Wöhling, 2005).

The aforementioned publications all propose modeling concepts which are based on the definition of a momentum-representative cross section (that is either fixed at the upstream boundary or travels with the wave's center of gravity). Furthermore, the underlying analytical procedures allow for a direct consideration of an arbitrary losses or yield function in the continuity and momentum equations, i.e., for the quantification of infiltration, lateral inflows, or rainfall. Moreover, the presented analytical solution concepts avoid the cumbersome assumption of a nonzero initial flow and circumvent any arbitrary assumptions on the water surface shape, especially at the wetting front of the flow domain.

Numerous applications for border irrigation (i.e., infiltrating overland flow), furrow irrigation, and flow in nonprismatic river channels proved the robustness and accuracy of the employed analytical ZI modeling procedures. The present thesis follows these concepts and develops a moving-boundary analytical model for advancing and infiltrating wadi flow, which is based on the zero-inertia equations for unsteady inflow and losses conditions, and is able to include nonprismatic geometries. The modeling concepts developed in this thesis are shown to perform well with respect to accuracy and robustness, not only covering flow in ephemeral wadi channels, but also under typical overland flow conditions.

Chapter 5

Novel Analytical Solution Approaches for the Zero-Inertia Equations

This chapter presents two analytical solution approaches for the zero-inertia model. First, a novel solution for open channel flow in permeable nonprismatic channels is derived which is based upon the extended zero-inertia equations, holding loss terms in the continuity and the momentum equations (cf. Section 3.5). The analytical solution is obtained under the assumption of a momentum-representative cross section, as first proposed by Schmitz and Seus (1987), and yields a set of two nonlinear equations. A space-discrete rather than a time-discrete iteration scheme is employed for solving the set of equations, which has specific advantages regarding computational effort and convergence behavior of the underlying solution procedure (cf. Section 4.4). The approach is similar to the one proposed by Schmitz et al. (2002) but accounts for the loss of mass and momentum attributable to infiltration. The required calculus is presented in depth in Section 5.1.

Second, the same basic concepts are applied for the more specific case of overland flow under lateral inflow/losses conditions as a consequence of rainfall and/or infiltration (Section 5.2). A very wide rectangular cross section is assumed. This simplifies the required calculus and leads to a set of nonlinear equations, similar to the open-channel case, which is again solved by employing a space-discrete iterative procedure.

5.1 A Novel Analytical Solution Approach for Zero-Inertia Open Channel Flow with Infiltration

A surge advancing over a dry wadi bed as a consequence of controlled release from a groundwater recharge dam represents a free boundary problem. After some time, when aiming for groundwater recharge, infiltration equals the inflow to the channel and, thus, the flow forms a kind of standing wave. The numerical treatment of such phenomena generally involves considerable problems. For avoiding numerical inconveniences emerging from the complex interacting surface/subsurface flow processes (cf. Section 4.4), an analytical solution of the slightly modified zero-inertia equations

is subsequently derived. The approach introduces a momentum-representative cross section for portraying the transient development of momentum and refers to a channel with constant slope and nonprismatic geometry. The subsequently derived analytical solution is very similar to one given in Schmitz et al. (2002), but, in contrast, accounts for a permeable channel bed, which allows for significant infiltration. Due to the mathematical structure of the solution, any arbitrary infiltration model can be used for quantifying infiltration losses. Moreover, the model does not introduce any simplifications regarding the description of the water surface shape, especially at the moving wave front.

5.1.1 Governing Equations

Surging flow in an irregular river bed with water losses through the channel bottom can be described by the extended zero-inertia equations, consisting of the continuity equation (3.7), holding the $-q^{\phi}$ mass loss term, and the ZI momentum equation (3.3), supplemented by the $\frac{q^{\phi}u}{gA}$ momentum loss term (cf. Section 3.5). In the momentum equation (3.3), friction slope S_f is expressed via a uniform flow formula (cf. Section 3.4):

$$\frac{\partial A}{\partial t} + \frac{\partial Q}{\partial x} = -q^{\phi} \tag{5.1}$$

$$\frac{\partial h}{\partial x} = S_0 - \frac{u^2}{K^2 R^{2\beta}} + \frac{q^{\phi}u}{gA} \tag{5.2}$$

in which t: time [T]; x: longitudinal space coordinate [L]; $A(x,t)$: wetted cross-sectional area [L^2]; $Q(x,t)$: discharge [$\mathrm{L}^3\mathrm{T}^{-1}$]; q^{ϕ}: volumetric rate of infiltration per unit length [$\mathrm{L}^2\mathrm{T}^{-1}$]; $h(x,t)$: water depth [L]; S_0: bottom slope [−]; $u(x,t)$: flow velocity [LT^{-1}]; $R(x,t)$: hydraulic radius [L]; K: roughness coefficient [$\mathrm{L}^{1-\beta}\mathrm{T}^{-1}$]; β: exponent of the flow formula [−] (e.g., for the Manning-Strickler equation $\beta = \frac{2}{3}$; Strickler, 1923); and g: acceleration due to Earth's gravity [LT^{-2}].

The first step towards the analytical solution of the system of Eqs. (5.1) and (5.2) is to multiply Eq. (5.2) by $R^{2\beta}$, yielding

$$R^{2\beta}\frac{\partial h}{\partial x} = \left(S_0 + \frac{q^{\phi}u}{gA}\right) R^{2\beta} - \frac{u^2}{K^2} \tag{5.3}$$

According to Schmitz and Seus (1990), Schmitz and Seus (1992), and Schmitz et al. (2002), the inflow boundary is assumed to be a *momentum-representative cross section* for the specific flow problem. In this approach, the momentum portrayed by the right-hand side of Eq. (5.3)—which is neglected in kinematic wave analysis—is continuously represented by the transient amount of momentum at the inflow boundary ($x = 0$). This way, the right-hand side of Eq. (5.3) no longer depends explicitly on x, and Eq. (5.3) can be rewritten as

$$R^{2\beta}\frac{\partial h}{\partial x} = \left(S_0 + \frac{q_0^{\phi}u_0}{gA_0}\right) R_0^{2\beta} - \frac{u_0^2}{K^2} = \left(S_0 - \frac{u_0^2}{K^2 R_0^{2\beta}} + \frac{q_0^{\phi}u_0}{gA_0}\right) R_0^{2\beta} \tag{5.4}$$

with $R_0 = R_0(t) = R(x = 0, t)$, $u_0 = u_0(t) = u(x = 0, t)$, $A_0 = A_0(t) = A(x = 0, t)$, and $q_0^{\phi} = q_0^{\phi}(t) = q^{\phi}(x = 0, t)$. The expression on the right-hand side of Eq. (5.4) can be considered as a measure of the transient momentum at $x = 0$, covering contributions from bottom slope, friction, and infiltration through the river bed.

5.1.2 Including Nonprismatic Channel Geometries Using Analytical Profile Functions

The arbitrarily varying cross-sectional geometry of a nonprismatic channel is described with the power laws

$$\tilde{h}(x, A) = h(x, t) = p_1(x)A(x, t)^{p_2} \tag{5.5}$$

$$\tilde{R}(x, A) = R(x, t) = p_3(x)A(x, t)^{p_4} \tag{5.6}$$

with $p_1(x)$, p_2, $p_3(x)$, and p_4: geometry parameters for relating water depth $h(x, A)$ and hydraulic radius of a river cross section $\tilde{R}(x, A)$ to the wetted cross-sectional area $\tilde{A}(x, t)$. For formal reasons, the functions describing the cross-sectional geometry, $\tilde{h}(x, A)$ and $\tilde{R}(x, A)$, have to be distinguished from the functions $h(x, t)$ and $R(x, t)$ which explicitly relate water depth and hydraulic radius to the independent variables of space and time.

Schmitz et al. (2002) showed that irregular cross sections of natural river beds can be closely approximated by adjusting the free parameters $p_1(x)$, p_2, $p_3(x)$, and p_4 of Eqs. (5.5) and (5.6) in a way that the right-hand side of the equations fits the functions $\tilde{h}(x, A)$ and $\tilde{R}(x, A)$. In particular, $p_1(x)$ and $p_3(x)$ account for the nonprismatic character of the river bed and have to be obtained for every cross section which is included in modeling. The values of p_2 and p_4 are not dependent on the space variable and account for some kind of common property, which is most evident for basic, regular cross-sectional geometries, e.g., $p_2 = p_4 = \frac{1}{2}$ for a triangular, $\frac{2}{3}$ for a parabolic, and 1 for a rectangular cross section. The parameters p_2 and p_4 have to be representative for the whole channel reach. Therefore, it is feasible to use the functions $\tilde{h}(x, A)$ and $\tilde{R}(x, A)$ which are most representative for a reach, or, alternatively, to average the profile functions over all cross sections along the channel.

The subsequently outlined analytical solution of the ZI equations requires the specification of the geometry parameters $p_1(x)$, p_2, $p_3(x)$, and p_4. Assuming the channel sections to be of a regular triangular, parabolic, or rectangular type, the values of $p_2 = p_4$ are predetermined ($\frac{1}{2}$, $\frac{2}{3}$, or 1) and the values of $p_1(x)$ and $p_3(x)$ can be straightforwardly estimated by describing the cross-sectional geometry with an exponential relationship of the form

$$z(x, y) = h_\mathrm{r} \left(\frac{y}{w_\mathrm{r}(x)} \right)^a \tag{5.7}$$

in which z: vertical space coordinate positive upwards [L]; y: horizontal space coordinate perpendicular to the channel axis x [L]; $w_\mathrm{r}(x)$: half the width of the cross section at a reference water depth h_r [L]; and a: a free cross-sectional shape parameter [−] ($a \geq 1$).

Thus, instead of estimating $p_1, ..., p_4$ in a way to fulfill Eqs. (5.5) and (5.6), the four parameters $p_1, ..., p_4$ can be analytically related to the two free parameters, a and w_r, such that the function $z(x, y)$ most closely fits the true cross-sectional geometry.[1] The portrayal of channel geometry by the power law Eq. (5.7) is illustrated in Fig. 5.1a. Figure 5.1b–c illustrates the influence of the parameters w_r and a on the representation of channel geometry. It can be seen that w_r parametrizes

[1] This can be achieved by applying a standard function fitting method, e.g., a least-squares fitting.

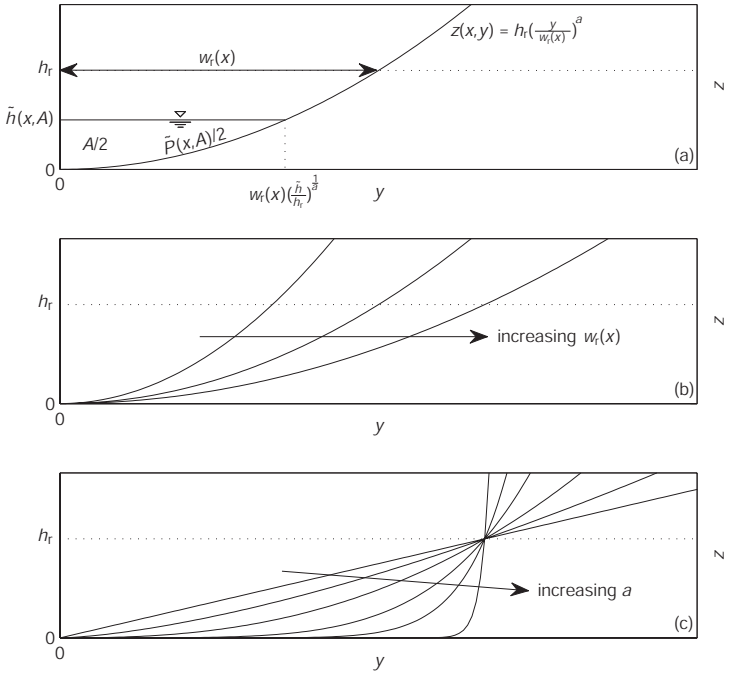

Figure 5.1: Sketches on the portrayal of half of a cross section with the power law Eq. (5.7), according to Schmitz et al. (2002). (a) Illustration of the representation of cross-sectional geometry $z(x, y)$ with a power law, holding the two free parameters w_r and a; (b) influence of the parameter w_r on $z(x, y)$; (c) influence of the parameter a on $z(x, y)$.

the general channel width and the channel's lateral slope, whereas a changes the channel shape from triangular ($a = 1$), over parabolic ($a = 2$), to rectangular ($a = \infty$).

For regular channel geometries, Schmitz et al. (2002) deliver the derivation of the following analytical expressions for $p_1, ..., p_4$, which read

$$p_1(x) = h_\mathrm{r} \left(\frac{a+1}{2a h_\mathrm{r} w_\mathrm{r}(x)} \right)^{\frac{a}{a+1}} \tag{5.8}$$

$$p_2 = \frac{a}{a+1} \tag{5.9}$$

$$p_3(x) = \frac{\left(\frac{2a}{a+1} h_\mathrm{r} w_\mathrm{r}(x) \right)^{\frac{1}{a+1}}}{2 w_\mathrm{r}(x) \sqrt{1 + 2\left(1 - \frac{1}{a}\right) \frac{h_\mathrm{r}}{w_\mathrm{r}(x)} + \left(\frac{h_\mathrm{r}}{w_\mathrm{r}(x)} \right)^2}} \tag{5.10}$$

$$p_4 = \frac{a}{a+1} \tag{5.11}$$

For the basic cross-sectional shapes, represented by $a = 1, 2, \infty$ (triangular, parabolic, rectangular), Eqs. (5.8) to (5.11) yield the relationships shown in Table 5.1. The expressions given therein can be used to straightforwardly compute the geometry parameters $p_1, ..., p_4$ for regular channel shapes.

In contrast, for channel geometries which are not triangular, parabolic, or rectangular, it is indicated to estimate the parameters $p_1, ..., p_4$ with respect to a given empirical function $z(x, y)$ which can be determined by using channel topography data, e.g., emerging from terrestrial surveying or a digital elevation model. As already illustrated in Section 3.6, continuous profile functions,

Table 5.1: Geometric representation of triangular, parabolic, and rectangular cross sections, according to Schmitz et al. (2002).

Parameter/ function	Dimension	Triangular cross section	Parabolic cross section	Rectangular cross section
a	[–]	1	2	∞
$p_1(x)$	$[\mathrm{L}^{1-2p_2}]$	$\sqrt{\frac{h_\mathrm{r}}{w_\mathrm{r}(x)}}$	$h_\mathrm{r}^{\frac{1}{3}}\left(\frac{3}{4w_\mathrm{r}(x)}\right)^{\frac{2}{3}}$	$\frac{1}{2w_\mathrm{r}(x)}$
p_2	[–]	$\frac{1}{2}$	$\frac{2}{3}$	1
$p_3(x)$	$[\mathrm{L}^{1-2p_4}]$	$\frac{1}{2\sqrt{\frac{w_\mathrm{r}(x)}{h_\mathrm{r}}+\frac{h_\mathrm{r}}{w_\mathrm{r}(x)}}}$	$\frac{\left(\frac{h_\mathrm{r}}{6w_\mathrm{r}(x)^2}\right)^{\frac{1}{3}}}{\sqrt{1+\frac{h_\mathrm{r}}{w_\mathrm{r}(x)}+\left(\frac{h_\mathrm{r}}{w_\mathrm{r}(x)}\right)^2}}$	$\frac{1}{2w_\mathrm{r}(x)+2h_\mathrm{r}}$
p_4	[–]	$\frac{1}{2}$	$\frac{2}{3}$	1
$\tilde{h}(x,A)$	[L]	$\sqrt{\frac{h_\mathrm{r}A}{w_\mathrm{r}(x)}}$	$h_\mathrm{r}^{\frac{1}{3}}\left(\frac{3A}{4w_\mathrm{r}(x)}\right)^{\frac{2}{3}}$	$\frac{A}{2w_\mathrm{r}(x)}$
$\tilde{P}(x,A)$	[L]	$2\sqrt{\left(\frac{w_\mathrm{r}(x)}{h_\mathrm{r}}+\frac{h_\mathrm{r}}{w_\mathrm{r}(x)}\right)A}$	$\sqrt{1+\frac{h_\mathrm{r}}{w_\mathrm{r}(x)}+\left(\frac{h_\mathrm{r}}{w_\mathrm{r}(x)}\right)^2}\left(\frac{6}{h_\mathrm{r}}w_\mathrm{r}(x)^2A\right)^{\frac{1}{3}}$	$2w_\mathrm{r}(x)+2h_\mathrm{r}$
$\tilde{R}(x,A)$	[L]	$\frac{1}{2}\sqrt{\frac{A}{\frac{w_\mathrm{r}(x)}{h_\mathrm{r}}+\frac{h_\mathrm{r}}{w_\mathrm{r}(x)}}}$	$\frac{\left(\frac{h_\mathrm{r}}{6w_\mathrm{r}(x)^2}\right)^{\frac{1}{3}}}{\sqrt{1+\frac{h_\mathrm{r}}{w_\mathrm{r}(x)}+\left(\frac{h_\mathrm{r}}{w_\mathrm{r}(x)}\right)^2}}A^{\frac{2}{3}}$	$\frac{A}{2w_\mathrm{r}(x)+2h_\mathrm{r}}$

as posed by Eqs. (5.5) and (5.6), are needed for a biunique relation of water depth, wetted cross-sectional area, and hydraulic radius within the hydrodynamic equations. The practical adjustment of the geometry parameters for a nonprismatic channel with irregular cross-sectional geometries is shown in Section 6.1.1.2.

5.1.3 Boundary and Initial Conditions

The system of partial differential equations (5.1);(5.4) requires the specification of boundary and initial conditions. The boundary condition at the fixed upstream boundary ($x = 0$) is

$$Q(0,t) = Q_0(t) \tag{5.12}$$

where the ZI assumptions induce the restriction that strongly falling functions of $Q(0,t)$ cannot be used as an upstream boundary condition (Schmitz et al., 2002). The downstream moving boundary is located at $x = x_\mathrm{tip}(t)$. At this moving point, the following conditions apply and have to be satisfied by the intended analytical solution of the governing equations:

$$A(x_\mathrm{tip},t) = 0 \tag{5.13}$$

$$q^{\phi}(x_{\mathrm{tip}}, t) = q^{\phi}_{\mathrm{tip}}(t) = 0 \tag{5.14}$$

$$u(x_{\mathrm{tip}}, t) = u_{\mathrm{tip}}(t) = \frac{\mathrm{d}x_{\mathrm{tip}}}{\mathrm{d}t} \tag{5.15}$$

where $x_{\mathrm{tip}}(t)$ is the transient location of the advancing wave tip and $u_{\mathrm{tip}}(t)$ is the wave tip's advance velocity. Of course, the wetted cross-sectional area $A(x_{\mathrm{tip}}, t)$ and the cross-sectional infiltration rate $q^{\phi}_{\mathrm{tip}}(t)$ equal zero at the advancing wave tip.

In contrast to the often applied assumption of a nonzero initial flow (cf. Section 4.4), the analytical solution assumes an initially dry channel reach further downstream of the wetting flow domain. This implies that, for a dry channel, the location of the flow domain has a spatial extent of zero. The initial condition of the considered flow problem, therefore, reads

$$x_{\mathrm{tip}}(t = 0) = 0 \tag{5.16}$$

5.1.4 Analytical Solution of the Momentum Equation

Subsequently, the analytical solution of the extended zero-inertia momentum equation (5.4) is derived. The calculus follows Schmitz et al. (2002), with the difference that the $\frac{q^{\phi}u}{gA}$ term—which accounts for a loss of flow momentum attributable to infiltration—is regarded herein. For this reason, and to be comprehensive, the following derivation is presented in detail. The momentum equation (5.4) can be rewritten in the form

$$R^{2\beta}\frac{\partial h}{\partial x} = \left(S_0 - \frac{u_0^2}{K^2 R_0^{2\beta}} + \frac{q_0^{\phi} u_0}{g A_0}\right) R_0^{2\beta} = \rho_0(t) \tag{5.17}$$

where $\rho_0(t)$ is a measure of the transient amount of momentum at the uppermost cross section at $x = 0$ [$\mathrm{L}^{2\beta}$], which is influenced by channel slope, friction slope, momentum loss attributable to infiltration, and the hydraulic radius. Employing the expression of the hydraulic radius, given by Eq. (5.6), the momentum equation (5.17) is recast[1], yielding

$$p_3(x)^{2\beta} A(x,t)^{2\beta p_4}\frac{\partial h}{\partial x} = \rho_0(t) \tag{5.18}$$

Making use of the relationship of water depth and wetted cross-sectional area, given by Eq. (5.5), delivers an expression for the spatial gradient of the water depth:

$$\frac{\partial h}{\partial x} = \frac{\mathrm{d}\tilde{h}}{\mathrm{d}x} = \frac{\partial \tilde{h}}{\partial x} + \frac{\partial \tilde{h}}{\partial A}\frac{\partial A}{\partial x} = \frac{\mathrm{d}p_1}{\mathrm{d}x}(x) A^{p_2} + p_1(x) p_2 A^{p_2 - 1}\frac{\partial A}{\partial x} \tag{5.19}$$

which is inserted into Eq. (5.18), yielding

$$\frac{\mathrm{d}p_1}{\mathrm{d}x}(x) A^{2\beta p_4 + p_2} + p_1(x) p_2 A^{2\beta p_4 + p_2 - 1}\frac{\partial A}{\partial x} = \rho_0(t) p_3(x)^{-2\beta} \tag{5.20}$$

For convenience, the abbreviation

$$\lambda = 2\beta p_4 + p_2 \tag{5.21}$$

[1] At this point—by relating cross-sectional area and hydraulic radius via the power law Eq. (5.6)—a regular cross-sectional geometry is assumed, which is a prerequisite for the subsequent calculus. This does not imply the channel geometry might not change in longitudinal direction, i.e., the geometry can be nonprismatic!

is introduced, which lets Eq. (5.20) be rewritten as

$$\frac{\mathrm{d}p_1}{\mathrm{d}x}(x)A^{\lambda} + p_1(x)p_2A^{\lambda-1}\frac{\partial A}{\partial x} = \rho_0(t)p_3(x)^{-2\beta} \tag{5.22}$$

which is a nonlinear and ordinary Bernoulli-type differential equation.

For linearizing Eq. (5.22), the substitution

$$\Gamma = p_1(x)^{\frac{\lambda}{p_2}}A^{\lambda} \tag{5.23}$$

$$\frac{\partial \Gamma}{\partial x} = \frac{\lambda}{p_2}p_1(x)^{\frac{\lambda}{p_2}-1}\frac{\mathrm{d}p_1}{\mathrm{d}x}(x)A^{\lambda} + \lambda p_1(x)^{\frac{\lambda}{p_2}}A^{\lambda-1}\frac{\partial A}{\partial x} \tag{5.24}$$

is introduced which allows recasting Eq. (5.22) to

$$p_1(x)^{\frac{\lambda}{p_2}-1}\frac{p_2}{\lambda}\frac{\partial \Gamma}{\partial x} = \rho_0(t)p_3(x)^{-2\beta} \tag{5.25}$$

Employing the boundary condition (5.13), Eq. (5.23) can be written as

$$\Gamma(x_{\mathrm{tip}},t) = p_1(x_{\mathrm{tip}})^{\frac{\lambda}{p_2}}A(x_{\mathrm{tip}},t)^{\lambda} = 0 \tag{5.26}$$

Using Eqs. (5.21) and (5.26), the general solution of the inhomogeneous differential equation (5.25) is

$$\Gamma(x,t) = -\frac{\lambda}{p_2}\rho_0(t)\int_x^{x_{\mathrm{tip}}(t)}\left(\frac{p_1(\xi)^{\frac{p_4}{p_2}}}{p_3(\xi)}\right)^{2\beta}\mathrm{d}\xi \tag{5.27}$$

where ξ indicates the integration variable in space direction. Resubstituting $A = p_1^{-\frac{1}{p_2}}\Gamma^{\frac{1}{\lambda}}$ yields the solution of the momentum equation

$$A(x,t) = p_1(x)^{-\frac{1}{p_2}}\left(-\frac{\lambda}{p_2}\rho_0(t)\int_x^{x_{\mathrm{tip}}(t)}\left(\frac{p_1(\xi)^{\frac{p_4}{p_2}}}{p_3(\xi)}\right)^{2\beta}\mathrm{d}\xi\right)^{\frac{1}{\lambda}} \tag{5.28}$$

Inserting Eq. (5.21) into Eq. (5.28) and employing the expression for $\rho_0(t)$, given by Eq. (5.17), leads finally to the analytical solution of the momentum equation

$$A(x,t) = p_1(x)^{-\frac{1}{p_2}}\left\{\left(1+\frac{2\beta p_4}{p_2}\right)\left(-S_0 + \frac{u_0^2}{K^2R_0^{2\beta}} - \frac{q_0^{\phi}u_0}{gA_0}\right)R_0^{2\beta}\int_x^{x_{\mathrm{tip}}(t)}\left(\frac{p_1(\xi)^{\frac{p_4}{p_2}}}{p_3(\xi)}\right)^{2\beta}\mathrm{d}\xi\right\}^{\frac{1}{2\beta p_4+p_2}} \tag{5.29}$$

5.1.5 Analytical Solution of the Continuity Equation

The continuity equation (5.1) is an inhomogeneous linear PDE in Q. Taking into account the upstream boundary condition (5.12), Eq. (5.1) can be directly integrated which yields

$$Q(x,t) = Q_0(t) - \int_0^x\left(\frac{\partial A}{\partial t}(\xi,t) + q^{\phi}(\xi,t)\right)\mathrm{d}\xi \tag{5.30}$$

where the integrand of Eq. (5.30) is obtained by differentiating Eq. (5.29) with respect to t. It has to be shown further that the downstream boundary condition (5.15) is satisfied by Eq. (5.30). In order to prove this, the mass balance in the wetted channel section is regarded by comparing the inflow volume to the channel with the volume of flow in the channel plus the infiltrated volume:

$$\int_0^t Q_0(\tau)\mathrm{d}\tau = \int_0^{x_{\mathrm{tip}}(t)} A(\xi,t)\mathrm{d}\xi + \int_0^t \int_0^{x_{\mathrm{tip}}(t)} q^{\phi}(\xi,\tau)\mathrm{d}\xi\mathrm{d}\tau \tag{5.31}$$

where τ indicates the infiltration opportunity time at a channel location x, respectively the integration variable in time. Equation (5.31) is differentiated with respect to t. Due to the boundary conditions (5.13) and (5.14), this yields

$$Q_0(t) = \int_0^{x_{\mathrm{tip}}(t)} \frac{\partial A}{\partial t}(\xi,t)\mathrm{d}\xi + A(x_{\mathrm{tip}},t)u_{\mathrm{tip}}(t) + \int_0^{x_{\mathrm{tip}}(t)} q^{\phi}(\xi,t)\mathrm{d}\xi + q^{\phi}_{\mathrm{tip}}(t) \tag{5.32}$$

which can be recast as

$$Q_0(t) = \int_0^{x_{\mathrm{tip}}(t)} \frac{\partial A}{\partial t}(\xi,t)\mathrm{d}\xi + \int_0^{x_{\mathrm{tip}}(t)} q^{\phi}(\xi,t)\mathrm{d}\xi = \int_0^{x_{\mathrm{tip}}(t)} \left(\frac{\partial A}{\partial t}(\xi,t) + q^{\phi}(\xi,t)\right)\mathrm{d}\xi \tag{5.33}$$

Inserting Eq. (5.33) into Eq. (5.30) delivers

$$Q(x,t) = \int_0^{x_{\mathrm{tip}}(t)} \left(\frac{\partial A}{\partial t}(\xi,t) + q^{\phi}(\xi,t)\right)\mathrm{d}\xi \tag{5.34}$$

and the flow velocity can be expressed as

$$u(x,t) = \frac{Q(x,t)}{A(x,t)} = \frac{\int_0^{x_{\mathrm{tip}}(t)} \left(\frac{\partial A}{\partial t}(\xi,t) + q^{\phi}(\xi,t)\right)\mathrm{d}\xi}{A(x,t)} \tag{5.35}$$

Applying L'Hôpital's rule and performing considerable but straightforward calculus, it can be shown that the boundary condition (5.15) is satisfied in such a way that

$$\lim_{x\to x_{\mathrm{tip}}} u(x,t) = \frac{\mathrm{d}x_{\mathrm{tip}}}{\mathrm{d}t} \tag{5.36}$$

Thus, the equations (5.29) and (5.30) solve the system (5.1);(5.4) and also satisfy the boundary conditions (5.12), (5.13), and (5.14). This solution accounts for the hydraulic feedback between the advance of a surge over an initially dry river bed and water losses due to infiltration across the continuously extending wetted channel bottom.

5.1.6 Algorithm for the Iterative Solution of the Nonlinear Problem

The solution for Eqs. (5.29) and (5.30) firstly requires evaluating the position of the advancing wave front $x_{\mathrm{tip}}(t)$ and the wetted cross-sectional area $A_0(t) = A(x = 0, t)$ at the inflow boundary by solving a nonlinear system of two equations iteratively. For this purpose, N observation points $(0 < x_1 < x_2 < ... < x_N)$ are defined and the arrival time of the wave tip t_n for each observation point, i.e., $x_{\mathrm{tip}}(t_n) = x_n$ (for $n = 1, 2, ..., N$), and the corresponding wetted cross-sectional area $A_{0,n} = A_0(t_n)$ at $x = 0$ are calculated.

The first of the above-mentioned nonlinear equations is obtained by setting $x = 0$ in Eq. (5.29). Making use of the relationships (5.4) and (5.6) in order to express the hydraulic radius in Eq. (5.29) yields

$$A_{0,n} = p_1(0)^{-\frac{1}{p_2}} \left\{ \left(1 + \frac{2\beta p_4}{p_2}\right) \psi_n \left(\frac{Q_0(t_n)^2}{K^2 A_{0,n}^2} - \left(S_0 + \frac{q_0^{\phi}(t_n) Q_0(t_n)}{g A_{0,n}^2} \right) p_3(0)^{2\beta} A_{0,n}^{2\beta p_4} \right) \right\}^{\frac{1}{2\beta p_4 + p_2}} \tag{5.37}$$

with the abbreviation

$$\psi_n = \int_0^{x_n} \left(\frac{p_1(\xi)^{\frac{p_4}{p_2}}}{p_3(\xi)} \right)^{2\beta} d\xi \tag{5.38}$$

To derive the second nonlinear equation, the wetted cross-sectional area, given by the analytical solution of the ZI momentum equation (5.29), has to be expressed for $t = t_n$. Dividing Eq. (5.29) by Eq. (5.37) relates the wetted cross-sectional area at a specific cross section location x to the wetted cross-sectional area at the inflow boundary, which yields

$$\frac{A(x,t_n)}{A_0(t_n)} = \left(\frac{p_1(x)}{p_1(0)} \right)^{-\frac{1}{p_2}} \left(\frac{\int_x^{x_n} \left(\frac{p_1(\xi)^{\frac{p_4}{p_2}}}{p_3(\xi)} \right)^{2\beta} \mathrm{d}\xi}{\int_0^{x_n} \left(\frac{p_1(\xi)^{\frac{p_4}{p_2}}}{p_3(\xi)} \right)^{2\beta} \mathrm{d}\xi} \right)^{\frac{1}{2\beta p_4 + p_2}} \tag{5.39}$$

Thus, $A(x,t_n)$ can be expressed as

$$A(x,t_n) = A_0(t_n) \left(\frac{p_1(x)}{p_1(0)} \right)^{-\frac{1}{p_2}} \left(\frac{\int_x^{x_n} \left(\frac{p_1(\xi)^{\frac{p_4}{p_2}}}{p_3(\xi)} \right)^{2\beta} \mathrm{d}\xi}{\int_0^{x_n} \left(\frac{p_1(\xi)^{\frac{p_4}{p_2}}}{p_3(\xi)} \right)^{2\beta} \mathrm{d}\xi} \right)^{\frac{1}{2\beta p_4 + p_2}} \tag{5.40}$$

Based on mathematical principles, it holds true that

$$\left(\frac{p_1(x)}{p_1(0)} \right)^{-\frac{1}{p_2}} = \left(\frac{p_1(0)}{p_1(x)} \right)^{\frac{1}{p_2}} \tag{5.41}$$

Using the definitions of Eqs. (5.21), (5.38), and (5.41), Eq. (5.40) can be rewritten as

$$A(x,t_n) = A_{0,n} \left(\frac{p_1(0)}{p_1(x)} \right)^{\frac{1}{p_2}} \left(1 - \frac{1}{\psi_n} \int_0^{x_n} \left(\frac{p_1(\xi)^{\frac{p_4}{p_2}}}{p_3(\xi)} \right)^{2\beta} \mathrm{d}\xi \right)^{\frac{1}{\lambda}} \tag{5.42}$$

Equation (5.42) holds an expression for the wetted cross-sectional area along the channel for a specific time t_n, associated with the arrival time of the flow domain at the nth channel cross section. Therefore, the volume of surface water in the channel at the time t_n may be expressed as

$$\int_0^{x_n} A(x,t_n) \mathrm{d}x = A_{0,n} \int_0^{x_n} \left(\left(\frac{p_1(0)}{p_1(x)} \right)^{\frac{1}{p_2}} \left(1 - \frac{1}{\psi_n} \int_0^{x_n} \left(\frac{p_1(\xi)^{\frac{p_4}{p_2}}}{p_3(\xi)} \right)^{2\beta} \mathrm{d}\xi \right)^{\frac{1}{\lambda}} \right) \mathrm{d}\xi \tag{5.43}$$

With the abbreviation

$$\omega_n = \int_0^{x_n} \left(\left(\frac{p_1(0)}{p_1(x)} \right)^{\frac{1}{p_2}} \left(1 - \frac{1}{\psi_n} \int_0^{x_n} \left(\frac{p_1(\xi)^{\frac{p_4}{p_2}}}{p_3(\xi)} \right)^{2\beta} \mathrm{d}\xi \right)^{\frac{1}{\lambda}} \right) \mathrm{d}\xi \tag{5.44}$$

Eq. (5.43) can be written briefly as

$$\int_0^{x_n} A(x, t_n)\mathrm{d}x = A_{0,n}\omega_n \tag{5.45}$$

Analogously to Eq. (5.31), the volume balance for a channel reach, cumulative over the time interval $[0, ..., t_n]$, reads

$$\int_0^{t_n} Q_0(\tau)\mathrm{d}\tau = A_{0,n}\omega_n + \int_0^{t_n} \int_0^{x_n} q^{\phi}(\xi, \tau)\mathrm{d}\xi\mathrm{d}\tau \tag{5.46}$$

Equations (5.37) and (5.46) can be quite straightforwardly rearranged to an iterative procedure (Appendix A.5 shows the derivation in detail), which accounts for the dynamic influence of infiltration on the surface flow, given by the two fixed-point equations[1]

$$A_{0,n}^{(k)} = \left(\frac{\lambda\psi_n \left(\frac{Q_0\left(t_n^{(k-1)}\right)}{K} \right)^2}{p_2 p_1(0)^{\frac{\lambda}{p_2}} + \lambda\psi_n \left(S_0 + \frac{q_0^{\phi}\left(t_n^{(k-1)}\right) Q_0\left(t_n^{(k-1)}\right)}{g\left(A_{0,n}^{(k-1)}\right)^2} \right) \frac{p_3(0)^{2\beta}}{\left(A_{0,n}^{(k-1)}\right)^{p_2}}} \right)^{\frac{1}{2+\lambda}} \tag{5.47}$$

$$t_n^{(k)} = t_n^{(k-1)} + \frac{A_{0,n}^{(k)}\omega_n + \int_0^{t_n^{(k-1)}} \int_0^{x_n} q^{\phi}(\xi, \tau)\mathrm{d}\xi\mathrm{d}\tau - \int_0^{t_n^{(k-1)}} Q_0(\tau)\mathrm{d}\tau}{Q_0\left(t_n^{(k-1)}\right)} \tag{5.48}$$

where $k = 1, 2, 3, ...$ denotes the iteration index.[2] The iterative scheme is described in more detail in the subsequent Section 5.1.7. A Taylor series expansion of the left-hand side of Eq. (5.46) around $t_n^{(k-1)}$ has been included in order to take the impact of infiltration through the permeable wadi bed into account. Starting values are provided by the results obtained from the preceding space step, i.e., $A_{0,n}^{(0)} = A_{0,n-1}$ and $t_n^{(0)} = t_{n-1}$. The convergence of the iterative procedure can be assessed by calculating an iteration convergence criterion and comparing it to a specific iteration precision criterion ε, e.g., $\varepsilon = 10^{-4}$:

$$\mathrm{ICC} = \max \left(\frac{\left| t_n^{(k-1)} - t_n^{(k)} \right|}{t_n^{(k-1)} + t_n^{(k)}}, \frac{\left| A_{0,n}^{(k-1)} - A_{0,n}^{(k)} \right|}{A_{0,n}^{(k-1)} + A_{0,n}^{(k)}} \right) < \varepsilon \tag{5.49}$$

5.1.7 Coupling Surface Flow and Infiltration

As discussed in Section 3.5, surface flow and infiltration are strongly interdependent phenomena. Such intricate and mutual processes can be modeled using a coupling approach, which includes

[1] In order to deliver the comprehensive derivation of Appendix A.5, Eq. (5.47) differs slightly from the corresponding expression in Philipp et al. (2010).

[2] Since the values of k are spread equidistantly, the iterative procedure belongs to the class of fixed-point iteration schemes. Fixed-point schemes applied to differential equations (as applies for the present case) are also referred to as Picard iteration schemes (Lindelöf, 1894).

the flow model and a loss model. Morita and Yen (2002) and Wöhling (2005) give an extensive overview of literature on coupled physically-based surface–subsurface modeling. If infiltration can be quantified with a functional relationship which is analytically determinable and differentiable, this relationship and its derivatives can be directly included in the hydrodynamic equations by means of mathematical analysis.

As previously shown, the iterative procedure (5.47);(5.48) establishes a fixed-point iteration scheme for coupling the surface flow and the infiltration model in order to obtain the wetted cross-sectional area at the inflow boundary $A_{0,n}$ and the wave tip's arrival time t_n at a specific location n, which allows for a space-discrete solution of the problem. The advantage of the fixed-point scheme is that no derivatives of the surface flow and the infiltration function are involved. According to the Banach fixed-point theorem (Banach, 1922), the method converges linearly under the given problem-specific conditions. The consecutively presented iterative solution procedure for the coupled surface flow–infiltration model for advancing wadi flow was implemented in MATLAB.

By defining N observation points along the channel, the iteration (5.47);(5.48) is carried out under an equidistant space step Δx.[1] As already discussed in Section 4.4, this leads to an adaption of the time step to wave dynamics. The spatial interval (i.e., the number of observation points N) is chosen according to a desired accuracy of the results and is typically in the range of some ten to some hundred meters. Wöhling (2005) and Wöhling et al. (2006) comprehensively investigated the numerical behavior of a comparable iterative procedure for coupled surface–subsurface flow, based on the analytical solution of the ZI equations for flow in irrigation furrows by Schmitz and Seus (1992). Both time and space discrete formulations were investigated. They showed that a space discretization of the problem—as applies for the iterative scheme presented in this thesis—leads to improved stability and convergence of the iteration procedure and is, therefore, economical with respect to computational effort.

Herein, the *alternating iterative coupling* strategy is applied, which is the method of choice if a more complex functional description of infiltration (e.g., via Richards' equation) is desired and/or surface flow and infiltration are strongly interconnected, which is, for example, the case in irrigated furrows or ephemeral channels with flow under transmission losses. Alternating iterative coupling means that the flow equations and the loss relationship are solved separately but for the same discretization step. Surface flow and losses are interlinked via infiltration as an internal boundary condition. Variables related to the momentum and volume balance are used to check for convergence with respect to a specific tolerance criterion. Figure 5.2 shows a simplified sketch of an alternating iterative coupling procedure for one observation location n. When convergence is obtained, the calculation proceeds to the next observation point, i.e., the next cross section. It is further assumed that the infiltration rate at one specific point in space and time is only dependent on the infiltration opportunity time, as also applies for the herein incorporated Kostiakov-Lewis infiltration model (cf. Section 6.1.1.1).[2] Following the concepts outlined by Wöhling et al. (2004b)

[1] Consistent with Section 5.1.8, Schmitz and Seus (1992) state: "This, however, must not be confused with the discretization of differential equations used to gain a numerical solution by replacing infinitely small differentials by finite differences. A procedure like this would include the well-known numerical effects of attenuation, as well as phase and discretization errors. Avoiding those undesirable issues was, aside from saving computer time, one of the main reasons for developing an analytical solution."

[2] It has to be emphasized that choosing the Kostiakov-Lewis model is not a concession made in order to cope with a potentially inadequate coupling approach. In fact, alternating iterative coupling allows for including any arbitrary infiltration relationship in the flow model, which is, furthermore, not constricted by the analytical solution strategy presented in this thesis. In fact, the relatively simple Kostiakov-Lewis infiltration model was selected in order to account for the specific transmission loss conditions present in ephemeral rivers, as already discussed in Section 1.3.

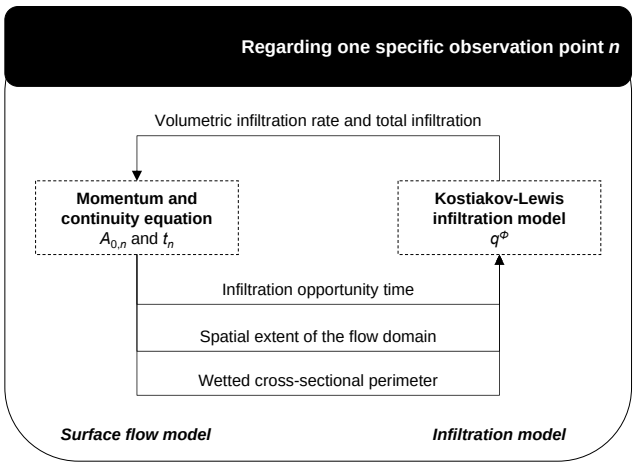

Figure 5.2: Principles of alternating iterative coupling.

Algorithm 5.1 General algorithm for the alternating iterative coupling procedure of the analytical ZI surface flow model and an infiltration model.

1: $\text{EPS} = 10^{-4}$ ▷ Define iteration precision criterion
2: **for** $n = 1 : N$ **do** ▷ Loop over space
3: $k = 1$ ▷ Set iteration counter
4: $A_{0,n}^{(k-1)}$ from Eq. (5.47) ▷ Calculate $A_{0,n}$ according to initial conditions
5: $t_n^{(k-1)}$ from Eq. (5.48) ▷ Calculate t_n according to initial conditions
6: **repeat**
7: τ from t_n ▷ Calculate infiltration opportunity time τ
8: P from Eqs. (5.42) and (5.6) ▷ Calculate wetted perimeter P acc. to $A_{0,n}$ and $P = \frac{A}{R}$
9: q^{ϕ} from Eqs. (6.1) and (6.2) ▷ Calculate q^{ϕ} according to P and τ
10: $A_{0,n}^{(k)}$ from Eq. (5.47) ▷ Calculate $A_{0,n}$ considering q^{ϕ}
11: $t_n^{(k)}$ from Eq. (5.48) ▷ Calculate t_n considering q^{ϕ}
12: ICC from Eq. (5.49) ▷ Calculate iteration convergence criterion
13: $k = k + 1$ ▷ Update iteration counter
14: **until** ICC $<$ EPS ▷ Compare ICC with EPS
15: **end for**

and Wöhling (2005), the incorporated fixed-point iteration scheme comprises four consecutive steps (Algorithm 5.1 delivers a pseudocode implementation):

Initialization: Within the first iteration (iteration count $k = 1$), the variables $A_{0,n}^{(k-1)}$ and $t_n^{(k-1)}$ are evaluated according to the initial condition and values of the inflow hydrograph $Q_0\left(t_n^{(k-1)}\right)$. For the following iteration cycles, the values of the variables are updated by employing the result of the respective preceding iteration cycle.

Infiltration calculation: The cross-sectional infiltration rate q^{ϕ} is a term in both the momentum equation (5.47) and the continuity equation (5.48), and is at the same time expressed by the incorporated infiltration model. Hence, for the current iteration count k, the cross-sectional infiltration rate $q^{\phi} = f\left(\tau(x,t)\right)$, given by the Kostiakov-Lewis model in form of Eq. (6.2), is calculated dependent on the infiltration opportunity time $\tau(x,t)$ at a predefined spatial location n, and taking into account the transiently wetted perimeter at each cross

section, which can be calculated by using Eqs. (5.42), (5.6), and the hydraulic principle $P = \frac{A}{R}$. During the advance of the infiltrating flow domain, the infiltration opportunity time at the upstream boundary equals the total simulation time, thus $\tau(x_0) = t$. In the downstream direction, the opportunity time decreases nonlinearly towards the moving wave tip, where, finally, the opportunity time equals zero. The total infiltration volume, given by the term $\int_0^{t_n^{(k-1)}} \int_0^{x_n} q^\phi(\xi,\tau)\mathrm{d}\xi\mathrm{d}\tau$ in Eq. (5.48)[1], is calculated by integrating q^ϕ over the wetted channel reach, i.e., the interval $[0, ..., x_{tip}]$. Furthermore, for being inserted into Eq. (5.47), the infiltration volume at the upper boundary $q_0^\phi\left(t_n^{(k-1)}\right)$ is calculated by employing the transiently wetted perimeter P_0 at $x = 0$.

Evaluation of $A_{0,n}^{(k)}$ and $t_n^{(k)}$: $A_{0,n}^{(k-1)}$ and $q_0^\phi\left(t_n^{(k-1)}\right)$ are inserted into Eq. (5.47) and $A_{0,n}^{(k)}$ is calculated. Consecutively, $A_{0,n}^{(k-1)}$ and the results of the integration $\int_0^{t_n^{(k-1)}} \int_0^{x_n} q^\phi(\xi,\tau)\mathrm{d}\xi\mathrm{d}\tau$ are inserted into Eq. (5.48) in order to calculate $t_n^{(k)}$. As commonly indicated for the iterative solution of nonlinear equations, a relaxation is included in order to prevent an overshooting of the solution or an alternating of subsequent solutions for consecutive observation points n.[2]

Check for convergence: The first three steps of the procedure yield the values of $A_{0,n}^{(k)}$, $A_{0,n}^{(k-1)}$, $t_n^{(k)}$, and $t_n^{(k-1)}$. Steps two and three are executed until the iteration convergence criterion (5.49) is not yet fulfilled. After convergence is reached, the scheme turns to the next observation point, i.e., $n + 1$.

After the convergence of the iteration procedure (5.47);(5.48) is achieved, the wetted cross-sectional area $A(x, t_n)$ can be straightforwardly computed from Eq. (5.42). To compute the discharge $Q(x, t)$, Eq. (5.42) is inserted into Eq. (5.30). This step again includes some numerical integration as well as again requires a functional relationship for quantifying the infiltration rate $q^\phi(\xi,\tau)$, i.e., established by the Kostiakov-Lewis model with regard to this work.

5.1.8 Additional Remarks

The boundary conditions given by Eqs. (5.13) to (5.16) are located at the moving interface between the flow domain and the dry channel. To preserve the concept of a moving lower boundary condition, the *virtual-wave concept* of Schmitz and Seus (1992) is applied. This means that the modeling domain is continuously extended in the downstream direction when the advancing wave tip reaches the end of the considered channel reach. This concept is presented in more detail in Section 5.2.4, which addresses the derivation of an analytical ZI model for overland flow processes.

Another remark has to be given concerning the label "analytical model" for the presented methodology of solving the governing equations. On the one hand, the described calculus yields the equations (5.37) and (5.46), which deliver an exact analytical description of the zero-inertia flow problem, without holding any partial derivatives. On the other hand, the solution of the working equations (5.47) and (5.48) requires some standard numerical techniques.

[1] Which is equivalent to Eq. (6.3) for $t_n = t$ and $x_{tip} = x$.

[2] In this context, relaxation means to weigh a current approximate solution, e.g., $A_{0,n}^{(k)}$ or $t_n^{(k)}$, to results from the preceding observation point where the iteration scheme already converged, e.g., $A_{0,n-1}$ and t_{n-1}, in such a way that

$$\begin{aligned} A_{0,n}^{(k)} &= r_A A_{0,n}^{(k)} - (1 - r_A) A_{0,n-1} \\ t_n^{(k)} &= r_t t_n^{(k)} \quad - (1 - r_t) t_{n-1} \end{aligned}$$

where $r_{A,t}$: relaxation parameter for $A_{0,n}$ or t_n, respectively. For practical application, $r_{A,t}$ can be set to 0.8.

It should be emphasized that those techniques are not applied to the governing PDEs (5.1);(5.2) of the flow problem—as would be the case for a numerical solution of the ZI equations—and, therefore, pose no approximation of the process description. Nevertheless, the derived solution procedure (5.47);(5.48) incorporates an iteration strategy and further requires some numerical integration regarding Eqs. (5.30), (5.42), (5.47), and (5.48). To be precise, the proposed solution strategy could be labeled a "semi-analytical solution". Herein, the terms "semi-analytical" and "analytical" are used synonymously, without questioning the aforementioned issues.

Besides motivating a space discretization for the solution procedure of an analytical ZI model very similar to the one presented in this thesis, Wöhling (2005) and Wöhling et al. (2006) further showed that employing a highly nonlinear functional relationship for the quantification of infiltration (e.g., Richards' equation) may cause poor convergence behavior of a linearly converging fixed-point iteration scheme (e.g., the afore-presented one). Therefore, the authors propose the application of a second-order convergent scheme, e.g., the nonlinear Newton-Raphson scheme (Ypma, 1995), which, however, requires the derivatives of the governing equations and leads to a more complex mathematical model. Nevertheless, the space-discrete fixed-point procedure (5.47);(5.48) with the Kostiakov-Lewis model for quantifying wadi channel infiltration performed well and exhibited a good convergence behavior, leading to accurate model results, which is proven in Chapter 6.

5.2 A Novel Analytical Solution Approach for Zero-Inertia Overland Flow under Time-Varying Rainfall Conditions

Subsequently, an analytical solution of the extended zero-inertia equations is derived for the purpose of overland flow modeling. Overland flow is a special case of open channel flow in a very wide channel. Consequently, the proposed analytical zero-inertia model is based on the sheet flow analogon of surface flow. This means, flow occurs in a very wide rectangular cross section with a uniform water depth perpendicular to the flow direction. This implies that the width of the cross section is much greater than the water depth h, such that the hydraulic radius R equals h.

It is intended to set up the analytical ZI overland model for flow over initially dry portions of a surface. Furthermore, the model should account for changes of the flow attributable to water originating from rainfall and/or infiltration excess, as well as water supervening from upper parts of the considered surface element. Model development and the proposed solution strategy can be carried out analogously to the nonprismatic open-channel case (cf. Section 5.1). Therefore, the subsequent calculus is not presented in depth, but in a brief and concise manner.

5.2.1 Governing Equations

The ZI equations are derived by neglecting the advective and local inertia terms $\frac{1}{g}\frac{\partial u}{\partial t}$ and $\frac{u}{g}\frac{\partial u}{\partial x}$ of the full hydrodynamic momentum equation (3.2). Additionally, for surface runoff influenced by rainfall—considering the momentum contribution of the falling rain as insignificant to the flow—the $\frac{qu}{gA}$ term of the momentum equation (3.8) can be neglected. Applying a uniform friction law to express the friction slope S_f leads to the ZI equations for overland flow for a unit width, where the wetted area A equals h:

$$\frac{\partial h}{\partial t} + \frac{\partial Q}{\partial x} = -q \tag{5.50}$$

$$\frac{\partial h}{\partial x} = S_0 - \frac{u^2}{K^2 h^{2\beta}} \tag{5.51}$$

where t: time [T]; x: longitudinal space coordinate [L]; $h(x,t)$: water depth [L]; $Q(x,t)$: discharge per unit width [$\mathrm{L^2T^{-1}}$]; $q(x,t)$: rate of positive/negative mass contribution attributable to rainfall or infiltration per unit surface area [$\mathrm{LT^{-1}}$]; S_0: bottom slope [−]; $u(x,t)$: flow velocity [$\mathrm{LT^{-1}}$]; K: roughness coefficient [$\mathrm{L^{1-\beta}T^{-1}}$]; β: exponent of the flow formula [−] (e.g., Chézy: $\beta = \frac{1}{2}$; Manning-Strickler: $\beta = \frac{2}{3}$). For further model development, β is set to $\frac{1}{2}$, i.e., the Chézy law (Chézy, 1776) is used for the quantification of friction losses, in which the Chézy roughness coefficient is labeled K_C.

The q term in the continuity equation (5.50) is signed negative if there is a volumetric loss of water (i.e., attributable to infiltration) or, vice versa, signed positive for a volumetric gain of water, e.g., from rainfall. Practically, the value of q can be calculated by relating the volumetric rate of rainfall q_rain [$\mathrm{LT^{-1}}$] and the infiltration rate q_inf [$\mathrm{LT^{-1}}$]:

$$q = (q_\mathrm{rain} - q_\mathrm{inf}) \begin{cases} < 0 & \text{for } q_\mathrm{inf} > q_\mathrm{rain} \\ = 0 & \text{for } q_\mathrm{inf} = q_\mathrm{rain} \\ > 0 & \text{for } q_\mathrm{inf} < q_\mathrm{rain} \end{cases} \tag{5.52}$$

where any arbitrary functional relationship can be used for the quantification of infiltration within the proposed analytical model.

Analogously to the calculus applied in Section 5.1, the first step for solving the system Eqs. (5.50);(5.51) is to multiply Eq. (5.51) by h, yielding

$$h\frac{\partial h}{\partial x} = S_0 h - \frac{u^2}{K_\mathrm{C}^2} \tag{5.53}$$

Again, the inflow boundary is considered as a momentum-representative cross section and Eq. (5.53) can be expressed as

$$h\frac{\partial h}{\partial x} = S_0 h_0 - \frac{u_0^2}{K_\mathrm{C}^2} \tag{5.54}$$

with $h_0 = h_0(t) = h(x = 0, t)$ and $u_0 = u_0(t) = u(x = 0, t)$. Schmitz and Seus (1987), Schmitz and Seus (1990) and Schmitz and Seus (1992) showed that another possible location of the momentum-representative cross section is the position of the center of gravity of the moving water body. This approach leads to a physically and mathematically equivalent solution. Herein, the momentum-representative cross section is placed at $x = 0$ because the subsequent calculus is more brief and this location introduces a well-defined coupling location when single-slope models should be cascaded.

5.2.2 Boundary and Initial Conditions

The solution of the system of partial differential Eqs. (5.50);(5.54) requires the specification of boundary and initial conditions. At the fixed upstream boundary ($x = 0$), the boundary condition is

$$Q(0,t) = Q_0(t) \tag{5.55}$$

with the restriction that strongly falling discharge hydrographs cannot be used as an upstream boundary condition because of the ZI assumptions (Schmitz et al., 2002). As a consequence,

the proposed analytical overland flow model covers the rising limb and the plateau part of the hydrograph (i.e., flow advance). At the moving downstream boundary ($x = x_{\mathrm{tip}}(t)$) the following conditions have to be satisfied:

$$h(x_{\mathrm{tip}}, t) = 0 \tag{5.56}$$

$$u(x_{\mathrm{tip}}, t) = u_{\mathrm{tip}}(t) = \frac{\mathrm{d}x_{\mathrm{tip}}}{\mathrm{d}t} \tag{5.57}$$

where $x_{\mathrm{tip}}(t)$ and $u_{\mathrm{tip}}(t)$ denote the location and velocity of the wave front, respectively. The initial condition of the flow problem over an initially dry surface is

$$x_{\mathrm{tip}}(t = 0) = 0 \tag{5.58}$$

5.2.3 Analytical Solution

Schmitz and Seus (1992) have derived the solution of the momentum equation (5.54) for a variety of regular cross-sectional geometries. In the present wide-channel (rectangular) case, their solution reads

$$h(x, t) = \sqrt{2\left(\frac{u_0^2}{K_{\mathrm{C}}^2} - S_0 h_0\right) \cdot (x_{\mathrm{tip}}(t) - x)} \tag{5.59}$$

Next, the continuity equation (5.50) is solved for Q. Considering the upstream boundary condition given by Eq. (5.55), a direct integration of the continuity equation yields an expression for a unit width and a rectangular channel ($A = h$), similar to Eq. (5.30):

$$Q(x, t) = Q_0(t) - \int_0^x \left(\frac{\partial h}{\partial t}(\xi, t) + q(\xi, t)\right) \mathrm{d}\xi \tag{5.60}$$

where the integrand can be obtained by differentiating Eq. (5.59) with respect to t, and ξ indicates the integration variable in spatial dimension. Eqs. (5.59) and (5.60) solve the system (5.50);(5.54) and satisfy the boundary conditions, given by Eqs. (5.55), (5.56), and (5.57).

5.2.4 Algorithm for the Iterative Solution of the Nonlinear Problem

Analogously to the open-channel case (cf. Section 5.1), the solution procedure for Eqs. (5.59) and (5.60) first requires evaluating the position of the advancing wave front $x_{\mathrm{tip}}(t)$ and the water depth $h_0(t) = h(x = 0, t)$ at the inflow boundary—which is not zero in case water emerges from upper catchment parts and not only laterally from rainfall—by solving a system of two nonlinear equations iteratively. For this purpose, N observation locations ($0 < x_1 < x_2 < ... < x_N$) are defined and the arrival time of the wave tip for each observation point t_n, i.e., $x_{\mathrm{tip}}(t_n) = x_n$ for ($n = 1, 2, ..., N$), and the corresponding water depth $h_{0,n} = h_0(t_n)$ at $x = 0$ is calculated.

The first aforementioned nonlinear equation is obtained by setting $x = 0$ in Eq. (5.59):

$$h_{0,n} = \sqrt{2x_n\left(\frac{(Q_0(t_n))^2}{K_{\mathrm{C}}^2 h_{0,n}^2} - S_0 h_{0,n}\right)} \tag{5.61}$$

Following the calculus in Sections 5.1.5 and 5.1.6, the second nonlinear equation is derived from the volume balance equation (5.60):

$$\int_0^{t_n} Q_0(\tau)\mathrm{d}\tau = \frac{2}{3}h_{0,n}x_n + \int_0^{t_n}\int_0^{x_n} q(\xi,\tau)\mathrm{d}\xi\mathrm{d}\tau \tag{5.62}$$

where ξ indicates the integration variable in space and τ the is infiltration opportunity time at a location x, or the integration variable in time, respectively.

Rearranging Eqs. (5.61) and (5.62) leads to the space-discrete iteration procedure

$$h_{0,n}^{(k)} = \left(\frac{2x_n \left(\frac{Q_0(t_n^{(k-1)})}{K_C} \right)^2}{1 + \frac{2x_n S_0}{h_{0,n}^{(k-1)}}} \right)^{\frac{1}{4}} \tag{5.63}$$

$$t_n^{(k)} = t_n^{(k-1)} + \frac{\frac{2}{3}h_{0,n}^{(k)}x_n + \int_0^{t_n^{(k-1)}}\int_0^{x_n} q(\xi,\tau)\mathrm{d}\xi\mathrm{d}\tau - \int_0^{t_n^{(k-1)}} Q_0(\tau)\mathrm{d}\tau}{Q_0\left(t_n^{(k-1)}\right)} \tag{5.64}$$

where $k = 1, 2, 3, ...$ denotes the iteration index. A Taylor series expansion of the left-hand side of Eq. (5.62) around $t_n^{(k-1)}$ has been included to take into account the impact of lateral inflow/outflow from rainfall and/or infiltration, respectively. Starting values are provided by the results obtained from the preceding space step, i.e., $h_{0,n}^{(0)} = h_{0,n-1}$ and $t_n^{(0)} = t_{n-1}$, and the fixed-point scheme (5.63);(5.64) can be treated according to Section 5.1.7, employing alternating iterative coupling to take account for gains/losses of water.

After the iteration (5.63);(5.64) has converged, the water depth $h(x, t_n)$ can be straightforwardly computed from

$$h(x,t_n) = h_{0,n}\sqrt{1 - \frac{x}{x_n}} \tag{5.65}$$

by making use of Eq. (5.59). Eq. (5.65) is inserted into Eq. (5.60) to compute the discharge per unit width, $Q(x,t)$. If there is—in addition to or instead of an a priori known lateral inflow—significant infiltration, this step requires either some standard formula, e.g., Kostiakov-Lewis, or some problem-specific functional relationship to quantify the infiltration rate $q(\xi,\tau)$.

For the iterative solution procedure for the open-channel ZI model (cf. Section 5.1.6), terms of the involved volume balance equation (5.30) and of Eq. (5.42) had to be integrated numerically. For the overland case, the volume of moving water atop an overland plane, expressed by the first integrand in the volume balance equation (5.60), can be calculated by analytical means. Moreover, Eq. (5.65) contains no integrals at all. Some details on the evaluation of the first integrand of Eq. (5.60) are given in Appendix A.6.

Since the formulation of the proposed analytical model assumes a free and moving lower boundary, the concept of the so-called "virtual wave" is used as proposed by Schmitz (1989), Schmitz and Seus (1990), and Schmitz and Seus (1992). This concept virtually extends the computational domain in case the moving wave tip reaches the lower boundary of the model domain, which is immediately the case assuming a homogeneous lateral rainfall input onto the test plane. Thus, the water body atop the test plane is filled up by the lateral rainfall input, forming a traveling virtual wave tip beyond the real extensions of the test plane. This traveling virtual wave tip represents the transient location of the lower boundary conditions (5.56) and (5.57). This way, the virtual wave provides

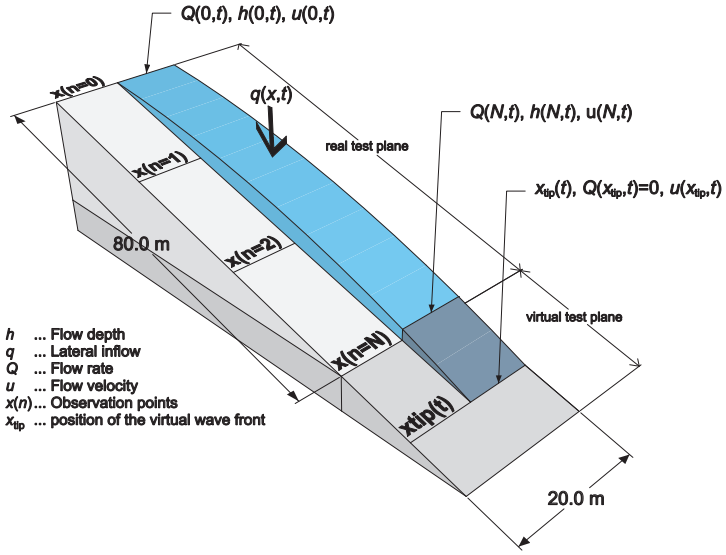

Figure 5.3: Schematic sketch of a synthetic overland flow plane under lateral inflow (rainfall) and an illustration of the virtual wave concept.

flow rate, water depth, and flow velocity along the test plane. Fig. 5.3 gives an illustration of the virtual wave concept.

5.3 Summary

The presented analytical solution approaches deliver analytical and straightforwardly applicable routing models for open channel flow in permeable nonprismatic channels and for overland flow. Due to their mathematical structure and the incorporated iterative solution procedure, the obtained models are not constricted by numerical imponderables, which are often associated with the numerical solution of the governing flow equations under the problem-specific conditions regarded herein, e.g., initially dry channel beds and significant infiltration losses (cf. Section 4.4), or overland flow on rough and steep surfaces (cf. Section 2.2).

Therefore, the developed analytical nonprismatic channel flow model seems to be ideal for simulating advancing surge flow phenomena downstream of groundwater recharge dams, notwithstanding the discontinuity when attaining the state of a "standing" wave and—looking at the straightforward applicability—evaluating reservoir release strategies and culvert design for specific groundwater recharge problems. The derived analytical overland flow model can represent a valuable element in a boundary condition coupled, cell-wise surface-runoff modeling environment since it is (a) accurate; (b) fast in terms of low computational demand; and (c) robust for a wide range of process dynamics.

Besides the expectable accuracy of both models' results, the proposed space-discrete iterative solution procedure promises a computationally efficient model application. Model accuracy as well as computational efficiency is proven in the subsequent chapter with a comparative analysis of the analytical models with generally accepted numerical solutions. In summary, the two derived analytical flow models are:

- ▷ robust and accurate;
- ▷ computationally efficient; and
- ▷ can be coupled with any arbitrary functional relationship for the quantification of losses or gains within the presented iterative solution scheme.

The iterative solution procedures (5.47);(5.48) and (5.63);(5.64), respectively, are based on evaluating the advance time of the moving lower boundary of the flow domain, traveling in the downstream direction. The derived models, therefore, do not cover a zero-advance condition because an advance velocity converging to zero leads to a nonconvergence of the employed iteration schemes. However, as subsequently shown in Section 6.1.4, the approach is able to cover quasi-standing wave effects connected to very low advance velocities, which is, for example, a prerequisite for estimating culvert release strategies in order to optimally utilize a specific downstream reach length with good infiltration characteristics for groundwater recharge. If a portrayal of flow recession (cf. Section 3.1) is desired, other modeling approaches are needed. One aim of this thesis is to develop an event-based integrated modeling system for wadi flow under dam control. Hence, for the proposed full modeling system, flow recession is taken into account with a state-of-the art numerical KW hydrodynamic model, which is coupled to the analytical ZI model as outlined in Section 7.1.1.2.

Chapter 6

Comparative Studies with the Novel Analytical Zero-Inertia Models and Generally Accepted Approaches

The preceding Chapter 5 delivered two analytical solution procedures for the zero-inertia model for open channel flow and for overland flow. In this chapter, results of both models are compared to results obtained by generally accepted numerical approaches in order to evaluate the performance of the analytical models. Model intercomparison is carried out with respect to mass balance conservation and the portrayal of process dynamics.

First, the analytical open channel flow model is applied for simulating the advance of an infiltrating wave in prismatic and nonprismatic channels. For comparison, simulations are carried out with an implicit finite difference solution of the full hydrodynamic model. Additionally, a first parameter sensitivity study is performed, which is supplemented by a more comprehensive analysis of parameter sensitivity in Section 7.2.2. Furthermore, the analytical model's suitability for the simulation of virtually standing wave processes is evaluated.

Consecutively, the derived analytical overland flow model is applied to simulate sheet flow from excess rainfall on an inclined synthetic plane of variable roughness. Numerical results obtained by the full hydrodynamic model and its zero-inertia and kinematic wave simplifications are used for intercomparison. Again, mass conservation and a preferably accurate match of process dynamics are the criteria for model performance assessment.

6.1 Open Channel Flow in Prismatic and Nonprismatic Permeable Open Channels

In this section, results of the analytical zero-inertia open channel flow model (cf. Section 5.1) and the ones obtained from a full hydrodynamic model are compared. The investigation focuses on permeable prismatic and nonprismatic synthetic test channels, thus, providing a first step towards

the application of the suggested analytical model for surge flow phenomena over permeable wadi beds. HEC-RAS (Brunner, 2008) is used as a reference for the full hydrodynamic process description. The numerical model employs the Preissmann scheme[1] (Preissmann, 1961; Cunge et al., 1980; Chau, 1990) for the solution of the governing equations. Modeling results are compared regarding predicted arrival times of the flow at specific channel locations. Additionally, the sensitivity of the cross-sectional parametrization (i.e., $p_1, ..., p_4$, S_0, K_{St}) used with the analytical ZI model is evaluated. Finally, the computational stability of the analytical ZI model is tested.

6.1.1 Test Setup

First, test examples incorporating prismatic and nonprismatic channel geometries are evaluated using the ZI model. In a second step, the flow is computed for the same input data using the full hydrodynamic numerical model. Therefore, the infiltration hydrograph is taken from the ZI calculations and considered as negative lateral inflow for the HEC-RAS model. Wadi transmission losses are quantified with the Kostiakov-Lewis infiltration model. Details of the test setup are subsequently presented.

6.1.1.1 Kostiakov-Lewis Infiltration Model

Generally, any arbitrary relationship can be used for the quantification of transmission losses within the proposed model setup. Specific for infiltration on alluvial material in semiarid and arid areas, only a portion of infiltration is a consequence of matrix flow; rather, macropore flow also impacts alluvial infiltration (Beven and Germann, 1982; Wood et al., 1997). Since the data situation omits the application of typical deterministic macropore and/or matrix flow models, an empirical model approach is assumed to be appropriate for transmission loss modeling in case infiltrometry data are available. The empirical Kostiakov-Lewis model (Kostiakov, 1932; Lewis, 1937) is, therefore, used for the quantification of infiltration losses.[2] This way, q^{ϕ} in Eqs. (3.7) and (3.8), as well as Eqs. (3.7) and (5.2), respectively, can be calculated by

$$q(x,t) = k_{\mathrm{a}} k_{\mathrm{k}} \tau^{(k_{\mathrm{a}}-1)} + k_{\mathrm{c}} \tag{6.1}$$

where $q(x,t)$: actual infiltration rate[3] at a defined channel location x per unit surface area [LT^{-1}]; τ: infiltration opportunity time at x [T]; k_{a}: empirical Kostiakov-Lewis coefficient [$-$]; k_{k}: empirical Kostiakov-Lewis coefficient [$\mathrm{LT}^{-k_{\mathrm{a}}}$]; and k_{c}: steady or final infiltration rate [LT^{-1}].

Assuming infiltration is occurring at the wetted perimeter $P(x,t)$, the volumetric infiltration rate per unit length $q^{\phi}(x,t)$ is given by

$$q^{\phi}(x,t) = q(x,t) P(x,t) \tag{6.2}$$

[1] Which is an implicit four-point finite difference scheme. Thus, the scheme theoretically allows information from the entire reach to influence the solution at a specific point in the solution domain. Details on the Preissmann scheme can be found in Appendix A.3.

[2] Strictly speaking, using the nomenclature of, e.g., Haverkamp et al. (1988), Furman et al. (2006), and Zolfaghari et al. (2012), the incorporated model is a *modified* Kostiakov-Lewis model. To keep brevity, the term "Kostiakov-Lewis model" is herein exclusively used for the modified Kostiakov-Lewis model.

[3] Kostiakov-Lewis models (cf. Section 1.3) are mostly given in a form which yields the cumulative infiltration over time. For this thesis, a temporal derivative of such a form is employed in order to yield infiltration rates. Furthermore, the herein employed Kostiakov-Lewis parameters are given per unit surface area as, e.g., applied by Furman et al. (2006).

and the quantity of total infiltrated water along the distance $[x_{n=1}, ..., x_{n=i}]$ can then be calculated by

$$I(t) = \int_0^t \int_{x_{n=1}}^{x_{n=i}} q^{\phi} \mathrm{d}x\mathrm{d}t \tag{6.3}$$

where $I(t)$ is the total cumulative infiltration [L^3] (cf. the second term on the right-hand side of Eq. (5.31)).

As discussed in Section 1.3, wadi infiltration is strongly—but not solely—driven by gravitational force. Nevertheless, some authors, e.g., Haimerl (2004) have experimentally proven that wadi infiltration occurs not only vertically, but also with a lateral component. Besides the fact that for the comparably wide wadi channels regarded in this study the wetted perimeter and the flow width do not differ much, one has to decide if cross-sectional infiltration q^{ϕ} should be assumed to occur orthogonal to the wetted perimeter—as usually practiced in furrow irrigation modeling—or only along a vertical projection of the flow width. Supported by the results of Haimerl (2004), this study assumes the former, which is reflected in Eq. (6.2). A more realistic image of infiltration could allegedly be drawn by employing the two-dimensional Richards' equation which delivers the flux and the fluxlines (i.e., the direction of the infiltrating flow) at every point of the wetted perimeter (Wöhling, 2005). Nevertheless, the application of matrix-flow models may be precluded under the specific conditions of wadi infiltration.

For the subsequent comparative calculations, the Kostiakov-Lewis model parameters were adopted from Haimerl and Zunic (2002) who carried out basin infiltrometry tests for Wadi Ahin (Fig. 6.1) where a noticeable decline of infiltration rates over time was observed. A nonlinear regression model was used for parameter fitting. Parameters were estimated to $k_{\mathrm{a}} = 0.864$, $k_{\mathrm{k}} = 7.7433 \cdot 10^{-5}\,\mathrm{m \cdot s^{-}}^{k_{\mathrm{a}}}$, and $k_{\mathrm{c}} = 1.8033 \cdot 10^{-5}\,\mathrm{m \cdot s^{-1}}$, where the coefficient of determination was 0.9997, which shows a nearly perfect portrayal of observed infiltrometry data by the Kostiakov-Lewis model.

6.1.1.2 Channel Geometry, Model Parameters, Boundary and Initial Conditions

Prismatic Test Channel: The investigated prismatic test channel with a length of 2,000 m features uniform parabolic cross sections. Thus, cross-sectional parameters $p_1(x)$ and $p_3(x)$ do not vary along the channel. The incorporated values of $p_1(x)$ and $p_2(x)$ are averaged for available geometry data of Wadi Ahin.[1] According to Schmitz et al. (2002), the parameters p_2 and p_4 are set to $\frac{2}{3}$ for a parabolic cross-sectional geometry. The spatial discretization of both the analytical ZI and the numerical HD model is set to $\Delta x = 100\,\mathrm{m}$. The temporal discretization for the HD model is $\Delta t = 5\,\mathrm{s}$ and is adaptive for the ZI model due to its specific solution strategy (cf. Section 5.1.6).

As discussed in Section 4.4, numerical flow modeling for initially dry channels can lead to numerical inconveniences (ranging from considerable mass balance errors to convergence problems) due to the steep gradients of the dependent process variables at the moving wave front (Schmitz, 1989; Garcia-Navarro et al., 1999). For this reason, the numerical HEC-RAS model is charged with an initial flow of $0.15\,\mathrm{m^3 \cdot s^{-1}}$. The ZI model is operated with a dry-channel initial condition. Table 6.1 shows the employed geometric data for the prismatic test channel, and Table 6.2 contains the upper boundary condition.

[1] See the subsequent paragraph for the applied methodology for the estimation of $p_1, ..., p_4$.

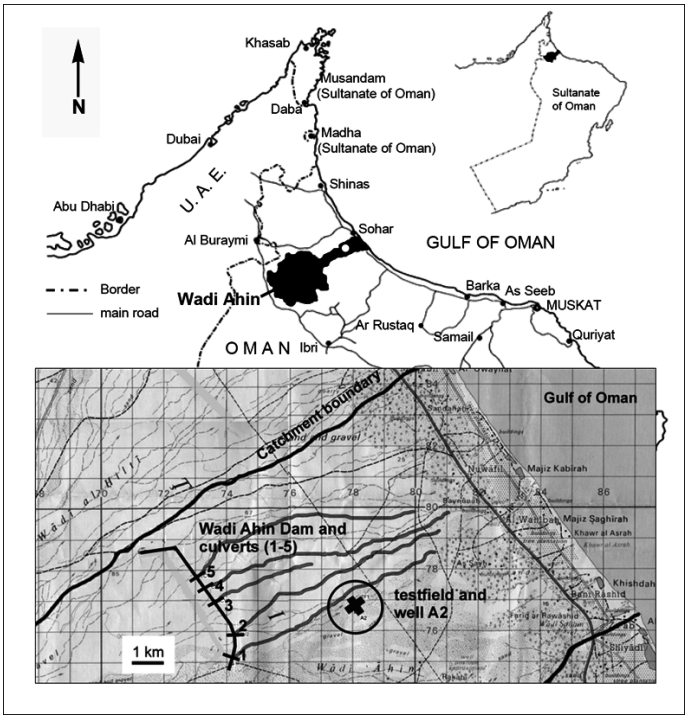

Figure 6.1: Overview map of Wadi Ahin and Wadi Ahin Dam site (according to Haimerl and Zunic, 2002 and Haimerl, 2004).

Table 6.1: Geometric data for the prismatic (parabolic) test channel.

Parameter	Value
Strickler roughness coefficient K_{St} ($\mathrm{m}^{\frac{1}{3}} \cdot \mathrm{s}^{-1}$)	33.33
Channel slope S_0	0.002
Cross-sectional parameter $p_1(x)$ (m^{1-2p_2})	0.2823
Cross-sectional parameter p_2	$\frac{2}{3}$
Cross-sectional parameter $p_3(x)$ (m^{1-2p_4})	0.1870
Cross-sectional parameter p_4	$\frac{2}{3}$
Channel length (m)	2,000
Profile type	parabolic
Spatial discretization Δx (m)	100

Table 6.2: Upper boundary condition for the prismatic (parabolic) test case.

Time t (s)	Inflow Q_0 ($\mathrm{m}^3 \cdot \mathrm{s}^{-1}$)
0	0.0
300	0.5
600	1.0
900	1.5
1,800	2.5
2,700	4.5
3,600	4.5

Table 6.3: Geometric data for the nonprismatic test channel.

Parameter	Value
Strickler roughness coefficient K_{St} ($\mathrm{m}^{\frac{1}{3}} \cdot \mathrm{s}^{-1}$)	33.33
Channel slope S_0	0.002
Cross-sectional parameter $p_1(x)$ (m^{1-2p_2})	variable
Cross-sectional parameter p_2	0.5795
Cross-sectional parameter $p_3(x)$ (m^{1-2p_4})	variable
Cross-sectional parameter p_4	0.5468
Channel length (m)	2,000
Profile type	nonprismatic
Spatial discretization Δx (m)	200

Nonprismatic Test Channel: A synthetic nonprismatic test channel with a length of 2,000 m is constructed using selected cross sections of Wadi Ahin (Haller, 2000; Haimerl and Zunic, 2002; Haimerl, 2004) which are placed every 200 m along the channel (Fig. 6.2). According to Section 5.1.2, the nonprismatic cross-sectional channel geometry can be portrayed by the geometry parameters $p_1(x)$, p_2, $p_3(x)$, p_4. For instance, these parameters can be simultaneously estimated by minimizing the residual mean squares, defined by

$$\mathrm{RMS}(\tilde{h}) = \int_0^{\tilde{A}(x)} \left(\tilde{h}(x,A) - p_1(x)A^{p_2}\right)^2 \mathrm{d}A \tag{6.4}$$

and

$$\mathrm{RMS}(\tilde{R}) = \int_0^{\tilde{A}(x)} \left(\tilde{R}(x,A) - p_3(x)A^{p_4}\right)^2 \mathrm{d}A \tag{6.5}$$

for each cross section. This can be achieved by applying an appropriate optimization strategy. For this work, a MATLAB implementation based on the Nelder-Mead simplex method[1] (Nelder and Mead, 1965) is used. Typically for natural wadi cross sections, the residuals for $\tilde{h}$ and $\tilde{R}$ are small (i.e., less than one decimeter), which underlines that the natural channel topography can be closely approximated by adjusting the geometry parameters $p_1, ..., p_4$ in Eqs. (6.4) and (6.5). This coincides with the findings of Schmitz et al. (2002), who applied a similar methodology to fit the geometry parameters to a natural irregular channel in Bavaria.

In Eqs. (6.4) and (6.5), the functions $\tilde{h}(x,A)$ and $\tilde{R}(x,A)$ denote the dependencies of both water depth and the hydraulic radius on the wetted cross-sectional area. The upper limit of the integration, $\tilde{A}(x)$, is selected for each cross section according to an appropriate reference water depth h_{r}. A pronounced variation of the geometry parameters $p_1(x)$ and $p_3(x)$ reflects pronounced morphological changes along the considered reaches of the channel. The maxima of $p_1(x)$ are commonly associated with narrow cross sections (cf. Figs. 6.2 and 6.3 at $x = 0\,\mathrm{m}$, 800 m, and 1,400 m), while the minima indicate more gentle lateral slopes of the cross sections (e.g., at 2,000 m). Applying Eqs. (6.4) and (6.5) for the incorporated cross-sectional data delivers the values of the constant geometry parameters p_2 and p_4 to $p_2 = 0.5795$ and $p_4 = 0.5468$. Table 6.3 summarizes the processed geometric data of the nonprismatic test channel. The temporal discretization for the HD model is again set to $\Delta t = 5\,\mathrm{s}$ and is adaptive for the ZI model. An initial flow rate of $0.15\,\mathrm{m}^3 \cdot \mathrm{s}^{-1}$ is applied for the numerical model. The spatial discretization of the HD and the ZI

[1] In MATLAB, this implementation is represented by the function fminsearch.

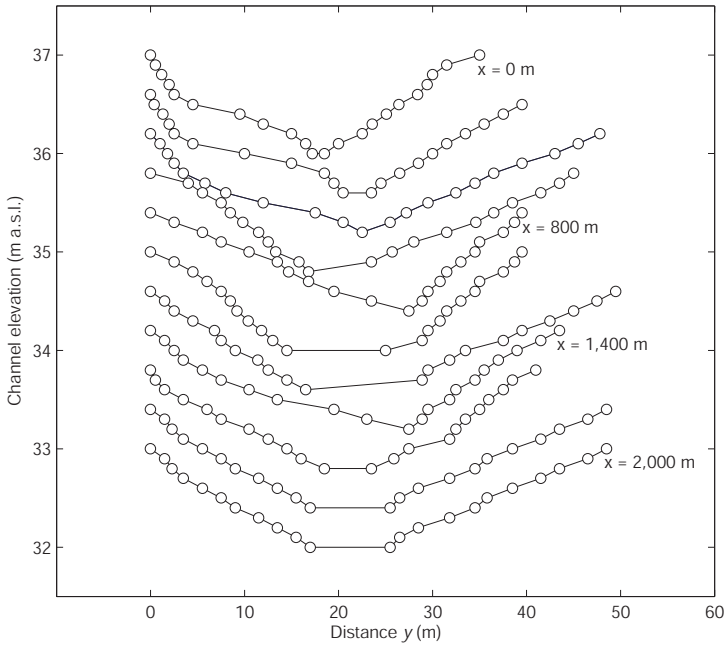

Figure 6.2: Cross-sectional profiles of the nonprismatic test channel.

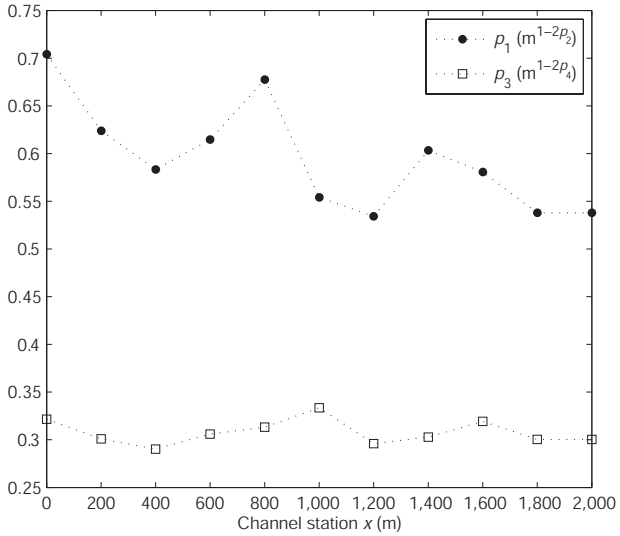

Figure 6.3: Development of the varying geometry parameters $p_1(x)$ and $p_3(x)$ along the nonprismatic test channel.

Table 6.4: Upper boundary condition for the nonprismatic test case.

Time t (s)	Inflow Q_0 ($m^3 \cdot s^{-1}$)
0	0.0
180	0.5
360	0.75
540	1.5
1,980	1.5

model is set to $\Delta x = 200\,\text{m}$. Table 6.4 shows the upper boundary condition applied to the two investigated models.

6.1.2 Comparison of Flow Dynamics

Model results for the prismatic test case are shown in Fig. 6.4. Modeled arrival times of the full hydrodynamic and the analytical zero-inertia model show a nearly perfect agreement. Compared to the HD results, ZI arrival times are underestimated by an average of 0.08 %. The continuously rising graph of the advance trajectory shows slight deviations from a straight line. This originates from two effects. Infiltration decelerates the advance of the wave tip, and—in contrast—the increasing inflow accelerates the advance. This recurs a couple of times during the simulation, namely, when the inflow rises according to Table 6.2. The results suggest that the analytical ZI model is well suited for predicting surge flow phenomena under significant infiltration in permeable prismatic channels.

Figure 6.5 depicts modeling results for the nonprismatic case. The results again reveal a slight underestimation of the wave tip arrival time by the ZI model, except for location $x = 400\,\text{m}$ with an overestimation of about 18 s. In addition to the prismatic case, wave arrival times are influenced not solely by inflow and infiltration; the changing channel geometry impacts the wave advance as well. Therefore, the convergence of the model results also evidently validates the representation of nonprismatic cross-sectional geometries by the proposed profile functions.

6.1.3 Analysis of the Geometry Parameter Sensitivity for the Nonprismatic Test Channel

A first sensitivity analysis is performed for the nonprismatic test channel in order to investigate the sensitivity of the geometry parameters $p_1(x)$, p_2, $p_3(x)$, p_4, channel slope, and channel roughness with respect to relative wave arrival times. A further and more comprehensive sensitivity analysis addressing the model's infiltration parameters can be found in Section 7.2.2 which outlines the implementation of the analytical ZI model within an integrated modeling framework for ephemeral channel routing under dam control. The initial model parametrization and the boundary conditions are adopted from the preceding nonprismatic model test. Each basal parameter (Table 6.5) is altered ±30 %, where one parameter is changed at one time and the remaining other process and input parameters are kept constant. Consecutively, the arrival times of the various model runs are compared.

The results of the sensitivity analysis are depicted in Fig. 6.6. Figure 6.6a–f shows the sensitivity of wave front propagation along the nonprismatic channel for the different altered parameters.

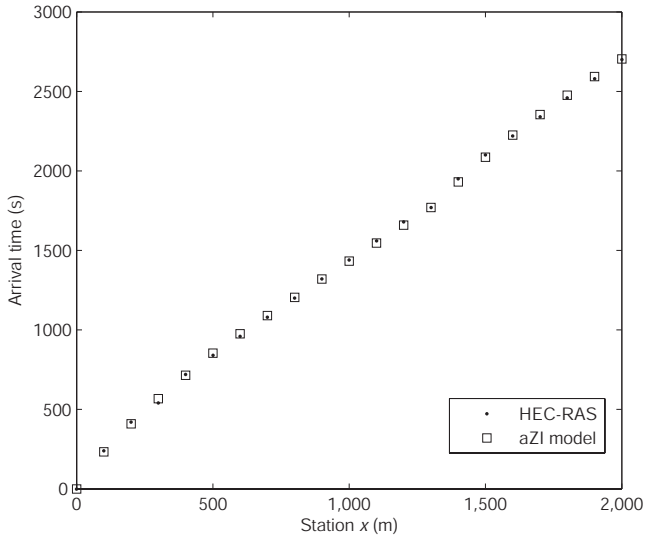

Figure 6.4: Wave front propagation in a prismatic (parabolic) test channel for the analytical ZI model and a full hydrodynamic model (HEC-RAS).

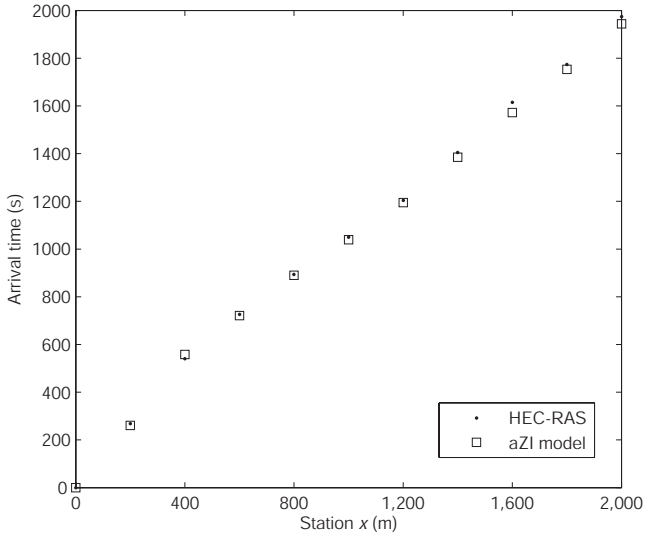

Figure 6.5: Wave front propagation in a nonprismatic test channel for the analytical ZI model and a full hydrodynamic model (HEC-RAS).

Table 6.5: Reference input data used for the sensitivity analysis.

Location x (m)	$p_1(x)$ (m^{1-2p_2})	p_2	$p_3(x)$ (m^{1-2p_4})	p_4	S_0	K_{St} ($m^{\frac{1}{3}} \cdot s^{-1}$)
0	0.7040		0.3215			
200	0.6240		0.3009			
400	0.5833		0.2902			
600	0.6147	⋮	0.3059	⋮	⋮	⋮
800	0.6775		0.3133			
1,000	0.5543	0.5795	0.3335	0.5468	0.002	33.33
1,200	0.5342	⋮	0.2959	⋮	⋮	⋮
1,400	0.6033		0.3028			
1,600	0.5808		0.3193			
1,800	0.5379		0.3004			
2,000	0.5379		0.3004			

Figure 6.6g shows the effects of positive and negative parameter variations on modeling results for the lowermost cross section at station +2,000 m. The relative deviations of the resulting arrival times t_{arr}^{var} from the reference t_{arr}^{ref} are calculated by

$$\frac{100\left(t_{arr}^{var} - t_{arr}^{ref}\right)}{t_{arr}^{ref}} \tag{6.6}$$

Channel roughness, the geometry parameter $p_3(x)$, and channel slope exhibit the strongest influence on arrival times, followed by the geometry parameters p_4, p_2, and $p_1(x)$. An increase of the values of the Manning-Strickler channel roughness coefficient (i.e., decreased roughness), channel slope, and the geometry parameters $p_1(x)$ and $p_3(x)$ leads to a faster wave advance, i.e., decreased arrival times. In contrast, an increase of p_2 and p_4 causes a slower wave propagation. According to the definition of the model's geometric parameters, higher values of $p_1(x)$ and $p_3(x)$ are related to more narrow cross sections, i.e., flow velocities increase and wave propagation is accelerated. In contrast, as already stated by Schmitz et al. (2002), increasing values of p_2 and p_4 leads to a reduced water depth and a reduced hydraulic radius, which would be the case for a wider cross section or, consequently, a higher channel friction. These findings indicate the need for a detailed determination of channel roughness and the hydraulic radius.

6.1.4 Evaluating the Stability of the Analytical Zero-Inertia Model for Weak Process Dynamics

The most important manageable factor of groundwater recharge dam operation is the rate of culvert release, considering a certain volume of water stored in the reservoir and a given channel length with suitable infiltration characteristics. The proposed analytical ZI model can serve as a robust and accurate tool for the adjustment of culvert release rates to enhance downstream infiltration, i.e., for a desired wadi reach. For Wadi Ahin (1,054 km^2), a groundwater recharge dam is located about 10 km inland from the sea (cf. Fig. 6.1). A 6.2 km wadi reach downstream of the dam offers good infiltration characteristics (Haimerl, 2004).

Regarding the design of a recharge dam's culverts, an important question would be: which (quasiconstant) dam release rate would lead to a practically standing wave—which means an infiltration quota of nearly 100 %—within a considered channel reach? For a simulation with the

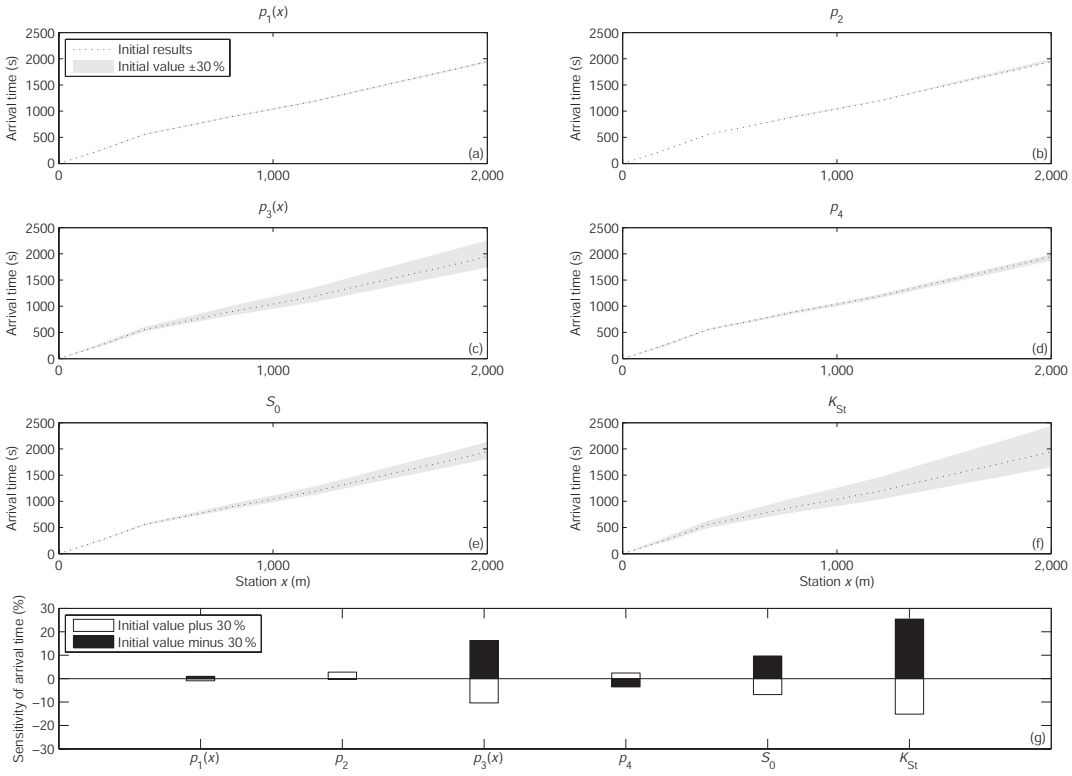

Figure 6.6: Results of the Parameter sensitivity analysis for the analytical zero-inertia model for a nonprismatic channel. (a–f) Absolute deviations of wave front arrival time due to alterations of geometry parameters, channel slope, and the roughness coefficient; (g) relative deviations of wave arrival times at the lowermost cross section (station +2,000 m) for parameter alterations of ±30 %.

analytical ZI model, original topographic channel data of lower Wadi Ahin (Haller, 2000; Haimerl and Zunic, 2002; Haimerl, 2004) are used. The longitudinal slope is 0.006 and channel roughness is estimated to $K_{\mathrm{St}} = 30\,\mathrm{m}^{\frac{1}{3}} \cdot \mathrm{s}^{-1}$, using tabulated values (Chow, 1959) and a verbal description of channel bed composition (Haller, 2000). The spatial domain is discretized with a resolution of $\Delta x = 100\,\mathrm{m}$. The model is charged with a steady upstream inflow rate (representing dam culvert release), which is incrementally lowered from 2.5 to almost $0.2\,\mathrm{m}^3 \cdot \mathrm{s}^{-1}$.

Figure 6.7 shows the respective ZI model results. For constant inflow rates around $0.23\,\mathrm{m}^3 \cdot \mathrm{s}^{-1}$, the flow barely reaches the lowermost station +6,200 m, which is reflected in an arrival time converging to infinity (Fig. 6.7b). Although virtually all inflow volume infiltrated (infiltration quota of 99.23 % for an inflow of $0.23\,\mathrm{m}^3 \cdot \mathrm{s}^{-1}$), the analytical model yields a stable solution with a mass balance error of less than 0.1 %. A stronger decrease of the steady inflow rate would lead to a shift of the standing wave tip towards a more upstream channel location.

6.1.5 Summary

The presented analytical surge flow model, based on the zero-inertia assumptions, offers a new tool for the simulation of flood wave propagation with infiltration losses through permeable beds. The analytical model showed its capability for the simulation of a surge traveling down an irregularly

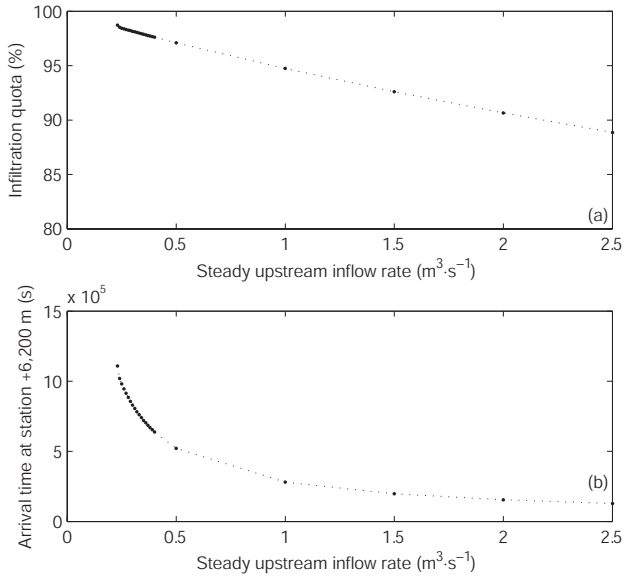

Figure 6.7: Results of the analytical zero-inertia model for high infiltration quotas, causing standing wave effects in Wadi Ahin, downstream of Ahin Dam. (a) Infiltration quota for the whole channel reach as a function of inflow, and (b) arrival time at station +6,200 m as a function of inflow.

shaped natural permeable stream bed, even under problem-specific restrictions, like an initially dry channel bed and/or significant transmission losses. Hence, the presented model seems to be ideal for simulating advancing surge flow phenomena downstream of groundwater recharge dams, notwithstanding the discontinuity when attaining the state of a "standing" wave and—looking at the straightforward applicability—evaluating reservoir release strategies and culvert design for specific groundwater recharge problems.

Test runs for prismatic and nonprismatic permeable channels showed excellent agreement with the full dynamic solution. Model applicability, therefore, seems not to be severely constricted by the underlying assumptions. Although the assumption of a spatially constant slope and an averaged roughness coefficient is obviously relying on the specific channel morphology, this apparently does not represent a serious restriction for model application for surge flows over alluvial wadi beds. The proposed approach circumvents any numerical imponderables which are potentially associated with free boundary value problems, and offers the possibility of incorporating nonprismatic channel geometries. Moreover, any arbitrary relationship for the quantification of infiltration losses through the channel bed can be coupled with the surface flow model, as already shown in Section 5.1.7.

6.2 Overland Flow on a Plane

In this section, results of the developed analytical zero-inertia overland flow model (aZI model; cf. Section 5.2) are compared with results obtained by numerical solutions of the Saint-Venant equations (nHD model), the zero-inertia (nZI) model, and the kinematic wave approximation (nKW model). This is done by modeling surface runoff produced by excess rainfall on a synthetic test plane with a specific roughness, as typically examined by numerous authors (e.g., Schmid, 1986;

Di Giammarco et al., 1995; Tsai and Yang, 2005). The results are compared with respect to mass balance errors, hydrograph shape, and computational efficiency of the considered approaches.

6.2.1 Test Setup

The test setup for the model intercomparison study is presented in this section. This comprises the characteristics of the employed synthetic overland flow plane, the specific parametrization of the incorporated numerical models and the analytical model, as well as the boundary and initial conditions.

6.2.1.1 Characteristics of the Synthetic Test Plane

For model intercomparison and the assessment of the proposed analytical zero-inertia overland flow model, the flow over a synthetic impervious test plane as proposed by Schmid (1986) (cf. Fig. 5.3) is simulated. This specific test plane is selected because modeling results of a kinematic wave model implementation for the mentioned test plane (Schmid, 1986) are available, which allows the opportunity to check first for the validness of flow models incorporated in the analysis. The considered synthetic test plane features the following parameters: rectangular domain, length of 80 m; width of 20 m; surface slope of 15 degrees. In order to keep consistency with Section 5.2.1, the Chézy law is applied for quantifying friction slope S_f, i.e., β is set to $\frac{1}{2}$ in Eq. (3.6). The comparative model simulations are carried out for Chézy roughness coefficients of $K_\mathrm{C} = 2.0, 5.0, 10.0, 20.0\,\mathrm{m}^{\frac{1}{2}} \cdot \mathrm{s}^{-1}$.

6.2.1.2 Specifics of the Model Setups

Numerical Full Hydrodynamic Model (nHD Model): The employed full hydrodynamic model is based on the Saint-Venant equations with a source term in the continuity equation, i.e., Eqs. (5.50) and (3.2). The equations are solved using a Preissmann finite difference scheme (Preissmann, 1961; Chau, 1990), which employs a fixed-point iteration scheme for the simultaneous solution of the resulting system of algebraic equations. The nHD model's spatial discretization is set to $\Delta x = 0.5\,\mathrm{m}$ and a time step of $\Delta t = 2\,\mathrm{s}$ is applied. The spatiotemporal resolution is selected on the basis of a prerequisite sensitivity analysis, which revealed—depending foremost on the magnitude of the inflow rate—that greater values of Δx and Δt provoke a declined convergence behavior of the incorporated iteration scheme or, finally, lead to numerical instabilities which avoids a convergent solution.[1]

Numerical Zero-Inertia Model (nZI Model): Equations (5.50) and (3.3) form the incorporated zero-inertia model. The employed numerical solution scheme for the ZI model is also based on the Preissmann scheme as proposed by numerous authors for the one-dimensional case (e.g., Bronstert and Bárdossy, 2003). As applies for the herein discussed numerical solutions of the full hydrodynamic model and the kinematic wave model, it is crucial to discretize the solution domain with an appropriate resolution in time and space to circumvent numerical errors. For consistency, the spatial and temporal discretization for the test scenario calculations is, therefore, set to $\Delta x = 0.5\,\mathrm{m}$ and $\Delta t = 2\,\mathrm{s}$.

[1] As outlined in Appendix A.3, the Preissmann scheme establishes an implicit solution scheme for the governing equations. The spatiotemporal discretization is, therefore, not constricted by the CFL condition (Eq. (4.1)). However, this does not imply that, for practical application, an inappropriate discretization may not lead to noticeable numerical errors (cf. Section 4.2.2).

Numerical Kinematic Wave Model (nKW Model): A one-dimensional kinematic wave model of surface flow (e.g., as proposed by Schmid, 1986) is implemented. The model incorporates the kinematic wave equations with a source term in the continuity equation, i.e., Eqs. (5.50) and (3.4). The governing equations are also solved with the aforementioned Preissmann finite difference scheme. The time step of the nKW model is set to $\Delta t = 2\,\mathrm{s}$ and the spatial discretization is set to $\Delta x = 0.5\,\mathrm{m}$ to prevent numerical instabilities and convergence problems and to keep consistency with the other incorporated numerical model setups.

Analytical Zero-Inertia Model (aZI Model): The analytical ZI model, given by Eqs. (5.50) and (5.51), is implemented according to Section 5.2. A fixed-point iteration scheme is applied for the iterative solution of the governing nonlinear equations (5.63);(5.64). According to Wöhling (2005), using a linearly converging fixed-point scheme for the iterative solution of Eqs. (5.63);(5.64) may not lead to satisfactory convergence rates at any time.[1] An algorithm of higher-order accuracy can help to improve the convergence behavior of the iterative solution procedure. Wöhling (2005) suggests the Newton-Raphson method (Ypma, 1995), which is of second-order accuracy, but demands the derivatives of the governing equations. However, the fixed-point scheme employed herein performs well under the investigated conditions. The number of iteration loops till convergence for each iteration run is typically less than 30, depending on convergence rate, the value of the selected iteration precision criterion, and the relaxation parameters $r_{A,t}$ (cf. Section 5.1.7), which are set to $r_{A,t} = 0.8$. The synthetic test plane is discretized with a spatial resolution of $\Delta x = 0.5\,\mathrm{m}$. Corresponding to the analytical solution procedure, the model time step is adaptive.

6.2.1.3 Boundary and Initial Conditions of the Test Scenarios

Four model-test scenarios with different upper boundary conditions are selected for the comparative model analysis. According to Fig. 5.3, the upper boundary condition is—as is usual for sheet flow modeling—given by a lateral inflow $q(t)$ to the model domain (i.e., rainfall). Additionally, the incorporation of a time-variable inflow $Q(0,t)$ at the uppermost model boundary at $x = 0$ is possible.[2] To maintain brevity, no model results for inflow via the upper boundary are shown. The maximum inflow rates are set to $q_{\max} = 20, 45, 90, 120\,\mathrm{mm \cdot h^{-1}}$, linearly rising from zero to the maximum value within 10 minutes and staying constant for the next 40 minutes (Table 6.6). The selected inflow rates span a wide range of magnitudes, leading to a noticeable flow over the plane. For all included models, a zero-flow initial condition is applied for all spatial nodes of the solution domain at $t = 0$. This does not endanger a numerical solution of the problem since the lateral boundary condition affects all spatial nodes for all time steps beyond $t = 0$.

Furthermore, for the numerical models, a zero-depth gradient (i.e., $\frac{\partial h}{\partial x} = 0$) is used as the downstream boundary condition. Infiltration is not taken into account to assure model comparability. The coupling of an infiltration model with the specific surface flow models would pose a source of uncertainties since the coupling strategies would differ, e.g., due to different temporal discretization strategies and the nonlinear dependency of surface and subsurface flow. If the inclusion of infiltration

[1] As discussed in Section 5.1.8, nonconvergence problems are mainly associated with a highly nonlinear relationship of flow properties and a loss term (e.g., occurring when describing infiltration with Richards' equation). For the case of overland flow, rainfall is considered as a source term. Since surface flow has no physical effect on rainfall and, thus, the source term is a priori determined, the aforementioned statement does not apply.

[2] Which would be indicated when cascading surface runoff elements for a distributed overland flow modeling.

Table 6.6: Lateral inflow rates $q(t)$ to the model domain for the test scenarios 1–4.

Time t (min)	Scenario 1 ($\mathrm{mm \cdot h^{-1}}$)	Scenario 2 ($\mathrm{mm \cdot h^{-1}}$)	Scenario 3 ($\mathrm{mm \cdot h^{-1}}$)	Scenario 4 ($\mathrm{mm \cdot h^{-1}}$)
0	0.0	0.0	0.0	0.0
1	2.0	4.5	9.0	12.0
2	4.0	9.0	18.0	24.0
3	6.0	13.5	27.0	36.0
4	8.0	18.0	36.0	48.0
5	10.0	22.5	45.0	60.0
6	12.0	27.0	54.0	72.0
7	14.0	31.5	63.0	84.0
8	16.0	26.0	72.0	96.0
9	18.0	40.5	81.0	108.0
10	20.0	45.0	90.0	120.0
⋮	⋮	⋮	⋮	⋮
50	20.0	45.0	90.0	120.0

is desired, any arbitrary functional relationship for describing transient infiltration could be taken into account with the presented analytical ZI approach, as shown in Section 6.1.

6.2.2 Comparison of Modeling Results

Since mass conservation should not solely be considered as a measure of model performance, the comparative analysis additionally addresses process dynamics and computational efficiency. Therefore, model performance is subsequently evaluated with respect to mass conservation, portrayal of hydrograph shape, and required CPU times. For the purpose of clarity, results for all Chézy roughness coefficients ($K_\mathrm{C} = 2.0, 5.0, 10.0, 20.0\,\mathrm{m^{\frac{1}{2}} \cdot s^{-1}}$) are included in tabular form, but modeling results in the form of hydrographs are shown only for model setups with the roughness coefficient set to $K_\mathrm{C} = 5.0\,\mathrm{m^{\frac{1}{2}} \cdot s^{-1}}$.

6.2.2.1 Mass Balance Check

The fulfillment of mass conservation of the four incorporated models is considered first. For this purpose, the four different lateral inputs of scenarios 1 to 4 are supplied to the synthetic test plane of a specific roughness. A mass conservation check is carried out for every model by comparing the sum of lateral inflow to the sum of modeled outflow at the plane's lowermost cross section at $x = 80\,\mathrm{m}$ after 50 minutes. The resulting relative mass balance errors are given in Table 6.7. The mass balance comparison unveils that the analytical zero-inertia model outperforms the numerical models for most constellations of lateral inflow rates and Chézy roughness coefficients. The deviations in the mass balance of the aZI model output amount to some 0.1 % for 14 out of 16 calculation runs and are therewith significantly smaller than for the numerical models in 11 out of 16 cases.

For the numerical models, the nKW model outperforms the nHD and nZI models with respect to mass conservation for all simulation runs. The errors of the incorporated numerical models are directly dependent on the spatial and temporal resolution of the solution scheme. The deviations of the aZI model from the reference can additionally be improved by tightening the precision criterion of the iteration procedure (5.63);(5.64). The mass balance error decreases with higher total peak inflow for all incorporated numerical models. For the aZI model, the relative mass balance errors

Table 6.7: Comparison of the relative mass conservation of the investigated overland flow models for different lateral inputs to the synthetic test plane after 50 minutes of inflow. Best results are set in bold font.

		Chézy coefficient ($\mathrm{m}^{\frac{1}{2}} \cdot \mathrm{s}^{-1}$)			
		2.0	5.0	10.0	20.0
$q_{\max} =$ $20\,\mathrm{mm} \cdot \mathrm{h}^{-1}$	nHD	−1.43 %	−1.75 %	−1.86 %	−2.29 %
	nZI	−1.43 %	−1.75 %	−1.86 %	−2.30 %
	nKW	**−0.51 %**	**−0.56 %**	−0.58 %	−0.60 %
	aZI	−1.38 %	−1.11 %	**−0.49 %**	**−0.53 %**
$q_{\max} =$ $45\,\mathrm{mm} \cdot \mathrm{h}^{-1}$	nHD	−1.32 %	−1.34 %	−1.81 %	−1.79 %
	nZI	−1.32 %	−1.34 %	−1.81 %	−1.80 %
	nKW	**−0.53 %**	−0.58 %	−0.59 %	**−0.61 %**
	aZI	−0.84 %	**−0.55 %**	**−0.37 %**	−0.63 %
$q_{\max} =$ $90\,\mathrm{mm} \cdot \mathrm{h}^{-1}$	nHD	−1.25 %	−1.26 %	−1.66 %	−1.30 %
	nZI	−1.25 %	−1.26 %	−1.67 %	−1.31 %
	nKW	**−0.56 %**	−0.59 %	−0.60 %	−0.61 %
	aZI	−0.64 %	**−0.48 %**	**−0.52 %**	**−0.58 %**
$q_{\max} =$ $120\,\mathrm{mm} \cdot \mathrm{h}^{-1}$	nHD	−1.24 %	−1.25 %	−1.64 %	−1.46 %
	nZI	−1.24 %	−1.25 %	−1.65 %	−1.43 %
	nKW	−0.56 %	−0.59 %	−0.60 %	−0.61 %
	aZI	**−0.26 %**	**−0.15 %**	**−0.18 %**	**−0.25 %**

are lowest for moderate roughness coefficients of $K_{\mathrm{C}} = 5.0, 10.0\,\mathrm{m}^{\frac{1}{2}} \cdot \mathrm{s}^{-1}$. Overall, the aZI model performed very well compared with the other models.

6.2.2.2 Hydrographs of the Test Scenario Calculations

The aforementioned boundary and initial conditions are applied to the four presented models and the simulated flow hydrographs for the lowermost observation point of the synthetic test plane (at $x = 80\,\mathrm{m}$) are compared. Fig. 6.8 depicts the resulting hydrographs for the scenario calculations (maximum inflow rate $q_{\max} = 20, 45, 90, 120\,\mathrm{mm} \cdot \mathrm{h}^{-1}$) for a roughness coefficient of $K_{\mathrm{C}} = 5.0\,\mathrm{m}^{\frac{1}{2}} \cdot \mathrm{s}^{-1}$. The results for other roughness coefficients ($K_{\mathrm{C}} = 2.0, 10.0, 20.0\,\mathrm{m}^{\frac{1}{2}} \cdot \mathrm{s}^{-1}$) look similar but with decreased/increased dynamics of the rising limb of the simulated flow hydrographs. Table 6.8 shows the quasistationary flow rates after 50 minutes at the lowermost cross section $x = 80\,\mathrm{m}$. The process dynamics of all scenarios are soundly portrayed by the four incorporated hydrodynamic models. These observations apply for the whole range of investigated Chézy roughness coefficients. Onset and rising limb of the hydrograph and transition to the quasistationary peak flow rate are convergent for the investigated models. The calculations for higher Chézy coefficients lead to a slightly better agreement of the resulting peak flow rates of the different models.

The analytical zero-inertia model nearly matches the stationary peak inflow rates of $q_{\max} = 20, 45, 90, 120\,\mathrm{mm} \cdot \mathrm{h}^{-1}$ for all applied Chézy roughness coefficients, which is supported by the analytical character of the model. The aZI model performs best for 15 out of 16 calculations presented herein. It is even possible to improve the quality of the aZI results by tightening the convergence precision criterion of the incorporated iterative solution procedure, which, in contrast, leads to higher computational effort. The aZI model shows the lowest relative peak flow errors for moderate Chézy coefficients. Relative peak flow errors of the aZI model decrease with increasing peak flow rates. For the numerical models, the nKW model performs best in matching quasistationary

Table 6.8: Comparison of absolute and relative quasistationary flow rates ($\mathrm{mm} \cdot \mathrm{h}^{-1}$) at the lowermost cross section after 50 minutes at location $x = 80\,\mathrm{m}$ for scenario calculations 1–4. The relative deviations from the maximum lateral inflow to the test plane $q_{\max}$ are given in parentheses. Best results are set in bold font.

		Chézy coefficient ($\mathrm{m}^{\frac{1}{2}} \cdot \mathrm{s}^{-1}$)			
		2.0	5.0	10.0	20.0
$q_{\max} =$ $20\,\mathrm{mm} \cdot \mathrm{h}^{-1}$	nHD	19.6664 (−1.67 %)	19.6142 (−1.93 %)	19.5944 (−2.03 %)	19.5086 (−2.46 %)
	nZI	19.6664 (−1.67 %)	19.6141 (−1.93 %)	19.5940 (−2.03 %)	19.5079 (−2.46 %)
	nKW	**19.8535 (−0.73 %)**	19.8358 (−0.82 %)	19.8471 (−0.76 %)	19.8231 (−0.88 %)
	aZI	19.7730 (−1.14 %)	**19.8923 (−0.54 %)**	**19.9350 (−0.33 %)**	**19.9283 (−0.36 %)**
$q_{\max} =$ $45\,\mathrm{mm} \cdot \mathrm{h}^{-1}$	nHD	44.3164 (−1.52 %)	44,3303 (−1.49 %)	44,1184 (−1.96 %)	44,1370 (−1.92 %)
	nZI	44.3162 (−1.52 %)	44,3296 (−1,49 %)	44,1168 (−1,96 %)	44,1332 (−1,93 %)
	nKW	44.6670 (−0.74 %)	44,6942 (−0,68 %)	44,5782 (−0,94 %)	44,4173 (−1,29 %)
	aZI	**44.6850 (−0.70 %)**	**44.8425 (−0.35 %)**	**44.8650 (−0.30 %)**	**44.7975 (−0.45 %)**
$q_{\max} =$ $90\,\mathrm{mm} \cdot \mathrm{h}^{-1}$	nHD	88.7156 (−1.43 %)	88.7314 (−1.41 %)	88.3846 (−1.79 %)	88.7334 (−1.41 %)
	nZI	88.7151 (−1.43 %)	88.7295 (−1.41 %)	88.3800 (−1.80 %)	88.7219 (−1.42 %)
	nKW	89.3272 (−0.75 %)	89.3021 (−0.78 %)	89.3449 (−0.73 %)	89.2886 (−0.79 %)
	aZI	**89.4375 (−0.63 %)**	**89.7075 (−0.33 %)**	**89.6625 (−0.38 %)**	**89.4825 (−0.58 %)**
$q_{\max} =$ $120\,\mathrm{mm} \cdot \mathrm{h}^{-1}$	nHD	118.2978 (−1.42 %)	118.3182 (−1.40 %)	117.8628 (−1.78 %)	118.0799 (−1.60 %)
	nZI	118.2970 (−1.42 %)	118.3152 (−1.40 %)	117.8555 (−1.79 %)	118.1176 (−1.57 %)
	nKW	119.0986 (−0.75 %)	119.0993 (−0.75 %)	118.9665 (−0.86 %)	119.1663 (−0.69 %)
	aZI	**119.4300 (−0.47 %)**	**119.7225 (−0.23 %)**	**119.6100 (−0.33 %)**	**119.4525 (−0.46 %)**

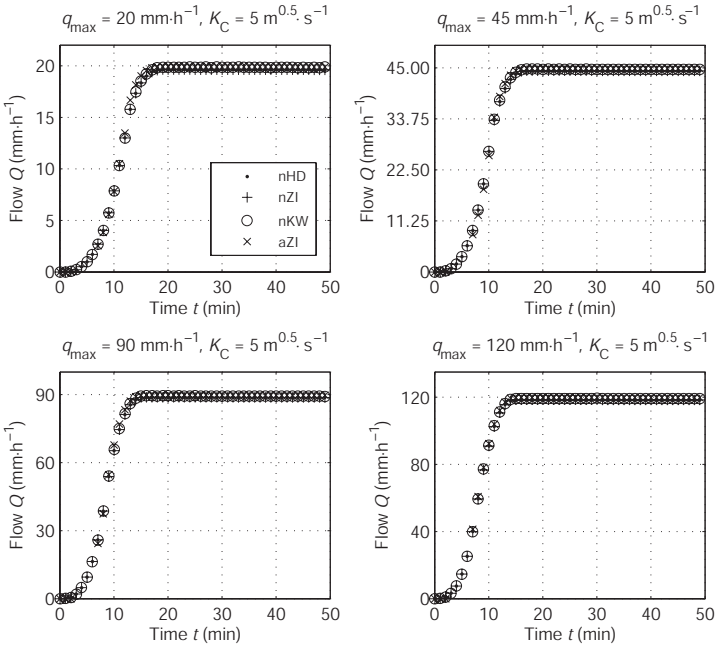

Figure 6.8: Flow hydrograph comparison for lateral input scenarios 1–4 (maximum inflow rate $q_{\max} = 20, 45, 90, 120\,\mathrm{mm \cdot h^{-1}}$) and Chézy roughness coefficient of $K_C = 5.0\,\mathrm{m^{\frac{1}{2}} \cdot s^{-1}}$ at the lower end of the synthetic test plane ($x = 80\,\mathrm{m}$).

peak flow rates. The respective relative errors of the nKW model are always lower than the errors of the nHD and the nZI model. Furthermore, the errors of the nHD and nZI model are nearly equal for the specific simulations. Like for the aZI model, relative peak flow errors of the numerical models decrease with increasing peak flow rates.

6.2.2.3 Computation Time Requirements

A comparison of CPU time requirements of the test scenario calculations is conducted. The numerical models are all implemented in FORTRAN language and compiled with the same compiler. The analytical zero-inertia model is implemented and executed in the MATLAB environment. A 1.6 GHz machine with 2 GB of memory is used for computation. The CPU times of each model for all 16 model setups are averaged and normalized by the mean CPU time requirement of the analytical ZI model:

$$\text{CPU time factor} = \frac{\text{CPU time}_{\text{nHD,nZI,nKW}}}{\text{CPU time}_{\text{aZI}}} \tag{6.7}$$

The mean CPU time and CPU time factors for the four different models are given in Table 6.9. As expected, CPU time increases with the complexity of the governing flow equations. The flow simulations with the nHD model require the highest CPU time, followed by the nZI and the nKW model. The aZI model has the lowest CPU time requirements. CPU time is mainly required for the iterative solution of the system (5.63);(5.64), which typically needs less than 30 iteration loops for yielding convergence in the study at hand. Tightening the iteration criterion leads to slightly better model results but higher CPU time requirements. It needs to be mentioned that the nHD, nKW, and nZI code were used as compiled executable code, whereas the aZI code was executed in the

Table 6.9: Comparison of average CPU time requirements of the nHD, nZI, nKW, and aZI models.

Model	Code execution	Space step (m)	Time step (s)	CPU time (s)	CPU time factor
nHD	compiled	0.5	2	9.56	1.40
nZI	compiled	0.5	2	8.97	1.31
nKW	compiled	0.5	2	6.92	1.01
aZI	interpreted	0.5	adaptive	6.83	1.00

MATLAB interpreter environment. It is assumed that a compiled version of the aZI code would outperform the other investigated models by far, considering CPU time requirements.

6.2.3 Summary

The presented analytical zero-inertia model showed a highly satisfactory performance for modeling typical scenarios of sheet flow on a synthetic plane, charged by time-varying rainfall events. In a comparative analysis, the aZI model delivered mostly better results than the commonly used numerical approaches in terms of an adequate mass conservation and matching peak runoff rates. Furthermore, the aZI model delivered a convergent solution for the flow dynamics compared with the numerical solutions. At the same time, the aZI model demanded less CPU time than the employed numerical solution schemes.

The mass balance error of the aZI model for the 16 simulation runs amounted to $-0.15\,\%$ to $-1.38\,\%$ which made the model superior for 11 out of 16 runs regarding mass conservation. The mass balance errors of the numerical models for all simulation runs spanned from $-1.24\,\%$ to $-2.29\,\%$ (nHD), $-1.24\,\%$ to $-2.30\,\%$ (nZI), and $-0.51\,\%$ to $-0.61\,\%$ (nKW). The errors of the aZI model for the representation of peak inflow rates were again comparatively small with $-0.23\,\%$ to $-1.14\,\%$. The nHD model ($-1.40\,\%$ to $-2.46\,\%$), nZI model ($-1.40\,\%$ to $-2.46\,\%$), and nKW model ($-0.68\,\%$ to $-1.29\,\%$) showed larger relative errors, related to peak inflow rates. The aZI model met the peak flow rates best for 15 out of 16 simulations. The performance of the aZI model regarding mass conservation and the portrayal of peak inflow rates is supported by the analytical character of the model.

The aZI model demanded the lowest computation times of all investigated models. However, CPU time requirements of the aZI model were only slightly lower than those of the nKW model for the flow calculations with the investigated simple geometry. The nHD model demanded the highest CPU times, which were a factor of 1.4 higher than those required for the aZI model. The benefit of lower CPU time of the aZI model will significantly improve spatially distributed surface flow modeling on catchment scale. At the same time, the aZI model is free of numerical inconveniences, like discretization errors, phase errors, and convergence problems, which often endanger the solution of numerical schemes, particularly regarding the weak process dynamics of typical sheet flow phenomena (cf. Section 2.2). To delimit such errors, a relatively fine spatial and temporal discretization of the employed numerical solution schemes had to be chosen which led to higher CPU times. Furthermore, the coupling of the aZI surface flow model with any arbitrary infiltration model can be carried out straightforwardly because of the analytical character of the surface flow model (cf. Sections 5.1 and 6.1).

Chapter 7

Flash Flood Routing under Transmission Losses and Dam Operation

This chapter focuses on the development and application of an integrated modeling system for flow routing in ephemeral rivers with groundwater recharge dams, such as in the Sultanate of Oman. The proposed system is based on a process-oriented description of wadi flow, infiltration, dam operation, and reservoir evaporation and allows for a robust application within a limited data situation, as is usually encountered in arid and semiarid regions.

Particularly, the proposed framework (a) accounts for the considerable loss of mass and momentum from the weakly dynamic flow downstream of a dam, attributable to transmission losses; (b) regards the transient character of transmission losses, which are nonlinearly dependent on time and changing channel flow conditions; and (c) circumvents any numerical inconveniences associated with the modeling of dam release flow over initially dry beds by employing an analytical solution procedure of the governing flow equations.

Following a comprehensive sensitivity analysis, relevant process parameters are estimated and the modeling system is applied to Wadi Ma'awil, Northern Oman. The application demonstrates both the system's accurateness and robustness for flash flood routing under transmission losses along the wadi, where a recharge dam causes strong flow retention. Therefore, the proposed modeling system can aid in deriving realistic groundwater recharge rates, which is of high importance for a sound water resources assessment in the study area.

7.1 Outline of the Structure of a Novel Integrated Modeling System for Ephemeral Channel Routing

The proposed wadi flow and dam simulation model (Fig. 7.1) satisfies the afore-discussed demands of a comprehensive process modeling of infiltrating ephemeral river flow influenced by dam retention. It consists of three main elements, each a hydrodynamic model for the upstream and the downstream reaches, as well a dam simulation model. The hydrodynamic models are coupled with an infiltration

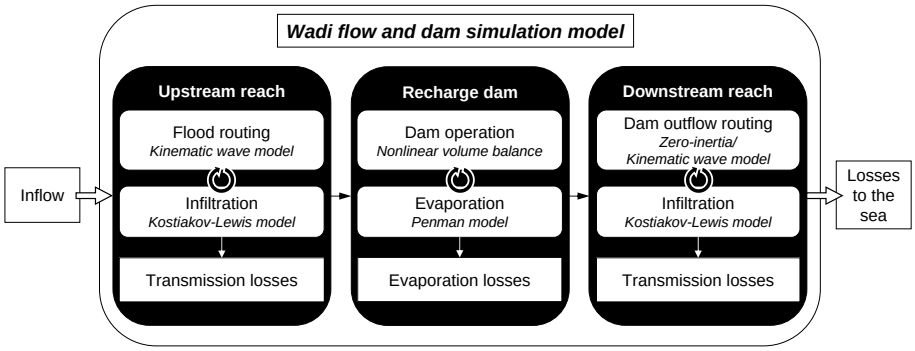

Figure 7.1: Components of the proposed wadi flow and dam simulation model.

model for the quantification of transmission losses. The dam simulation model incorporates an evaporation modeling component. All sub-models are one-dimensional and are coupled horizontally via the flow $Q(t)$. The integrated modeling system is implemented in MATLAB and is presented in the following.

7.1.1 Wadi Flow Routing Models

Two flow routing models are developed aiming at a comprehensive representation of the specific flow processes in the upstream and downstream reaches of a recharge dam. For the pronounced flow in the upstream reaches, a KW model is implemented, following the outcomes of the discussion in Section 3.7.1. To accommodate for the more complex character of the flow downstream of the dam, flow advance and recession are treated separately. It is important to match the dynamics and nonlinearity of the advancing flow in an initially dry channel under considerable infiltration. To circumvent numerical instabilities and to pay attention to the influence of infiltration, a tailor-made analytical ZI model, as derived in Section 5.1, is set up for modeling the advancing flow domain. In turn, flow recession in the downstream reaches—which is not covered by the analytical ZI solution—is modeled with the KW equations again. The same applies for dam outflow influenced by spillway operation (cf. Section 3.7.1). Evaporation from wadi flow is neglected since evaporation rates are usually two orders of magnitude below infiltration rates (cf. Section 1.1).

7.1.1.1 Numerical Kinematic Wave Model (Upstream Model)

Making use of the continuity equation (3.7), the KW momentum equation (3.4)—which assumes a parallelism of bottom and friction slope—and the uniform flow formula (3.5) yield an explicit expression of the KW model. According to the derivation outlined in Appendix A.1 and with β set to $\frac{2}{3}$ for the Manning-Strickler formula, the KW model reads

$$\frac{\partial Q}{\partial x} = \left(\left(K_{\mathrm{St}} S_0^{\frac{1}{2}} \frac{2}{3} R^{\frac{1}{3}} \frac{\partial R}{\partial x} A \right) + \left(K_{\mathrm{St}} S_0^{\frac{1}{2}} R^{\frac{2}{3}} \frac{\partial A}{\partial x} \right) \right) \tag{7.1}$$

where K_{St} is the respective Strickler roughness coefficient $[\mathrm{L}^{\frac{1}{3}}\mathrm{T}^{-1}]$.

Equation (7.1) is inserted into the continuity Eq. (3.7) and the resulting equation is numerically solved using a finite differencing scheme on the basis of the argumentation given in Section 4.4. A second-order Runge-Kutta method is applied for approximating the partial differential quotients of

Eqs. (7.1) and (3.7).[1] Further following Section 4.4, an explicit formulation of the difference equations is chosen. Appendix A.2 exemplarily shows the derivation of the corresponding second-order scheme as is used in this work.

The numerical solution requires the specification of boundary and initial conditions. The upstream boundary condition at $x = 0$ is the inflow hydrograph

$$Q_0 = Q_0(t) = Q(x = 0, t) \tag{7.2}$$

The downstream boundary can be characterized either by an advancing wave tip or a rating curve, e.g., coming from the assumption of outflow at normal depth at the end of the model domain. For the first case, the boundary conditions would read

$$A(x_{\mathrm{tip}}, t) = 0 \tag{7.3}$$

$$u(x_{\mathrm{tip}}, t) = u_{\mathrm{tip}}(t) = \frac{\mathrm{d}x_{\mathrm{tip}}}{\mathrm{d}t} \tag{7.4}$$

where $x_{\mathrm{tip}}(t)$ is the location of the advancing wave tip.

The ideal dry-channel initial condition would be

$$x_{\mathrm{tip}}(t = 0) = 0 \tag{7.5}$$

For this study, this ideal dry-channel initial condition is alleviated to prevent numerical issues. A constant minimum flow is introduced and the other dependent hydraulic variables are calculated prior to the numerical integration, assuming uniform flow conditions. This practice is quite common, albeit introducing some errors (Cunge et al., 1980). Nevertheless, for greater flood magnitudes, such as those present in the upstream wadi sections, the incorporation of a nonzero minimum flow is feasible, as discussed in Section 4.4. A normal-depth lower boundary condition is placed at the lowermost cross section, i.e., the location of the recharge dam.[2]

Since cross-sectional infiltration is dependent on the wetted perimeter, and vice versa, the flow equation is coupled with the time-dependent Kostiakov-Lewis infiltration function (Eqs. (6.1) to (6.3)) by employing alternating iterative coupling, based on a fixed-point iteration scheme (cf. Section 5.1.7). Algorithm 7.1 illustrates a pseudocode implementation of the incorporated iteration scheme. In contrast to the iterative procedures given by Eqs. (5.47);(5.48) and (5.63);(5.64) which employ an adaptive temporal discretization (cf. Section 4.4), the coupling is carried out at the equidistant spatiotemporal nodes $\Delta(x, t)$ of the underlying finite difference scheme. Furthermore, it is important to account for the transient spatial extents of the flow domain in order to obtain an exact assessment of infiltration. To encounter the nonzero minimum flow assumption, only flow above the initial flow rate is taken into account for the calculation of infiltration.

[1] The class of Runge-Kutta methods essentially comprises single-step methods of various order (which might be evaluated for intermediate steps as discussed in Section 4.2.2) and, therefore, also covers the first-order Euler method (cf. Appendix A.1). The classification is made regardless of the applied formulation of the solution scheme (i.e., explicit or implicit). The fourth-order Runge-Kutta method is the "original" method, which is usually addressed by referring to "*the* Runge-Kutta method". Concisely, the Runge-Kutta method applied herein is a second-order scheme with intermediate nodes, located at $\frac{1}{2}\Delta t$ (the so-called midpoint method).

[2] Since the employed flow model is based upon the (steady) kinematic wave assumptions and perturbations cannot travel in upstream direction, this boundary condition type poses no serious restriction for the validity of the KW results calculated for the interior points.

Algorithm 7.1 Algorithm for the alternating iterative procedure for coupling the numerical kinematic wave model with the Kostiakov-Lewis infiltration model.

EPS $= 10^{-4}$ ▷ Define iteration precision criterion
for $j = 1 : \Delta t : t_{\text{end}}$ **do** ▷ Loop over time
  for $i = 1 : \Delta x : x_{\text{end}}$ **do** ▷ Loop over space
    $k = 1$ ▷ Set iteration counter
    $q^{\phi}_{(k-1)} = 0$ ▷ Initially estimate cross-sectional infiltration q^{ϕ}
    repeat
      Solve the KW model with respect to $q^{\phi}_{(k-1)}$ (Eqs. (7.1) and (3.7), according to Appendices A.1 and A.2) to obtain infiltration opportunity times and wetted perimeter
      $q^{\phi}_{(k)}$ from Eqs. (6.1) and (6.2) ▷ Calculate new estimate of q^{ϕ}
      ICC $= \left| q^{\phi}_{(k)} - q^{\phi}_{(k-1)} \right|$ ▷ Calculate iteration convergence criterion
      $k = k + 1$ ▷ Update iteration counter
    until ICC $<$ EPS ▷ Compare ICC with EPS
  end for
end for

The alternating iterative coupling of the surface flow and the infiltration model yields a proper convergence behavior, which allows for a straightforward coupled computation of flow and infiltration with, for instance, less than 20 iteration loops under a quite strict iteration precision criterion of 10^{-4}. The nonprismatic cross-sectional geometry is included via an analytical power law fit of the empirical profile functions $\tilde{h}(x, A)$ and $\tilde{R}(x, A)$, derived from topographic data. The procedure required because of this is the same as used for the processing of the cross-sectional data for the analytical ZI model, shown in Section 5.1.2. Thus, the corresponding values of water depth, wetted cross-sectional area, and hydraulic radius can be mapped onto each other on an analytical basis.

A prerequisite model validation was carried out by Six (2011) for a prismatic rectangular test channel (width of 100 m; slope of 0.008; Strickler roughness coefficient of $K_{\text{St}} = 30.30\,\text{m}^{\frac{1}{3}} \cdot \text{s}^{-1}$; zero infiltration) in order to compare the results of the KW model with those obtained from a full hydrodynamic model, which was implemented in HEC-RAS.[1] It can be seen exemplarily from Fig. 7.2 that the KW model slightly overestimates values around the peak and underestimates their timing in comparison to the HD model. These effects are more pronounced for higher flow rates, i.e., the more unsteady portions of the hydrograph, and are attributable to the neglecting of secondary terms in the KW model (cf. Section 3.7.1). In contrast, the HD model preserves those terms, leading to the observed wave deceleration and dispersion. However, the results of the two models are in good agreement, especially for the portions of the hydrographs which are associated with moderate flow rates.

7.1.1.2 Coupled Analytical ZI Advance Model–Numerical Kinematic Wave Recession Model (Downstream Model)

Dam release leads to an outflow which is advancing in the downstream direction. Therefore, the flow processes can be modeled with the analytical zero-inertia approach, presented in Section 5.1. Generally, the advance rate of the wave tip decreases with increasing time and increasing extent

[1] The comparison was carried out disregarding the influence of the applied numerical solution schemes, namely an explicit Runge-Kutta scheme for the KW model (cf. Appendix A.2) and an implicit Preissmann scheme for the HD model (cf. Appendix A.3). However, some of the difference in the model outputs may emerge from the differing solution schemes.

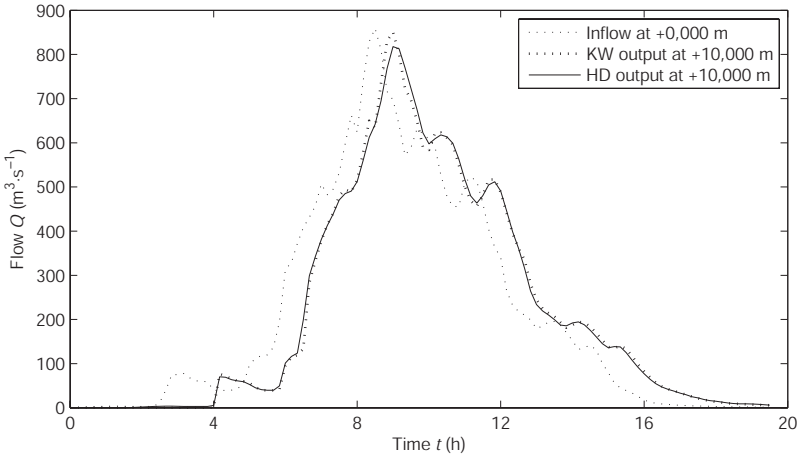

Figure 7.2: Comparison of simulation results obtained by the kinematic wave model with those of a full hydrodynamic model for station +10,000 m of a rectangular test channel under zero infiltration. Inflow event recorded on 06/06/07 at Afi gauging station, according to Section 7.2.1. Values in the output were aggregated to 10 min intervals; spatial discretization for both models was 100 m; temporal discretization was 10 s for the HD model and 1 s for the KW model, respectively.

of the infiltrating domain. Assuming an infinitely long permeable channel bed and a quasisteady inflow, the advance would cease if infiltration rates equal inflow rates. Approaching such a state of zero advance leads to a rapidly growing number of iterations for solving the system (5.47);(5.48). Furthermore, if dam outflow rates are lower than infiltration rates, the flow domain would start receding in the upstream direction. Such conditions are not covered by the iterative solution procedure of the ZI model presented herein.

Therefore, from the point in time when the flow approaches such a zero-advance condition, hydrodynamics are modeled with a KW approach, following the concepts discussed in Section 7.1.1.1. This approach is reasonable since (a) the flow momentum is negligible when the flow advance velocity converges to zero, and (b) inflow rates have already become comparably low, which justifies the KW assumption that the change of the water depth along the channel is very small ($\frac{\partial h}{\partial x} \approx 0$). Practically, specific criteria are required in order to evaluate the zero-advance condition; the analytical ZI model is, therefore, applied until one of the following relations is harmed

$$\frac{(t_n - t_{n-1})}{(t_{n-1} - t_{n-2})} \overset{!}{\leq} \sigma \tag{7.6}$$

$$k \overset{!}{\leq} \varsigma \tag{7.7}$$

with σ: an upper limit for the allowed increase rate of advance times and ς: maximum tolerable number of iterations for solving the procedure (5.47);(5.48).

For the first case, the rate of increase of the advance times between the equidistant channel locations $x_{n,\ldots,n-2}$ is evaluated, as illustrated by Fig. 7.3. If the condition (7.6) is not fulfilled anymore, the actual ZI model results for the time slice $t = t_n$ are passed to the initial condition of a

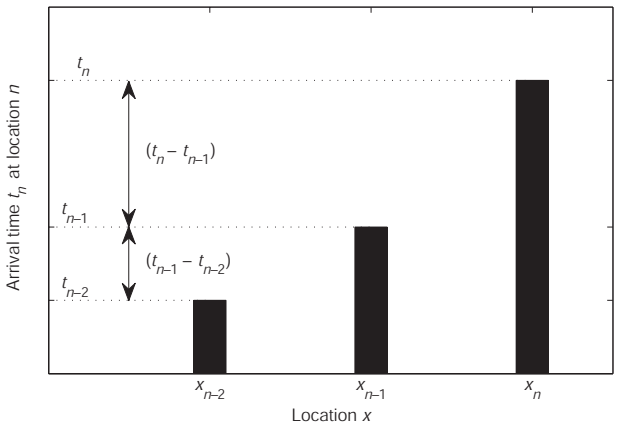

Figure 7.3: Illustration of the employed zero-advance criterion, given by Eq. (7.6).

KW model, which is set up following the concepts already discussed.[1] The KW model is employed to simulate the further development of the flow variables, related to the initial condition for $t = t_n$ and to the upper boundary condition $Q_0(t)$ from $t = t_n$ to $t = t_{\text{end}}$. The end time of the simulation, t_{end}, might be defined a priori the simulation or dynamically, e.g., related to the condition if all inflow volume had already infiltrated or left the modeling domain through the channel. In case condition (7.7) is harmed first, differing from the aforesaid, the solution procedure (5.47);(5.48) had not yet converged and, therefore, yielded no result for t_n. Therefore, switching between the ZI and the KW model is performed for the time slice $t = t_{n-1}$. Practically, adjusting σ to values between 3 and 5 and ς to 200 to 500 leads to a balancing of computation time and model accuracy.

Besides culvert release, a comprehensive modeling approach has to account for spillway release as well. However, spillway release is a fairly rare condition for the operation of the recharge dam investigated in this thesis, located in Wadi Ma'awil (cf. Section 7.2.1). The dam construction report (MAF, 1989; cf. Table 7.2) assesses the design storage to $10 \cdot 10^6\,\text{m}^3$, which is related to a return period of roughly 30 years.

Generally, total outflow rates under spillway release are high compared to culvert outflow alone. This implies a negligible impact of infiltration on flow momentum during spillway operation. Furthermore, the spillway outflow features strongly falling hydrographs, which renders the analytical ZI approach not applicable. Dam outflow during spillway operation is, therefore, simulated again with a KW model, set up as outlined previously. When the spillway is activated, ZI results are passed to the initial condition of the KW model, and vice versa when the spillway outflow ceases. The downstream hydrodynamic model combined in this way, consisting of a ZI model and a KW model for routing the advancing/receding culvert outflow and an additional KW model for flow routing during spillway operation, is referred to as a coupled ZI/KW model in the following.

7.1.2 Dam Simulation Model with Evaporation Component

Within the frame of the proposed integrated modeling system, dam operation is simulated with an incremental solution of the nonlinear storage equation. Attributable to the morphology found at the

[1] If the spatial resolution of the KW model does not equal that of the ZI model, this step would require an inter/extrapolation of the values of the dependent variables according to the chosen spatial resolution of the KW model.

Omani dam sites, the water surface area connected to a specific storage volume is comparably large. Additionally, the dams are filled for a couple of days which may yield a significant evaporation loss under the given climatic conditions. Evaporation from the free water surface is, therefore, taken into account in the dam water balance.

7.1.2.1 Reservoir Routing Model

The dynamic change of the water volume within a retention reservoir under varying inflow conditions can be expressed by the differential storage equation, representing continuity. Sedimentation causes clogging of the reservoir bottom and, consequently, infiltration through the bottom will tend to zero (Haimerl, 2004). Due to the specific cubature of the herein considered groundwater recharge reservoirs—located in the coastal plain—the inclined side areas of the reservoir, which are less prone to clogging and, therefore, typically permeable, only make up a small fraction of total reservoir area. For this reason, infiltration losses can be neglected in the reservoir balance. The continuity equation of the storage volume, therefore, reads

$$\frac{\mathrm{d}V}{\mathrm{d}t}(t) = Q_{\mathrm{in}}(t) - Q_{\mathrm{out}}(t) - E(t) \tag{7.8}$$

where t: time [T]; $V(t)$: storage volume [L^3]; $Q_{\mathrm{in}}(t)$: inflow to the reservoir [$\mathrm{L}^3\mathrm{T}^{-1}$]; $Q_{\mathrm{out}}(t)$: total outflow from the reservoir [$\mathrm{L}^3\mathrm{T}^{-1}$]; $E(t)$: evaporation from the reservoir's surface [$\mathrm{L}^3\mathrm{T}^{-1}$]. According to the morphology of the dam site, the reservoir storage volume $V(t)$ is a function of the water level, $W(t)$ [L]: $V(t) = f(W(t)) = V(W)$. The water surface area of the reservoir $A_{\mathrm{r}}(t)$ [L^2] can be related to the water level as well: $A_{\mathrm{r}}(t) = f(W(t)) = A_{\mathrm{r}}(W)$. Furthermore, evaporation is—besides the climatic influence—a function of the evaporating free water surface area: $E(t) = f(A_{\mathrm{r}}(t))$.

The outflow $Q_{\mathrm{out}}(t)$ is constituted of the outflow through the dam culverts $Q_{\mathrm{out}_{\mathrm{c}_m}}(t)$ and—depending on a certain water level which activates the spillway—the outflow over the spillway $Q_{\mathrm{out}_{\mathrm{s}}}(t)$ if active:

$$Q_{\mathrm{out}}(t) = \sum_{m=1}^{M} Q_{\mathrm{out}_{\mathrm{c}_m}}(t) + Q_{\mathrm{out}_{\mathrm{s}}}(t) \tag{7.9}$$

where $m = 1, ..., M$ is the culvert index [−] and M is the total number of culverts.

The outflow through the culverts and over the spillway is nonlinearly dependent on water depth $W(t)$. Assuming the outflow is not controlled from downstream[1], the outflow through each of the culverts and over the spillway can be modeled with an exponential stage–discharge relationship in the form (Chow, 1959)

$$Q_{\mathrm{out}_{\mathrm{c}_m,\mathrm{s}}}(t) = \begin{cases} \alpha_{\mathrm{c}} A_{\mathrm{c}} \left(W(t) - H_{\mathrm{c}_m}\right)^{\frac{1}{2}} & \text{for the culverts} \\ \alpha_{\mathrm{s}} L_{\mathrm{s}} \left(W(t) - H_{\mathrm{s}}\right)^{\frac{3}{2}} & \text{for the spillway} \end{cases} \tag{7.10}$$

where $\alpha_{\mathrm{c,s}}$: empirical hydraulic discharge coefficient of the culverts and the spillway, respectively [−], which is dependent on the design of the culvert inlets and the spillway crest; A_{c}: culvert inlet area [L^2] (which may be variable due to control, e.g., with a movable gate); $H_{\mathrm{c}_m,\mathrm{s}}$: elevation of the culvert inlet axes (i.e., of the projected inlet area's center of gravity) and the spillway crest, respectively [L]; and L_{s}: length of the spillway [L].

[1] This assumption is made in accordance with the construction report of the dam investigated herein (MAF, 1989).

For the culverts, Eq. (7.10) applies for submerged conditions. For part-full conditions, further discrimination of the flow situation is needed. There is no flow if the water level is lower than the culvert bottom. According to Chow (1959) and Vischer and Hager (1999), free surface flow conditions can be assumed if the water level is higher than the culvert bottom but lower than 1.2 times the culvert diameter. The free surface flow in the culverts is assumed to be normal and critical[1] and can be calculated for an ideally circular culvert with the relationship (Vischer and Hager, 1999)

$$Q_{\mathrm{out}_{\mathrm{c}_m}}(t) = \left(\frac{3\left(W(t) - (H_{\mathrm{c}_m} - \frac{1}{2}D_{\mathrm{c}})\right)}{5D_{\mathrm{c}}} \right)^{\frac{5}{3}} \left(gD_{\mathrm{c}}^5\right)^{\frac{1}{2}} \tag{7.11}$$

where D_{c}: culvert diameter [L]; and g: acceleration due to Earth's gravity [LT^{-2}].

Defining t_j as a specific point in time and integrating Eq. (7.8) by applying the trapezoidal rule with the discrete increment Δt leads to the storage equation in the form

$$\begin{aligned} &V(t_j + \Delta \mathrm{t}) = \\ &\quad V(t_j) + \frac{\Delta t}{2}\left(Q_{\mathrm{in}}(t_j) + Q_{\mathrm{in}}(t_j + \Delta t) - Q_{\mathrm{out}}(t_j) - Q_{\mathrm{out}}(t_j + \Delta t) - E(t_j) - E(t_j + \Delta t)\right) \end{aligned} \tag{7.12}$$

7.1.2.2 Iterative Solution of the Nonlinear Storage Equation

The nonlinear system (7.9);(7.12) is solved for $V(t_j + \Delta t)$ with a fixed-point iteration scheme, i.e., initially estimating $Q_{\mathrm{out}}(t_j + \Delta t)$ and iteratively improving this estimate until convergence is reached, regarding a specific precision criterion. This solution accounts for the nonlinear dependency of dam outflow, evaporation, and water level. More precisely, for estimating $Q_{\mathrm{out}}(t)$, it is feasible to use the water level $W(t)$ as the iteration variable, which is related to $Q_{\mathrm{out}}(t)$ and $V(t)$ via the dam hydraulic properties and morphological characteristics. Algorithm 7.2 shows a pseudocode implementation for the iterative calculation of the dam outflow. For the sake of clarity and brevity, evaporation is omitted in the pseudocode. In the full code, evaporation is estimated for every time step as a function of the water surface area (which is a function of the water level) and is then considered in the storage equation as an additional loss term.

7.1.2.3 Penman Evaporation Model

For the quantification of transient evaporation from the dam water surface, any arbitrary functional relationship can be included within the proposed modeling framework. To utilize the quite detailed available climate data (cf. Section 7.2.1), evaporation is calculated with the Penman model (Penman, 1948), which combines aerodynamic mass transport of evaporated water away from the liquid phase with an energy balance equation. A potential oasis effect is not taken into account. The Penman model reads

$$E(t) = \frac{sE_G + \gamma + v(e_0 - e)}{s + \gamma} A_{\mathrm{r}} \tag{7.13}$$

where $E(t)$: evaporation from the reservoir's surface [$\mathrm{L}^3\mathrm{T}^{-1}$]; $s(T)$: gradient of the saturated water vapor pressure curve [$\mathrm{ML}^{-1}\mathrm{T}^{-2}\Theta^{-1}$], with $T(t)$: temperature [Θ]; $E_G(t)$: evaporation equivalent of global radiation $G(t)$ [LT^{-1}]; $\gamma(T)$: psychrometric constant [$\mathrm{ML}^{-1}\mathrm{T}^{-2}\Theta^{-1}$]; $v(t)$: wind function,

[1] Which can easily be validated by calculating the Froude number of the flow as a function of the culvert water level, for example, by using the Manning-Strickler law and employing a culvert slope of 2 % and a culvert roughness coefficient of $K_{\mathrm{St}} = 62.5\,\mathrm{m}^{\frac{1}{3}} \cdot \mathrm{s}^{-1}$, both given by the dam engineering report (MAF, 1989).

Algorithm 7.2 Iterative Solution of the system of Eqs. (7.12);(7.9) with a fixed-point iteration scheme.

require: dam characteristics $V(W)$, $W(V)$, $Q_{\text{out}}(W)$ and inflow hydrograph $Q_{\text{in}}(t_j)$
EPS $= 10^{-4}$ ▷ Define iteration precision criterion
for $j = \Delta t : t_{\text{end}}$ **do** ▷ Loop over time
  $k = 1$ ▷ Set iteration counter
  $W^{(k-1)} = W(t_{j-1})$ ▷ Initially estimate water level from preceding time step
  repeat
    $Q_{\text{out}}^{(k-1)}$ from $Q_{\text{out}}(W)$ ▷ Calculate outflow corresponding to water level $W^{(k-1)}$
    $V^{(k-1)}$ from $V(W)$ ▷ Calculate storage volume corresponding to water level $W^{(k-1)}$
    $V^{(k)}$ from Eq. (7.12) ▷ Calculate new estimate of storage volume considering $Q_{\text{in}}(t_j)$
    $W^{(k)}$ from $W(V)$ ▷ Calculate new estimate of water level from volume $V^{(k)}$
    ICC $= \left|W^{(k)} - W^{(k-1)}\right|$ ▷ Calculate iteration convergence criterion
    $k = k + 1$ ▷ Update iteration counter
  until ICC $<$ EPS ▷ Compare ICC with EPS
end for
return: outflow hydrograph $Q_{\text{out}}(t_j)$, storage volume over time $V(t_j)$, and water level over time $W(t_j)$

dependent on site conditions and wind speed $w(t)$ [LT^{-1}]; $e_0(t)$: saturated water vapor pressure [$\mathrm{ML}^{-1}\mathrm{T}^{-2}$]; $e(t)$: actual water vapor pressure [$\mathrm{ML}^{-1}\mathrm{T}^{-2}$]; and $A_{\text{r}}(t)$: the water surface area of the reservoir [L^2].

The parameters of the Penman model can be calculated by obtaining temperature $T(t)$, actual vapor pressure $e(t)$, global radiation $G(t)$ [$\mathrm{ML}^2\mathrm{T}^{-3}\mathrm{L}^{-2}$], and wind speed $w(t)$ (for details see, e.g., Brutsaert, 1982). Basically, the saturated water vapor pressure can be estimated by employing the August-Roche-Magnus formula (August, 1828) which reads

$$e_0(t) = 6.11 e(t)^{\frac{17.62T(t)}{243.12 + T(t)}} \tag{7.14}$$

The gradient of the saturated water vapor pressure curve can then be calculated with the relationship

$$s(t) = e_0(t)\frac{4284}{243.12 + T(t)} \tag{7.15}$$

The psychrometric "constant" in Eq. (7.13) is actually not a constant but at least slightly dependent on the air pressure. Nevertheless, a constant value of $\gamma = 0.65\,\mathrm{hPa} \cdot \mathrm{K}^{-1}$, which is followed here, is often assumed since it is valid under normal atmospheric pressure conditions (1013 hPa). The evaporation equivalent of global radiation results from the water's latent heat of vaporization and can be calculated by using the relationship

$$E_G(t) = \frac{G(t)}{\iota} \tag{7.16}$$

with the conversion factor $\iota = 245\,\mathrm{J} \cdot \mathrm{cm}^{-1}$ when G is given in $\mathrm{J} \cdot \mathrm{cm}^{-2}$.

The wind function relates the measured wind speed to the wind speed at the evaporating surface, which is dependent on the elevation of the measurement (usually two meters above ground) and

the surface roughness. A logarithmic relationship is often assumed for the surface layer, i.e., the first 60 or 100 m of the planetary boundary layer[1], which reads

$$v(t) = w(t)\ln\frac{z_w}{z_0} \tag{7.17}$$

where z_w is the elevation of the wind speed measurement [L] and z_0 is the dynamic roughness length [L], which expresses the height above ground where the wind function becomes zero. For free water surfaces, this value is comparably small since the laminar surface boundary layer is thin. A typical value for z_0 over water is 0.0001 m, which is used within this thesis.

Within the dam simulation model, the total evaporation volume is calculated for every time step Δt, using the evaporation height $E(t)$ and the known relationship between the reservoir's water level $W(t)$ and the corresponding area of the evaporating water surface, $A_\mathrm{r}(t)$, which is derived a priori using dam morphology data.

7.2 Real-World Application of the Modeling System for an Arid Region

This section demonstrates the functionality and applicability of the wadi flow and dam simulation model for a case study under realistic data conditions. Before applying and validating the full modeling system for an extreme flood event in Wadi Ma'awil, two preliminary tasks are performed. First, a parameter sensitivity analysis is carried out in order to identify the sensitivity of process parameters which are associated with flow and transmission loss modeling. Second, the afore-identified parameters are estimated regarding their sensitivity and range. Finally, the full modeling system is used to simulate wadi flow and transmission loss dynamics, influenced by dam operation. The investigated 2007 event, caused by cyclonic storm Gonu (event 06/06/07), led to highest peak flow rates at Afi station and highest inflow volumes to Ma'awil Dam.[2] The operational storage capacity of the dam was totally filled and the spillway was activated.

To account for the insufficient data situation, the sensitive parameters are calibrated for a neighboring and morphologically very similar catchment and then transferred to the investigation area. In Wadi Ma'awil, downstream gauge data, which would be helpful for an empirical analysis of transmission losses, are lacking. Theoretically, an inverse reconstruction of event-related dam inflow would be possible on the basis of stage recorder data. Specifically for the investigation area, such an approach is questionable due to (a) the possibly very dynamic change of dam inflow rates, which is not resolved by the stage recorder since culvert outflow dynamics are comparably slow, and (b) the uncertain relationship of dam water level and outflow rates under spillway release conditions, caused by the high hydraulic capacity of the spillway.

To tackle these challenges, the proposed integrated modeling system is used to correlate upstream wadi flow data and stage recorder data of the downstream recharge dam. Dam operation parameters are taken from the dam engineering report and are assumed to be valid; they are, therefore, not subject to calibration. All relevant process parameters of the routing models are calibrated for the

[1] Mostly referred to as Prandtl boundary layer, named after Ludwig Prandtl.

[2] Following the definitions given by Graf (2002), the considered event would be classified as a single-peak event rather than as a flash flood event, since it was caused by a large tropical storm system and was not the consequence of smaller-scale convective rainfall.

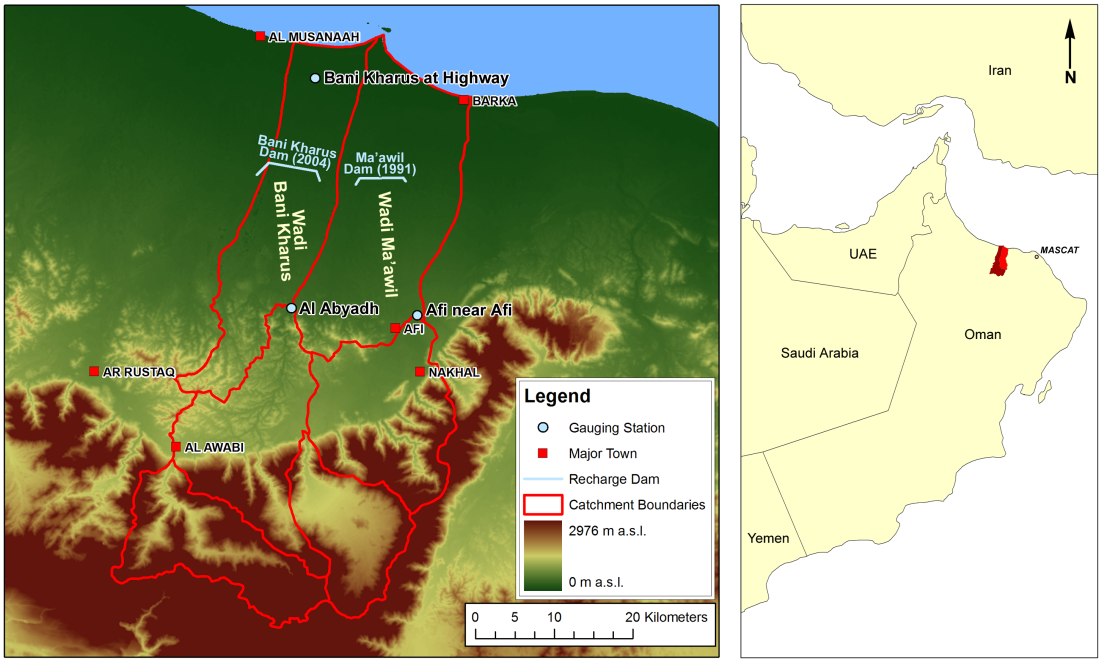

Figure 7.4: Overview map of the study area in Oman.

neighboring catchment of Wadi Bani Kharus, using data of two associated gauges from the period prior the year 2004 when Bani Kharus dam was constructed. Then, the parameters estimated in this way are transferred to Wadi Ma'awil. Finally, this parametrization is validated by routing the gauged flow to the dam, then simulating the dam operation and, finally, comparing the modeled dam water level development with stage recorder data.

7.2.1 Study Area and Available Data

The study area is located in the south-eastern Batinah Region, Sultanate of Oman (Fig. 7.4), and covers two catchments: Wadi Ma'awil (total area 835 km^2; Fig. 7.10) and Wadi Bani Kharus (total area 1,183 km^2; Fig. 7.5c). Both catchments are bordered by the Gulf of Oman in the north and by the Hajar Mountain Range in the south, which has peaks up to a height of 3,000 m a.s.l. A three to five kilometer broad strip along the coast is used for intensely irrigated agriculture, whereas the more remote parts of the coastal plain are nearly bare. Groundwater uptake for irrigation makes up over 50 % of total water use (Al-Shaqsi, 2004). Fresh water resources are scarce in the region and the coastal alluvial aquifer is threatened by over-abstraction and, consequently, saltwater intrusion. A progressive increase of irrigation water salinity caused a shifting of crop patterns away from the coastline (Fig. 7.5a). Traditionally, irrigated agriculture was established in the frontal area of the Hajar Range. A system of man-made channels routed water from the mountains to oases that mainly harvested dates and bananas for food, and maize and sorghum for fodder. These channels are called Aflaj (Fig. 7.5b) and guaranteed sustainable agriculture over centuries.

Rainfall of up to 350 $\mathrm{mm} \cdot \mathrm{a}^{-1}$ in the mountains and 50 $\mathrm{mm} \cdot \mathrm{a}^{-1}$ in the plain is strongly contrasted by a potential evaporation of approximately 2,000 $\mathrm{mm} \cdot \mathrm{a}^{-1}$. The variability of rainfall patterns in space and time is extreme, where relatively wet periods can be followed by extremely dry periods (Fisher, 1994; Wheater, 2002; McIntyre et al., 2007; Al-Rawas and Valeo, 2009). This

(a) Abandoned date plantation near the coastline (photo by Jens Grundmann, 2009).

(b) Aflaj channel in the Hajar Range (photo by Andy Philipp, 2011).

(c) Wadi Bani Kharus leaving the mountains (photo by Alexander Gerner, 2009).

(d) Alluvial wadi bed material (photo by Alexander Gerner, 2009).

Figure 7.5: Impressions of the study area.

is illustrated by Fig. 7.6, where the number of days with runoff per year is displayed for station Afi near Afi, situated in Wadi Ma'awil at the outlet of the mountains (Fig. 7.4). The flow regime in the neighboring catchment of Wadi Bani Kharus shows similar characteristics.

Flow is most often a consequence of convective rainfall in the mountains, leading to flash floods. Alternatively, tropical storm systems (cyclones) can cause heavy rainfall and severe flooding. During dry years, typically two or less events occur. After passing the mountain front, the surface flow enters the plain where ephemeral flood events have led to thick alluvial deposits (Fig. 7.5d). Usually a significant amount of flood flow can infiltrate through the wadi beds, which is supported by the infiltration conditions of the alluvium and the decreasing general slope in the plain. Nevertheless, especially during larger floods, fresh water is lost to the sea. Several groundwater recharge dams have been constructed in the Batinah plain in order to minimize these losses and to promote the replenishing of the coastal aquifer. A much more comprehensive summary of the study area's physical geography, lithology, hydrogeology, climate, and water balance, as well as associated primary data can be found in Al-Shaqsi (2004).

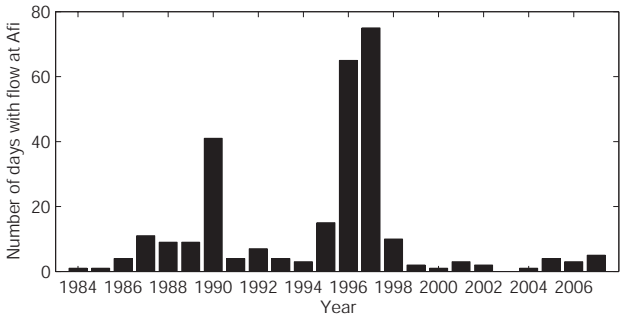

Figure 7.6: Number of days with flow at Afi gauging station, years 1984 to 2007.

Table 7.1: Summary of required input data for the full modeling system.

Data	Parameter(s)	Assessment	Notes
Wadi cross-sectional data	$\tilde{h}(x, A)$, $\tilde{R}(x, A)$; resp. $p_1(x)$, p_2, $p_3(x)$, p_4	Obtained from digital elevation model and aerial imagery	Cross-sectional data included via specific profile functions
Longitudinal profile	S_0†	Obtained from digital elevation model	Calculated from thalweg of cross sections
Channel roughness	K_{St}†	Calibration (based on flow observations)	Initial estimate from field assessment
Infiltration characteristics	k_{a}†, k_{k}†, k_{c}†	Calibration (based on observed transmission losses)	Infiltration modeled with empirical Kostiakov-Lewis model
Dam characteristics	$V(W)$, $A_{\mathrm{r}}(W)$, $\alpha_{\mathrm{c,s}}$, $H_{\mathrm{c}_m,\mathrm{s}}$, L_{s}, D_{c}	Engineering report of the dam	Outflow characteristics determinable a priori
Flow data	$Q(t)$	Obtained at gauging stations	Daily and sub-daily values, peak values
Dam water level over time	$W(t)$	Water level recorder	Timely-resolved data are scarce
Climate data	$T(t)$, $e(t)$, $G(t)$, $w(t)$	Seeb climate station	Evaporation modeled with Penman model

†Parameters are included in the analysis of parameter sensitivity.

A set of specific data is required for setting up the proposed modeling system. Required input data are: cross-sectional wadi profile parameters; corresponding general slopes of the upstream and downstream wadi sections; roughness coefficients of the wadi sections; parameters of the infiltration model; dam characteristics, including morphological, culvert and spillway characteristics; time series of inflow to the model domain; and climate data for evaporation modeling. Table 7.1 summarizes data requirements and gives information on data assessment for the application presented herein. The data situation is highlighted in the following.

Morphological Data: Morphological data of the wadis are derived from a digital elevation model (DEM). The publicly available and spaceborne-obtained ASTER (Advanced Spaceborne Thermal Emission and Reflection Radiometer) data sets (Abrams, 2000) are used. Cross-sectional cut lines are extracted from the DEM using GIS functionality and superimposed aerial imagery to capture typical flow widths. Figure 7.7 shows plots of the general profile of the main channels of Wadi Ma'awil (Fig. 7.7a) and Wadi Bani Kharus (Fig. 7.7b). Since there are two gauging stations located

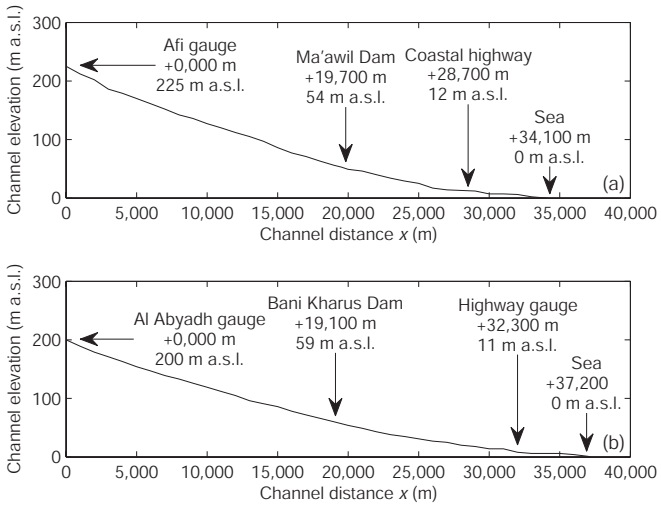

Figure 7.7: General profile plots. (a) Wadi Ma'awil between Afi gauging station and the Gulf of Oman, and (b) Wadi Bani Kharus between Al Abyadh gauging station and the Gulf of Oman.

along the lower reaches of Wadi Bani Kharus (stations Al Abyadh and Bani Kharus at Highway), flow data situation is generally better than for Wadi Ma'awil (with only station Afi near Afi[1]). Furthermore, Bani Kharus Dam was constructed in 2004 and, a significant portion of available flow data were, therefore, unaffected by dam operation, which allows for a direct estimation of transmission losses. This is not the case for Wadi Ma'awil, where most flow data were affected by dam operation and, furthermore, no valid downstream flow data are available.

Fluvial geomorphology of Wadi Ma'awil and Wadi Bani Kharus features wide cross-sectional profiles, which change only gradually in the downstream direction. Typically, effective flow widths range from 40 to 150 m, mainly depending on event magnitude. For minor events, a braided network of smaller wadi channels routes the flow, whereas major events tend to promote a better horizontal interconnection of flow-effective cross-sectional areas (Tooth, 2000). Wadi material is very heterogeneous in size and composition, ranging from stones to gravel to sand and silt, with the silt material in depressions of the bed. The general slope of Wadi Ma'awil between Afi gauging station and Ma'awil Dam is estimated to 0.00868 and 0.00375 downstream of the dam. The neighboring Wadi Bani Kharus exhibits a very comparable morphology (Fig. 7.7). Channel slope is estimated to 0.00738 for upper Wadi Bani Kharus (Al Abyadh gauging station to Bani Kharus Dam) and 0.00326 for the lower section (dam to sea).

Infiltrometry Data: Infiltrometry measurements were carried out in the area in order to assess suitable dam locations (MAF, 1985; MAF, 1990). Nevertheless, observed transmission losses in ephemeral channels tend to actually be lower than those inferred from infiltrometry tests (Wheater, 2002). Borehole analyses estimated the thickness of the upper gravel layer, which covers the deeper and more cemented alluvium, to 20 to 40 m. The alluvium extends down to -220 m a.s.l. in the area of Ma'awil Dam (MAF, 1990). MAF (1985) performed 60 double-ring infiltrometry tests which delivered mean infiltration rates from 0.744 to 4.920 $\mathrm{m \cdot d^{-1}}$ for a four-hour duration. Furthermore,

[1] Although there is another gauging station located at the coastal highway (cf. Fig. 7.7), data are lacking or available data cannot be used due to quality issues.

the study found that infiltration rates were highest ($>4.8\,\mathrm{m}\cdot\mathrm{d}^{-1}$) for recently reworked wadi materials, moderate (2.4 to $4.8\,\mathrm{m}\cdot\mathrm{d}^{-1}$) where sandy deposits were found, and lowest ($<2.8\,\mathrm{m}\cdot\mathrm{d}^{-1}$) where a denser surface texture was present.

MAF (1990) conducted a program of 68 four-hour double-ring infiltrometry tests in the area. Obtained mean infiltration rates ranged from 0.94 to $40.13\,\mathrm{m}\cdot\mathrm{d}^{-1}$ with a mean value of $11.16\,\mathrm{m}\cdot\mathrm{d}^{-1}$, while the maximum value was not used for the calculation of the mean value. Tests conducted at the surface and at 1 m depth did not show significant differences for measured infiltration rates. However, the tests suggest that infiltration rates will change during an event, e.g., as a consequence of event-specific sedimentation. In contrast, numerous authors modeled transmission losses in ephemeral rivers with a steady-state infiltration rate (e.g., Morin et al., 2009). It has to be proven if a timely-variable infiltration modeling might improve the portrayal of transmission losses for the specific application case.

Recharge Dam Data: The present study specifically addresses the recharge dam which was constructed in 1991, spanning Wadi Ma'awil with a length of 7.5 km. Figure 7.8 gives some impressions of the dam. Table 7.2 summarizes the main properties of Ma'awil Dam, obtained from the dam engineering report (MAF, 1989). Figure 7.9 shows the reservoir's morphological and hydraulic characteristics, respectively: $V(W)$, $A_\mathrm{r}(W)$, and $Q_\mathrm{out}(W)$, based on data provided by the dam operating authority and the engineering report. The maximum outflow was estimated to ca. $0.26\cdot10^6\,\mathrm{m}^3$ per day per culvert by the engineering report (ca. $3\,\mathrm{m}^3\cdot\mathrm{s}^{-1}$). The outflow relationship in Fig. 7.9b is calculated as lined out in the dam model section, using the parametrization given in Table 7.2.

The construction report estimates the reservoir's end-life dead storage to $1.6\cdot10^6\,\mathrm{m}^3$ after 30 years. An in-situ assessment in 2009 (18 years after dam construction) suggested that the construction report's estimate is too high; assuming a mean storage reduction of $0.053\cdot10^6\,\mathrm{m}^3\cdot\mathrm{a}^{-1}$, sedimentation would have reduced the storage capacity by approximately $1.0\cdot10^6\,\mathrm{m}^3$ until 2009. Referring to the dam's original storage curve (Fig. 7.9a), the sediment intake would have led to a sedimentation of parts of the culverts, which were not able to be observed in situ. Therefore, storage reduction due to sedimentation is at first neglected, but should be regarded with respect to the discussion of real-world results.

Surface Flow Data: For Wadi Ma'awil, surface flow data are available for Afi gauging station (Fig. 7.10). The employed records comprise 24 years (years 1984 to 2007) and exhibit characteristics, typical for arid dryland rivers. Figure 7.11 shows the flood frequency curve for Afi gauging station which features a steep gradient, resulting in very high ratios of the annual peak flow and the 100-year and 500-year flood beyond 25 and 40, respectively. The frequency distribution of the peak discharges is highly skewed, attributable to a high ratio of small to large events.

Gauging data with a temporal resolution of one hour are available for the years 1984 to 1995 and since 1996 with a resolution of five minutes. Within the 24 years of observation, 83 runoff events were observed. Six of 44 events from the years 1996 to 2007 can be fairly related to water level recorder data of Ma'awil Dam. For five of six events, only peak dam water levels are available. A reconstruction of total flow volumes at the dam site is only possible with stage recorder data which is resolved in a timely manner. The 2007 event caused by cyclonic storm Gonu (event 06/06/07) led to the highest observed peak flow rates ($881\,\mathrm{m}^3\cdot\mathrm{s}^{-1}$) and highest flow volumes ($15.156\cdot10^6\,\mathrm{m}^3$)

(a) View parallel to the longitudinal dam axis with the upstream face on the right-hand side. Mind the long, gabion-enforced spillway crest.

(b) View of the downstream wadi with coarser alluvial bed material, allowing pronounced infiltration.

(c) One of the dam's 10 culvert inlets.

(d) Stage gauge.

Figure 7.8: Impressions of Ma'awil Dam (photos by Alexander Gerner, 2009).

at Afi station. Ma'awil Dam's operational storage capacity was completely filled and the spillway was activated. Outflow volumes of the dam are coarsely estimated to ca. $14 \cdot 10^6\,\mathrm{m}^3$, using stage recorder data and reservoir characteristics, delivering the stage dependent outflow.

It is important to mention that although timely-resolved stage recorder data are available for event 06/06/07, the reconstruction of total retention and release of Ma'awil Dam—which would be of superior interest for the quantification of losses between Afi gauging station and the dam—is very uncertain. This is caused by the high hydraulic capacity of the spillway with a length of over 4 km. If the spillway is activated, the resolution of the recorded water levels allows merely for a loose estimation of actual spillway overflow and, therefore, of the dam's outflow balance. Moreover, available stage recordings for the event ended before the dam's storage was cleared.

Wadi Bani Kharus is gauged at the outlet of the mountains (Al Abyadh gauging station) and 32.3 km downstream at the coastal highway (station Wadi Bani Kharus at Highway), which permits an event-based connection of flow data. Nevertheless, highly-resolved data were lacking due to the fact that five-minute records are available as recently as 1997, which limits usable data unaffected

Table 7.2: Main properties of Ma'awil Dam (according to MAF, 1989 and MRMEWR, 2007).

Parameter	Value
Dam type	Gravel dam with asphalt concrete core
Dam crest height (m)	8.3
Dam crest length (m)	7,500 (including wing embankment)
Dam slope	2 : 1
Dam base width (m)	45.0
Design storage (10^6 m^3)	10.0
Spillway type	Broad-crested gabion weir
Spillway crest width (m)	5.0
Spillway crest length L_s (m)	4,040
Spillway crest elevation H_s (m a.s.l.)	59.00
Spillway discharge coefficient α_s	1.350
Spillway design flood ($m^3 \cdot s^{-1}$)	4,000 ($0.5 \cdot$ PMF)
Number of culverts M	10
Culvert type	Circular ductile pipe
Culvert diameter D_c (m)	0.8
Culvert inlet area A_c (m^2)	$\pi(0.5 \cdot D_c)^2 = 0.50265$
Culvert inlet axis elevations H_{c_m} (m a.s.l.)	54.36, 54.07, 54.53, 54.75, 54.07, 54.53, 54.53, 54.53, 54.07, 55.20
Culvert discharge coefficient α_c	2.726

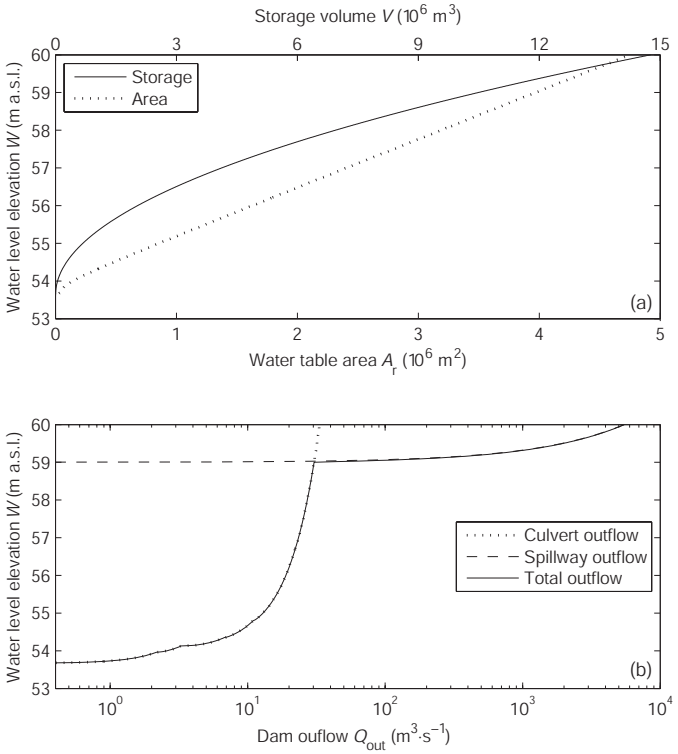

Figure 7.9: Morphological and hydraulic characteristics of Ma'awil Dam. (a) Storage volume V and water table area A_r as a function of water level elevation W, and (b) dam outflow Q_{out} as a function of water level elevation W.

Figure 7.10: Cross section of Wadi Ma'awil at Afi gauging station with the gauge in front (photo by Alexander Gerner, 2009).

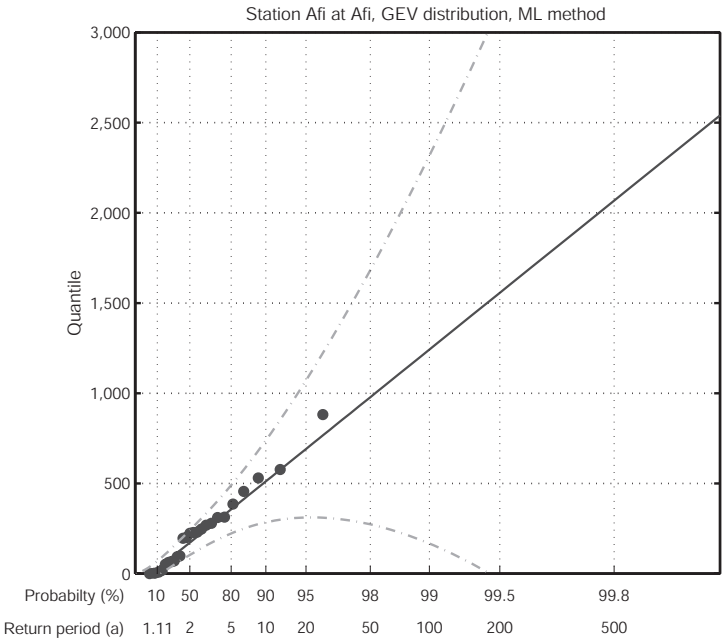

Figure 7.11: Flood frequency analysis for Afi gauging station, years 1984 to 2007. A generalized extreme-values (GEV) probability distribution function was fitted with a maximum likelihood (ML) estimation. Quantiles given in $m^3 \cdot s^{-1}$.

Table 7.3: Mean monthly climate data of station Seeb near Airport, years 1990 to 2010.

Month	Air temperature (°C)	Water vapor pressure (10^2 Pa)	Global radiation (10^6 J · m^2)	Wind speed (knots)
January	20.7	15.6	15.5	4.8
February	22.0	16.4	19.6	4.9
March	24.8	17.8	22.9	5.1
April	29.4	18.5	26.8	5.3
May	33.9	20.0	28.7	5.4
June	35.0	26.2	28.4	5.5
July	34.0	30.7	25.6	5.5
August	32.0	31.7	24.8	5.3
September	31.0	28.0	24.0	4.7
October	29.2	22.7	21.5	4.4
November	25.2	19.6	17.9	4.2
December	22.3	18.0	15.7	4.3

by dam operation (dam constructed in 2004) to the years of 1997 to 2003 (with approximately three events per annum). Gauging data of a least four flood events with a temporal resolution of five minutes can be correlated by roughly validating travel times between the two gauging stations. Additionally, the influence of lateral inflow can be excluded for these events by analyzing event-related rainfall patterns.

Climate Data: Climate data required for evaporation modeling are taken from Seeb International Airport station, located in the Batinah plain at 8.4 m a.s.l. at a distance of ca. 50 km east of the dam site and ca. 3 km to the coast. Available station records comprise daily values of temperature $T(t)$, water vapor pressure $e(t)$, global radiation $G(t)$, and wind speed $w(t)$ for the years 1990 to 2010 (Table 7.3). Thus, all relevant data for an event-related evaporation modeling with the Penman model are available. Actual daily values are used for evaporation modeling. Typical modeled event-related evaporation heights (Eq. 7.13) range from 3 to 10 mm · d^{-1}, which usually causes evaporation losses between only few to 25 % of retained flow volumes.

7.2.2 Parameter Sensitivity Analysis of the Integrated Modeling System

Before applying the modeling system for observed events in Wadi Ma'awil, the sensitivity of selected process parameters is estimated. A synthetic input hydrograph is routed with the full model under varied parameters and the results are subsequently compared. Each single parameter is altered ±30 % for each model run, whereas the remaining parameters are held to their respective initial values. The parameters of the dam simulation sub-model can be estimated with certainty by referring to the construction report of the dam and are excluded from the sensitivity analysis. Sensitivity is, therefore, checked for parameters referring to the hydrodynamic and infiltration models for the upstream and the downstream reaches. Parameters included in the analysis are indicated with a cross in Table 7.1.

Channel slope is assumed to be homogeneous for the whole wadi reach and is set to $S_0 = 0.00660$. The initial channel roughness was estimated to $K_{\mathrm{St}} = 30\,\mathrm{m}^{\frac{1}{3}} \cdot \mathrm{s}^{-1}$ during an in-situ assessment of wadi bed material in 2009, using tabulated values (Chow, 1959). The initial parameters of the Kostiakov-Lewis infiltration model ($k_{\mathrm{a}} = 0.8640$ and $k_{\mathrm{k}} = 7.7433 \cdot 10^{-5}\,\mathrm{m} \cdot \mathrm{s}^{-k_{\mathrm{a}}}$) are taken from a

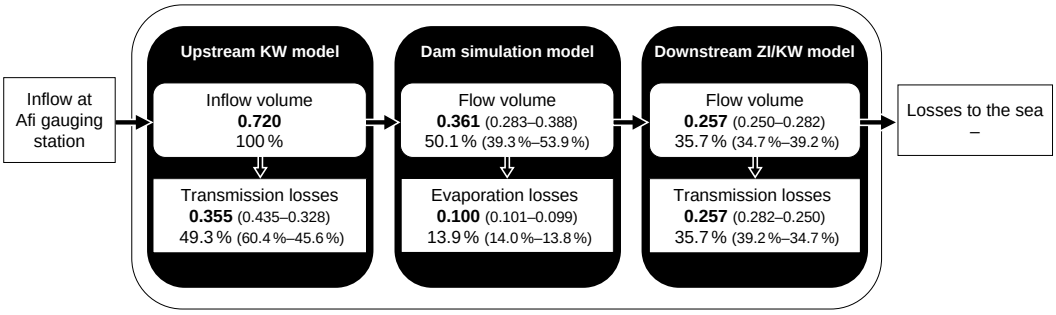

Figure 7.12: Results of the parameter sensitivity analysis. Initial values and mean upper and lower values of flow volumes and transmission/evaporation losses for a variation of selected process parameters of ±30 %. The values are given in $10^6\,\mathrm{m}^3$. The percentages relate the absolute values to the total inflow volume at Afi gauging station.

model fitted for infiltrometry tests in Wadi Ahin (Haimerl and Zunic, 2002), located 125 km west of Wadi Ma'awil (cf. Section 6.1.1.1), whereas the steady-state infiltration rate k_c is set to an initial value of $2.3148 \cdot 10^{-5}\,\mathrm{m \cdot s^{-1}}$, which equals $2.0\,\mathrm{m \cdot d^{-1}}$ and is, therefore, covered by the discussed infiltrometry data.

Spatial and temporal discretization of the upstream KW routing model are set to $\Delta x = 50\,\mathrm{m}$ and $\Delta t = 1\,\mathrm{s}$, respectively. The time step of the dam simulation model is set to $\Delta t = 60\,\mathrm{s}$. Further parametrization of the dam simulation model is carried out as outlined in the preceding section. The coupled ZI/KW downstream routing model is used for modeling culvert release flow. The spillway is not activated under the considered inflow conditions. The ZI/KW model is discretized with $\Delta x = 100\,\mathrm{m}$ in space and with an adaptive time step for the ZI component, and $\Delta t = 1\,\mathrm{s}$ for the KW component. To circumvent numerical oscillations, the upstream KW model is supplied with a low virtual baseflow rate of $0.1\,\mathrm{m^3 \cdot s^{-1}}$. Only flow above this level is taken into account for transmission loss modeling.

A synthetic triangular flow hydrograph of a two-hour duration and with a peak value of $200\,\mathrm{m^3 \cdot s^{-1}}$ (peak return period of ca. 2.5 years and a flow volume of $0.720 \cdot 10^6\,\mathrm{m}^3$) is implemented as the upper boundary condition at Afi gauging station and routed with the full modeling system. Mean climate data of Seeb station for the month of July are employed for evaporation modeling. Process parameter sensitivity is estimated with respect to flow arrival times, maximum extent of the infiltrating flow domain, transmission losses, and evaporation volumes. Table 7.4 and Figure 7.12 show the results of the sensitivity analysis.

All investigated parameters turned out to be sensitive to a certain degree. Channel roughness (coefficient K_St) has the strongest impact on arrival times, followed by bed slope S_0. Increased slope and decreased channel roughness (higher values of K_St) cause a faster advance of the flow. In contrast, the maximum extent of the infiltrating flow is only weakly controlled by channel slope and roughness. Increased slope and decreased roughness lead to a slight extension of the infiltrating flow domain. The final position of the flow domain is foremost determined by the parameters of the infiltration model, where k_a is dominant. For smaller values of k_a, less water infiltrates and the flow persists over a longer distance, and vice versa. The furthest extent is reached for k_a set to 0.6048 (−30 %) with the flow at station +31,800 m (sea at +34,100 m).

Table 7.4: Results of the parameter sensitivity analysis of the full modeling system under a total inflow of $0.720 \cdot 10^6 \mathrm{m}^3$ at gauging station Afi near Afi, Wadi Ma'awil.

		Δ (%)	S_0	K_{St} ($\mathrm{m}^{\frac{1}{3}} \cdot \mathrm{s}^{-1}$)	k_{a}	k_{k} (10^{-5} $\mathrm{m} \cdot \mathrm{s}^{-k_{\mathrm{a}}}$)	k_{c} (10^{-5} $\mathrm{m} \cdot \mathrm{s}^{-1}$)	Mean value
Upper parameter value		+30	0.0086	39.0	1.123	10.0663	3.0092	–
Initial parameter value		±0	0.0066	30.0	0.864	7.7433	2.3148	–
Lower parameter value		−30	0.0046	21.0	0.605	5.4203	1.6204	–
Arrival time		+30	2.1	2.0	∞	2.3	2.3	2.2
at Ma'awil Dam (+19,700 m)		±0	2.3	2.3	2.3	2.3	2.3	2.3
(h)		−30	2.5	2.8	2.2	2.3	2.3	2.4
Maximum extent		+30	24,900	25,200	17,100	23,700	23,800	22,980
of infiltrating flow		±0	24,700	24,700	24,700	24,700	24,700	24,700
(m)		−30	24,300	24,000	31,800	26,200	26,800	26,620
Arrival time at		+30	8.8	11.2	0.1	9.8	9.8	8.0
maximum extent of flow		±0	9.5	9.5	9.5	9.5	9.5	9.5
(days)		−30	8.5	10.2	9.0	9.1	9.9	9.4
	Transmission losses	+30	0.343	0.333	0.719	0.390	0.390	0.435
	Afi–Ma'awil Dam	±0	0.355	0.355	0.355	0.355	0.355	0.355
	(10^6 m^3)	−30	0.374	0.392	0.237	0.319	0.318	0.328
Upstream	Inflow	+30	0.376	0.386	0.000	0.326	0.327	0.283
KW	Ma'awil Dam	±0	0.361	0.361	0.361	0.361	0.361	0.361
model	(10^6 m^3)	−30	0.341	0.323	0.478	0.397	0.398	0.388
	Relative mass	+30	0.194	0.141	0.139	0.488	0.439	0.280
	balance error	±0	0.560	0.560	0.560	0.560	0.560	0.560
	(% of total inflow)	−30	0.680	0.641	0.635	0.489	0.598	0.609
	Evaporation	+30	0.100	0.101	–	0.098	0.098	0.099
	Ma'awil Dam	±0	0.100	0.100	0.100	0.100	0.100	0.100
	(10^6 m^3)	−30	0.099	0.098	0.104	0.101	0.101	0.101
Dam	Outflow	+30	0.269	0.281	–	0.225	0.225	0.250
simulation	Ma'awil Dam	±0	0.257	0.257	0.257	0.257	0.257	0.257
model	(10^6 m^3)	−30	0.238	0.221	0.369	0.292	0.292	0.282
	Relative mass	+30	0.888	0.639	–	0.569	0.549	0.661
	balance error	±0	0.556	0.556	0.556	0.556	0.556	0.556
	(% of total inflow)	−30	0.646	0.706	0.677	0.630	0.563	0.644
	Transmission losses	+30	0.269	0.281	–	0.225	0.225	0.250
	Ma'awil Dam–sea	±0	0.257	0.257	0.257	0.257	0.257	0.257
Down-	(10^6 m^3)	−30	0.238	0.221	0.369	0.292	0.292	0.282
stream	Losses to	+30	0.000	0.000	–	0.000	0.000	0.000
coupled	the sea	±0	0.000	0.000	0.000	0.000	0.000	0.000
ZI/KW	(10^6 m^3)	−30	0.000	0.000	0.000	0.000	0.000	0.000
model	Relative mass	+30	0.057	0.058	–	0.067	0.067	0.062
	balance error	±0	0.043	0.043	0.043	0.043	0.043	0.043
	(% of total inflow)	−30	0.042	0.057	0.026	0.095	0.091	0.062
Overall relative error		+30	1.025	0.723	0.139	0.990	1.055	0.786
of full modeling system		±0	1.159	1.159	1.159	1.159	1.159	1.159
(% of total inflow)		−30	1.368	1.290	1.338	1.025	1.252	1.255

Total transmission losses are influenced most strongly by the parameters of the infiltration model. The parameter k_a again shows the highest sensitivity. Looking at Eq. (6.1), it is obvious that, if k_k approaches zero, the influence of k_a disappears and actual infiltration rates equal the steady-state infiltration rate k_c. In turn, a value of $k_a = 1$ also leads to a constant modeled infiltration rate. Therefore, the sensitivity of the infiltration model parameters changes depending on their initial values. For k_a set to 1.1232 (+30 %), infiltration *increases* from the start. This leads to a total consumption of surface flow before Ma'awil Dam is reached. The flow is consumed by infiltration after ca. 2.5 h and reaches station +17,100 m for this specific model run, whereas Ma'awil Dam is located at station +19,700 m. This result of the upstream routing sub-model is affected by some uncertainties due to a transmission loss quota of 100 %. These uncertainties are a consequence of neglecting infiltration in the momentum equation of the incorporated kinematic wave equations and their numerical solution during the advance phase of the flow.

Although transmission losses and arrival times are comparably variable, evaporation volumes simulated by the dam model only slightly differ for the considered scenarios. Besides the climatic forcing, evaporation is dependent on the development of the dam water level over time. Since outflow rates of the dam are low compared with inflow rates, evaporation is almost completely related to the maximum water level elevation caused by an event, which consequently determines how long the evaporating water table persists. Due to the positive dependency of water level area and water level elevation, evaporation volumes are slightly higher for higher inflow volumes, and vice versa. For the scenarios incorporated in the sensitivity analysis, the relative portion of evaporation is around 14 % of total inflow volume. This—in comparison with evaporation estimates of observed events (cf. Strobl and Haimerl, 1999)—rather high value is caused by the moderate dam inflow volumes and the pronounced forcing of the employed climate data from the month of July.

For the downstream wadi section, all available water infiltrates before reaching the sea (station +34,100 m) for every investigated parameter combination due to slow culvert release. Taking into account the similar dam evaporation for all scenarios, higher upstream transmission losses cause lower dam inflows and, therefore, lower downstream transmission losses. This leads to an only seemingly contradictory influence of parameter variations on transmission losses for the upstream and the downstream wadi sections. The maximum extent of the flow domain is typically reached after a couple of days, which is the case if total infiltration rates equal inflow rates for the wadi downstream of the dam. Generally, higher inflow rates lead to a faster advance of the flow. The incorporated ZI/KW model for routing the dam culvert outflow is capable of accurately portraying such weak process dynamics in the initially dry wadi. This is reflected in an exact solution for the extending flow domain together with very small mass balance errors.

The overall relative mass balance errors in Table 7.4 are calculated for every investigated parameter combination by comparing the sum of transmission losses upstream and downstream of the dam, dam evaporation, as well as losses to the sea with the total inflow of $0.720 \cdot 10^6\,\mathrm{m}^3$. The errors range between 0.139 % and 1.368 % for the investigated parameter variations. This yields the full model's mean relative mass balance error to be ca. 1.1 % of total inflow. Looking at the relative errors of the incorporated sub-models, it is obvious that all models perform well with respect to mass conservation. The downstream ZI/KW model features the lowest mass balance errors, which is supported by the advance model's analytical character. The errors of the ZI/KW model range between 0.026 % and 0.095 % of total inflow. The KW model for the upstream wadi reaches causes mass balance errors between 0.139 % and 0.680 %, which is a consequence of its

approximate numerical model solution. The dam simulation model shows slightly higher deviations with mean errors between 0.549 % and 0.888 %. These errors mainly emerge from the iterative solution of the dam retention equation.

7.2.3 Optimization-Based Process Parameter Estimation

The KW routing model is now applied for simulating flood wave movement and transmission losses for the westerly adjacent, morphologically similar, and well-monitored catchment of Wadi Bani Kharus (cf. Figs. 7.4 and 7.7b) for events of the period prior the construction of Bani Kharus Dam in the year 2004. This is performed in terms of an inverse modeling in order to obtain a robust estimate of wadi channel roughness and infiltration parameters, which can then be adopted for flow simulations in Wadi Ma'awil. Channel slope and cross-sectional profiles are estimated as outlined previously. The comparably pronounced slope of $\gg 0.001$ and the missing weakening influence of dam operation on flow dynamics make the KW model applicable for the considered wadi reach between the stations Al Abyadh and Bani Kharus at Highway (Ponce, 1991). The spatial and temporal discretization of the routing model are set to $\Delta x = 50\,\mathrm{m}$ and $\Delta t = 1\,\mathrm{s}$, respectively. As for the sensitivity analysis, the numerical KW model is charged with a very low initial base flow rate of $0.1\,\mathrm{m}^3 \cdot \mathrm{s}^{-1}$ to impede numerical oscillations.

The employed KW model is calibrated for one of the available four events (03/27/97, cf. Table 7.5) with respect to channel roughness K_{St} (according to Manning-Strickler) and Kostiakov-Lewis parameters k_{a}, k_{k}, and k_{c}. Regarding flow volumes and peak flow rates, the smallest event is chosen for calibration to challenge the model's extrapolation ability in the subsequent validation. Calibration is performed simultaneously for the four considered parameters using the CMA-ES methodology, an evolutionary-strategy optimization technique based on covariance matrix adaption (Hansen, 2006). The root-mean-square error (RMSE), calculated from the simulated and the gauged flow hydrograph at the highway station, is used as a performance criterion for the CMA-ES algorithm:

$$\mathrm{RMSE} = \sqrt{\frac{\sum_{1}^{O} \left(Q_{\mathrm{obs}} - Q_{\mathrm{sim}}\right)^2}{O}} \tag{7.18}$$

where $Q_{\mathrm{obs}}(t)$ and $Q_{\mathrm{sim}}(t)$: observed and simulated flow at a specific station x [$\mathrm{L}^3\mathrm{T}^{-1}$]; and O: number of flow observations [−].

Furthermore, the Nash-Sutcliffe model efficiency coefficient (Nash and Sutcliffe, 1970) is used to evaluate model quality, defined by

$$\mathrm{NSE} = 1 - \frac{\sum_{1}^{O} \left(Q_{\mathrm{obs}} - Q_{\mathrm{sim}}\right)^2}{\sum_{1}^{O} \left(Q_{\mathrm{obs}} - \overline{Q_{\mathrm{obs}}}\right)^2} \tag{7.19}$$

where $\overline{Q_{\mathrm{obs}}(t)}$: mean value of observed flow at a specific station x [$\mathrm{L}^3\mathrm{T}^{-1}$].

Roughness and infiltration parameters are calibrated to $K = 26.67\,\mathrm{m}^{\frac{1}{3}} \cdot \mathrm{s}^{-1}$, $k_{\mathrm{a}} = 0.5406$, $k_{\mathrm{k}} = 9.9980 \cdot 10^{-4}\,\mathrm{m} \cdot \mathrm{s}^{-k_{\mathrm{a}}}$, and $k_{\mathrm{c}} = 5.5198 \cdot 10^{-7}\,\mathrm{m{\cdot}s^{-1}}$. The calibrated value of the roughness coefficient coincides with a coarse bed material and might be an indicator of strong sediment transport processes. A NSE of 0.9719 indicates a nearly perfect convergence of modeled and gauged

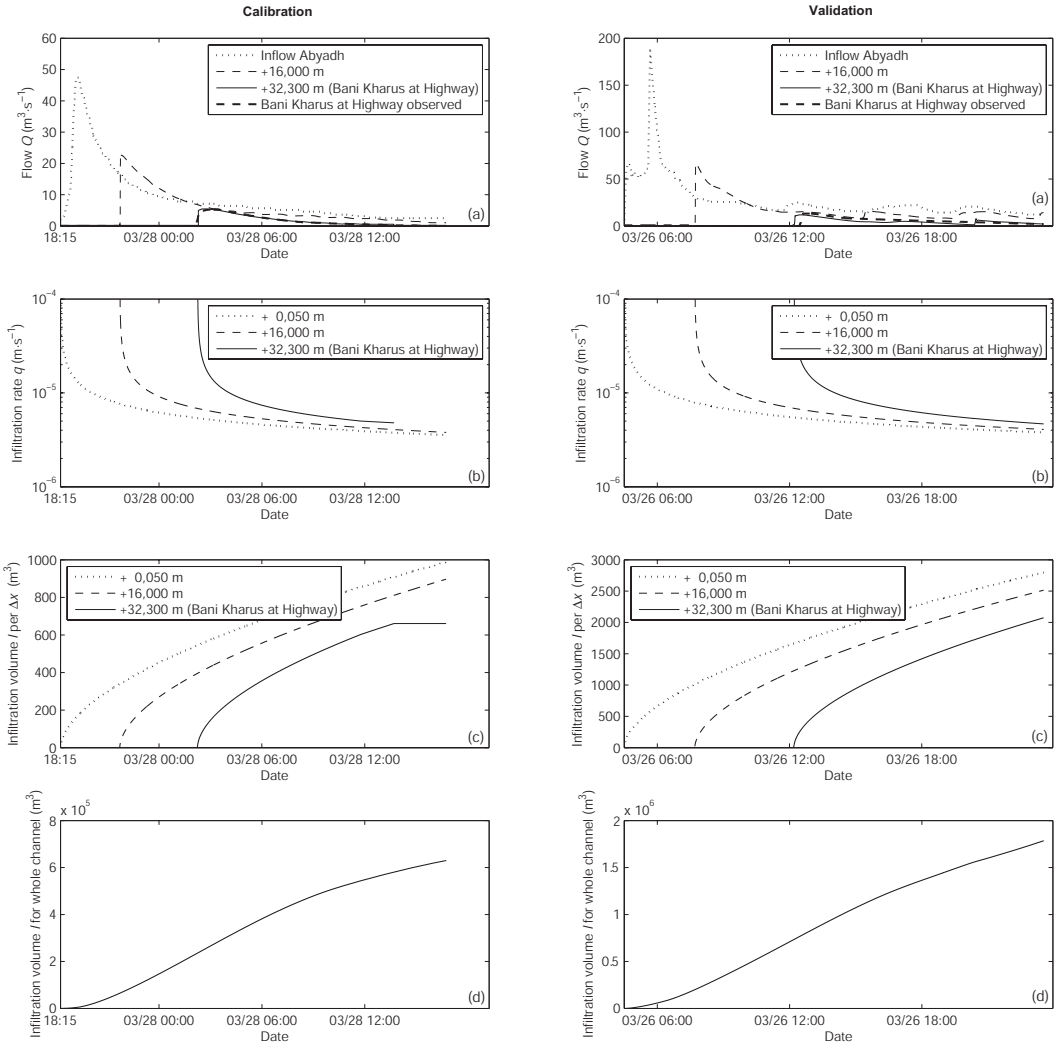

Figure 7.13: Modeling results of the kinematic wave flood routing model for Wadi Bani Kharus. Left column: calibration event 03/27/97. Right column: validation event 03/26/97. (a) Flow hydrographs at different channel locations; (b) infiltration rates over time at different channel locations; (c) cumulative infiltration volumes over time at different channel locations; (d) cumulative infiltration volumes over time for the whole channel reach Abyadh–sea.

flow, which can also be seen from Fig. 7.13a, left column, where observed and modeled flow nicely match at station Bani Kharus at Highway. For the calibration event, flow is consumed by infiltration ca. 11 h after the arrival of the flow at the highway station, which is reflected by the respective graphs of the infiltration rate (b) and the cumulative infiltration volume over time (c). Due to persisting inflow to the model domain, water still infiltrates in the more upstream channel sections, which can be seen from the graph of infiltration volumes over time for the whole channel (d). Observed transmission losses are just slightly underestimated by 0.8 % and the flow arrival time at the highway station is overestimated by 10 min (cf. Table 7.5). Furthermore, peak flow rates are accurately modeled (overestimation of 5.8 %).

Validation is carried out for three events of the year 1997 (03/26/97, 03/30/97a, and 03/30/97b). Table 7.5 summarizes the main results of the validation model runs. Graphical results are shown

Table 7.5: Overview of calibration and validation results of the kinematic wave flood routing model for Wadi Bani Kharus between stations Al Abyadh and Bani Kharus at Highway (TL: transmission losses; calibration event: 03/27/97; times are rounded to five-minute increments).

	Peak flow date at Abyadh			
	03/26/97	03/27/97	03/30/97a	03/30/97b
NSE at highway	0.4373	0.9719	−4.1332	0.4994
RMSE at highway ($m^3 \cdot s^{-1}$)	2.6001	0.2819	8.1391	1.6983
Inflow volume at Abyadh ($10^6\,m^3$)	1.8415	0.7073	1.1227	1.2868
Flow volume observed at highway ($10^6\,m^3$)	0.2422	0.0887	0.1689	0.1180
Flow volume modeled at highway ($10^6\,m^3$)	0.2089	0.0943	0.3508	0.1631
Observed TL Abyadh–highway (% of total inflow)	86.8	87.5	85.0	90.8
Modeled TL Abyadh–highway (% of total inflow)	88.7	86.7	68.8	87.3
Observed peak flow at highway ($m^3 \cdot s^{-1}$)	13.2	5.2	10.9	7.6
Modeled peak flow at highway ($m^3 \cdot s^{-1}$)	11.8	5.5	30.4	9.3
Arrival time lag modeled–observed at highway (min)	−15	+10	+10	+10

exemplarily for event 03/26/97 in the right column of Fig. 7.13. With a peak flow rate of $190\,m^3 \cdot s^{-1}$—compared with less than $50\,m^3 \cdot s^{-1}$ for the calibration event—the physically-based routing model is operated in its extrapolation domain. A NSE of 0.4373 usually indicates that the model only acceptably simulates the flow observations. Nevertheless, flow volume and peak rate observations at the highway station ($0.2422 \cdot 10^6\,m^3$ and $13.2\,m^3 \cdot s^{-1}$) are adequately met by the model ($0.2089 \cdot 10^6\,m^3$ and $11.8\,m^3 \cdot s^{-1}$). The arrival time lag between observation and model output is 15 min. Additionally, the dynamics of the hydrograph's falling limb are soundly matched. This shows that the rather low NSE is mainly caused by the phase differences of modeled and observed rising hydrograph values. Moreover, the NSE is not calculated over the whole simulation period but only starting from the onset of the flow, whereas including the preceding zero values would apparently improve the NSE. For flash flood routing under intense transmission losses, such validation results are very encouraging. It should be pointed out that despite the fact that total infiltration volumes are higher compared with the calibration event (mainly due to broader flow widths), arrival times of the infiltrating flow are similar (cf. Fig. 7.13). This coincides, e.g., with the findings of Mudd (2006).

Validation events 03/30/97a and 03/30/97b both belong to a single event which features two independent peaks and extends over two days. Results are again presented in Table 7.5. The model validation for event 03/30/97a leads to a rather low NSE of −4.1332 due to flow volumes and, therefore, transmission losses are not adequately modeled. Transmission losses are underestimated by 16.2 % and the peak flow rate is overestimated by almost a factor of three. Nevertheless, dynamics of the flow at the highway station are acceptably met, which can be seen from a slight overestimation of the flow arrival time of 10 min. In contrast, event 03/30/97b is, again, quite soundly modeled with respect to volume, peak flow, and arrival time at the highway station (NSE = 0.4994, underestimation of transmission losses of 3.5 %, overestimation of peak flow of 22.4 %, arrival time lag of 10 min).

With the exception of event 03/30/97a, modeled transmission losses and flow dynamics nicely match the observations. For the investigated events, flow volumes are comparably low and, vice versa, transmission losses are high, which causes mass balance errors of slightly over 1 %. Modeled transmission losses range between 68.8 % and 88.7 % of total inflow, whereas observed transmission losses range between 85.0 % and 90.8 %. Nevertheless, the validation results suggest that the

calibrated set of roughness coefficient and infiltration parameters delivers a robust model parametrization, which is representative for a realistic range of event magnitudes and characteristics. The derived parameter set can, therefore, be transferred to the neighboring catchment of Wadi Ma'awil, for which this parametrization is subsequently validated.

7.2.4 Model Application for Wadi Ma'awil

The presented wadi flow and dam simulation model—consisting of the hydrodynamic models for the upstream and the downstream wadi reaches and the dam simulation model—is now applied for the most extreme runoff event ever observed in the Batinah area. The flood event caused by cyclonic storm Gonu in June 2007 led to the highest observed flows at Afi gauging station. Flow observations with a temporal resolution of five minutes are used as the upper boundary condition for the upstream KW model. Cross-sectional and longitudinal data are extracted from the ASTER DEM as outlined previously. Roughness and infiltration parameters are transferred from the neighboring catchment of Wadi Bani Kharus as shown in the preceding section. This also applies for the downstream ZI/KW routing model.

Spatial and temporal discretization of the upstream and downstream routing models are again set to $\Delta x = 50\,\mathrm{m}$ and $\Delta t = 1\,\mathrm{s}$, respectively. An initial flow rate of $0.1\,\mathrm{m}^3 \cdot \mathrm{s}^{-1}$ is applied for the upstream KW model. The temporal resolution is adaptive for the downstream ZI component. The dam model's outflow is used as an upper boundary condition for the downstream ZI/KW model. The advancing culvert outflow is modeled with the ZI component, whereas dam outflow influenced by spillway release is modeled with the KW equations. The same applies for the recession of the flow domain. The parameters of the dam retention model are adopted from the dam engineering report (Table 7.2). Evaporation is calculated using actual climate data of Seeb station. The time step of the dam simulation model is set to $\Delta t = 60\,\mathrm{s}$.

The results of the upstream hydrodynamic model are shown in Fig. 7.14. The pronounced dynamics of this event are reflected in a surging flow with a modeled arrival time of the strongly rising limb of ca. 1.5 h and a peak propagation time of ca. 1 h between Afi gauging station (+0,000 m) and Ma'awil Dam (+19,700 m). Due to generally high flow volumes and low infiltration opportunity times, modeled transmission loss quotas are comparably low for the upper wadi section. The inflow volume to the dam is modeled to $14.299 \cdot 10^6\,\mathrm{m}^3$, which is 94.3 % of total inflow to the model domain ($15.156 \cdot 10^6\,\mathrm{m}^3$). Transmission losses in the upstream section are modeled to $0.813 \cdot 10^6\,\mathrm{m}^3$, which is 5.4 % of total inflow. As already discussed in the error analysis section, the given values are affected by small mass balance errors (<0.3 % of total inflow volume). Flow is significantly higher than zero after the start of the simulation at 06:00 UTC. Therefore, infiltration starts right away and—together with increasing flow widths—initially consumes a large portion of the flow. Nevertheless, total flow volumes are low in the first three hours of the event, which limits infiltration and causes only slowly rising total infiltration volumes (Fig. 7.14f).

Figure 7.15 shows the results of the consecutive dam simulation model. For the investigated event, the total outflow of the dam is modeled to $14.166 \cdot 10^6\,\mathrm{m}^3$ (93.5 % of total inflow volume) and total evaporation to $0.133 \cdot 10^6\,\mathrm{m}^3$ (0.9 % of total inflow volume). Again, the values are affected by small mass balance errors (<0.1 % of total inflow volume). Since the inflow of Ma'awil Dam is not gauged, stage recorder data are used for model validation. For this purpose, the modeled and the recorded water level development over time are compared. Stage recorder data are available in form

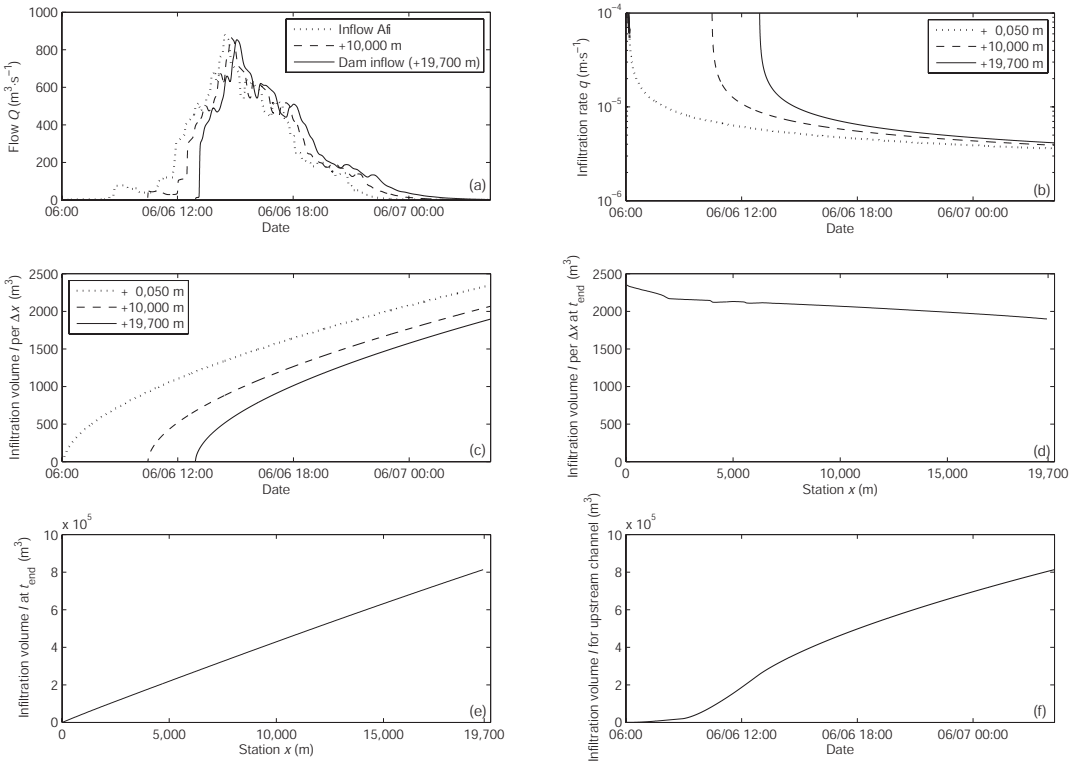

Figure 7.14: Modeling results of the upstream kinematic wave flood routing model for Wadi Ma'awil, Afi station to Ma'awil Dam, event 06/06/07. (a) Flow hydrographs at different channel locations, as well as inflow hydrograph to Ma'awil Dam; (b) infiltration rates over time at different channel locations; (c) cumulative infiltration volumes over time at different channel locations; (d) cumulative infiltration volumes over time for every spatial increment of the channel; (e) cumulative infiltration volumes at the end of the simulation over the channel reach; (f) cumulative infiltration volumes over time for the channel reach Afi–dam.

of an analog limnigraph sheet which was digitized by hand. The peak inflow rate of $853\,\mathrm{m}^3 \cdot \mathrm{s}^{-1}$ is retained to $237\,\mathrm{m}^3 \cdot \mathrm{s}^{-1}$ in the dam outflow. Modeled peak water level is 59.11 m, whereas the recorded peak is 59.09 m. Modeled outflow continues for over eight days until the dam is cleared.

Unfortunately, the available limnigraph sheet ends before the dam is empty. Due to the very high hydraulic capacity of the spillway, water level recordings above 59 m a.s.l. (elevation of the spillway crest) only allow for a coarse estimation of the dam outflow over time and, therefore, outflow volumes. Nevertheless, the recorded limnigraph is quite adequately matched by the dam simulation model (Fig. 7.15c) and the initial estimate of the event-related outflow volume of ca. $14 \cdot 10^6\,\mathrm{m}^3$ can be validated (cf. Section 7.2.1). This supports not only the chosen parametrization of the dam model, but foremost the reasonable estimates of inflow volumes and inflow dynamics, delivered by the upstream KW model. These findings effectively validate the routing and infiltration parameters of the upstream KW model, which were calibrated for the neighboring catchment of Wadi Bani Kharus.

Furthermore, the reservoir simulation results confirm that the initial assumption that only a small amount of the storage volume is ineffective for flood retention due to sedimentation is feasible, since the minimum recorded dam water level is below 54 m a.s.l. which renders the maximum

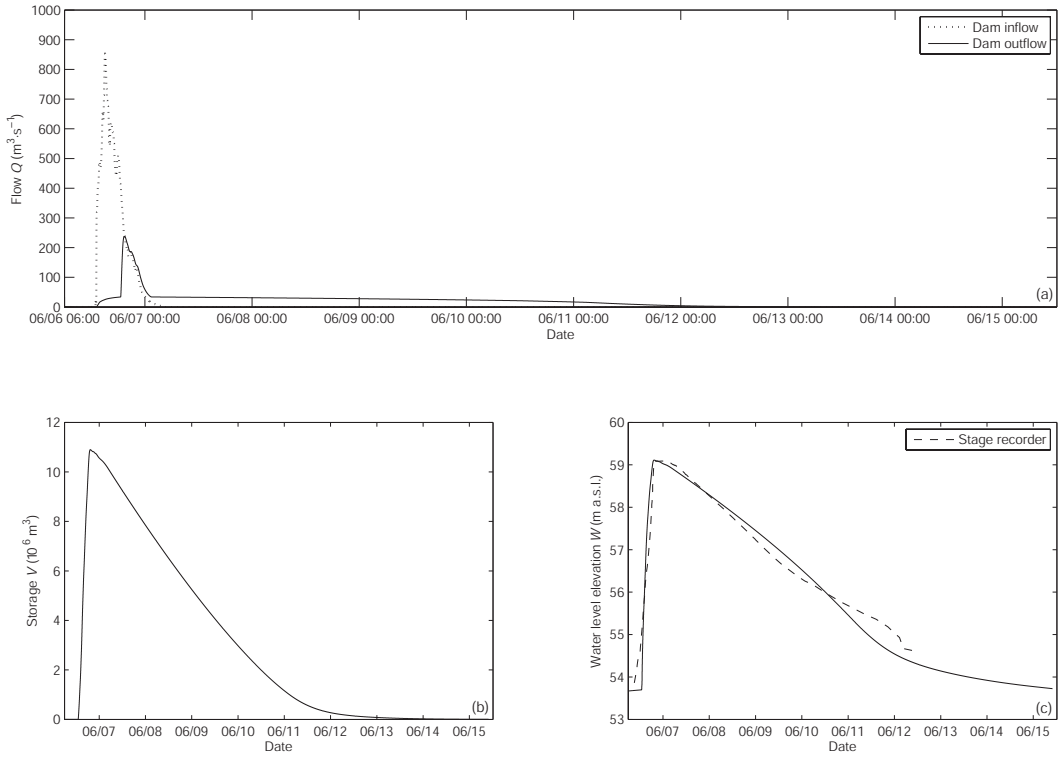

Figure 7.15: Results of the dam simulation model for Ma'awil Dam, event 06/06/07. (a) Inflow and outflow over time; (b) development of retained flow volume over time; and (c) comparison of the modeled and recorded water level over time.

possible dead storage volume to be less than $0.03 \cdot 10^6\,\mathrm{m}^3$. This is only 0.3 % of the design storage, according to dam morphology data (cf. Fig. 7.9a) and, therefore, does not significantly impact the results presented herein. However, if an operational application of the modeling system is intended, a reassessment of dam morphology data, including a dead storage estimation, is strongly recommended.

Figure 7.16 shows the results of the downstream coupled ZI/KW model. For the investigated extreme event, a significant portion of flow is lost to the sea. Losses to the sea are modeled to $11.762 \cdot 10^6\,\mathrm{m}^3$ (77.6 % of total inflow volume) and transmission losses to $2.403 \cdot 10^6\,\mathrm{m}^3$ (15.9 % of total inflow volume). However, the initial advance of the flow domain towards the sea is a consequence of culvert release. The sea is reached at ca. 20:00 UTC on 06/06/07 (Fig. 7.16a). This advance is controlled by the nonlinear interaction of flow dynamics and infiltration, which in turn affects flow volumes and momentum, and it is therefore possible for it to be adequately modeled by the proposed analytical ZI model component. Less extreme events would feature weaker downstream dynamics, which would pose a stronger indication for the ZI advance model. Nevertheless, the investigated event is the only one with sufficient data available.

The spillway is activated between 20:25 UTC on 06/06/07 and 04:15 UTC on 06/07/07, leading to a very dynamic outflow which is routed with the KW component. The remaining culvert outflow persists over days and, therefore, establishes a major portion of the transmission losses (ca. 85 %). As seen in Fig. 7.16c, the infiltrating flow domain starts receding in the upstream direction after a certain time. This happens when inflow rates are lower than infiltration rates. Flow and, therefore,

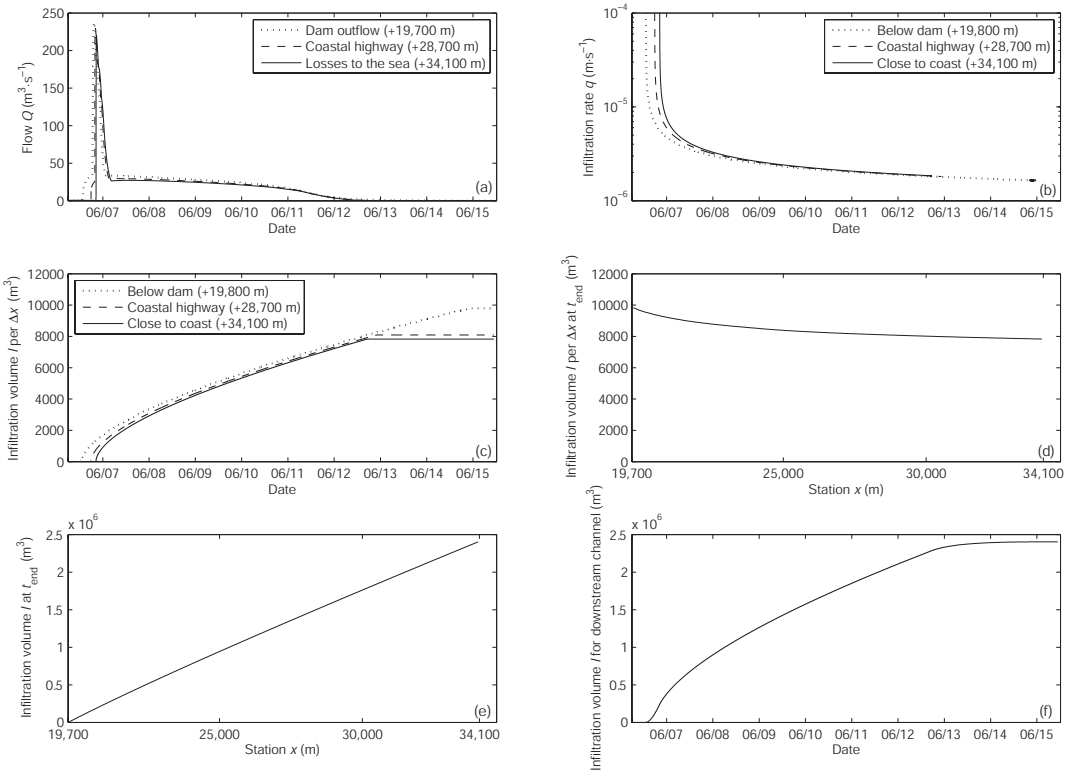

Figure 7.16: Modeling results of the downstream coupled zero-inertia/kinematic wave hydrodynamic model for Wadi Ma'awil, Ma'awil Dam to the Sea of Oman, event 06/06/07. (a) Outflow hydrograph of Ma'awil Dam and flow hydrographs at different channel locations; (b) infiltration rates over time at different channel locations; (c) cumulative infiltration volumes over time at different channel locations; (d) cumulative infiltration volumes over time for every spatial increment of the channel; (e) cumulative infiltration volumes at the end of the simulation over the channel reach; (f) cumulative infiltration volumes over time for the channel reach dam–sea.

infiltration ceases at a specific point, which shifts upstream over time. According to the results of the incorporated KW model, recession begins close to the coast after ca. 6.5 days and lasts for two days until infiltration ceases directly below the dam. Advance and recession trajectories calculated with the ZI/KW model are shown in Fig. 7.17.

The presented modeling results for the downstream reach are affected by very small mass balance errors (less than 0.01 % of total inflow volume). Despite the dynamic character of the investigated event—with spillway operation and losses to the sea—relative errors are not higher than for the scenarios investigated in the sensitivity analysis. This is mainly due to higher total flow volumes which leads to lower transmission loss quotas and, therefore, lower relative mass balance errors. Figure 7.18 shows the overall volume balance of the investigated event. The full model's total mass balance error is ca. 0.3 % of total inflow volume and is calculated by comparing the inflow at Afi to the sum of transmission losses, evaporation losses, and losses to the sea. Although total transmission loss quotas are comparably low (21.3 % of total inflow), absolute values ($3.216 \cdot 10^6$ m^3) are high compared with flow volumes of other gauged events.

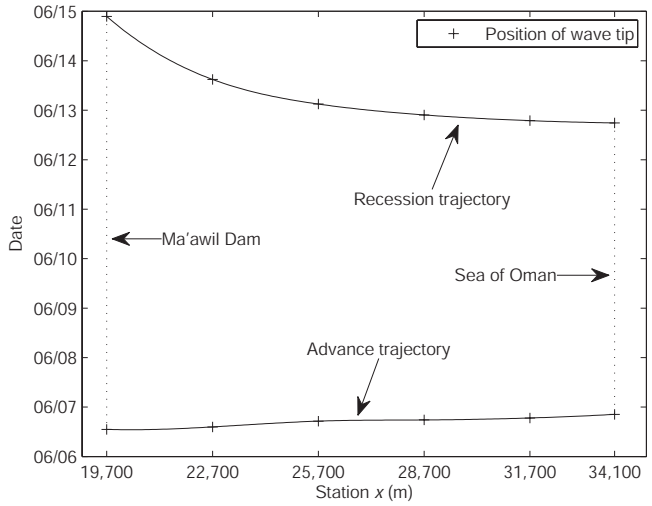

Figure 7.17: Advance and recession trajectories calculated with the downstream ZI/KW model for Wadi Ma'awil, Ma'awil Dam to the Sea of Oman, event 06/06/07.

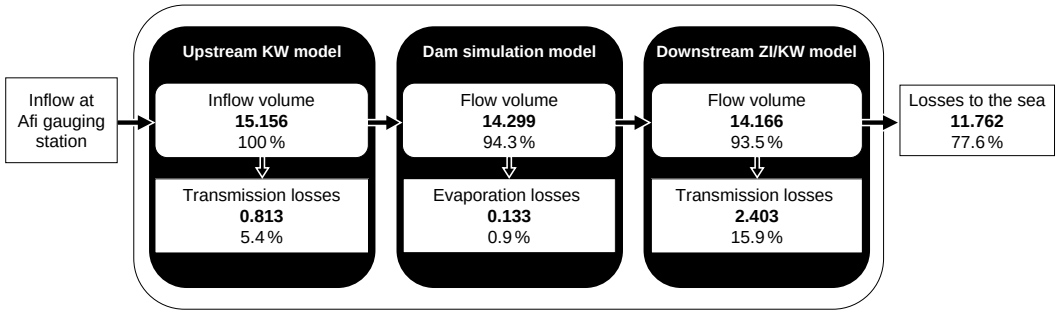

Figure 7.18: Modeling results of the wadi flow and dam simulation model for Wadi Ma'awil, event 06/06/07. The absolute values are given in 10^6 m^3. The percentages relate the absolute values to the total inflow volume at Afi station.

7.3 Summary

This chapter presented a comprehensive and process-oriented modeling system for routing ephemeral river flow under the influence of a groundwater recharge dam. A special focus of model development was set on the representation of intricate process dynamics under significant transmission losses. It was possible to soundly model flow and infiltration dynamics downstream of the recharge dam by implementing an analytical ZI model for the flow advance phase, as derived in Section 5.1 and tested in Section 6.1. Flow under zero-advance conditions and the successive flow recession was considered as quasi-steady flow with a rectified water surface profile (i.e., $\frac{\partial h}{\partial x} = 0$) and it was, therefore, possible to model them successfully with a kinematic wave approach.

Besides accounting for dam release flow, the proposed integrated modeling framework holds modeling components for simulating both the dam inflow dynamics and for dam operation. Dam operation was portrayed with a robust reservoir routing approach, based on an iterative solution of the storage equation coupled with the nonlinear dam outflow relationships and a Penman evaporation model. The flow upstream of the dam was simulated with a numerical kinematic wave

model. This approach was chosen since the KW model is appropriate for modeling flow on steep slopes, which is the case for the study area. As applies for the wadi reaches downstream of the dam, the upstream hydrodynamic model was iteratively coupled with an infiltration model to account for the transient interaction of surface flow and channel transmission losses.

Infiltration was modeled with the empirical Kostiakov-Lewis formula. Although any arbitrary functional relationship for quantifying transient infiltration could be used within the developed modeling framework, an empirical approach for infiltration modeling was preferred. Infiltration on alluvial wadi bed material is strongly driven by gravitational force and influenced by macropore effects. On the other hand, comprehensive infiltrometry data were available for the study area, which essentially indicated that (a) infiltration is highly variable in space and time, and (b) initial infiltration rates are very pronounced with typical rates up to some ten meters per day.

The full modeling system was applied at first for Wadi Ma'awil in order to carry out a comprehensive sensitivity and error analysis. The sensitivity of $\pm 30\,\%$ variations of channel slope, roughness coefficient, and infiltration model parameters on transmission losses, flow dynamics, and dam evaporation was evaluated. Total transmission losses were influenced by the infiltration parameters most strongly. Channel slope and channel roughness had a major influence on flow dynamics with respect to arrival times, whereas the final extents of the infiltrating flow domain were again controlled most strongly by the infiltration parameters. The influence of parameter variations on dam evaporation was small compared to flow and transmission loss volumes. The overall mean relative mass balance error of the full modeling system was only around $1.1\,\%$. The downstream hydrodynamic modeling component—which employed the analytical ZI advance model—featured extraordinary small mass balance errors, being at least one order of magnitude below the errors introduced by the numerical model components (i.e., the numerical KW model for upstream hydrodynamics and the reservoir routing model).

Consecutively, infiltration parameters and channel roughness were calibrated for Wadi Bani Kharus, employing an initial parametrization of the Kostiakov-Lewis model which was inferred from infiltrometry data. Data of a flash flood event which were obtained at an upstream (Al Abyadh) and a downstream gauge (highway station) were, therefore, used. Model calibration yielded a nearly perfect match of the observed and modeled hydrographs at the downstream gauge ($\mathrm{NSE} > 0.97$). A subsequent validation proved the suitability of the modeling system for accurately predicting transmission losses along a natural wadi reach. The mean error between observed and modeled transmission loss volumes was around $5\,\%$, which is an excellent result regarding the underlying high transmission loss quotas, being beyond $80\,\%$ of inflow volumes. Furthermore, the model turned out to deliver feasible results for peak flow rates and arrival times of the flood wave. The mean arrival time error at the downstream station was below 5 minutes and the mean relative peak error was around $35\,\%$, which is a fairly good result when taking into account the initially high inflow rates to the wadi section.

A subsequent application of the modeling system for the most intense observed natural flood event in Wadi Ma'awil, caused by cyclone Gonu, was carried out, employing infiltration and roughness parameters which were calibrated for the neighboring catchment of Wadi Bani Kharus. The dam parametrization was taken from the dam construction report without modification, and climate data were obtained from the Seeb Airport data set. An observed hydrograph at Afi was routed using the parametrized full modeling system. For validation, the simulated temporal development of the dam water level was compared with data obtained from a limnigraph sheet

Table 7.6: Comparison of absolute and relative flow volumes, transmission losses, and evaporation losses for the results of the sensitivity analysis (mean values from 11 simulations) and the Gonu simulation.

	Mean values from the sensitivity analysis		Values from the Gonu simulations	
	Relative values (%)	Absolute values (10^6 m^3)	Relative values (%)	Absolute values (10^6 m^3)
Upstream inflow volume	100.0	0.720	100.0	15.156
Upstream transmission losses	49.3	0.355	5.4	0.813
Dam inflow volume	50.1	0.361	94.3	14.299
Evaporation losses	13.9	0.100	0.9	0.133
Dam outflow volume	35.7	0.257	93.5	14.166
Downstream transmission losses	35.7	0.257	15.9	2.403
Losses to the sea	0.0	0.000	77.6	11.762
Total transmission losses	85.0	0.612	21.3	3.216
Total mass balance error	1.1	0.008	0.3	0.045

which was written during the event. The modeled water level development matched the observations very closely with respect to process dynamics and the peak water level, which was overestimated by only 2 cm. Unfortunately, missing stage recordings during dam depletion precluded a comparison of modeled and observed flow volumes. However, the accurate match of dam water level dynamics implicitly validated the upstream model parametrization (i.e., infiltration model parameters and roughness coefficient), assuming the dam parametrization obtained from the dam construction report to be valid.

Finally, it is interesting to compare the Gonu results to those of the sensitivity analysis with respect to absolute and relative flow volumes, transmission losses, and evaporation losses. Table 7.6 summarizes the respective values. It was observed that relative transmission losses were low for the Gonu event (around 20 % of the inflow volume of $15.156 \cdot 10^6$ m^3) and high for the scenarios investigated in the sensitivity analysis (85 % of $0.720 \cdot 10^6$ m^3). However, absolute transmission losses of the Gonu event doubled those of the sensitivity scenarios for the upstream reaches and were ten times higher for the downstream reaches. These findings reflect that transmission losses were limited by available inflow for the sensitivity analysis scenarios.

Despite the differences in the inflow volumes, absolute evaporation losses only slightly differed (around 30 %) for the investigated inflow events. The reasons for this are that: (a) the applied climatic forcing was quite similar (actual values of June 2006 for Gonu and mean July values of the years 1990–2010 for the sensitivity analysis); (b) as a consequence of the comparably low hydraulic capacity of the culvert outlets, the total operation time of the dam was always around 8–9 days for both the Gonu event and the various inflow scenarios regarded in the sensitivity analysis; and (c) for the Gonu event, a significant amount of water was released over the spillway, which significantly depleted the volume of water available for a more decelerated culvert release. This, consequently, led to a similar water level development for all investigated events, although the Gonu event caused a higher maximum dam water level, which in the end led to slightly higher absolute evaporation volumes.

Chapter 8

Summary and Conclusions

This thesis developed a process-oriented modeling system for estimating alluvial infiltration from flash floods (so-called transmission losses) influenced by the operation of groundwater recharge dams. Recharge dams amplify natural indirect recharge by (a) reducing flow rates in such a way that ideally no surface flow is lost beyond a reach with good recharge properties (or to the sea), and (b) by increasing both infiltration opportunity times and the wetted channel area. Therefore, artificially increased indirect recharge can exceed natural recharge from wadis greatly (Strobl and Haimerl, 1999; Bouwer, 2002; Haimerl, 2004; to name only a few). On the one hand, a sound description of the highly nonlinear and intricate surface flow and infiltration processes is of interest for planning and operating recharge dams with respect to available wadi reach length. On the other hand, better insight into the spatiotemporal dynamics of transmission losses is of high importance for assessing the regional water balance, which is, in turn, a prerequisite for planning any mitigation strategies that aim at relieving the pressure from the natural water resources.

Under the conditions which are typically found in arid regions, surface flow is ephemeral and transmission losses have to be assessed on an event-related temporal scale. A review of applicable approaches for transmission loss estimation revealed the need of a surface-water based and process-oriented approach if an event-specific assessment of transmission losses is indicated. Such process-oriented approaches cover the surface flow processes by means of physically-based, hydrodynamic models. Coming from the full hydrodynamic model, it was discussed which simplifications of the Saint-Venant equations are applicable under the problem-specific conditions of infiltrating wadi flow. It was outlined that the zero-inertia model poses a feasible process description for advancing dam release flow downstream of groundwater recharge dams. It was further discussed that the kinematic wave approximations are applicable under certain conditions.

The hydrodynamic model equations (full hydrodynamic, zero-inertia, kinematic wave) are usually solved by approximate, numerical methods. With respect to modeling infiltrating wadi flow on alluvial beds, it was outlined that applying numerical solution schemes to the governing flow equations may be prone to failure due to:

- ▷ mass balance errors and stability issues, attributable to an inappropriate representation of the flow variables' gradients, particularly at the interface of the flow domain and the initially dry channel bed;

- ▷ the interaction of surface flow and subsurface processes, which requires the dynamic coupling of modeling components (i.e., the surface flow model with an infiltration model) in a manner that the natural interdependency of both processes is represented;
- ▷ the fact that the typically high transmission loss quotas add further errors to the mass and the momentum balance if the surface–subsurface processes are not adequately portrayed.

Consequently, based mainly on previous work of Schmitz and Seus (1992) and Schmitz et al. (2002), an analytical solution strategy for the zero-inertia equations was derived, essentially describing flow in permeable nonprismatic open channels. Furthermore, the same mathematical concepts were applied for deriving a model for overland flow on an inclined surface element. A subsequent comprehensive and comparative analysis showed the advantages of the analytical approaches over generally accepted numerical solutions in terms of mass conservation, an accurate portrayal of flow dynamics, and computational efficiency.

Moreover, the analytical ZI open channel flow model proved its excellent applicability for simulating infiltrating wadi flow with very high infiltration quotas ($> 90\,\%$ of inflow volumes) under almost zero-advance conditions, which was achieved by iteratively solving the involved nonlinear equations with an adaptive time step at predefined channel locations. The analytical ZI model made up one component of an integrated modeling framework, which was supplemented by hydrodynamic models for describing wadi flow in the upper reaches, dam operation, as well as flow recession downstream of a recharge dam. The full modeling system could be soundly calibrated and validated and exposed low mass balance errors.

Assuming validity of the flow data used for calibration, three important properties of the modeled infiltrating open channel flow were observed. First, the hydrographs tend to steepen in the downstream direction, leading to a surging flow. This steepening tendency is amplified by initially high transmission losses (calibrated initial infiltration rates were almost $10^{-3}\,\mathrm{m \cdot s^{-1}}$ or $86.4\,\mathrm{m \cdot d^{-1}}$). Second, therefore, assuming a constant infiltration rate over time—as proposed by numerous authors—will not necessarily lead to a satisfactory representation of hydrograph shape under significant transmission losses. Third, mean modeled infiltration rates for typical event durations (hours to days) were in the lower range or lower (10^{-6} to $10^{-5}\,\mathrm{m \cdot s^{-1}}$) than suggested by infiltrometry testing (10^{-5} to $10^{-4}\,\mathrm{m \cdot s^{-1}}$). This is covered, e.g., by the findings of Wheater (2002), who stated that observed transmission losses in ephemeral channels tend to actually be lower than those inferred from infiltrometry tests.

The latter point clearly shows that using empirical infiltrometry data for transmission loss modeling is problematic, even if the tremendous variability in the infiltrometry measurements could be neglected. Compared to infiltration rates derived from infiltrometry tests, mean in-channel infiltration tends to be different for several reasons:

- ▷ Pronounced flow dynamics lead to erosion and a reworking of wadi material which promotes infiltration.
- ▷ During wave recession, sedimentation leads to clogging and, as a consequence, to a reduction of infiltration rates.
- ▷ In-channel infiltration varies with changing driving gradients and, therefore, with changing water levels.

The listing illustrates that assuming event-independent and spatially invariant infiltration parameters for transmission loss modeling—as employed herein (i.e., the same parameter set upstream and downstream of a recharge dam)—introduces considerable uncertainties. Nevertheless, an event-related calibration of an in-channel infiltration model seems to be more reasonable than just picking an arbitrary or mean infiltration rate from infiltrometry testing, where observed infiltration rates may span several orders of magnitudes in space *and* time. However, further event-related observations of surface flow and transmission losses are urgently needed to cope with the aforementioned problems, especially for the wadi section downstream of the investigated recharge dam, were virtually no observation data were available for validating the modeled transmission losses.

Furthermore, as comprehensively reviewed by Tooth (2000), dryland rivers undergo a pronounced morphological change, even on an event scale. Therefore, some further remarks have to be made on the herein incorporated assumptions that the roughness coefficient, channel morphology, and bottom slope are temporally invariant. Theoretically, an erosion–sedimentation model could be connected with the methodology applied in this thesis in order to describe transient channel morphology, i.e., by accounting for a change in the cross-sectional profile functions. A further concern is posed by the dependency of friction and the suspended load. Despite the fact that there are numerous studies on suspended load transport dynamics in ephemeral rivers, the mutual relationship of friction and sediment load often remains unclear beyond lab scale (e.g., Vanoni and Brooks, 1957; Martin-Vide et al., 1999).

Moreover, in the absence of a friction law for unsteady flows, velocity, channel roughness, channel geometry, and friction slope are commonly related using a steady flow formula, e.g., of the Manning-Strickler type. Consequently, friction is portrayed with the help of an effective parameter (i.e., the roughness coefficient) which only delivers a mean and, at best, event-specific description of friction. Nevertheless, the herein presented modeling framework is intended to aid as a prognosis tool. Recalling the tremendous uncertainties of the driving rainfall, the uncertainties and inadequatenesses in the portrayal of ephemeral river morphology and friction are not the major source of the model's predictive uncertainty.

Despite the fact that the proposed modeling system was able to be successfully applied, the imponderables of hydraulic modeling in arid environments became very clear. The major problem is the lack of data, which strongly limits model calibration and validation; this is due to the rareness of events together with sparse observation networks for precipitation and flow. Additionally, surface and subsurface flow processes are strongly interconnected and very dynamic in space and time. All available data should, therefore, be exploited thoroughly.

Chapter 9

Outlook

The approaches developed in this thesis generally cover two aspects which are related to the urgent need for fostering water resources management in the study region of Northern Oman: improving water resources assessment (i.e., using the modeling system to estimate indirect groundwater recharge) and, on the other hand, optimizing groundwater recharge. Both aspects need to be regarded for mitigating the problems associated with the intense over-exploitation of the coastal aquifer system in Oman's Batinah plain.

9.1 The Modeling System for Improving Water Resources Assessment

It is of very basic interest to improve the water resources assessment in the study region with respect to gain a better status-quo estimation of the present situation, which should be the basis for the planning and evaluation of any mitigation measures. In this light, the process-modeling strategy proposed herein should be validated more comprehensively and—if needed—improved. Foremost, this requires a sound assessment, collection, and verification of process-relevant data, including

- ▷ event-related wadi gauge data, preferably for a series of gauges;
- ▷ observations of the maximum extent of dam release flows;
- ▷ event-related rainfall data for validating flow data, preferably from radar measurements;
- ▷ wadi morphology data; and
- ▷ event-related reservoir data, including inflow, water level development, dam operation parameters, and sediment intake.

The aforementioned listing comprises data which are to a certain extent operationally collected by the Omani authorities. However, the rareness and pronounced dynamics of flash flood events may negatively affect data availability and quality. Therefore, data analyses should always be carried out synoptically, employing all available information.

Beyond this, further research is required in order to improve the modeling of wadi flow dynamics and recharge processes, and to account for uncertainties which affect the recharge assessment.

Based on the experience gained through this study, four important areas which require further investigation are evident:

- ▷ Accounting for the impact of uncertain process parameters (e.g., infiltration parameters and channel roughness) and the probability distribution of the driving data (e.g., flow data and climate data) on recharge estimates;
- ▷ the assessment and inclusion of typically changing wadi morphology and topology, especially for smaller flood events with no distinct horizontal connection of the flow network;
- ▷ the investigation of the interdependency of event-related sediment balance, wadi morphology, as well as their interactions with flow dynamics, emerging from changes in flowpaths, wadi cross sections, and—finally—channel roughness and infiltration properties; and
- ▷ the more detailed assessment of surface-water related processes, which were not regarded in this study, namely, storage and re-evaporation of already infiltrated water from the upper alluvial layer.

Addressing the first point is a prerequisite if the recharge assessment should be accompanied by a probability information (e.g., expected value of recharge as a function of the return period) which is connected to an information on the validness of such estimates (e.g., in form of uncertainty bands). During the last decade, statistical post-processors relying on Bayesian inference[1] have become widely used by hydrologists for such tasks (e.g., Krzysztofowic, 1999; Sikorska et al., 2012; Pokhrel et al., 2012). Together with appropriate statistical sampling techniques, such as Markov chain Monte Carlo (MCMC) methods, Bayesian methods are highly valuable for uncertainty modeling. However, Bayesian inference needs prior information, i.e., observed transmission losses. Furthermore, such methods are computationally demanding which often calls for high-performance computers.

Related to the second point, a potentially promising way to cope with changing morphology and topology is to turn away from a static description of the channels towards a more abstract one which is able to match the characteristic features of the very variable ephemeral flow patterns (Schick, 1988; Graf, 2002). Fractal approaches seem to be ideal for deriving a generally applicable model of channel characteristics. A very comprehensive work on the self-organization of river networks and their abstract description is provided by Iturbe and Rinaldo (1997). However, such morphological models need to be supplemented with appropriate data, which can be provided, for example, by remote-sensing satellites. For instance, Mett and Aufleger (2009) and Mett and Aufleger (2010) recently presented a detailed methodology for deriving morphology data for Omani wadis from various satellite products. The aforementioned authors are currently working on a very promising approach to relate morphological changes to a specific flow energy of an occurred event, which may allow the estimation of unobserved flow properties such as peak flow rates.

The third complex of issues has been subject to investigations for decades (e.g., Nomicos, 1956; Vanoni and Brooks, 1957). However, the modeling of erosion and sediment transport is very demanding and requires comprehensive data to feed most often empirically coined transport models. Nevertheless, the proposed modeling framework would allow the inclusion of a sediment transport model, which would only be reasonable with accompanying and cumbersome sediment monitoring

[1] Based on Bayes' theorem (Bayes, 1763), Bayesian inference allows the calculation of a posterior probability distribution function (e.g., for event-related transmission losses) as a consequence of prior information, as observed transmission losses for upstream inflows and a known or assumed distribution of infiltration parameters.

(e.g., Martin-Vide et al., 1999; López-Tarazón et al., 2012). However, the channel-scale interactions of bed roughness, flow properties, and sediment load are also an important field of future research.

The fourth point paramountly requires thorough field investigations (e.g., such as those carried out by Haimerl, 2004) in order to evaluate a potential need for regarding such further processes. Including appropriate modeling concepts within the existing modeling framework is possible but—of course—is only justified if required data (e.g., on the antecedent wetness conditions) are available for model calibration, validation, and operation.

9.2 The Modeling System for Optimizing Groundwater Recharge

In the study region, the predominant portion of indirect recharge occurs downstream of groundwater recharge dams. In-channel recharge is influenced foremost by downstream infiltration opportunity times, reservoir evaporation, and potential losses to the sea. All the aforementioned influences are a consequence of the applied dam release strategy. Up to now, dam operation in Oman is carried out on a more or less empirical basis, focusing mainly on the hard restriction that the reservoir needs to be emptied within 12 to 14 days after the inflow of an event (MAF, 1989).

However, this thesis made clear that a beneficial release of stored water should also focus on an optimal wetting of the available downstream alluvial sections, which feature good infiltration properties. Releasing water as fast as possible (i.e., without causing losses to the sea) diminishes evaporation losses, which can be significant, most importantly for smaller inflow events. Furthermore, it was shown that flow dynamics and infiltration are strongly nonlinearly interdependent. Therefore, a simulation-based evaluation of feasible release strategies is indicated in order to maximize future groundwater recharge. This could be done, for example, by altering a given release rule with respect to maximal downstream infiltration and minimal dam evaporation for a set of inflow hydrographs. This set can, e.g., comprise synthetically generated inflow hydrographs in order to sample the naturally occurring inflow properties with respect to inflow volumes and inflow dynamics. Consequently, for a given inflow situation, a feasible release strategy can be selected.

For obtaining maximal infiltration quotas, it is apparently indicated to guarantee a more or less quasiconstant release rates (cf. Section 6.1.4). As the emptying of the reservoir leads to a falling water level, the culvert outlets theoretically need to be adjusted permanently which, of course, would require on-site electricity, telemetry of water level measurements, motor-actuated culvert sluice gates, and a control logic for each of the culverts. It is questionable if such a sophisticated technology effort would justify the achievable enhancement of groundwater recharge in comparison to more robust operation rules, e.g., based on a daily adaption of the culvert outlets by hand.

Investigations assessing an optimal—which in this context means not only regarding recharge, but also institutional and technological effort—dam operation strategy need, therefore, to be carried out in close exchange with the Omani authorities, most importantly the MRMEWR and its branches. This outlines the strong need for a further and deepened cooperation with the Omani authorities in order to optimize the existing artificial groundwater augmentation facilities.

Bibliography

Abbott, M. B. *Computational Hydraulics*. Pitman Publishing London, 1979.

Abrams, M. The Advanced Spaceborne Thermal Emission and Reflection Radiometer (ASTER): data products for the high spatial resolution imager on NASA's Terra platform. *International Journal of Remote Sensing*, 21(5): 847–859, 2000.

Al-Qurashi, A. *Rainfall–Runoff Modelling in Arid Areas*. PhD thesis, Imperial College London, Department of Civil and Environmental Engineering, 2008.

Al-Qurashi, A., N. McIntyre, H. S. Wheater, and C. Unkrich. Application of the KINEROS2 rainfall–runoff model to an arid catchment in Oman. *Journal of Hydrology*, 355(1–4): 91–105, 2008.

Al-Rawas, G. A. *Flash Flood Modelling in Omani Wadis*. PhD thesis, University of Calgary, Department of Civil Engineering, 2009.

Al-Rawas, G. A. and C. Valeo. Characteristics of rainstorm temporal distributions in arid mountainous and coastal regions. *Journal of Hydrology*, 376(1–2): 318–326, 2009.

Al-Shaqsi, S. R. *The Socio-Economic and Cultural Aspects in the Implementation of Water Demand Management: A Case Study in the Sultanate of Oman*. PhD thesis, University of Nottingham, Department of Geography, 2004.

August, E. F. Über die Berechnung der Expansivkraft des Wasserdunstes. *Annalen der Physik und Chemie*, 89(5): 122–137, 1828.

Bachmann, P. *Analytische Zahlentheorie*. Teubner, Leipzig, 1894.

Baiamonte, G. and C. Agnese. An analytical solution of kinematic wave equations for overland flow under Green-Ampt infiltration. *Journal of Agricultural Engineering*, 1(1): 41–48, 2010.

Banach, S. Sur les opérations dans les ensembles abstraits et leur application aux équations intégrales. *Fundamenta Mathematicae*, 3(1): 133–181, 1922.

Battashi, N. and A. S. Rashid. *The Role of Artificial Recharge Schemes in Water Resources Development in Oman*. Technical report, Ministry of Water Resources, Sultanate of Oman, 1998.

Bayes, T. R. An essay towards solving a problem in the doctrine of changes. *Philosophical Transactions of the Royal Society of London*, 53: 370–418, 1763.

Beven, K. and P. Germann. Macropores and water flow in soils. *Water Resources Research*, 18(5): 1311–1325, 1982.

Bouwer, H. Design considerations for earth linings for seepage control. *Ground Water*, 20(5): 531–537, 1982.

Bouwer, H. *Hydraulic Design Handbook*, chapter Artificial Recharge of Groundwater: Systems, Design, and Management, pages 24.1–24.44. McGraw-Hill, New York, 1999.

Bouwer, H. Artificial recharge of ground water: hydrogeology and engineering. *Hydrogeology Journal*, 10(1): 121–142, 2002.

Bronstein, I. N. and K. A. Semendjajev. *Taschenbuch der Mathematik*. B. G. Teubner Verlagsgesellschaft, Leipzig, 1966.

Bronstert, A. Capabilities and limitations of detailed hillslope hydrological modelling. *Hydrological Processes*, 13(1): 21–48, 1999.

Bronstert, A. and A. Bárdossy. Uncertainty of runoff modelling at the hillslope scale due to temporal variations of rainfall intensity. *Physics and Chemistry of the Earth*, 28(6–7): 283–288, 2003.

Bronstert, A. and E. Plate. Modelling of runoff generation and soil moisture dynamics for hillslopes and micro-catchments. *Journal of Hydrology*, 198(1–4): 177–195, 1997.

Brunner, G. W. *HEC-RAS User's Manual*. U. S. Army Corps of Engineers, Hydrologic Engineering Center, Davis, California, 2008.

Brutsaert, W. *Evaporation Into the Atmosphere: Theory, History and Applications*. D. Reidel Publishing Company, Dordrecht, 1982.

Chalfen, M. and A. Niemiec. Analytical and numerical solution of the Saint-Venant equations. *Journal of Hydrology*, 86(1–2): 1–13, 1986.

Chapman, T. G. Modelling stream recession flows. *Environmental Modelling and Software*, 18(1): 683–692, 2003.

Chau, K. W. Application of the Preissmann scheme on flood propagation in river systems in difficult terrain. In *Proceedings of the IAHS Conference on Hydrology in Mountainous Regions, Lausanne, Switzerland*. 1990.

Chow, V. T. *Open Channel Hydraulics*. McGraw-Hill, New York, 1959.

Chung, W. H. and Y. L. Kang. Analytical solutions of Saint-Venant equations decomposed in frequency domain. *Journal of Mechanics*, 20(3): 187–197, 2004.

Chézy, A. Formule pour trouver la vitesse de l'eau conduit dans une rigole donnée. *Dossiers de l'École National des Ponts et Chaussées*, 847, 1776.

Costa, A. C., A. Bronstert, and J. C. Araújo. A channel transmission losses model for different dryland rivers. *Hydrology and Earth System Sciences*, 16(4): 1111–1135, 2012.

Costelloe, J. F., R. B. Grayson, R. M. Argent, and T. A. McMahon. Modelling the flow regime of an arid zone floodplain river, Diamantina River, Australia. *Environmental Modelling and Software*, 18(8–9): 693–703, 2003.

Courant, R., K. Friedrichs, and H. Lewy. Über die partiellen Differenzengleichungen der mathematischen Physik. *Mathematische Annalen*, 100(1): 32–74, 1928.

Cunge, J. A., F. M. Holly, and A. Verwey. *On the Practical Aspects of Computational River Hydraulics*. Pitman Publishing London, 1980.

Daluz Vieira, J. H. Conditions governing the use of approximations for the Saint-Venant equations for shallow surface water flow. *Journal of Hydrology*, 60(3): 43–58, 1983.

Delis, A. I. and C. P. Skeels. TVD schemes for open channel flow. *International Journal for Numerical Methods in Fluids*, 26(1): 791–809, 1998.

Di Giammarco, P., E. Todini, and P. Lamberti. A conservative finite elements approach to overland flow: the control volume finite element formulation. *Journal of Hydrology*, 175(1–4): 267–291, 1995.

Duchesne, S., A. Mailhot, E. Dequidt, and J.-P. Villeneuve. Mathematical modeling of sewers under surcharge for real time control of combined sewer overflows. *Urban Water*, 3(4): 241–252, 2001.

Dunkerley, D. and K. Brown. Flow behaviour, suspended sediment transport and transmission losses in a small (sub-bank-full) flow event in an Australian desert stream. *Hydrological Processes*, 13(11): 1577–1588, 1999.

Dunne, T. and B. F. Aubry. *Hillslope Processes*, chapter Evaluation of Horton's Theory of Sheetwash and Rill Erosion on the Basis of Field Experiments, pages 31–54. Allen and Unwin, Winchester, Massachusetts, 1986.

Eagleson, P. S. *Dynamic Hydrology*. McGraw-Hill, New York, 1970.

Edenhofer, J. and G. H. Schmitz. Ein implizites Charakteristikenverfahren zur Lösung von Anfangsrandwertaufgaben bei hyperbolischen Systemen und seine Konvergenz. *Computing*, 26(1): 257–264, 1981.

El-Hames, A. S. and K. S. Richards. An integrated, physically based model for arid region flash flood prediction capable of simulating dynamic transmission loss. *Hydrological Processes*, 12(8): 1219–1232, 1998.

Esteves, M., X. Faucher, S. Galle, and M. Vauclin. Overland flow and infiltration modelling for small plots during unsteady rain: numerical versus observed values. *Journal of Hydrology*, 228(3–4): 265–282, 2000.

Fan, P. and J. C. Li. Diffusive wave solutions for open channel flows with uniform and concentrated lateral inflow. *Advances in Water Resources*, 29(7): 1000–1019, 2004.

Fisher, M. Another look at the variability of desert climates, using examples from Oman. *Global Ecology and Biogeography Letters*, 4(1): 79–87, 1994.

Fread, D. L. *Handbook of Hydrology*, chapter Flow Routing, pages 10.1–10.36. McGraw-Hill, New York, 1993.

Furman, A., A. W. Warrick, D. Zerihun, and C. A. Sanchez. Modified Kostiakov infiltration function: accounting for initial and boundary conditions. *Journal of Irrigation and Drainage Engineering*, 132(6): 587–596, 2006.

Garcia-Navarro, P., A. Fras, and I. Villanueva. Dam-break flow simulation: some results for one-dimensional models of real cases. *Journal of Hydrology*, 216(3–4): 227–247, 1999.

Garoussi, A. A. Underground gardens: dry-farmed grapes in Busher. In *Proceedings of the UNESCO Regional Workshop on Traditional Water Harvesting Systems, Tehran, Iran.* 1999.

Gheith, H. and M. Sultan. Construction of a hydrologic model for estimating wadi runoff and groundwater recharge in the Eastern Desert, Egypt. *Journal of Hydrology*, 263(1): 36–55, 2000.

Goodrich, D. C., D. G. Williams, C. L. Unkrich, J. F. Hogan, R. L. Scott, K. R. Hultine, D. Pool, A. L. Coes, and S. Miller. Comparison of methods to estimate ephemeral channel recharge, Walnut Gulch, San Pedro River basin, Arizona. In Phillips, F. M., J. F. Hogan, and B. Scanlon, editors, *Recharge and Vadose Zone Processes: Alluvial Basins of the Southwestern United States*, pages 77–99. American Geophysical Union, Washington DC, 2004.

Govindaraju, R. S., S. E. Jones, and M. L. Kavvas. On the diffusion wave model for overland flow: 1. solution for steep slopes. *Water Resources Research*, 24(5): 734–744, 1988.

Govindaraju, R. S., M. L. Kavvas, and S. E. Jones. Approximate analytical solutions for overland flows. *Water Resources Research*, 26(12): 2903–2912, 1990.

Govindaraju, R. S., M. L. Kavvas, and G. Tayfur. A simplified model for two-dimensional overland flows. *Advances in Water Resources*, 15(1–2): 133–141, 1992.

Grabs, W. E. On the envisaged improvement of the Omani Flash Flood Warning System, 2012. Personal correspondence.

Graf, W. L. *Fluvial Processes in Dryland Rivers.* Blackburn, New Jersey, 2002.

Grundmann, J., N. Schütze, G. H. Schmitz, and S. R. Al-Shaqsi. Towards an integrated arid zone water management using simulation-based optimisation. *Environmental Earth Sciences*, 65(5): 1381–1394, 2012.

Haimerl, G. *Groundwater Recharge in Wadi Channels Downstream of Dams.* Number 99 in Berichte des Lehrstuhls und der Versuchsanstalt für Wasserbau und Wasserwirtschaft. Technische Universität München, Institut für Wasserwesen, 2004.

Haimerl, G. and F. Zunic. Infiltration tests and numerical solution to evaluate the efficiency of infiltration in arid countries. In *Proceedings of the 3rd International Conference on Water Resources and Environmental Research (ICWRER), Dresden, Germany.* 2002.

Haller, J. *Data Collection and Data Analysis of Hydrological and Hydrogeological Data of Wadi Ahin in the Sultanate of Oman.* Master's thesis, Technische Universität München, Institut für Wasserwesen, Lehrstuhl und Versuchsanstalt für Wasserbau und Wasserwirtschaft, 2000.

Hansen, N. The CMA evolution strategy: a comparing review. In Lozano, J., P. Larranaga, I. Inza, and E. Bengoetxea, editors, *Towards a new evolutionary computation. Advances on estimation of distribution algorithms*, pages 75–102. Springer, 2006.

Haverkamp, R., M. Kutilek, J. Y. Parlange, L. Rendon, and M. Krejca. Infiltration under ponded conditions: 2. infiltration equations tested for parameter time-dependence and predictive use. *Soil Science*, 145(5): 317–329, 1988.

Hayami, S. On the propagation of flood waves. *Bulletin of the Disaster Prevention Research Institute, Kyoto University*, 1(1): 1–16, 1951.

Henderson, F. M. *Open Channel Flow*. Macmillan, New York, 1966.

Henderson, F. M. and R. A. Wooding. Overland flow and groundwater flow from a steady rainfall of finite duration. *Journal of Geophysical Research*, 69(8): 1531–1540, 1964.

Hjelmfelt, A. T. Overland flow from time-distributed rainfall. *Journal of the Hydraulics Division of the ASCE*, 107(2): 227–238, 1981.

Hjelmfelt, A. T. Convolution and the kinematic wave equations. *Journal of Hydrology*, 75(1–4): 301–309, 1984.

Howes, D. A., A. D. Abrahams, and E. B. Pitman. One- and two-dimensional modelling of overland flow in semiarid shrubland, Jornada basin, New Mexico. *Hydrological Processes*, 20(5): 1027–1046, 2006.

Hughes, D. A. and K. Sami. A semi-distributed, variable time interval model of catchment hydrology—structure and parameter estimation procedures. *Journal of Hydrology*, 115(1–2): 265–291, 1994.

Iturbe, R.-I. and A. Rinaldo. *Fractal River Basins—Chance and Self-Organization*. Cambridge University Press, New York, 1997.

Jaber, F. H. and R. H. Mohtar. Stability and accuracy of two-dimensional kinematic wave overland flow modeling. *Advances in Water Resources*, 26(11): 1189–1198, 2003.

Kincaid, D. C. *Hydrodynamics of Border Irrigation*. PhD thesis, Colorado State University, Fort Collins, Colorado, 1970.

Kirkby, M. Hillslope runoff processes and models. *Journal of Hydrology*, 100(1–3): 315–339, 1988.

Kostiakov, A. N. On the dynamics of the coefficient of water percolation in soils and on the necessity of studying it from a dynamic point of view for purposes of amelioration. In *Transactions of the Sixth Commission of the International Society of Soil Science, Moscow, Russia*. 1932.

Kowsar, A. *An Introduction to Flood Mitigation and Optimization of Flood Water Utilization: Flood Irrigation, Artificial Recharge of Ground Water, Small Earth Dams*. Technical report, Research Center of the Construction Crusade, Tehran, Iran, 1996.

Krzysztofowic, R. Bayesian theory of probabilistic forecasting via deterministic hydrologic model. *Water Resources Research*, 35(9): 2739–2750, 1999.

Kummerow, C., W. Barnes, T. Kozu, J. Shiue, and J. Simpson. The Tropical Rainfall Measuring Mission (TRMM) sensor package. *Journal of Atmospheric and Oceanic Technology*, 15(3): 809–817, 1998.

Lange, J. Dynamics of transmission losses in a large arid stream channel. *Journal of Hydrology*, 306(1–4): 112–126, 2005.

Lange, J., C. Leibundgut, N. Greenbaum, and A. P. Schick. A noncalibrated rainfall–runoff model for large arid catchments. *Water Resources Research*, 35(7): 2161–2172, 1999.

Lax, P. D. and R. D. Richtmyer. Survey of the stability of linear finite difference equations. *Communications on Pure and Applied Mathematics*, 9(1): 267–293, 1956.

Lerner, D. N. *Geochemical Processes, Weathering, and Groundwater Recharge in Catchments*, chapter Groundwater Recharge, pages 109–150. A. A. Balkema Publishers, Rotterdam, 1997.

Lerner, D. N., A. S. Issar, and I. Simmers. *Groundwater Recharge: A Guide to Understanding and Estimating Natural Recharge*. A. A. Balkema Publishers, Rotterdam, 1990.

Lewis, M. R. The rate of infiltration of water in irrigation-practice. *Transactions of the American Geophysical Union*, 18(2): 361–368, 1937.

Liedl, R. *Funktionaldifferentialgleichungen zur Beschreibung von Wasserbewegungen in Böden natürlicher Variabilität – Beiträge zur Theorie und Entwicklung eines numerischen Entwicklungsverfahrens*. Number 67 in Berichte des Lehrstuhls und der Versuchsanstalt für Wasserbau und Wasserwirtschaft. Technische Universität München, Institut für Wasserwesen, 1991.

Lighthill, M. J. and G. B. Whitham. On kinematic waves: 1. flood movement in long rivers. *Proceedings of the Royal Society of London*, A229(1178): 281–316, 1955.

Lindelöf, E. Sur l'application de la méthode des approximations successives aux équations différentielles ordinaires du premier ordre. *Comptes Rendus des Séances de l'Académie des Sciences Paris*, 114(1): 454–457, 1894.

Liu, Q. Q., L. Chen, J. C. Li, and V. P. Singh. Two-dimensional kinematic wave model of overland-flow. *Journal of Hydrology*, 291(1–2): 28–41, 2004.

López-Tarazón, J. A., R. J. Batalla, D. Vericat, and T. Francke. The sediment budget of a highly dynamic mesoscale catchment: the River Isábena. *Geomorphology*, 138(3–4): 210–221, 2012.

MacArthur, R. and J. J. DeVries. *Introduction and Application of Kinematic Wave Routing Techniques Using HEC-1*. U. S. Army Corps of Engineers, Hydrologic Engineering Center, Davis, California, 1993.

MAF. *Infiltrometry Testing in Wadi Ma'awil*. Technical report, Ministry of Agriculture and Fisheries of the Sultanate of Oman, 1985.

MAF. *Groundwater Recharge Schemes for Barka-Rumais Areas: Feasibility Report Engineering and Economics*. Technical report, Ministry of Agriculture and Fisheries of the Sultanate of Oman, 1989.

MAF. *Groundwater Recharge Schemes for Barka-Rumais Areas: Feasibility Report Hydrogeology.* Technical report, Ministry of Agriculture and Fisheries of the Sultanate of Oman, 1990.

MAF. *Groundwater Recharge Dam on Wadi Ahin, Wilayat Saham: Hydrology and Design Criteria Report.* Technical report, Ministry of Agriculture and Fisheries of the Sultanate of Oman, 1992.

Martin-Vide, J. P., D. Niñerola, A. Bateman, A. Navarro, and E. Velasco. Runoff and sediment transport in a torrential ephemeral stream of the Mediterranean coast. *Journal of Hydrology*, 225(3–4): 118–129, 1999.

Massau, J. Appendice au mémoire sur l'integration graphique. *Annales de l'Association des Ingénieurs Sortis des Ecoles Spéciales de Gand, Belgique*, 12(1): 135–444, 1889.

McIntyre, N., A. Al-Qurashi, and H. S. Wheater. Regression analysis of rainfall–runoff data from an arid catchment in Oman. *Hydrological Sciences—Journal des Sciences Hydrologiques*, 52(6): 1103–1118, 2007.

Menk, P. *Evaporation—A Critical Factor for Groundwater Recharge Dams?* Master's thesis, Technische Universität München, Institut für Wasserwesen, Lehrstuhl und Versuchsanstalt für Wasserbau und Wasserwirtschaft, 1998.

Mett, M. and M. Aufleger. Optical satellite pictures—the up to date source for discharge determination in arid countries. In *Proceedings of the 8th World Wide Workshop for Young Environmental Scientists, Arcueil, France.* 2009.

Mett, M. and M. Aufleger. Observation of flashflood-related morphology changes in arid areas with the help of optical satellite data—case study Al-Batinah plain in Oman. In *Proceedings of the 2010 EGU General Assembly, Vienna, Austria.* 2010.

Miller, J. E. *Basic Concepts of Kinematic Wave Models.* USGS Professional Paper 1302, U. S. Geological Survey, 1984.

Mizumura, K. Analytical solutions of nonlinear kinematic wave model. *Journal of Hydrologic Engineering*, 11(6): 539–546, 2006.

Mizumura, K. and Y. Ito. Analytical solution of nonlinear kinematic wave model with time-varying rainfall. *Journal of Hydrologic Engineering*, 16(9): 736–745, 2011a.

Mizumura, K. and Y. Ito. Influence of moving rainstorms on overland flow of an open book type using kinematic wave. *Journal of Hydrologic Engineering*, 16(11): 926–934, 2011b.

Morin, E., T. Grodek, O. Dahan, G. Benito, C. Kulls, Y. Jacoby, G. V. Langenhove, M. Seely, and Y. Enzel. Flood routing and alluvial aquifer recharge along the ephemeral arid Kuiseb River, Namibia. *Journal of Hydrology*, 368(1–4): 262–275, 2009.

Morita, M. and B. C. Yen. Modeling of conjunctive two-dimensional surface—three-dimensional subsurface flows. *Journal of Hydraulic Engineering*, 128(2): 184–200, 2002.

Morris, E. M. and D. A. Woolhiser. Unsteady one-dimensional flow over a plane: partial equilibrium and recession hydrographs. *Water Resources Research*, 16(2): 355–360, 1980.

MRMEWR. Dams in the Sultanate of Oman (Booklet). Ministry of Regional Municipalities, Environment and Water Resources of the Sultanate of Oman. 2007.

Mudd, S. M. Investigation of the hydrodynamics of flash floods in ephemeral channels: scaling analysis and simulation using a shock-capturing flow model incorporating the effects of transmission losses. *Journal of Hydrology*, 324(1–4): 65–79, 2006.

Munz, C.-D. and T. Westermann. *Numerische Behandlung gewöhnlicher und partieller Differenzialgleichungen*. Springer-Vieweg, Berlin, Heidelberg, 2012.

Nash, J. E. and J. V. Sutcliffe. River flow forecasting through conceptual models part I—a discussion of principles. *Journal of Hydrology*, 10(3): 282–290, 1970.

Nelder, J. A. and R. Mead. A simplex method for function minimization. *Computer Journal*, 7(4): 308–313, 1965.

Nomicos, G. N. *Effects of Sediment Load on the Velocity Field and Friction Factor of Turbulent Flow in an Open Channel*. PhD thesis, California Institute of Technology, Pasadena, 1956.

O'Brien, G. C., M. A. Hyman, and S. Kaplan. A study of the numerical solution of partial differential equations. *Journal of Mathematics and Physics of the Massachusetts Institute of Technology*, 29(4): 223–251, 1951.

Penman, H. L. Natural evaporation from open water, bare soils and grass. *Proceedings of the Royal Society of London*, 193(1032): 120–145, 1948.

Philipp, A. and J. Grundmann. Integrated modeling system for flash flood routing in ephemeral rivers under the influence of groundwater recharge dams. *Journal of Hydraulic Engineering*, 139(12): 1–13, 2013.

Philipp, A., R. Liedl, and T. Wöhling. Analytical model of surface flow on hillslopes based on the zero-inertia equations. *Journal of Hydraulic Engineering*, 138(5): 391–399, 2012.

Philipp, A., G. H. Schmitz, and R. Liedl. Analytical model of surge flow in nonprismatic permeable channels and its application in arid regions. *Journal of Hydraulic Engineering*, 136(5): 290–298, 2010.

Pokhrel, P., D. E. Robertson, and Q. J. Wang. A Bayesian joint probability post-processor for reducing errors and quantifying uncertainty in monthly streamflow predictions. *Hydrology and Earth System Sciences*, 17(2): 795–804, 2012.

Ponce, V. M. Nature of wave attenuation in open channel flow. *Journal of the Hydraulics Division of the ASCE*, 108(2): 257–262, 1982.

Ponce, V. M. The kinematic wave controversy. *Journal of Hydraulic Engineering*, 117(4): 511–525, 1991.

Ponce, V. M., R.-M. Li, and D. B. Simons. Applicability of kinematic and diffusion waves. *Journal of the Hydraulics Division of the ASCE*, 104(3): 353–360, 1978.

Ponce, V. M. and D. B. Simons. Shallow wave propagation in open channel flow. *Journal of the Hydraulics Division of the ASCE*, 103(12): 1461–1476, 1977.

Ponce, V. M. and D. Windingland. Kinematic shock: sensitivity analysis. *Journal of Hydraulic Engineering*, 111(4): 600–611, 1985.

Preissmann, A. Propagation des intumescences dans les canaux et rivières. In *Comptes Rendus Premier Congrès de l'Association Française du Calcul, Grenoble, France*. 1961.

Press, W. H., S. A. Teukolsky, W. T. Vetterling, and B. P. Flannery. *Numerical Recipes*. Cambridge University Press, New-York, 1992.

Quilis, R. O., M. Hoogmoed, M. Ertsen, J. W. Froppen, R. Hut, and A. de Vries. Measuring and modeling hydrological processes of sand-storage dams on different spatial scales. *Physics and Chemistry of the Earth*, 34(1): 289–298, 2009.

Rayej, M. and W. Wallender. Furrow irrigation simulation time reduction. *Journal of Irrigation and Drainage Engineering*, 111(2): 134–146, 1985.

Renard, K. G. and R. V. Keppel. Hydrographs of ephemeral streams in the Southwest. *Journal of the Hydraulics Division of the ASCE*, 92(2): 33–52, 1966.

Richtmyer, R. D. and K. W. Morton. *Difference Methods for Initial-Value Problems*. Interscience Publishers, New York, London, Sydney, 1967.

Ross, B. B., D. N. Contractor, and V. O. Shanholtz. A finite-element model of overland and channel flow for assessing the hydrologic impact of land-use change. *Journal of Hydrology*, 41(1–2): 11–30, 1979.

Rushton, K. *Recharge of Phreatic Aquifers in (Semi-)Arid Areas*, chapter Recharge from Permanent Water Bodies. A. A. Balkema Publishers, Rotterdam, 1997.

Saber, M., T. Hamaguchi, T. Kojiri, and K. Tanaka. Spatiotemporal runoff features of hydrological modeling in Arabian wadi basins through comparative studies. *Annuals of the Disaster Prevention Research Institute, Kyoto University*, 52(B): 813–830, 2009.

de Saint-Venant, J. C. Théorie du mouvement non permanent des eaux, avec application aux crues des rivières et à l'introduction des marées dans leur lit. *Comptes Rendus des Séances de l'Académie des Sciences Paris*, 73(1): 147–154, 1871.

Scanlon, B. R. and R. W. Healy. Choosing appropriate techniques for quantifying groundwater recharge. *Hydrogeology Journal*, 10(1): 18–39, 2002.

Schick, A. P. *Flood Geomorphology*, chapter Hydrologic Aspects of Floods in Extreme Arid Environments, pages 189–203. Wiley Interscience, New York, 1988.

Schmid, B. H. *Zur mathematischen Modellierung der Abflussentstehung an Hängen*. Number 68 in Wiener Mitteilungen. Technische Universität Wien, Institut für Hydraulik, Gewässerkunde und Wasserwirtschaft, 1986.

Schmid, B. H. *A Study on Kinematic Cascades*. Number 90 in Wiener Mitteilungen. Technische Universität Wien, Institut für Hydraulik, Gewässerkunde und Wasserwirtschaft, 1990.

Schmitz, G. H. *Instationäre Eichung mathematischer Hochwasserablauf-Modelle auf der Grundlagen eines neuen Lösungsprinzips für hyperbolische Differentialgleichungssysteme.* Number 46 in Berichte des Lehrstuhls und der Versuchsanstalt für Wasserbau und Wasserwirtschaft. Technische Universität München, Institut für Wasserwesen, 1981.

Schmitz, G. H. *Strömungsvorgänge auf der Oberfläche und im Bodeninnern beim Bewässerungslandbau.* Number 60 in Berichte des Lehrstuhls und der Versuchsanstalt für Wasserbau und Wasserwirtschaft. Technische Universität München, Institut für Wasserwesen, 1989.

Schmitz, G. H., R. Haverkamp, and O. Palacios-Velez. A coupled surface–subsurface model for shallow water flow over initially dry soil. In *Proceedings of the 21st International IAHR Congress, Melbourne, Australia.* 1985.

Schmitz, G. H., R. Liedl, and R. Volker. Analytical solution to the zero inertia problem for surge flow phenomena in nonprismatic channels. *Journal of Hydraulic Engineering*, 128(6): 604–615, 2002.

Schmitz, G. H. and G. J. Seus. Analytical solution of simplified surge flow equations. *Journal of Irrigation and Drainage Engineering*, 113(4): 605–610, 1987.

Schmitz, G. H. and G. J. Seus. Mathematical zero-inertia modeling of surface irrigation: advance in borders. *Journal of Irrigation and Drainage Engineering*, 116(5): 603–615, 1990.

Schmitz, G. H. and G. J. Seus. Mathematical zero-inertia modeling of surface irrigation: advance in furrows. *Journal of Irrigation and Drainage Engineering*, 118(1): 1–18, 1992.

Sharma, K. D. and J. S. R. Murthy. Estimating transmission losses in an arid region—a realistic approach. *Journal of Arid Environments*, 27(2): 107–112, 1994.

Sharma, K. D. and J. S. R. Murthy. Hydrologic routing of flow in arid ephemeral channels. *Journal of Hydraulic Engineering*, 121(6): 466–471, 1995.

Sharma, K. D. and J. S. R. Murthy. Ephemeral flow modelling in arid regions. *Journal of Arid Environments*, 33(2): 161–178, 1996.

Sharon, D. The spottiness of rainfall in a desert area. *Journal of Hydrology*, 17(1): 161–175, 1972.

Shentsis, I., L. Meirovich, A. Ben-Zvi, and E. Rosenthal. Assessment of transmission losses and groundwater recharge from runoff events in a wadi under shortage of data on lateral inflow, Negev, Israel. *Hydrological Processes*, 13(11): 1649–1663, 1999.

Shentsis, I. and E. Rosenthal. Recharge of aquifers by flood events in an arid region. *Hydrological Processes*, 17(4): 695–712, 2003.

Sikorska, A. E., A. Scheidegger, K. Banasik, and J. Rieckermann. Bayesian uncertainty assessment of flood predictions in ungauged urban basins for conceptual rainfall-runoff models. *Hydrology and Earth System Sciences*, 16(4): 1221–1236, 2012.

Singh, V. P. Accuracy of kinematic wave and diffusion wave approximations for space independent flows. *Hydrological Processes*, 8(1): 45–62, 1994.

Singh, V. P. *Kinematic Wave Modeling in Water Resources.* John Wiley and Sons, New York, 1996.

Singh, V. P. Is hydrology kinematic? *Hydrological Processes*, 16(3): 667–719, 2002.

Six, A. *Flash Floods in Wadis – Erarbeitung und Anwendung von Simulationswerkzeugen für Grundwasseranreicherungssysteme in ariden Gebieten.* Master's thesis, Technische Universität Dresden, Institut für Hydrologie und Meteorologie, Lehrstuhl für Hydrologie, 2011.

Smith, R. E., D. C. Goodrich, and J. N. Quinton. Dynamic, distributed simulation of watershed erosion: the KINEROS2 and EUROSEM models. *Journal of Soil and Water Conservation*, 50(5): 517–520, 1995.

Sophocleous, M. Interactions between groundwater and surface water: the state of the science. *Hydrogeology Journal*, 10(1): 52–67, 2002.

Sorman, A. U. and M. J. Abdulrazzak. Infiltration-recharge through wadi beds in arid regions. *Hydrological Sciences—Journal des Sciences Hydrologiques*, 38(3): 173–186, 1993.

Stanley, E. H. and J. B. Jones. *Streams and Ground Waters*, chapter Surface–Subsurface Intercations: Past, Present, and Future, pages 405–417. Academic Press, San Diego, 2000.

Stoker, J. J. *Water Waves: The Mathematical Theory With Applications.* Interscience Publishers, New York, London, 1957.

Strelkoff, T. and N. D. Katopodes. Border-irrigation hydraulics with zero inertia. *Journal of Irrigation and Drainage Engineering*, 103(3): 325–342, 1977.

Strickler, A. Beiträge zur Frage der Geschwindigkeitsformel und der Rauhigkeitszahlen für Ströme, Kanäle und geschlossene Leitungen. *Mitteilungen des Amtes für Wasserwirtschaft, Bern, Switzerland*, 16: 357–434, 1923.

Strobl, T. and G. Haimerl. Optimization of the recharge process downstream of groundwater recharge dams. In *Proceedings of the 5th Civil and Environmental Engineering Converence, Bangkok, Thailand.* 1999.

Subramanya, K. *Flow in Open Channels.* McGraw-Hill, New Delhi, 2009.

Tarboton, D. G. A new method for the determination of flow directions and upslope areas in grid digital elevation models. *Water Resources Research*, 33(2): 309–319, 1997.

Tayfur, G. and M. L. Kavvas. Areally-averaged overland flow equations at hillslope scale. *Hydrological Sciences—Journal des Sciences Hydrologiques*, 43(3): 361–378, 1998.

Tenman, R. *Navier-Stokes Equations: Theory and Numerical Analysis.* AMS Chelsea Publishing, 1977.

The World Bank. *Making the Most of Scarcity: Accountability for Better Water Management Results in the Middle East and North Africa.* The International Bank for Reconstruction and Development, Washington, DC, 2007.

Todd, D. K. *Annotated Bibliography on Artificial Recharge of Ground Water Through 1954.* Water-Supply Paper 1477, U. S. Geological Survey, 1959.

Tooth, S. Process, form and change in dryland rivers: a review of recent research. *Earth-Science Reviews*, 51(1–4): 67–107, 2000.

Tsai, T. L. and J. C. Yang. Kinematic wave modeling of overland flow using characteristics method with cubic-spline interpolation. *Advances in Water Resources*, 28(7): 661–670, 2005.

UNEP. *World Atlas of Desertification*. United Nations Environment Programme, 1997.

UNEP. *Sourcebook of Alternative Technologies for Freshwater Augmentation in Some Countries in Asia*. United Nations Environment Programme, Division of Technology, Industry and Economics, Osaka, Japan, 1998.

Vanoni, V. A. and N. H. Brooks. *Laboratory Studies of the Roughness and Suspended Load of Alluvial Streams*. Technical Report E-68, California Institute of Technology, Pasadena, 1957. Report to the U. S. Army Corps of Engineers.

Vischer, D. L. and W. H. Hager. *Dam Hydraulics*. John Wiley and Sons, Chichester, 1999.

Voss, K. A., J. S. Famiglietti, M. Lo, C. de Linage, M. Rodell, and S. C. Swenson. Groundwater depletion in the middle east from GRACE with implications for transboundary water management in the Tigris-Euphrates-Western Iran region (accepted article). *Water Resources Research*, 2013.

de Vries, J. J. and I. Simmers. Groundwater recharge: an overview of processes and challenges. *Hydrogeology Journal*, 10(1): 5–17, 2002.

Walker, W. R. and A. S. Humpherys. Kinematic-wave furrow irrigation model. *Journal of Irrigation and Drainage Engineering*, 109(4): 377–392, 1983.

Walters, M. O. Transmission losses in arid regions. *Journal of Hydraulic Engineering*, 116(1): 129–138, 1990.

Wang, G.-T., S. Chen, J. Boll, C. O. Stockle, and D. K. McCool. Modelling overland flow based on Saint-Venant equations for a discretized hillslope system. *Hydrological Processes*, 16(12): 2409–2421, 2002.

Wasantha Lal, A. M. Performance comparison of overland flow algorithms. *Journal of Hydraulic Engineering*, 124(4): 342–349, 1998.

Wheater, H. S. *Hydrology of Wadi Systems*. UNESCO, Paris, 2002.

Wöhling, T. *Physically Based Modeling of Furrow Irrigation Systems During a Growing Season*. Number 2 in Dresdner Schriften zur Hydrologie. Technische Universität Dresden, Institut für Hydrologie und Meteorologie, Lehrstuhl für Hydrologie, 2005.

Wöhling, T., A. Fröhner, and G. H. Schmitz. Efficient solution of the coupled one-dimensional surface–two-dimensional subsurface flow during furrow irrigation advance. *Journal of Irrigation and Drainage Engineering*, 132(4): 380–388, 2006.

Wöhling, T. and J.-C. Mailhol. Physically based coupled model for simulating 1D surface–2D subsurface flow and plant water uptake in irrigation furrows. II: model test and evaluation. *Journal of Irrigation and Drainage Engineering*, 133(6): 548–558, 2007.

Wöhling, T. and G. H. Schmitz. Physically based coupled model for simulating 1D surface–2D subsurface flow and plant water uptake in irrigation furrows. I: model development. *Journal of Irrigation and Drainage Engineering*, 133(6): 538–547, 2007.

Wöhling, T., G. H. Schmitz, and J.-C. Mailhol. Modeling two-dimensional infiltration from irrigation furrows. *Journal of Irrigation and Drainage Engineering*, 130(4): 296–303, 2004a.

Wöhling, T., R. Singh, and G. H. Schmitz. Physically based modeling of interacting surface–subsurface flow during furrow irrigation advance. *Journal of Irrigation and Drainage Engineering*, 130(5): 349–356, 2004b.

WMO. *Manual for Estimation of Probable Maximum Precipitation.* Operational Hydrology Reports. Secretariat of the World Meteorological Organization, Geneva, Switzerland, 1986.

Wood, W. W., K. A. Rainwater, and D. B. Thompson. Quantifying macropore recharge: examples from a semi-arid area. *Ground Water*, 35(6): 1097–1106, 1997.

Woolhiser, D. A. and J. A. Liggett. Unsteady one-dimensional flow over a plane—the rising hydrograph. *Water Resources Research*, 3(3): 753–771, 1967.

Yen, B. C. and C. W.-S. Tsai. On noninertia wave versus diffusion wave in flood routing. *Journal of Hydrology*, 244(1–2): 97–104, 2001.

Ypma, T. J. Historical development of the Newton-Raphson method. *SIAM Review*, 37(4): 531–551, 1995.

Zhang, W. and T. W. Cundy. Modeling of two-dimensional overland flow. *Water Resources Research*, 25(9): 2019–2035, 1989.

Zolfaghari, A. A., S. Mirzaee, and M. Gorji. Comparison of different models for estimating cumulative infiltration. *International Journal of Soil Sciences*, 7(3): 108–115, 2012.

Appendix A

Mathematical Supplements

A.1 Derivation of an Explicit First-Order Finite Difference Scheme for the Kinematic Wave Model

In the following example, the kinematic wave model is approximated by a first-order single-step explicit finite difference scheme (explicit Euler method). This is done in order to outline, in principle, the application of finite difference methods for the considered hydrodynamic models. Making use of the relationship $Q = uA$ and inserting Eq. (3.6) into Eq. (3.4) yields

$$0 = S_0 - \frac{Q^2}{K^2 R^{2\beta} A^2} \tag{A.1}$$

Rearranging Eq. (A.1) and solving for Q gives

$$Q = K S_0^{\frac{1}{2}} R^{\beta} A \tag{A.2}$$

and differentiating Eq. (A.2) with respect to x (product rule) leads to

$$\frac{\partial Q}{\partial x} = \left(\left(K S_0^{\frac{1}{2}} \beta R^{\beta-1} \frac{\partial R}{\partial x} A \right) + \left(K S_0^{\frac{1}{2}} R^{\beta} \frac{\partial A}{\partial x} \right) \right) \tag{A.3}$$

Assuming K and S to be constant, the dependent variables and their derivatives in Eq. (A.3) are approximated by means of first-order finite backward differences. Referring to Fig. A.1, the spatial differences of Eq. (A.2) are set up parallel to the abscissa (spatial dimension, indexed with i), solely addressing already known values in the time domain (which is indexed with j). If the unknown function value at a point $\mathrm{A}_{(i,j)}$ is sought, already known values of the temporal cut along $(\forall i, j-1)$ are taken into account. Assuming that the major portion of mass and momentum is transported in positive spatial direction, the values at D and C are influencing the solution at A. In turn, the temporal differences are set up along the ordinate (temporal dimension), including values at A (which are unknown) and D (which is located in the same spatial cut, $(i, \forall j)$). This approach only provides an accurate approximation if the CFL condition (Eq. (4.1)) is satisfied; in other words, the solution lies below a diagonal connection of the points C and A (i.e., a characteristic curve, cf. Section 4.1).

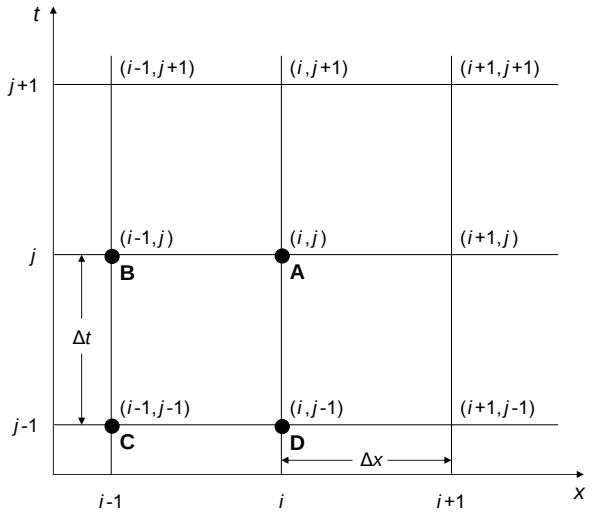

Figure A.1: Discretized solution domain of the explicit Euler method.

The corresponding finite difference quotients read

$$R \approx \left(\frac{R_{(i,j-1)} + R_{(i-1,j-1)}}{2} \right) \tag{A.4}$$

$$\frac{\partial R}{\partial x} \approx \frac{\Delta R}{\Delta x} = \left(\frac{R_{(i,j-1)} - R_{(i-1,j-1)}}{\Delta x} \right) \tag{A.5}$$

$$A \approx \left(\frac{A_{(i,j-1)} + A_{(i-1,j-1)}}{2} \right) \tag{A.6}$$

$$\frac{\partial A}{\partial x} \approx \frac{\Delta A}{\Delta x} = \left(\frac{A_{(i,j-1)} - A_{(i-1,j-1)}}{\Delta x} \right) \tag{A.7}$$

The temporal derivative of the cross-sectional area in the continuity equation (3.1) is approximated by

$$\frac{\partial A}{\partial t} \approx \frac{\Delta A}{\Delta t} = \left(\frac{A_{(i,j)} - A_{(i,j-1)}}{\Delta t} \right) \tag{A.8}$$

Inserting Eq. (A.3) into Eq. (3.1) and applying the relationships (A.4) to (A.8) delivers

$$\begin{aligned} &\left\{ K S_0^{\frac{1}{2}} \beta \left(\frac{R_{(i,j-1)} + R_{(i-1,j-1)}}{2} \right)^{\beta-1} \right. \\ &\left. \left(\frac{R_{(i,j-1)} - R_{(i-1,j-1)}}{\Delta x} \right) \left(\frac{A_{(i,j-1)} + A_{(i-1,j-1)}}{2} \right) \right\} + \\ &\left(K S_0^{\frac{1}{2}} \left(\frac{R_{(i,j-1)} + R_{(i-1,j-1)}}{2} \right)^{\beta} \left(\frac{A_{(i,j-1)} - A_{(i-1,j-1)}}{\Delta x} \right) \right) + \\ &\left(\frac{A_{(i,j)} - A_{(i,j-1)}}{\Delta t} \right) = 0 \end{aligned} \tag{A.9}$$

Solving Eq. (A.9) for $A_{(i,j)}$, which is the only unknown, delivers a relationship for $A_{(i,j)}$ where only known values appear on the left-hand side of the equation and $A_{(i,j)}$ is, therefore, given explicitly as

$$\begin{aligned} &-\Delta t \left\{ K S_0^{\frac{1}{2}} \beta \left(\frac{R_{(i,j-1)} + R_{(i-1,j-1)}}{2} \right)^{\beta-1} \right. \\ &\left. \left(\frac{R_{(i,j-1)} - R_{(i-1,j-1)}}{\Delta x} \right) \left(\frac{A_{(i,j-1)} + A_{(i-1,j-1)}}{2} \right) \right\} - \\ &\Delta t \left(K S_0^{\frac{1}{2}} \left(\frac{R_{(i,j-1)} + R_{(i-1,j-1)}}{2} \right)^{\beta} \left(\frac{A_{(i,j-1)} - A_{(i-1,j-1)}}{\Delta x} \right) \right) + \\ &A_{(i,j-1)} = A_{(i,j)} \end{aligned} \tag{A.10}$$

Consecutively, the initially unknown hydraulic radius $R_{(i,j)}$ can be obtained by employing two profile functions, as Eqs. (3.9) and (3.10), for establishing a lookup table of $\tilde{R}$ depending on $\tilde{A}$, i.e., $R_{(i,j)} = f\left(A_{(i,j)}\right)$ (cf. Section 3.4). The flow rate $Q_{(i,j)}$ can then be calculated by using a uniform flow equation such as Eq. (A.2). For calculating values for the whole spatiotemporal domain, it is feasible to first calculate the values of the dependent variables at all temporal nodes j for one spatial cut i (e.g., a cross section) and then proceed to $i+1$. Such an approach is represented by Algorithm 7.1.

In case there are inflows or losses (e.g., resulting from infiltration through a permeable bed), the extended continuity equation (3.7) is used. Defining a mean inflow/loss rate as

$$q^{\phi} \approx \left(\frac{q^{\phi}_{(i,j-1)} + q^{\phi}_{(i-1,j-1)}}{2} \right) \tag{A.11}$$

and employing Eqs. (3.7), (A.2), (A.4) to (A.8), and (A.11) leads—analogously to the previously outlined derivation—to the finite difference equation of the KW model with a source/sink term, postulating that inflows (gaining flows) are signed positive and losses negative:

$$\begin{aligned} &-\Delta t \left\{ K S_0^{\frac{1}{2}} \beta \left(\frac{R_{(i,j-1)} + R_{(i-1,j-1)}}{2} \right)^{\beta-1} \right. \\ &\left. \left(\frac{R_{(i,j-1)} - R_{(i-1,j-1)}}{\Delta x} \right) \left(\frac{A_{(i,j-1)} + A_{(i-1,j-1)}}{2} \right) \right\} - \\ &\Delta t \left(K S_0^{\frac{1}{2}} \left(\frac{R_{(i,j-1)} + R_{(i-1,j-1)}}{2} \right)^{\beta} \left(\frac{A_{(i,j-1)} - A_{(i-1,j-1)}}{\Delta x} \right) \right) - \\ &\left(\frac{q^{\phi}_{(i,j-1)} + q^{\phi}_{(i-1,j-1)}}{2} \right) + \\ &A_{(i,j-1)} = A_{(i,j)} \end{aligned} \tag{A.12}$$

The scheme exhibits a consistency order of $\mathcal{O}(\Delta x, \Delta t)$, since the spatial and temporal derivatives of the model equations are approximated by backward differences (Press et al., 1992).

A.2 Derivation of an Explicit Second-Order Finite Difference Scheme for the Kinematic Wave Model

Concisely, the Runge-Kutta method applied herein is a second-order scheme with intermediate nodes in the temporal domain, located at $\frac{1}{2}\Delta t$ (the so-called midpoint method). Using backward differences (as in Appendix A.1), the finite difference equations are first evaluated at the intermediate nodes $\left(i, j-\frac{1}{2}\right)$ and, in a second step, the results for the target node at (i,j) are calculated. Hence, the finite difference form of the KW model at $\left(i, j-\frac{1}{2}\right)$ reads

$$
\begin{aligned}
-\frac{1}{2}\Delta t \Bigg\{ K S_0^{\frac{1}{2}} \beta \left(\frac{R_{(i,j-1)} + R_{(i-1,j-1)}}{2} \right)^{\beta-1} \\
\left(\frac{R_{(i,j-1)} - R_{(i-1,j-1)}}{\Delta x} \right) \left(\frac{A_{(i,j-1)} + A_{(i-1,j-1)}}{2} \right) \Bigg\} - \\
\frac{1}{2}\Delta t \left(K S_0^{\frac{1}{2}} \left(\frac{R_{(i,j-1)} + R_{(i-1,j-1)}}{2} \right)^{\beta} \left(\frac{A_{(i,j-1)} - A_{(i-1,j-1)}}{\Delta x} \right) \right) - \\
\left(\frac{q^{\phi}_{(i,j-1)} + q^{\phi}_{(i-1,j-1)}}{2} \right) + \\
A_{(i,j-1)} = A_{(i,j-\frac{1}{2})}
\end{aligned}
\tag{A.13}
$$

As shown in Appendix A.1, $R_{(i,j-\frac{1}{2})}$ is obtained by using an empirical or analytical relationship of A and R. The values of the dependent variables at the spatiotemporal node (i,j) are calculated by

$$
\begin{aligned}
-\Delta t \Bigg\{ K S_0^{\frac{1}{2}} \beta \left(\frac{R_{(i,j-\frac{1}{2})} + R_{(i-1,j-\frac{1}{2})}}{2} \right)^{\beta-1} \\
\left(\frac{R_{(i,j-\frac{1}{2})} - R_{(i-1,j-\frac{1}{2})}}{\Delta x} \right) \left(\frac{A_{(i,j-\frac{1}{2})} + A_{(i-1,j-\frac{1}{2})}}{2} \right) \Bigg\} - \\
\Delta t \left(K S_0^{\frac{1}{2}} \left(\frac{R_{(i,j-\frac{1}{2})} + R_{(i-1,j-\frac{1}{2})}}{2} \right)^{\beta} \left(\frac{A_{(i,j-\frac{1}{2})} - A_{(i-1,j-\frac{1}{2})}}{\Delta x} \right) \right) - \\
\left(\frac{q^{\phi}_{(i,j-\frac{1}{2})} + q^{\phi}_{(i-1,j-\frac{1}{2})}}{2} \right) + \\
A_{(i,j-1)} = A_{(i,j)}
\end{aligned}
\tag{A.14}
$$

$A_{(i,j-\frac{1}{2})}$ is obtained with the help of Eq. (A.13). The term $A_{(i-1,j-\frac{1}{2})}$ is related to an already known spatial cut $(i-1, \forall j)$ which is, e.g., the upper boundary condition for $i-1=0$. Thus, the values of $A_{(i-1,j-\frac{1}{2})}$ can be calculated by linear interpolation:

$$
A_{(i-1,j-\frac{1}{2})} = \frac{A_{(i-1,j+1)} + A_{(i-1,j)}}{2} \tag{A.15}
$$

The outlined Runge-Kutta scheme exhibits a consistency order of $\mathcal{O}(\Delta x, \Delta t^2)$.

A.3 Basic Concept of an Implicit Finite Difference Scheme with Interior Point (Preissmann Scheme)

The Preissmann scheme (or box scheme) is a (third-order) four-point implicit scheme (i.e., the scheme incorporates initially unknown function values). Corresponding to Fig. A.2, space derivatives and function values are evaluated at the interior point E. Since the scheme is implicit, the CFL condition (Eq. (4.1)) does not apply and the employed time step can be significantly larger than for explicit schemes.

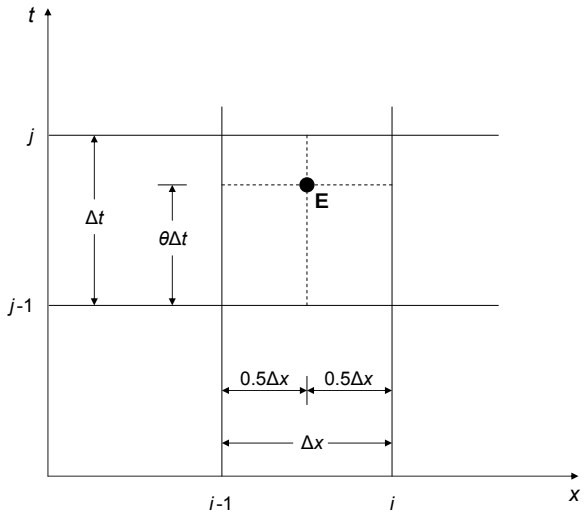

Figure A.2: Finite difference cell for the Preissmann (box) scheme.

Assuming Φ to be a general expression for the function of a specific dependent variable (e.g., $Q(x,t)$, $A(x,t)$, etc.), the implicit finite difference form for a time derivative reads

$$\frac{\partial \Phi}{\partial t} = \frac{\Delta \Phi}{\Delta t} = \frac{\left(\Phi_{(i-1,j)} + \Phi_{(i,j)}\right) - \left(\Phi_{(i-1,j-1)} + \Phi_{(i,j-1)}\right)}{2\Delta t} \tag{A.16}$$

for the space derivative

$$\frac{\partial \Phi}{\partial x} = \frac{\Delta \Phi}{\Delta x} = \frac{\theta\left(\Phi_{(i,j)} - \Phi_{(i-1,j)}\right)}{\Delta x} + \frac{(1-\theta)\left(\Phi_{(i,j-1)} - \Phi_{(i-1,j-1)}\right)}{\Delta x} \tag{A.17}$$

and for a function value

$$\Phi = \frac{\theta\left(\Phi_{(i,j)} + \Phi_{(i-1,j)}\right)}{2} + \frac{(1-\theta)\left(\Phi_{(i,j-1)} + \Phi_{(i-1,j-1)}\right)}{2} \tag{A.18}$$

where $\theta = [0, ..., 1]$ is the so-called implicit weighting factor.

It can be directly seen from Eqs. (A.17) and (A.18) that for $\theta = 0$ the scheme is fully explicit (i.e., only values of the known temporal cut at $j-1$ are regarded). Vice versa, for $\theta = 1$ the scheme is fully implicit, and only values from the initially unknown temporal level j are taken into account.

It can be proven that the difference scheme outlined above is (theoretically) unconditionally stable for $\theta > 0.5$ (Cunge et al., 1980; Fread, 1993), which means that the size of the chosen time interval does not affect stability. However, numerical damping increases for increased values of θ. In practice, non-stability of the scheme can occur independent from the selected value of θ. Factors that may endanger stability (and, therefore, convergence) include changes in the cross-sectional geometry, abruptly changing channel slopes, and characteristics of the boundary conditions (e.g., a steep flood wave).

Applying the previously outlined box scheme consequently leads to a system of (nonlinear) simultaneous equations. This system is usually linearized and the resulting system of linear equations is solved with a standard method, mostly based upon iteration (e.g., fixed-point iteration or Newton-Raphson method). For the implementations of the Preissmann scheme utilized herein, a fixed-point iteration scheme was applied. While the Preissmann scheme is based on each two spatial and temporal nodes, it exhibits a consistency order of $\mathcal{O}(\Delta x^2, \Delta t^2)$ (Cunge et al., 1980; Subramanya, 2009).

A.4 Analytical Solution of the Kinematic Wave Model by Obtaining Characteristic Solutions

The solution presented subsequently is following basic concepts outlined by Singh (1996). A rectangular cross section is assumed. Thus, the hydraulic radius equals the quotient of the wetted cross-sectional area and the wetted perimeter:

$$R = \frac{A}{P} \tag{A.19}$$

The momentum and continuity equations of the kinematic wave model for a flow without losses or inflows read

$$\frac{\partial A}{\partial t} + \frac{\partial Q}{\partial x} = 0 \tag{A.20}$$

$$S_\mathrm{f} = S_0 \tag{A.21}$$

and the momentum equation can be expressed by employing a friction law (cf. Sections 3.4 and Appendix A.1) in the form

$$A = \delta Q^\eta \tag{A.22}$$

where η is a coefficient depending on the cross-sectional geometry (Singh, 1996). For a wide rectangular cross section, η is $\frac{2}{3}$ (Miller, 1984). The coefficient δ is given by

$$\delta = \left(\frac{P^\beta}{K S^{\frac{1}{2}}} \right)^\eta \tag{A.23}$$

where β is the exponent of the employed friction law. By inserting Eq. (A.22) into Eq. (A.20), the continuity equation can be recast in such a way that Q is dependent on x:

$$\frac{\partial Q}{\partial x} + \delta\beta Q^{\eta-1} \left(\frac{\partial Q}{\partial t} \right) = 0 \tag{A.24}$$

or on t:

$$\frac{\partial Q}{\partial t} + \frac{1}{\delta\beta Q^{\eta-1}} \left(\frac{\partial Q}{\partial x} \right) = 0 \tag{A.25}$$

Calculating the total derivative of Q yields

$$\mathrm{d}Q = \frac{\partial Q}{\partial x}\mathrm{d}x + \frac{\partial Q}{\partial t}\mathrm{d}t \tag{A.26}$$

and dividing Eq. (A.26) by $\mathrm{d}t$ gives

$$\frac{\mathrm{d}Q}{\mathrm{d}t} = \frac{\partial Q}{\partial x}\frac{\mathrm{d}x}{\mathrm{d}t} + \frac{\partial Q}{\partial t} \tag{A.27}$$

Postulating a constant discharge (i.e., $\frac{\mathrm{d}Q}{\mathrm{d}t} = 0$), Eq. (A.27) can be set equal to Eq. (A.25):

$$\frac{\partial Q}{\partial x}\frac{\mathrm{d}x}{\mathrm{d}t} + \frac{\partial Q}{\partial t} = \frac{\partial Q}{\partial t} + \frac{1}{\delta\eta Q^{\eta-1}} \left(\frac{\partial Q}{\partial x} \right) \tag{A.28}$$

and subtracting by $\frac{\partial Q}{\partial t}$ as well as dividing by $\frac{\partial Q}{\partial x}$ yields

$$\frac{\mathrm{d}x}{\mathrm{d}t} = \frac{1}{\delta\eta Q^{\eta-1}} \tag{A.29}$$

The continuity equation (A.20) may be rewritten as

$$\frac{\partial x}{\partial t} = \frac{\partial Q}{\partial A} = \frac{\mathrm{d}x}{\mathrm{d}t} = \frac{\mathrm{d}Q}{\mathrm{d}A} \tag{A.30}$$

A constant discharge ($\frac{\mathrm{d}Q}{\mathrm{d}t} = 0$) is propagated along a straight line in (x, t), given by

$$\frac{\mathrm{d}x}{\mathrm{d}t} = \frac{1}{\delta\eta Q^{\eta-1}} = \frac{\mathrm{d}Q}{\mathrm{d}A} \tag{A.31}$$

Such a line is called characteristic line (cf. Section 4.1) and Eq. (A.31) is the characteristic equation of the kinematic wave model. The term

$$\frac{\mathrm{d}x}{\mathrm{d}t} = \frac{\mathrm{d}Q}{\mathrm{d}A} = \frac{1}{\delta\eta Q^{\eta-1}} = c_\kappa \tag{A.32}$$

describes the so-called *kinematic wave celerity* [LT^{-1}] and the relationship $c_\kappa = \frac{\mathrm{d}Q}{\mathrm{d}A}$ is called the Kleitz-Seddon law (Lighthill and Whitham, 1955). Under the assumed single-valued stage–discharge relationship, the wave celerity depends on the water depth alone, i.e., points of the wave profiles with the same depth travel with the same velocity.

Under the assumption of a rectangular cross section ($\mathrm{d}A = B\mathrm{d}h$), c_κ can be expressed in terms of the water depth:

$$c_\kappa = \frac{1}{B}\frac{\mathrm{d}Q}{\mathrm{d}h} \tag{A.33}$$

By applying the wide channel assumption ($R \approxeq h$), the Manning-Strickler formula ($\beta = \frac{2}{3}$) reads

$$Q = K_{\mathrm{St}} A R^\beta S_0^{\frac{1}{2}} = K_{\mathrm{St}} B h\, h^\beta S_{\mathrm{f}}^{\frac{1}{2}} = K_{\mathrm{St}} B h^{\frac{5}{3}} S_0^{\frac{1}{2}} \tag{A.34}$$

and solving this expression for for h yields

$$h = \left(\frac{Q}{K_{\mathrm{St}} B S_0^{\frac{1}{2}}}\right)^{\frac{3}{5}} \tag{A.35}$$

Calculating the derivative of Q with respect to h delivers

$$\frac{\mathrm{d}Q}{\mathrm{d}h} = \frac{5}{3} K_{\mathrm{St}} B S_0^{\frac{1}{2}} h^{\frac{2}{3}} \tag{A.36}$$

and expressing h by means of Q by using Eq. (A.35) gives

$$\frac{\mathrm{d}Q}{\mathrm{d}h} = \frac{5}{3} K_{\mathrm{St}} B S_0^{\frac{1}{2}} \left(\frac{Q}{K_{\mathrm{St}} B S_0^{\frac{1}{2}}}\right)^{\frac{2}{5}} \tag{A.37}$$

This way, the kinematic wave celerity c_κ can be expressed in terms of Q:

$$c_\kappa = \frac{1}{B}\frac{\mathrm{d}Q}{\mathrm{d}h} = \frac{1}{B}\frac{5}{3}K_{\mathrm{St}}BS_0^{\frac{1}{2}}\left(\frac{Q}{K_{\mathrm{St}}BS_0^{\frac{1}{2}}}\right)^{\frac{2}{5}} = \frac{1}{B}\frac{5}{3}K_{\mathrm{St}}BS_0^{\frac{1}{2}}\left(\frac{1}{K_{\mathrm{St}}BS_0^{\frac{1}{2}}}\right)^{\frac{2}{5}}Q^{\frac{2}{5}} = \mu Q^{\frac{2}{5}} \tag{A.38}$$

where μ is a constant factor for a channel reach with no changes in roughness, slope, and cross-sectional geometry.

The solution for $Q(x,t)$ requires the specification of initial conditions, i.e., $Q(x,t=0)$, and boundary conditions, i.e., $Q(x=0,t)$. A cross section at $x=L$ is considered, where L [L] is the distance between this cross section and the location of the upper inflow boundary. To predict the flow at $x=L$, the function $Q(L,t)$ is sought. Assuming a constant c_κ[1], the equation of the kinematic wave celerity reads[2]

$$\frac{\mathrm{d}x}{\mathrm{d}t} = c_\kappa(Q) \tag{A.39}$$

Integration of Eq. (A.39) on the interval $[0,...,L] = x$ reads

$$\int_0^L \mathrm{d}x = \int_{t_\mathrm{u}(Q)}^{t_\mathrm{d}(Q)} c_\kappa(Q)\mathrm{d}t \tag{A.40}$$

and yields

$$L = \left(t_\mathrm{d}(Q) - t_\mathrm{u}(Q)\right)c_\kappa(Q) \tag{A.41}$$

Rearranging delivers

$$t_\mathrm{d}(Q) = t_\mathrm{u}(Q) + \frac{L}{c_\kappa(Q)} \tag{A.42}$$

where $t_\mathrm{d}(Q)$ indicates the time which a specific inflow $Q(t_\mathrm{u})$ needs for traveling the distance L. Combining Eqs. (A.42) and (A.38) gives

$$t_\mathrm{d}(Q) = t_\mathrm{u}(Q) + \frac{L}{\mu Q^{\frac{2}{5}}} \tag{A.43}$$

which is an analytical solution of the kinematic wave model for variable (but—as a consequence of the KW assumptions—quasisteady) inflows. According to the previously demanded restrictions (wide rectangular channel), the model preserves a specific inflow value and the flow process is governed solely by advection. If c_κ were not exclusively dependent on Q, which would be the case, e.g., if lateral sources/sinks were regarded in the continuity equation (cf. Section 3.5), the characteristic lines would become characteristic curves and a specific inflow value is modified in space and time.

[1] This yields a *linear* kinematic wave model.

[2] Compare the similarity of Eq. (A.39) to the definition of the Courant number, Eq. (4.2).

A.5 Details on the Derivation of the Iterative Procedure (5.47);(5.48)

Using the relationships given by Eqs. (5.17), (5.21), (5.38), and (5.44), Eq. (5.37) can be briefly expressed as

$$A_{0,n} = A_0(t_n) = A(0,t_n) = p_1(0)^{-\frac{1}{p_2}} \left(-\rho_0(t)\frac{\lambda\psi_n}{p_2}\right)^{\frac{1}{\lambda}} \tag{A.44}$$

Based on the hydraulic principle $u = \frac{Q}{A}$ and using the expression for the hydraulic radius given by Eq. (5.6), Eq. (5.17) can be written as

$$-\rho_0(t) = \frac{(Q_0(t_n))^2}{K^2\,(A_0(t_n))^2} - \left(S_0 + \frac{q_0^{\phi}(t_n)Q_0(t_n)}{g\,(A_0(t_n))^2}\right) p_3(0)^{2\beta}\,(A_0(t_n))^{2\beta p_4} \tag{A.45}$$

Inserting Eq. (A.45) into Eq. (A.44) yields

$$A(0,t_n) = p_1(0)^{-\frac{1}{p_2}} \left\{\frac{\lambda\psi_n}{p_2}\left\{\frac{(Q_0(t_n))^2}{K^2\,(A_0(t_n))^2} - \left(S_0 + \frac{q_0^{\phi}(t_n)Q_0(t_n)}{g\,(A_0(t_n))^2}\right) p_3(0)^{2\beta}\,(A_0(t_n))^{2\beta p_4}\right\}\right\}^{\frac{1}{\lambda}} \tag{A.46}$$

which is equivalent to the expression

$$(A(0,t_n))^{\lambda} = p_1(0)^{-\frac{\lambda}{p_2}} \left\{\frac{\lambda\psi_n}{p_2}\left\{\frac{(Q_0(t_n))^2}{K^2\,(A_0(t_n))^2} - \left(S_0 + \frac{q_0^{\phi}(t_n)Q_0(t_n)}{g\,(A_0(t_n))^2}\right) p_3(0)^{2\beta}\,(A_0(t_n))^{2\beta p_4}\right\}\right\} \tag{A.47}$$

Multiplying both sides of Eq. (A.47) by $(A(0,t_n))^2$ yields

$$(A(0,t_n))^{2+\lambda} = p_1(0)^{-\frac{\lambda}{p_2}} \left\{\frac{\lambda\psi_n}{p_2}\left\{\frac{(Q_0(t_n))^2}{K^2} - \left(S_0 + \frac{q_0^{\phi}(t_n)Q_0(t_n)}{g\,(A_0(t_n))^2}\right) p_3(0)^{2\beta}\,(A_0(t_n))^{2\beta p_4+2}\right\}\right\} \tag{A.48}$$

and multiplying both sides of Eq. (A.48) by $p_1(0)^{\frac{\lambda}{p_2}} p_2$ leads to

$$(A(0,t_n))^{2+\lambda}\, p_1(0)^{\frac{\lambda}{p_2}} p_2 = \lambda\psi_n \left\{\frac{(Q_0(t_n))^2}{K^2} - \left(S_0 + \frac{q_0^{\phi}(t_n)Q_0(t_n)}{g\,(A_0(t_n))^2}\right) p_3(0)^{2\beta}\,(A_0(t_n))^{2\beta p_4+2}\right\} \tag{A.49}$$

which can be recast to

$$\lambda\psi_n \frac{\left(Q_0(t_n)\right)^2}{K^2} = \left(A(0,t_n)\right)^{2+\lambda} p_1(0)^{\frac{\lambda}{p_2}} p_2 + \lambda\psi_n \left(S_0 + \frac{q_0^{\phi}(t_n) Q_0(t_n)}{g\left(A_0(t_n)\right)^2} \right) p_3(0)^{2\beta} \left(A_0(t_n)\right)^{2\beta p_4 + 2} \quad \text{(A.50)}$$

Based on Eq. (5.21), it holds true that $2\beta p_4 + p_2 = \lambda$ and, therefore, $2\beta p_4 + 2 = \lambda - p_2 + 2$. Equation (A.50) can now be written as

$$\lambda\psi_n \frac{\left(Q_0(t_n)\right)^2}{K^2} = \left(A(0,t_n)\right)^{2+\lambda} p_1(0)^{\frac{\lambda}{p_2}} p_2 + \lambda\psi_n \left(S_0 + \frac{q_0^{\phi}(t_n) Q_0(t_n)}{g\left(A_0(t_n)\right)^2} \right) p_3(0)^{2\beta} \left(A_0(t_n)\right)^{\lambda - p_2 + 2} \quad \text{(A.51)}$$

which equals

$$\lambda\psi_n \frac{\left(Q_0(t_n)\right)^2}{K^2} = \left(A(0,t_n)\right)^{2+\lambda} \left\{ p_1(0)^{\frac{\lambda}{p_2}} p_2 + \lambda\psi_n \left(S_0 + \frac{q_0^{\phi}(t_n) Q_0(t_n)}{g\left(A_0(t_n)\right)^2} \right) \frac{p_3(0)^{2\beta}}{\left(A_0(t_n)\right)^{p_2}} \right\} \quad \text{(A.52)}$$

Equation (A.52) can be solved for $\left(A(0,t_n)\right)^{2+\lambda}$ which yields

$$\left(A(0,t_n)\right)^{2+\lambda} = \frac{\lambda\psi_n \left(\frac{Q_0(t_n)}{K}\right)^2}{p_1(0)^{\frac{\lambda}{p_2}} p_2 + \lambda\psi_n \left(S_0 + \frac{q_0^{\phi}(t_n) Q_0(t_n)}{g\left(A_0(t_n)\right)^2} \right) \frac{p_3(0)^{2\beta}}{\left(A(0,t_n)\right)^{p_2}}} \quad \text{(A.53)}$$

which equals

$$A(0,t_n) = \left(\frac{\lambda\psi_n \left(\frac{Q_0(t_n)}{K}\right)^2}{p_1(0)^{\frac{\lambda}{p_2}} p_2 + \lambda\psi_n \left(S_0 + \frac{q_0^{\phi}(t_n) Q_0(t_n)}{g\left(A_0(t_n)\right)^2} \right) \frac{p_3(0)^{2\beta}}{\left(A(0,t_n)\right)^{p_2}}} \right)^{\frac{1}{2+\lambda}} \quad \text{(A.54)}$$

which can be rewritten as the iteration equation (5.47):

$$A_{0,n}^{(k)} = \left(\frac{\lambda\psi_n \left(\frac{Q_0\left(t_n^{(k-1)}\right)}{K}\right)^2}{p_2 p_1(0)^{\frac{\lambda}{p_2}} + \lambda\psi_n \left(S_0 + \frac{q_0^{\phi}\left(t_n^{(k-1)}\right) Q_0\left(t_n^{(k-1)}\right)}{g\left(A_{0,n}^{(k-1)}\right)^2} \right) \frac{p_3(0)^{2\beta}}{\left(A_{0,n}^{(k-1)}\right)^{p_2}}} \right)^{\frac{1}{2+\lambda}} \quad \text{(A.55)}$$

The second equation of the iterative procedure (5.47);(5.48) is derived using the continuity equation for the permeable channel (5.46). The inflow volume to the wadi over time can be calculated by

$$\int_0^{t_n^{(k)}} Q_0(\tau)\mathrm{d}\tau = \int_0^{t_n^{(k-1)}} Q_0(\tau)\mathrm{d}\tau + \int_{t_n^{(k-1)}}^{t_n^{(k)}} Q_0(\tau)\mathrm{d}\tau \quad \text{(A.56)}$$

The expression $\int_{t_n^{(k-1)}}^{t_n^{(k)}} Q_0(\tau)\mathrm{d}\tau$ may be written as $Q_0\left(t_n^{(k-1)}\right)\left(t_n^{(k)} - t_n^{(k-1)}\right)$ which allows to rewrite Eq. (A.56) as

$$\int_0^{t_n^{(k)}} Q_0(\tau)\mathrm{d}\tau = \int_0^{t_n^{(k-1)}} Q_0(\tau)\mathrm{d}\tau + Q_0\left(t_n^{(k-1)}\right)\left(t_n^{(k)} - t_n^{(k-1)}\right) \tag{A.57}$$

Setting the inflow volume, given by the right-hand side of Eq. (A.57), equal to the volume of water in the channel plus the infiltration volume, given by the right-hand side of Eq. (5.46), delivers

$$\int_0^{t_n^{(k-1)}} Q_0(\tau)\mathrm{d}\tau + Q_0\left(t_n^{(k-1)}\right)\left(t_n^{(k)} - t_n^{(k-1)}\right) = A_{0,n}\omega_n + \int_0^{t_n}\int_0^{x_n} q^{\phi}(\xi,\tau)\mathrm{d}\xi\mathrm{d}\tau \tag{A.58}$$

which can be straightforwardly rearranged to yield the second iteration equation (5.48):

$$t_n^{(k)} = t_n^{(k-1)} + \frac{A_{0,n}^{(k)}\omega_n + \int_0^{t_n^{(k-1)}}\int_0^{x_n} q^{\phi}(\xi,\tau)\mathrm{d}\xi\mathrm{d}\tau - \int_0^{t_n^{(k-1)}} Q_0(\tau)\mathrm{d}\tau}{Q_0\left(t_n^{(k-1)}\right)} \tag{A.59}$$

A.6 Details on the Evaluation of the First Integrand in Equation (5.60)

Using a continuous formulation, Eq. (5.65) can be written as

$$h(x,t) = h_0\sqrt{1-\frac{x}{x_{\mathrm{tip}}}} \tag{A.60}$$

where both h_0 and x_{tip} depend on time. Differentiating Eq. (A.60) with respect to t, therefore, yields

$$\frac{\partial h}{\partial t} = \frac{\mathrm{d}h_0}{\mathrm{d}t}\sqrt{1-\frac{x}{x_{\mathrm{tip}}}} + \frac{h_0}{2\sqrt{1-\frac{x}{x_{\mathrm{tip}}}}}\frac{x}{x_{\mathrm{tip}}^2}u_{\mathrm{tip}} \tag{A.61}$$

This result can be inserted for the first integrand in Eq. (5.60):

$$\int_0^x \frac{\partial h}{\partial t}(\xi,t)\mathrm{d}\xi = \frac{\mathrm{d}h_0}{\mathrm{d}t}\int_0^x \sqrt{1-\frac{\xi}{x_{\mathrm{tip}}}}\mathrm{d}\xi + \frac{h_0 u_{\mathrm{tip}}}{2x_{\mathrm{tip}}^2}\int_0^x \frac{\xi}{\sqrt{1-\frac{\xi}{x_{\mathrm{tip}}}}}\mathrm{d}\xi \tag{A.62}$$

Both integrals on the right-hand side of Eq. (A.62) can be explicitly evaluated (Bronstein and Semendjajev, 1966) and the resulting expression reads

$$\begin{aligned}\int_0^x \frac{\partial h}{\partial t}(\xi,t)\mathrm{d}\xi &= -\frac{2}{3}x_{\mathrm{tip}}\frac{\mathrm{d}h_0}{\mathrm{d}t}\left(\left(1-\frac{x}{x_{\mathrm{tip}}}\right)^{\frac{3}{2}}-1\right) - \frac{1}{3}u_{\mathrm{tip}}h_0\left(\left(2+\frac{x}{x_{\mathrm{tip}}}\right)\sqrt{1-\frac{x}{x_{\mathrm{tip}}}}-2\right)\\ &= \frac{2}{3}\frac{\mathrm{d}}{\mathrm{d}t}(x_{\mathrm{tip}}h_0) - \frac{2}{3}x_{\mathrm{tip}}\frac{\mathrm{d}h_0}{\mathrm{d}t}\left(1-\frac{x}{x_{\mathrm{tip}}}\right)^{\frac{3}{2}} - \frac{1}{3}u_{\mathrm{tip}}h_0\left(2+\frac{x}{x_{\mathrm{tip}}}\right)\sqrt{1-\frac{x}{x_{\mathrm{tip}}}}\end{aligned} \tag{A.63}$$

The first term on the right-hand side of Eq. (A.63) equals $Q_0 - \int_0^{x_{\mathrm{tip}}} q^{\phi}(\xi,t)\mathrm{d}\xi$, which can be seen from Eq. (5.62). Consequently, Eq. (5.60) can be simplified to

$$Q(x,t) = \frac{2}{3}x_{\mathrm{tip}}\frac{\mathrm{d}h_0}{\mathrm{d}t}\left(1-\frac{x}{x_{\mathrm{tip}}}\right)^{\frac{3}{2}} + \frac{1}{3}u_{\mathrm{tip}}h_0\left(2+\frac{x}{x_{\mathrm{tip}}}\right)\sqrt{1-\frac{x}{x_{\mathrm{tip}}}} + \int_x^{x_{\mathrm{tip}}} q^{\phi}(\xi,t)\mathrm{d}\xi \tag{A.64}$$

Appendix B

Selected Publications of the Author

Page 159

Philipp, A., G. H. Schmitz, and R. Liedl

Analytical Model of Surge Flow in Nonprismatic Permeable Channels and Its Application in Arid Regions

Journal of Hydraulic Engineering, 136(5): 290–298, 2010. With permission from ASCE.

Page 169

Philipp, A., R. Liedl, and T. Wöhling

Analytical Model of Surface Flow on Hillslopes Based on the Zero-Inertia Equations

Journal of Hydraulic Engineering, 138(5): 391–399, 2012. With permission from ASCE.

Page 179

Philipp, A. and J. Grundmann

Integrated Modeling System for Flash Flood Routing in Ephemeral Rivers under the Influence of Groundwater Recharge Dams

Journal of Hydraulic Engineering, 139(12), 2013. With permission from ASCE.

Analytical Model of Surge Flow in Nonprismatic Permeable Channels and Its Application in Arid Regions

A. Philipp[1]; G. H. Schmitz[2]; and R. Liedl[3]

Abstract: A surge running down a dry wadi bed as a consequence of a controlled water release from a reservoir—e.g., for artificial groundwater recharge—represents a free boundary problem. After some time, when aiming for groundwater recharge, the infiltration equals inflow and thus forms a kind of "standing" wave. The numerical solution of such phenomena generally involves considerable problems. For avoiding the numerical inconvenience resulting from the complex interacting surface/subsurface flow, we present an analytical solution of the slightly modified zero-inertia (ZI) equations. The development introduces a momentum-representative cross section for portraying the transient development of momentum and refers to a channel with constant slope, irregular geometry, and a permeable channel bed with significant infiltration. Due to the structure of the solution, any arbitrary infiltration model can be used for quantifying the infiltration losses. For both synthetic prismatic and nonprismatic test channels, the robust and easy-to-use analytical ZI model shows an excellent match with the results of a comparative numerical simulation. Finally, the ZI model is employed for simulating a surge flow downstream of the Wadi Ahin groundwater recharge dam (Oman), in order to perform a scenario for artificial groundwater recharge in a natural wadi channel reach. This realistic application illustrates the potential of the new approach by even computing an almost standing wave and shows its applicability for an accurate and robust evaluation of release strategies.

DOI: 10.1061/(ASCE)HY.1943-7900.0000172

CE Database subject headings: Surge; Groundwater recharge; Infiltration; Channels; Arid land.

Author keywords: Surge flow; Artificial groundwater recharge; Zero-inertia equations; Infiltration; Nonprismatic channels; Wadi flow.

Introduction

Surge flow problems have been treated by a variety of approaches. Existing models can be grouped into four classes—volume balance, kinematic, zero-inertia (ZI), and full dynamic models. For example, Schmitz et al. (2002) underline the applicability of ZI models for surge flow phenomena. Despite the simplifications of the ZI flow description, the solution of the underlying equations often requires numerical techniques due to complex hydraulics (Katopodes and Strelkoff 1977; Jaynes 1986). Many writers, such as Henderson (1966), Schmitz and Seus (1990), and Schmitz et al. (2002), developed analytical solutions for the ZI equations for prismatic and nonprismatic channels, however, without considering the impact of significant infiltration losses.

In arid regions, water resources are limited and the shortage of water has always been one of the most important restricting factors for socioeconomic development. Since the growing water demand in arid and semiarid regions cannot always be covered by available surface water, groundwater has been extensively used. In some areas, the amount of extracted groundwater has exceeded the natural groundwater recharge; socioeconomic changes, population growth, and ongoing urbanization will lead to enhanced water stress (Kowsar 1991; Kowsar 1996; Battashi and Rashid 1998; Bouwer 2002; Haimerl and Zunic 2002; Haimerl 2004) and make technical solutions for enhanced groundwater recharge indispensable. One of the most economic and effective methods of groundwater recharge is the controlled releasing of stored flood water in natural channels downstream of recharge dams which creates a surge traveling down the channel.

This study focuses on the development and the application of an analytical model for the surge flow in permeable nonprismatic channels. We use an analytical solution of the slightly modified ZI equations and employ the model for describing the surge flow in the presence of significant infiltration such as surge flow in a permeable wadi channel for artificial groundwater recharge from a reservoir. Furthermore, the model's analytical character allows the straightforward incorporation of any infiltration model.

Analytical Model

The unsteady surge flow in an irregular river bed with water losses through the bottom can be described by the extended ZI equations

$$\frac{\partial A}{\partial t} + \frac{\partial Q}{\partial x} = -q \tag{1}$$

$$\frac{\partial h}{\partial x} = S_0 - \frac{u^2}{K^2 R^{2\beta}} + \frac{qu}{gA} \tag{2}$$

in which t=time $[T]$; x=longitudinal space coordinate $[L]$; $A(x,t)$=wetted cross-sectional area $[L^2]$; $Q(x,t)$=discharge

[1]Research Associate, Chair of Hydrology, Technische Univ. Dresden, 01187 Dresden, Germany (corresponding author). E-mail: andy.philipp@tu-dresden.de

[2]Professor for Hydrology, Technische Univ. Dresden, 01187 Dresden, Germany. E-mail: muich@rcs1.urz.tu-dresden.de

[3]Professor for Groundwater Management, Technische Univ. Dresden, 01277 Dresden, Germany. E-mail: rudolf.liedl@mailbox.tu-dresden.de

Note. This manuscript was submitted on December 19, 2008; approved on October 27, 2009; published online on October 29, 2009. Discussion period open until October 1, 2010; separate discussions must be submitted for individual papers. This paper is part of the ***Journal of Hydraulic Engineering***, Vol. 136, No. 5, May 1, 2010. ©ASCE, ISSN 0733-9429/2010/5-290–298/$25.00.

$[L^3T^{-1}]$; $u(x,t)$=flow velocity $[LT^{-1}]$; $h(x,t)$=water depth $[L]$; q=volumetric rate of infiltration per unit width $[L^2T^{-1}]$; $R(x,t)$=hydraulic radius $[L]$; K=velocity coefficient $[L^{1-\beta}T^{-1}]$; S_0=bottom slope $[-]$; g=acceleration due to Earth's gravity $[LT^{-2}]$; and β=exponent of the flow formula $[-]$ (e.g., for the Manning-Strickler equation $\beta=2/3$).

In contrast to the standard ZI equations (e.g., Katopodes and Strelkoff 1977), Eqs. (1) and (2) each contain an additional term for quantifying the impact of water losses through the bottom of the river bed on volume and momentum conservation. Furthermore, the inclusion of the qu/gA term in the analytical development (2) does not cause any inconvenience. Including this term allows incorporating inflow with significant momentum contribution to the channel under arbitrary angles. This maintains the generality of the solution. For the presented application of the model, the term qu/gA could be omitted.

The first step toward a solution of the system [Eqs. (1) and (2)] is to multiply Eq. (2) by $R^{2\beta}$ yielding

$$R^{2\beta}\frac{\partial h}{\partial x}=\left(S_0+\frac{qu}{gA}\right)R^{2\beta}-\frac{u^2}{K^2} \tag{3}$$

According to Schmitz et al. (2002) the inflow boundary can be considered as a kind of momentum-representative cross section for surge flow problems. In this approach, the momentum (which is set equal to zero in the kinematic wave analysis) described by the right-hand side of Eq. (3) is continuously represented by the transient amount of momentum at $x=0$. Thus, the right-hand side of Eq. (3) no longer depends explicitly on x and Eq. (3) can be expressed as

$$R^{2\beta}\frac{\partial h}{\partial x}=\left(S_0+\frac{q_0u_0}{gA_0}\right)R_0^{2\beta}-\frac{u_0^2}{K^2}=\left(S_0-\frac{u_0^2}{K^2R_0^{2\beta}}+\frac{q_0u_0}{gA_0}\right)R_0^{2\beta} \tag{4}$$

with $A_0=A_0(t)=A(x=0,t)$; $R_0=R_0(t)=R(x=0,t)$; $u_0=u_0(t)=u(x=0,t)$; and $q_0=q_0(t)=q(x=0,t)$. The expression on the right-hand side of Eq. (4) may be regarded as the measure of the transient momentum at $x=0$ covering contributions from the bottom slope, friction, and infiltration through the river bed.

The description of the arbitrarily varying cross sections of the river uses the relationships

$$\tilde{h}(x,A)=h(x,t)=p_1(x)A(x,t)^{p_2} \tag{5}$$

$$\tilde{R}(x,A)=R(x,t)=p_3(x)A(x,t)^{p_4} \tag{6}$$

with $p_1(x)$, p_2, $p_3(x)$, and p_4=geometry parameters for describing the water depth and hydraulic radius of a river cross section. These are expressed in Eqs. (5) and (6) by the functions which depend on the spatial coordinate x and the wetted cross-sectional area $A=A(x,t)$. For formal reasons, the functions characterizing the cross-sectional geometry are distinguished from the functions $h(x,t)$ and $R(x,t)$ which explicitly relate the water depth and hydraulic radius to the independent variables of space and time.

Schmitz et al. (2002) showed that irregular cross sections of natural river beds can be closely approximated by adjusting the free parameters $p_1(x)$, p_2, $p_3(x)$, and p_4 of Eqs. (5) and (6). In particular, $p_1(x)$ and $p_3(x)$ take care of the nonprismatic character of the river bed. The values of p_2 and p_4 are not dependent on the space variable and account for some kind of common property, which is most evident for basic cross-sectional geometries, e.g., $p_2=p_4=1/2$ for a triangular, 2/3 for a parabolic, and 1 for a rectangular cross section. The practical adjustment of the geometry parameters for a nonprismatic channel is shown in the "Model Applications" section.

The system of partial differential equations (1) and (4) requires the specification of initial and boundary conditions. At the fixed upstream boundary ($x=0$), the boundary condition is

$$Q(0,t)=Q_0(t) \tag{7}$$

with the restriction that strongly falling discharge hydrographs cannot be used as an upstream boundary condition due to the ZI assumptions (Schmitz et al. 2002). At the downstream moving boundary, $x=x_{tip}(t)$, the following conditions have to be satisfied:

$$A(x_{tip},t)=0 \tag{8}$$

$$u(x_{tip})=u_{tip}(t)=\frac{dx_{tip}}{dt} \tag{9}$$

with $x_{tip}(t)$ and $u_{tip}(t)$ denoting the location and the velocity of the wave front, respectively.

The initial condition of the surge flow problem is

$$x_{tip}(t=0)=0 \tag{10}$$

Using the expression for the hydraulic radius as defined by Eq. (6), the solution of the momentum Eq. (4) reads

$$A(x,t)=p_1(x)^{-1/p_2}\left\{\left(1+\frac{2\beta p_4}{p_2}\right)\left(\frac{u_0^2}{K^2R_0^{2\beta}}-S_0-\frac{q_0u_0}{gA_0}\right)\cdot R_0^{2\beta}\int_x^{x_{tip}(t)}\left(\frac{p_1(\xi)^{p_4/p_2}}{p_3(\xi)}\right)^{2\beta}d\xi\right\}^{1/(p_2+2\beta p_4)} \tag{11}$$

Next, considering the upstream boundary condition (7), a direct integration of the continuity Eq. (1) yields the discharge $Q(x,t)$ as

$$Q(x,t)=Q_0(t)-\int_0^x\left[\frac{\partial A}{\partial t}(\xi,t)+q(\xi,t)\right]d\xi \tag{12}$$

where the integrand can be obtained by differentiating Eq. (11) with respect to t. Eqs. (11) and (12) solve the system [Eqs. (1) and (4)] and also satisfy boundary conditions (7) and (9). This solution accounts for the hydraulic feedback between the advance of a surge over an initially dry river bed and water losses due to the infiltration across the continuously extending wetted river bottom.

Iterative Solution of the Nonlinear Problem

The solution procedure for Eqs. (11) and (12) first requires evaluating the position of the advancing wave front $x_{tip}(t)$ and the wetted cross-sectional area $A_0(t)=A(x=0,t)$ at the inflow boundary by solving a nonlinear system of two equations iteratively. For this purpose, N observation points $(0<x_1<x_2<\cdots<x_N)$ are defined, the arrival time of the wave tip t_n for each observation point, i.e., $x_{tip}(t_n)=x_n$ (for $n=1,2,\ldots,N$), and the corresponding wetted cross-sectional area $A_{0,n}=A_0(t_n)$ at $x=0$ is calculated. The first of the aforementioned nonlinear equations is obtained by setting $x=0$ in Eq. (11). Making use of relationships (4) and (6) yields

$$A_{0,n} = p_1(0)^{-1/p_2}\left\{\left(1+\frac{2\beta p_4}{p_2}\right)\cdot s_n\left[\frac{Q_0(t_n)^2}{K^2 A_{0,n}^2} - \left(S_0 + \frac{q_0(t_n)Q_0(t_n)}{gA_{0,n}^2}\right)p_3(0)^{2\beta}A_{0,n}^{2\beta p_4}\right]\right\}^{1/(p_2+2\beta p_4)} \quad (13)$$

with

$$s_n = \int_0^{x_n}\left[\frac{p_1(\xi)^{p_4/p_2}}{p_3(\xi)}\right]^{2\beta} d\xi \quad (14)$$

The second equation is derived from the volume balance

$$\int_0^{t_n} Q_0(\tau)d\tau = A_{0,n}\omega_n + \int_0^{t_n}\int_0^{x_n} q(\xi,\tau)d\xi d\tau \quad (15)$$

where the abbreviation

$$\omega_n = \int_0^{x_n}\left[\frac{p_1(0)}{p_1(\xi)}\right]^{1/p_2}\left\{1-\frac{1}{s_n}\int_0^{\xi}\left[\frac{p_1(\tilde{\xi})^{p_4/p_2}}{p_3(\tilde{\xi})}\right]^{2\beta} d\tilde{\xi}\right\}^{1/(p_2+2\beta p_4)} d\xi \quad (16)$$

is used. Rearranging Eqs. (13) and (15) leads to the iterative procedure

$$A_{0,n}^{(k)} = \left(\frac{\left(1+\frac{p_1(0)}{p_1(\xi)}\right)s_n\left[\frac{Q_0(t_n^{(k-1)})^2}{K}\right]}{p_1(0)^{[1+(2\beta p_4/p_2)]} + \left(1+\frac{2\beta p_4}{p_2}\right)s_n\left[S_0+\frac{q_0(t_n^{(k-1)})Q_0(t_n^{(k-1)})}{g\cdot(A_{0,n}^{(k-1)})^2}\right]\frac{p_3(0)^{2\beta}}{(A_{0,n}^{(k-1)})^{p_2}}}\right)^{1/(2+p_2+2\beta p_4)} \quad (17)$$

$$t_n^{(k)} = t_n^{(k-1)} + \frac{A_{0,n}^{(k)}\omega_n + \int_0^{t_n^{(k-1)}}\int_0^{x_n} q(\xi,\tau)d\xi d\tau - \int_0^{t_n^{(k-1)}} Q_0(\tau)d\tau}{Q_0(t_n^{(k-1)})} \quad (18)$$

where $k=1,2,3,\ldots$ denotes the iteration index. A Taylor series expansion of the left-hand side of Eq. (15) around $t_n^{(k-1)}$ was included in order to take into account the impact of infiltration through pervious river beds. Starting values are provided by the results obtained from the preceding time step, i.e., $A_{0,n}^{(0)}=A_{0,n-1}$ and $t_n^{(0)}=t_{n-1}$. After the convergence of the iteration procedure [Eqs. (17) and (18)] is achieved, the wetted cross-sectional area $A(x,t_n)$ can be straightforwardly computed from

$$A(x,t_n) = A_0(t_n)\left[\frac{p_1(0)}{p_1(x)}\right]^{1/p_2}\left\{\frac{\int_x^{x_n}\left[\frac{p_1(\xi)^{p_4/p_2}}{p_3(\xi)}\right]^{2\beta} d\xi}{\int_0^{x_n}\left[\frac{p_1(\xi)^{p_4/p_2}}{p_3(\xi)}\right]^{2\beta} d\xi}\right\}^{1/(p_2+2\beta p_4)} = A_{0,n}\left[\frac{p_1(0)}{p_1(x)}\right]^{1/p_2}\left\{1-\frac{1}{s_n}\int_0^{x_n}\left[\frac{p_1(\xi)^{p_4/p_2}}{p_3(\xi)}\right]^{2\beta} d\xi\right\}^{1/(p_2+2\beta p_4)} \quad (19)$$

making use of Eqs. (11) and (14). Eq. (19) is inserted into Eq. (12) to compute the discharge $Q(x,t)$. This step includes a numerical integration and, in addition, requires either some standard formula, e.g., Kostiakov-Lewis, or some other problem-specific functional relationship quantifying the infiltration rate $q(\xi,\tau)$.

Table 1. Geometric Profile Data and Inflow Hydrograph for the Prismatic (Parabolic) Test Channel

Geometric profile data	
Velocity coefficient K ($m^{1/3}/s$)	33.33
Channel slope S_0 (m/m)	0.002
Cross-sectional parameter p_1 (m^{1-2p_2})	0.2823
Cross-sectional parameter p_2 [−]	2/3
Cross-sectional parameter p_3 (m^{1-2p_4})	0.1870
Cross-sectional parameter p_4 [−]	2/3
Channel length (m)	2,000
Cross-section type	Parabolic

Upstream inflow hydrograph	
t (s)	Q (m^3/s)
0	0
300	0.5
600	1.0
900	1.5
1,800	2.5
2,700	4.5
3,600	4.5

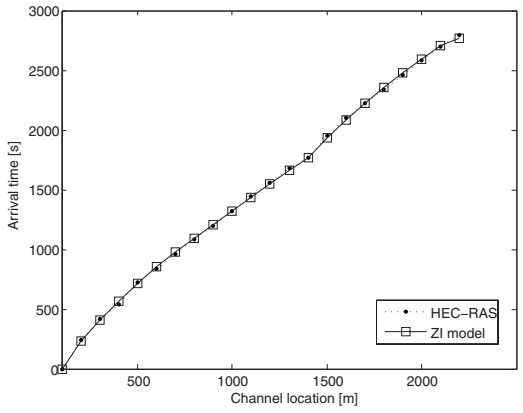

Fig. 1. Comparison of wave front propagation along the prismatic (parabolic) channel computed with the ZI model and compared to the results of the fully dynamic simulation (HEC-RAS)

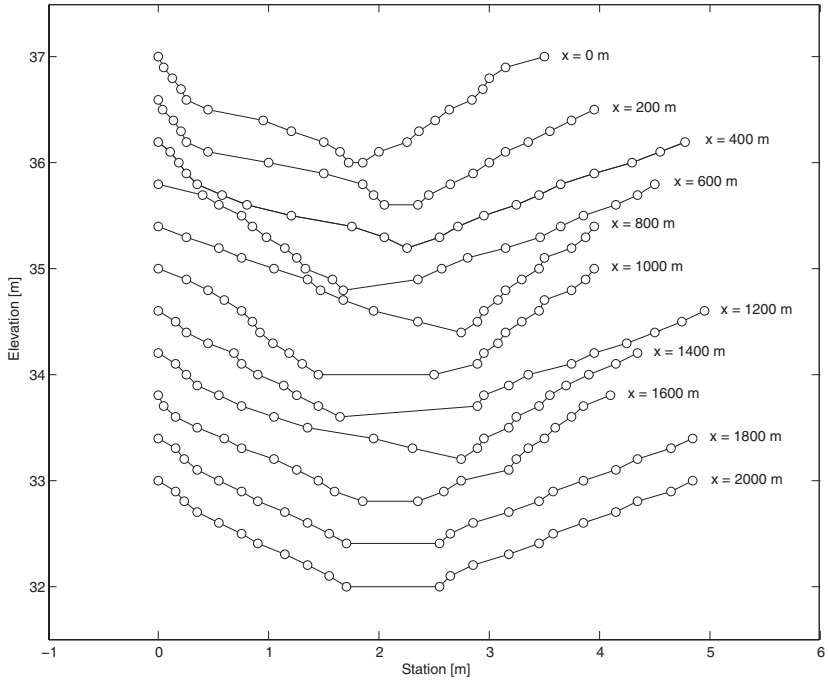

Fig. 2. Cross-sectional profiles for the nonprismatic test channel at different channel locations x

The evaporation could be easily included as a loss term (computed by any appropriate model) in the iterative solution procedure of the kinematic wave. This is not crucial due to the low order of magnitude of the rate of evaporation losses compared to the infiltration. This is, for example, stated by Wheater (2002).

Model Applications

In this section, some features of the ZI surge flow model are analyzed by comparing the results of the analytical model and the ones obtained from a full hydrodynamic model. The investigation focuses on permeable prismatic and nonprismatic channels, thus, providing a first step prior to the application of the suggested analytical model for surge flow phenomena in wadi beds and an application to problems of groundwater recharge by means of reservoir release.

Infiltration characteristics are exemplarily represented by the empirical Kostiakov-Lewis equation (Walker and Skogerboe 1987; Walker 1998) which is given by

$$I(t) = K_k \cdot t^{K_a} + K_c \cdot t \tag{20}$$

where $I(t)$=cumulative infiltration volume per channel section $[L^3L^{-1}]$; t=time $[T]$; K_a=empirical Kostiakov-Lewis exponent $[-]$; K_k=empirical Kostiakov-Lewis exponent $[L^3T^{-K_a}L^{-1}]$; and K_c=steady or final infiltration rate $[L^3T^{-1}L^{-1}]$.

Based on the infiltration basin test data measured by Haimerl and Zunic (2002) and Haimerl (2004) in Wadi Ahin, Sultanate of Oman, the Kostiakov-Lewis model parameters were fitted to dry initial conditions providing $K_k[\mathrm{m}^3/\mathrm{min}^{K_a}/\mathrm{m}]=0.004\,646$, $K_a[-]=0.864$, and $K_c[\mathrm{m}^3/\mathrm{min}/\mathrm{m}]=0.001\,082$. The duration of the corresponding infiltration experiment was 5.977 min; the area of the infiltration basin was 38.5 m^2. The adjusted coefficient of determination R^2 and the root-mean-square error (RMSE) of the fitted Kostiakov-Lewis model were $R^2=0.9997$ and RMSE=0.087 21.

Model Comparison between the Analytical ZI Model and a Fully Hydrodynamic Model

The results of the flow computations with the analytical surge flow model are subsequently compared to the numerical solution of the full Saint-Venant equations (fully dynamic approach), emerging from simulations with the Hydrologic Engineering Centers River Analysis System (HEC-RAS) model (Brunner 2002). First, test examples incorporating prismatic and nonprismatic channel geometries are evaluated using the ZI model. In a second step, the flow is computed for the same input data using the fully dynamic numerical model. Therefore, the infiltration hydrograph is taken from the ZI calculations and considered as negative lateral inflow in HEC-RAS. Modeling in initially dry channels can lead to considerable numerical inconveniences due to the steep gradient at the downward moving wave tip (Schmitz et al. 2002). For this reason, we run the fully dynamic numerical HEC-RAS model with an initial channel flow of 0.15 m^3/s. We employ a time discretization of 5 s for the further simulations with the numerical model.

We first set up the analytical ZI model and the fully dynamic numerical model for a hypothetical prismatic channel (see next subsection) and continue with simulations of the flow in a hypothetical nonprismatic channel (see second subsection). The main goal of the comparisons presented in the following subsections is

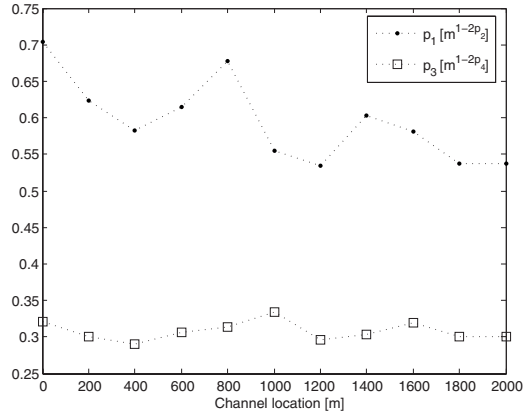

Fig. 3. Development of the varying geometry parameters $p_1(x)$ and $p_3(x)$ along the nonprismatic test channel

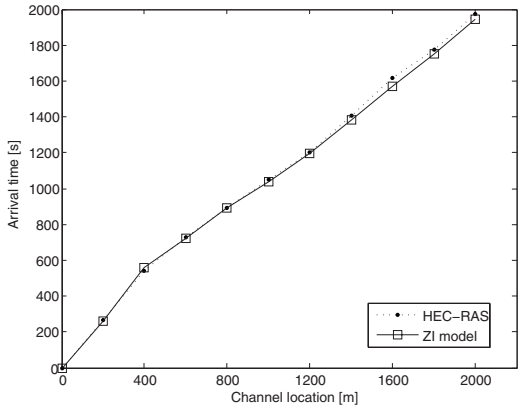

Fig. 4. Comparison of wave front propagation along the nonprismatic channel computed with the ZI model and compared to the results of the fully dynamic simulation (HEC-RAS)

to check the validity of the analytical solution, i.e., the inclusion of infiltration in the developed mathematical framework together with the implementation of the code.

Model Comparison for a Permeable Prismatic Channel

We tested the ZI model for a hypothetical permeable prismatic channel with a length of 2,000 m and uniform parabolic cross sections. Therefore, cross-sectional parameters $p_1(x)$ and $p_3(x)$ do not vary along the channel. Observation points for the intercomparison with the results of the fully dynamic numerical model are placed every 100 m along the channel. The parameters of the Kostiakov-Lewis infiltration model are obtained from the Wadi Ahin field study of Haimerl and Zunic (2002) and Haimerl (2004). The geometric profile data and the inflow hydrograph can be seen from Table 1. Fig. 1 shows the computed arrival times of the wave tip along the channel.

Both the results of the hydrodynamic and the ZI models show a perfect agreement. The difference between the ZI approach and the fully hydrodynamic solution lies in an underestimation in the mean arrival times of the ZI model of only 0.08%. The continuously rising graph of the advance trajectory shows slight deviations from a straight line. This originates from the superposition of two effects: infiltration decelerates the advance of the wave tip and—in contrast—the increasing inflow accelerates the advance. This recurs a couple of times during the simulation, namely, when the inflow rises according to Table 1. The results suggest that the analytical ZI model is well suited for predicting surge flow phenomena in permeable prismatic channels.

Table 2. Inflow Hydrograph for the Nonprismatic Test Channel for the ZI Model and the Fully Dynamic Model

Upstream inflow hydrograph	
Time (s)	Flow (m^3/s)
0	0
180	0.5
360	0.75
540	1.5
1,980	1.5

Model Comparison for a Permeable Nonprismatic Channel

An important aspect relates to a more realistic description of the wadi geometry. According to Schmitz et al. (2002), the geometric properties of the considered channels are evaluated using Eqs. (5) and (6) where the geometric parameters $p_1(x)$, p_2, $p_3(x)$, and p_4 are calculated by minimizing the residual mean squares (RMSs)

$$\mathrm{RMS}(\tilde{h}) = \int_0^{\tilde{A}(x)} [\tilde{h}(x,A) - p_1(x)A^{p_2}]^2 dA \tag{21}$$

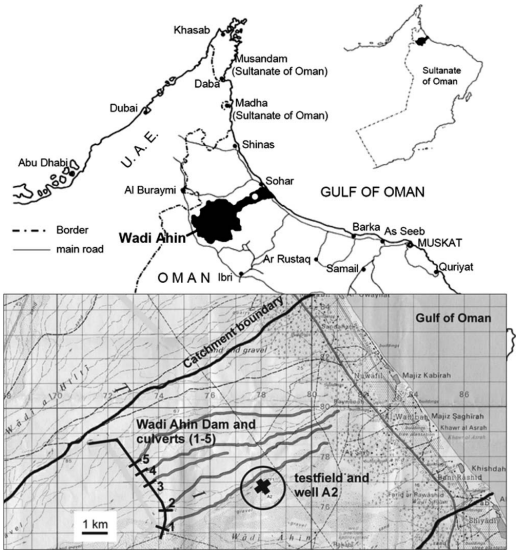

Fig. 5. Overview map of Wadi Ahin and Wadi Ahin recharge dam with Wadi Channels 1–5, Sultanate of Oman (after Haimerl and Zunic 2002 and Haimerl 2004)

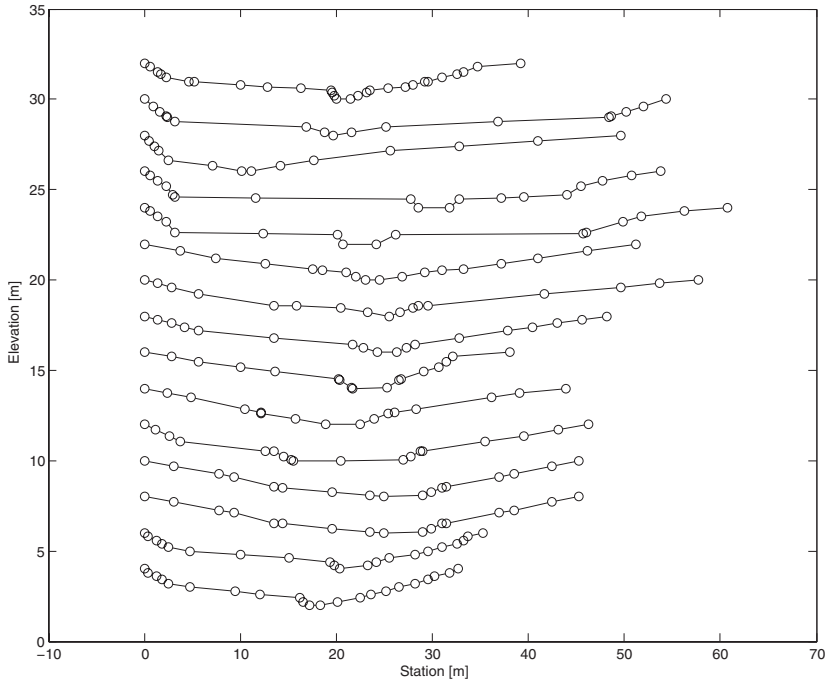

Fig. 6. Typical cross-sectional profiles of Wadi Ahin, Sultanate of Oman (after Haimerl and Zunic 2002)

$$\mathrm{RMS}(\widetilde{R}) = \int_0^{\widetilde{A}(x)} [\widetilde{R}(x,A) - p_3(x)A^{p_4}]^2 dA \qquad (22)$$

for each cross-sectional location. In Eqs. (21) and (22), the functions $\widetilde{h}(x,A)$ and $\widetilde{R}(x,A)$ denote the dependencies of both water depth and hydraulic radius on the wetted cross-sectional area. The upper limit of the integration, $\widetilde{A}(x)$, is selected for each cross section according to an appropriate reference water depth. A pronounced variation of the geometry parameters $p_1(x)$ and $p_3(x)$ reflects pronounced morphological changes along the considered reaches of the channel. The maxima of $p_1(x)$ and $p_3(x)$ are commonly associated with narrow cross sections, while the minima indicate more general lateral slopes of the cross sections (see Figs. 2 and 3).

A sensitivity analysis showed only a weak dependency of the ZI solution (in terms of computed arrival times) on the parameter $p_1(x)$ but a strong relationship with the parameter $p_3(x)$. Regarding Eqs. (5) and (6) and Eqs. (21) and (22), $p_3(x)$ strongly accounts for the nonprismatic character of the channel. The incorporation of the longitudinal varying channel parameters [especially $p_3(x)$] therefore seems appropriate for a sound process modeling which is supported by the investigations of Schmitz et al. (2002).

The test channel used in the following example is constructed of selected cross sections of Wadi Ahin. The cross sections are placed every 200 m along the channel; the length of the channel is 2,000 m. The Strickler velocity coefficient is constant along the channel and equals 33.33 $\mathrm{m}^{1/3}/\mathrm{s}$ (this equals a Manning's value of $n=0.03$). The longitudinal profile slope is set constant to 0.002. The constant profile parameters equal $p_2=0.5795$ and $p_4=0.5468$; $p_1(x)$ and $p_3(x)$ can be obtained from Fig. 3. The infiltration parameters are taken from the experimentally derived parameters for Wadi Ahin (after Haimerl and Zunic 2002 and Haimerl 2004). The inflow hydrograph for the test setup is given in Table 2.

Fig. 4 depicts the time required for the advancing wave front to reach the respective channel locations. The results reveal a slight underestimation of the wave tip arrival time, except for the location at 400 m with an overestimate of about 18 s. The results underline the good performance of the analytical ZI model for simulating surge flow phenomena also in nonprismatic channels.

Application of the Analytical Model for a Nonprismatic Channel of Wadi Ahin (Sultanate of Oman) for the Optimization of Flood Water Release from a Groundwater Recharge Dam

In this section, the analytical ZI model is used for simulating the surge flow resulting from reservoir release with respect to groundwater recharge. The catchment of Wadi Ahin (approximately 1,054 km^2; Haller 2000) is located at the Northern coast of Oman (see Fig. 5). A recharge dam is located about 10 km inland from the Oman Sea obstructing the main wadi channel. The dam features five culverts for the downstream release of water (Fig. 5). Downstream of Wadi Ahin dam, five nonprismatic permeable channels were investigated. Fig. 6 shows examples of some typical wadi cross sections of the five wadi channels.

The most important manageable factor of artificial groundwater recharge measures is the rate of culvert release, considering a certain volume of water stored in the reservoir and a given chan-

Table 3. Release Hydrographs (Scenarios 1 and 2) for the Calculation of Cumulative Downstream Infiltration

Scenario 1		Scenario 2	
Time (s)	Flow (m^3/s)	Time (s)	Flow (m^3/s)
0	0	0	0
300	1.2	60	0.2
600	2.8	1,800	0.2
4,535	2.8	1,860	0.3
		41,490	0.3
Cumulative release (m^3)	12,268	Cumulative release (m^3)	12,267

nel length with suitable infiltration characteristics. The proposed analytical ZI model can serve as a robust and accurate tool for the adjustment of culvert release rates to enhance the downstream infiltration, i.e., for a desired wetted wadi reach. In the following, we show the applicability of the ZI model for the estimation of an appropriate release strategy exemplarily for the first of the aforementioned wadi channels downstream of the Wadi Ahin recharge dam.

McIntyre et al. (2007) indicated flow volumes of some ten thousand to some million cubic meters for Hayl flow gauge located about 30 km^2 up from the Ahin dam at the transition of the coastal plain to the mountains. Since the catchment of the Ahin dam is not significantly larger than the Hayl catchment and rainfall mostly occurs in the mountains, flow volumes derived for the Hayl gauge are also representative for the catchment of the Ahin dam. According to Mott-MacDonald International (1992), the Ahin reservoir features a total volume of 6.5×10^6 m^3 in order to retain a flood of 10 years return period.

We use the ZI model to obtain suitable release hydrographs out of the reservoir with respect to high cumulative downstream infiltration. The order of magnitude of the selected filling of the reservoir and the derived hydrographs used for the simulation seem appropriate for smaller events with frequent occurrence. The Wadi Channel 1 (Fig. 5) is mapped by 12 cross sections and has a length of about 6,200 m. The longitudinal slope is 0.006, the Manning-Strickler velocity coefficient is estimated to be 30 $m^{1/3}/s$, and the channel is assumed to be initially dry. As mentioned before, any arbitrary functional relationship for quantifying the infiltration losses can be used with the proposed approach. For convenience we again employ the Kostiakov-Lewis model [Eq. (20)].

Table 3 presents two unsteady flow hydrographs released to the downstream channel. The same total volume of water is released in both scenarios. However, the release is much slower in Scenario 2. Fig. 7 depicts the results of the arrival time, infiltration volume, and infiltration percentage under both scenarios for Wadi Channel 1.

Under Scenario 1, the release of about 12.3×10^3 m^3 of water within a time of 1 h and 18 min leads to a total cumulative infiltration of about 1×10^3 m^3, which is equivalent to an infiltration quota of about 8%. Under Scenario 2, the release of about 12.3×10^3 m^3 of water within a time of 11 h and 31 min leads to a total cumulative infiltration of about 10×10^3 m^3, which is equivalent to an infiltration volume of about 80% compared to the

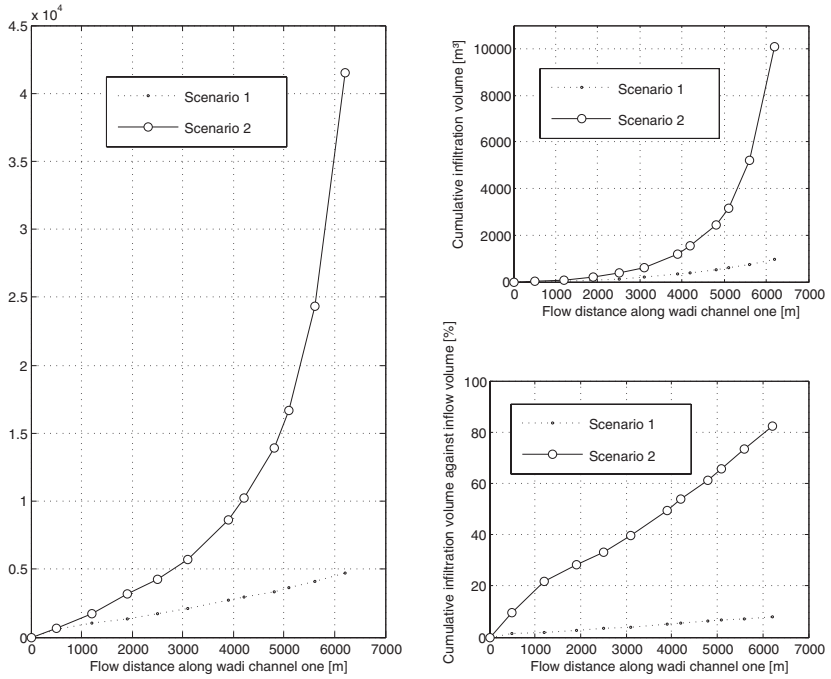

Fig. 7. Arrival time, infiltration volume, and infiltration percentage for Scenarios 1 and 2 for Wadi Channel 1 downstream of Wadi Ahin recharge dam

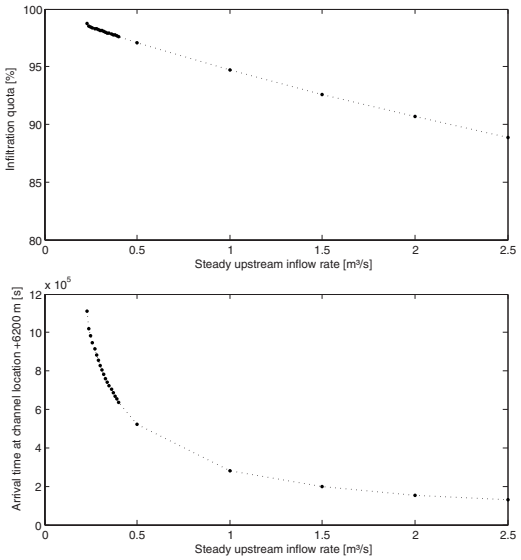

Fig. 8. ZI model results for standing wave computations with full infiltration for Wadi Channel 1 downstream of Wadi Ahin recharge dam

released volume (infiltration quota). A study for Wadi Channels 2–5, employing the same assumptions as before, delivered infiltration quotas ranging from 3.7 to 8.1% for Scenario 1 and 81.4 to almost 90% for Scenario 2.

As a final step, we evaluate the reservoir release rate leading to a practically standing wave within a considered channel reach due to the complete infiltration of constantly released water along the channel. This is an important question when looking at the design of the culverts with regard to the available channel reach length and an aspired infiltration quota. Fig. 8 shows the results of the computation. We consider the steady state to be reached with an infiltration quota of over 99%. It becomes clear, that for a constant release rate of 0.2 m^3/s and less nearly the whole inflow volume infiltrates, resulting in a practically standing wave with the wave tip at the most downstream cross section at 6,200 m. The further decrease of the steady inflow rate leads to a shift of the standing wave tip toward upstream locations.

Summary and Conclusions

The presented analytical surge flow model, based on the zero-inertia assumptions, offers a new tool for the simulation of flood wave propagation with infiltration losses through permeable beds. The analytical model showed its capability for the simulation of a surge moving down an irregularly shaped natural permeable stream bed even under problem specific restrictions such as an initially dry channel bed and a significant infiltration. Therefore, the presented model seems to be ideal for simulating surge flow phenomena downstream of groundwater recharge dams, notwithstanding the discontinuity when attaining the state of a standing wave and—looking at the straightforward applicability—evaluating reservoir release strategies and culvert design for specific groundwater recharge problems.

The test runs for the prismatic and nonprismatic permeable channels showed excellent agreement with the fully dynamic numerical solution. The model applicability therefore seems not to be severely restricted by the underlying assumptions. Although the incorporation of a spatially constant slope and velocity coefficient is obviously dependent on the channel morphology, it apparently does not represent a serious restriction for the model application for surge flow modeling in ephemeral alluvial wadi beds. The approach circumvents any numerical trouble of the free boundary value problem and offers the possibility of incorporating nonprismatic channel geometries and any appropriate model for the quantification of infiltration losses through the channel bed.

Further model applications and modifications that stand out to be tested are (1) the incorporation of significant momentum contributions under varying angles. This might be the case if the outflow of the five reservoir culverts unites downstream of the dam. (2) The implementation of a more comprehensive infiltration model that could be adjusted for the wetted perimeter like this is done in software packages such as SIRMOD (Walker and Skogerboe 1987; Walker 1998).

Acknowledgments

This paper is dedicated to the memory of Mr. Farnush Ghasempour. Mr. Ghasempour participated in the research on this topic and provided material which could later be used in the paper but he regrettably passed away in the year 2005. The paper was completed within the research project IWAS funded by the German Federal Ministry of Education and Research (BMBF) under Grant No. 02WM1028.

References

Battashi, N., and Rashid, A. S. (1998). "The role of artificial recharge schemes in water resources development in Oman." *Technical Rep.*, Ministry of Water Resources, Sultanate of Oman.

Bouwer, H. (2002). "Artificial recharge of groundwater: Hydrogeology and engineering." *Hydrogeol. J.*, 10, 121–142.

Brunner, G. W. (2002). *HEC-RAS river analysis system: Hydraulic reference manual*, Hydrologic Engineering Center of the USACE, Davis, Calif.

Haimerl, G. (2004). "Groundwater recharge in wadi channels downstream of dams." Ph.D. thesis, Institute of Hydraulic Engineering and Water Resources, Munich Univ. of Technology, Munich, Germany.

Haimerl, G., and Zunic, F. (2002). "Infiltration test and numerical solution to evaluate the efficiency of infiltration in arid countries." *Proc., 3rd Int. Conf. on Water Resources and Environmental Research (ICWRER)*, Eigenverlag des Forums für Abfallwirtschaft und Altlasten e. V., Pirna, Germany.

Haller, J. (2000). "Data collection and data analysis of hydrological and hydrogeological data of Wadi Ahin in the Sultanate of Oman." MS thesis, Institute of Hydraulic Engineering and Water Resources, Munich Univ. of Technology, Munich, Germany.

Henderson, F. M. (1966). *Open channel flow*, Macmillan, New York.

Jaynes, D. B. (1986). "Simple model of border irrigation." *J. Irrig. Drain. Eng.*, 112(2), 172–184.

Katopodes, N. D., and Strelkoff, T. (1977). "Hydrodynamics of border-irrigation: Complete model." *J. Irrig. Drain. Eng.*, 103(3), 309–324.

Kowsar, A. (1991). "Flood water spreading for desertification control: An integrated approach." *Des. Cont. Bull. (UNEP)*, 19, 3–18.

Kowsar, A. (1996). "An introduction to flood mitigation and optimization of flood water utilization: Flood irrigation, artificial recharge of

groundwater, small earth dams." *Technical Rep.*, Research Center of the Construction Crusade, Tehran, Iran.

McIntyre, N., Al-Qurashi, A., and Wheater, H. S. (2007). "Regression analysis of rainfall-runoff data from an arid catchment in Oman." *Hydrol. Sci. J.*, 52(6), 1103–1118.

Mott-MacDonald International. (1992). "Groundwater recharge dam on Wadi Ahin." *Wilayat Saham: Hydrology and Design Criteria Technical Rep.*, Ministry of Agriculture and Fisheries Wealth, Sultanate of Oman.

Schmitz, G. H., Liedl, R., and Volker, R. (2002). "Analytical solution to the zero-inertia problem for surge flow phenomena in non-prismatic channels." *J. Hydraul. Engrg.*, 128(6), 604–615.

Schmitz, G. H., and Seus, G. J. (1990). "Mathematical zero-inertia modeling of surface irrigation: Advance in borders." *J. Irrig. Drain. Eng.*, 116(5), 603–615.

Walker, W. (1998). "SIRMOD—Surface irrigation modeling software." *Technical Rep.*, Utah State Univ., Utah.

Walker, W., and Skogerboe, G. (1987). *Surface irrigation: Theory and practice*, Prentice-Hall, New York.

Wheater, H. S. (2002). *Hydrology of wadi systems*, UNESCO, Paris.

Analytical Model of Surface Flow on Hillslopes Based on the Zero Inertia Equations

Andy Philipp[1]; Rudolf Liedl[2]; and Thomas Wöhling[3]

Abstract: Coming from the zero inertia (ZI) equations, an analytical model to describe sheet flow phenomena with a special focus on rainfall runoff processes is developed. A slight modification of the ZI equations, which draws upon the concept of a momentum-representative cross-section of the moving water body, leads—after comprehensive mathematical calculus—to an analytical solution describing essentially one-dimensional, shallow overland flow. In a test series, the analytical ZI model is applied together with three numerical models, one based on the Saint-Venant equations, one on the kinematic wave equations, and another one on diffusion wave equations. The test application refers to a typical rainfall runoff situation, i.e., rather shallow overland flow on a hillslope as a consequence of excess rainfall. Contrary to the analytical model, the comparative analysis clearly shows the difficulties of the numerical solutions in terms of exactness and robustness when approaching typical shallow water depths. This problem of numerical models is tackled by applying small time and space discretization, which, however, comes along with higher CPU execution times. Besides the good computational efficiency and freedom of any numerical inconvenience, the new analytical model outperforms the numerical models for typical overland flow simulations. This particularly refers to a highly satisfactory fulfillment of the mass balance and a nearly perfect match of peak flow rates. **DOI: 10.1061/(ASCE)HY.1943-7900.0000519.** *© 2012 American Society of Civil Engineers.*

CE Database subject headings: Sheet flow; Overland flow; Diffusion; Slopes; Hydrology.

Author keywords: Surface flow; Sheet flow; Overland flow; Zero inertia model; Diffusion wave; Analytical model; Hillslope hydrology.

Introduction

Surface flow on hillslopes can be a driving process of runoff formation, especially during flood prone hydro-meteorological situations. Flow on the surface is affected by morphology and micro relief of the catchment, positive and negative mass (and momentum) contributions by precipitation and infiltration, antecedent wetness conditions, and water supervening from upper parts of the catchment. The preceding listing illustrates the complex character of surface flow processes and renders their closed physically based description nearly impossible, since the relevant processes are strongly interconnected, highly nonlinear, and available data for such an ambitious process modeling will always be lacking for real meso-scale catchments.

The concept of sheet flow is commonly used to tackle the aforementioned problems of a physically based description of surface flow. This means that the flowing water on the surface is considered as a somehow virtual moving water body (or sheet of water) traveling down a characteristic rough slope without considering the real flow conditions in rills and small channels. Nevertheless, only the average characteristics of water movement are portrayed this way. For the one-dimensional case there are only few studies (e.g., Tayfur and Kavvas 1998) that try to overcome the simplifications of the sheet flow concept toward a more realistic portrayal of rill flow, which of course results in a mostly unrealistically high data demand.

The literature shows—beside simple volume balance techniques—three general concepts of physically based one-dimensional overland flow modeling: (1) the full hydrodynamic description on the basis of the Saint-Venant equations, (2) the diffusion wave or zero inertia (ZI) approximation (which some authors consider synonym, and some do not), and (3) the kinematic wave approximation. Despite that the kinematic wave approach for overland flow modeling has been extensively studied (Henderson and Wooding 1964; Ross et al. 1979; Hjelmfelt 1981; Hjelmfelt 1984; Govindaraju et al. 1992; Jaber and Mohtar 2003; Liu et al. 2004) and a great number of researchers (Woolhiser and Liggett 1967; Zhang and Cundy 1989; Esteves et al. 2000, to name only a few) investigated the usability of one- and two-dimensional Saint-Venant models for this task, far less has been reported on the validity, limits, and applicability of the zero inertia/diffusion wave approximation. Furthermore, many authors report of serious problems, such as attenuation errors, phase errors, and discretization errors, when applying numerical solution schemes to the commonly used overland flow equations (e.g., Singh 2002; Jaber and Mohtar 2003; Tsai and Yang 2005).

Morris and Woolhiser (1980) first used the diffusion wave simplification of the full Saint-Venant equations for overland flow modeling. They showed that the often-assumed validity of the kinematic wave approximation can be harmed under highly subcritical flow conditions (e.g., on a flat and/or very rough terrain). Daluz Vieira (1983) compared 150 simulations on the basis of the Saint-Venant equations with those obtained by the kinematic and the

[1]Research Associate, Chair of Hydrology, Institute of Hydrology and Meteorology, Technische Universität Dresden, Bergstraße 66, 01069 Dresden, Germany (corresponding author). E-mail: andy.philipp@tu-dresden.de

[2]Professor, Groundwater Management, Technische Universität Dresden, Bergstraße 66, 01069 Dresden, Germany.

[3]Senior Research Scientist, Water & Earth System Science Research Center (WESS), Univ. of Tübingen, Institute for Geoscience, Sigwartstraße 10, 72076 Tübingen, Germany; Lincoln Ventures Limited, Private Bag 3062, Hamilton, New Zealand.

Note. This manuscript was submitted on January 7, 2011; approved on September 30, 2011; published online on October 3, 2011. Discussion period open until October 1, 2012; separate discussions must be submitted for individual papers. This paper is part of the ***Journal of Hydraulic Engineering***, Vol. 138, No. 5, May 1, 2012. ©ASCE, ISSN 0733-9429/2012/5-391–399/$25.00.

diffusion wave approximation for a range of flow conditions, rendered by different kinematic wave numbers and Froude numbers. Their study showed the wide applicability and validness of the diffusion wave approximation for Froude numbers smaller than 0.5 and kinematic wave numbers greater than 5.0. Govindaraju et al. (1988) showed that for high Froude numbers and low kinematic wave numbers, the kinematic wave approximation may fail.

Govindaraju et al. (1988) proposed an analytical solution of the zero inertia problem for steep slopes under invariant rainfall conditions. They replaced the commonly used critical flow depth boundary condition by a zero-depth gradient boundary condition. This methodology—as in the case of the research presented in this paper—leads to nonlinear equations that can be solved with any standard numerical method and deliver a solution for the rising and the recession hydrograph. Govindaraju et al. (1990; 1992) expanded the aforementioned concepts to an approximate analytical solution for space-time-varying rainfall input and lateral inflow for the one- and two-dimensional case. Furthermore, literature shows no evidence of an exact analytical solution of the zero inertia equations under arbitrarily time varying rainfall.

Besides these publications, research on analytical solutions of the zero inertia equations for overland flow problems remains limited. A number of authors introduced and expanded a free boundary formulation of the zero inertia problem. They proposed an exact—and not only approximate—analytical solution to the problem. The developed models already performed well for a wide range of model applications, e.g., border and furrow irrigation (Schmitz and Seus 1990; 1992), coupled one-dimensional surface and two-dimensional subsurface flow (Wöhling et al. 2004; 2006; Wöhling and Mailhol 2007), surge flow in prismatic and nonprismatic channels over initially dry channels (Schmitz et al. 2002), and surge flow in initially dry, nonprismatic channels with significant infiltration effect on mass and momentum balance and weak process dynamics (Philipp et al. 2010). The objective of this paper is to develop and test an exact analytical solution of the zero inertia equations for runoff problems on hillslopes under time varying rainfall.

Analytical Model

Considering the flexibility and universality of numerical flow models, the question arises: why are analytical solutions of the governing equations needed? Arguments that are given in the literature are (1) straightforward model applicability since only physically based parameters are needed, (2) the sensitivity and influence of single parameters can often be directly seen from the computation formulas, (3) the data situation omits the application of numerical methods, (4) there are no numerical inconveniences, and (5) the analytical solution can serve as a reference for numerical models, e.g., to quantify the influence of different numerical methods on the quality of the solution. The authors set up an analytical zero inertia model of the commonly incorporated sheet flow analogon of surface flow, which assumes flow in a very wide cross-section with a uniform flow depth perpendicular to the flow direction. A wide rectangular cross-section is assumed. This implies that the width of the cross-section is much greater than the water depth h, such that the hydraulic radius R equals h. It is intended to set up the model for flow over initially dry portions of a surface. Furthermore, the model should account for changes of the flow attributable to water originating from rainfall and/or infiltration excess as well water supervening from upper parts of the catchment.

The extended ZI equations (Schmitz et al. 2002) are derived by neglecting the local and advective inertia terms $\partial u/\partial t$ and $u \cdot \partial u/\partial x$ of the full hydrodynamic shallow water flow equations for the one-dimensional case, which are mostly referred to as Saint-Venant equations (Yen and Tsai 2001). Additionally, for surface runoff influenced by rainfall—considering the momentum contribution of the falling rain to the flow insignificant—the $qu/(gA)$ term of the momentum equation of the Saint-Venant equations can be neglected. The rainfall contributing to the flow is taken into account by the q term of the continuity equation. This leads to the standard ZI equations (continuity and momentum equation):

$$\frac{\partial h}{\partial t} + \frac{\partial Q}{\partial x} = q \tag{1}$$

$$\frac{\partial h}{\partial x} = S_0 - \frac{u^2}{K^2 h^\beta} \tag{2}$$

where t = time (T); x = longitudinal space coordinate (L); $Q(x,t)$ = discharge per unit width (L^2T^{-1}); $u(x,t)$ = flow velocity (LT^{-1}); $h(x,t)$ = water depth (L); $q(x,t)$ = rate of positive/negative mass contribution attributable to rainfall or infiltration ($L^2T >^{-1}$); K = discharge coefficient ($L^{1-\beta}T^{-1}$); β = exponent of h, depending on the flow formula (Chézy: $\beta = 1$; Manning: $\beta = 1.333\ldots$); and S_0 = bottom slope (-). For further model development, β is set to 1 (Chézy law is used for the quantification of friction losses).

The first step toward the solution of the system of Eqs. (1) and (2) is to multiply Eq. (2) by h, yielding

$$h\frac{\partial h}{\partial x} = S_0 h - \frac{u^2}{K^2} \tag{3}$$

According to Schmitz and Seus (1990), the inflow boundary can be considered as a kind of momentum-representative cross-section for the specific flow problem. In this approach, the momentum described by the right-hand side of Eq. (3)—which is set equal to zero in kinematic wave analysis (Hjelmfelt 1981; Yen and Tsai 2001)—is continuously represented by the transient amount of momentum at $x = 0$. Thus, the right-hand side of Eq. (3) no longer depends explicitly on x, and Eq. (3) can be expressed as

$$h\frac{\partial h}{\partial x} = S_0 h_0 - \frac{u_0^2}{K^2} \tag{4}$$

where $h_0 = h_0(t) = h(x = 0, t)$; and $u_0 = u_0(t) = u(x = 0, t)$. Schmitz and Seus (1990; 1992) showed that another possible location of the momentum-representative cross-section is the position of the center of gravity of the moving water body. This approach leads to a physical and mathematical equivalent solution. For this study, the authors place the momentum-representative cross-section at $x = 0$ because the subsequent calculus is more brief and this location introduces a well-defined coupling location when single-slope models should be cascaded.

The solution of the system of partial differential Eqs. (1) and (4) requires the specification of boundary and initial conditions. At the fixed upstream boundary ($x = 0$), the boundary condition is

$$Q(0,t) = Q_0(t) \tag{5}$$

with the restriction that strongly falling discharge hydrographs cannot be used as an upstream boundary condition because of the ZI assumptions (Schmitz et al. 2002). As a consequence, the model covers the rising limb and the plateau part of the hydrograph. At the moving downstream boundary ($x = x_{tip}(t)$) the following conditions have to be satisfied:

$$h(x_{tip}, t) = 0 \tag{6}$$

$$u(x_{tip}, t) = u_{tip}(t) = \frac{dx_{tip}}{dt} \tag{7}$$

where $x_{tip}(t)$ and $u_{tip}(t)$ denotes the location and velocity of the wave front, respectively. The initial condition of the flow problem over an initially dry surface is

$$x_{tip}(t = 0) = 0. \tag{8}$$

Schmitz et al. (2002) have derived the solution of the momentum Eq. (4) for arbitrary cross-section geometries. In our rectangular case, their solution reads

$$h(x, t) = \sqrt{2\left(\frac{u_0^2}{K^2} - S_0 h_0\right) \cdot [x_{tip}(t) - x]}. \tag{9}$$

Next, the continuity Eq. (1) is solved for Q. Considering the upstream boundary condition given by Eq. (5), a direct integration of the continuity equation yields

$$Q(x, t) = Q_0(t) - \int_0^x \left[\frac{\partial h}{\partial t}(\xi, t) + q(\xi, t)\right] d\xi \tag{10}$$

where the integrand can be obtained by differentiating Eq. (9) with respect to t, and ξ indicates the integration variable in time. Eqs. (9) and (10) solve the system Eqs. (1) and (4) and satisfy the boundary conditions given by Eqs. (5)–(7).

The solution procedure for Eqs. (9) and (10) first requires evaluating the position of the advancing wave front $x_{tip}(t)$ and the water depth $h_0(t) = h(x = 0, t)$ at the inflow boundary—which is not zero in case water emerges from upper catchment parts and not only laterally from rainfall—by solving a nonlinear system of two equations iteratively. For this purpose, N observation locations $(0 < x_1 < x_2 < \ldots < x_N)$ are defined and the arrival time of the wave tip t_n for each observation point, i.e., $x_{tip}(t_n) = x_n$ for $(n = 1, 2, \ldots, N)$, and the corresponding water depth $h_{0,n} = h_0(t_n)$ at $x = 0$ is calculated.

The first aforementioned nonlinear equation is obtained by setting $x = 0$ in Eq. (9):

$$h_{0,n} = \sqrt{2x_n\left(\frac{Q_0 t_n^2}{K^2 h_{0,n}^2} - S_0 h_{0,n}\right)} \tag{11}$$

The second nonlinear equation is derived from the volume balance

$$\int_0^{t_n} Q_0(\tau) d\tau = \frac{2}{3} h_{0,n} x_n + \int_0^{t_n} \int_0^{x_n} q(\xi, \tau) d\xi d\tau \tag{12}$$

where ξ and τ indicate the integration variables in the dimensions of space and time.

Rearranging Eqs. (11) and (12) leads to the iterative procedure defined by Eqs. (13) and (14):

$$h_{0,n}^{(k)} = \left\{\frac{2x_n\left[\frac{Q_0(t_n)}{K}\right]^2}{1 + \frac{2x_n S_0}{h_{0,n}^{(k-1)}}}\right\}^{1/4} \tag{13}$$

$$t_n^{(k)} = t_n^{(k-1)} + \frac{2/3\ h_{0,n}^{(k)} x_n + \int_0^{t_n^{(k-1)}} \int_0^{x_n} q(\xi, \tau) d\xi d\tau - \int_0^{t_n^{(k-1)}} Q_0(\tau) d\tau}{Q_0[t_n^{(k-1)}]} \tag{14}$$

where $k = 1, 2, 3, \ldots$ denotes the iteration index. A Taylor series expansion of the left-hand side of Eq. (12) around $t_n^{(k-1)}$ has been included to take into account the effect of lateral inflow/outflow from rainfall and/or infiltration, respectively. Initial values are provided by the results obtained from the preceding time step, i.e., $h_{0,n}^{(0)} = h_{0,n-1}$ and $t_n^{(0)} = t_{n-1}$.

After the iteration in Eqs. (13) and (14) has converged, the water depth $h(x, t_n)$ can be straightforwardly computed from

$$h(x, t_n) = h_{0,n}\sqrt{1 - \frac{x}{x_n}} \tag{15}$$

by making use of Eq. (9). Eq. (15) is inserted into Eq. (10) to compute the discharge per unit width, $Q(x, t)$. If there is—beside or instead of known lateral inflow—significant infiltration, this step requires either some standard formula, e.g., Kostiakov-Lewis, or some problem-specific functional relationship quantifying the infiltration rate and to calculate $q(\xi, \tau)$. Additionally, some details on the evaluation of the integral of Eq. (10) are given in the Appendix.

Since the formulation of the proposed analytical model assumes a free and moving lower boundary, the concept of the so-called "virtual wave" is used as proposed by Schmitz (1989) and Schmitz and Seus (1990). This concept virtually extends the computational domain in case the moving wave tip reaches the lower boundary of the model domain—which is immediately the case assuming a homogeneous lateral rainfall input to the test plane. Thus, the water body atop the test plane is filled up by the lateral rainfall input, forming a traveling virtual wave tip beyond the real extensions of the test plane. This traveling virtual wave tip is the transient location of the lower boundary conditions of Eqs. (6) and (7). In this way, the virtual wave provides flow rate, flow depth, and flow velocity along the test plane. Fig. 1 gives an illustration of the virtual wave concept.

Comparative Analysis

In this section, results of the developed analytical zero inertia model (analytical ZI model or aZI model) are compared with results obtained by numerical solutions of the Saint-Venant equations (numerical HD model or nHD model), the kinematic wave approximation (numerical KW model or nKW model), and the diffusion wave or zero inertia model (numerical ZI model or nZI model). This is done by modeling surface runoff as a consequence of excess rainfall on a synthetic test plane with a specific roughness as typically examined by many authors (e.g., Schmid 1986; Di Giammarco et al. 1995; Tsai and Yang 2005).

Test Setup

Characteristics of the Synthetic Test Plane

For model intercomparison and subsequent assessment of the proposed analytical zero inertia model, the flow over a synthetic impervious test plane as proposed by Schmid (1986) (see Fig. 1) was simulated. This specific test plane was selected because of the availability of model results of another kinematic wave model implementation for the discussed test plane, which gave the opportunity to check for validness of the incorporated flow models first. The used synthetic test plane featured the following parameters: rectangular domain, length of 80 m, width of 20 m, surface slope of 15°, and Chézy friction coefficients of $K_C = 2.0, 5.0, 10.0, 20.0\ m^{1/2}/s$. For the purpose of clarity, results for all aforementioned friction coefficients are included in tabular form but model

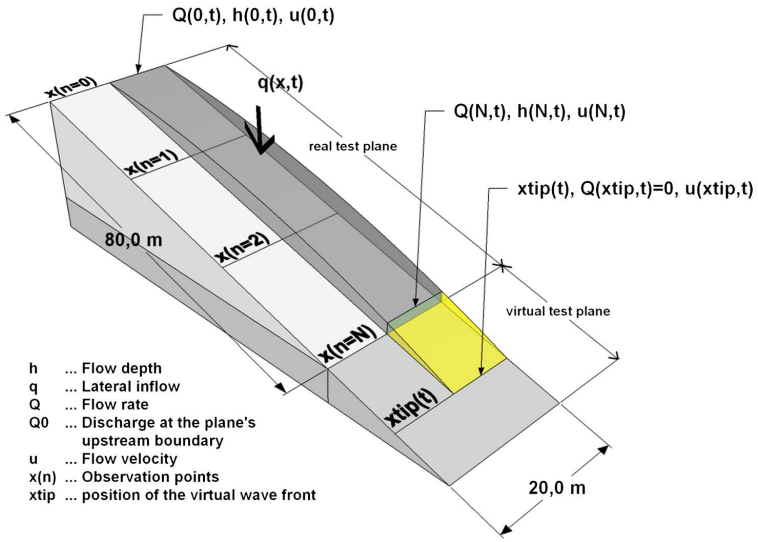

Fig. 1. Schematic sketch of the synthetic test plane for overland flow and illustration of the virtual wave concept

results in form of hydrographs are shown only for setups with the friction coefficient set to $K_C = 5.0\ \mathrm{m}^{1/2}/\mathrm{s}$.

Specifics of the Model Setups

Numerical Full Hydrodynamic Model (nHD Model)
The employed full hydrodynamic model is based on the Saint-Venant equations (Strelkoff 1970) that pose a reliable process model for unsteady shallow water flow of incompressible fluids. In general, the governing system of continuity and momentum equation cannot be solved analytically. A large number of studies have been conducted to verify the applicability and validity of different numerical solution approaches for the one and two-dimensional Saint-Venant equations. For the one-dimensional case most often finite differencing schemes are applied. For this study, the authors used a centered implicit finite differencing scheme that employs Picard iteration for the convergent solution of the resulting system of nonlinear equations. The nHD model's spatial resolution was set to $\Delta x = 0.5$ m, and a temporal resolution of $\Delta t = 2$ s was chosen. This spatial/temporal resolution was selected on the basis of a prerequisite sensitivity analysis that revealed—depending foremost on the magnitude of the inflow rate—that greater values of Δx and Δt did provoke a declined convergence behavior of the relaxation scheme or, finally, led to numerical instabilities that avoided a convergent solution.

Numerical Kinematic Wave Model (nKW Model)
A standard one-dimensional kinematic wave model of surface flow (e.g., as proposed by Schmid 1986) was implemented. The model uses the common kinematic wave approximations (Lighthill and Whitham 1955), which indicates that the inertia terms of the Saint-Venant equations are neglected and, additionally, bottom slope is set equal to friction slope. These assumptions are in contrast to the full hydrodynamic process description as they cause a bijective relationship of flow rate and flow depth. Because of their character as partial differential equations, the kinematic wave equations are mostly solved numerically, which is performed by a large number of authors for the one- and two-dimensional case (e.g., Schmid 1986; Liu et al. 2004; Tsai and Yang 2005; Howes et al. 2006). The governing equations were solved with an implicit differencing scheme too. The time step of the nKW model was set to $\Delta t = 2$ s, and the spatial resolution was set to $\Delta x = 0.5$ m to prevent numerical instabilities and convergence problems and to keep consistency with the other incorporated numerical model setups.

Numerical Zero Inertia Model (nZI Model)
The zero inertia or diffusion wave approach neglects the terms of local and advective momentum but does not assume the parallelism of friction slope and bottom slope. The incorporated numerical solution scheme for the nZI model is based on a centered implicit finite differencing scheme as proposed by numerous authors for the one-dimensional case (e.g., Bronstert and Bárdossy 2003). As applies for the afore-discussed numerical solutions of the full hydrodynamic model and the kinematic wave model, it was crucial to discretize the solution domain with an appropriate resolution in time and space to prevent larger numerical errors. For consistency, the spatial resolution for the test scenario calculations was therefore set to $\Delta x = 0.5$ m, and a discretization time step of $\Delta t = 2$ s was applied. Additionally, a coarser resolution in space and/or time led to numerical issues, depending on process dynamics and magnitude of the flow.

Analytical Zero Inertia Model (aZI Model)
The analytical ZI model concept presented in this paper already showed its ability to portray flow processes associated with free boundary problems as met in initially dry channels, weak process dynamics (e.g., flows connected with standing wave phenomena under significant infiltration losses), and flows over small to zero slopes up to fast surges (Schmitz and Seus 1990; Schmitz and Seus 1992; Schmitz et al. 2002; Wöhling et al. 2004; Wöhling et al. 2006; Wöhling and Schmitz 2007; Wöhling and Mailhol 2007; Philipp et al. 2010). Therefore, the proposed aZI model seems to offer a robust and reliable solution of a comprehensive process description of surface flow without the potential errors of numerical solution procedures. The model is based on the MATLAB implementation of the furrow advance phase model with space discretization (FAPS) by Wöhling et al. (2006). The model was modified

to account for lateral mass contribution along a wide flow plane ($h \approx R$) by the authors. According to Wöhling et al. (2006) and as outlined in the model development section, a space discretization for incrementing the iterative solution procedure in Eqs. (13) and (14) was included. The synthetic test plane was discretized by introducing observation points with a spatial resolution of $\Delta x = 0.5$ m. Any standard algorithm could be used (e.g., fixpoint iteration) for the iterative solution of the governing nonlinear equations, but this may not lead to satisfactory convergence rates at any time. To improve convergence of the iterative solution procedure, an algorithm of higher order accuracy is indicated. According to Wöhling et al. (2006), the Newton-Raphson algorithm was applied. This algorithm is of second-order accuracy, but demands the derivatives of the governing equations. Wöhling et al. (2006) has more details on the therefore required calculus. The number of iteration loops till convergence for each iteration run typically amounts to fewer than 20 when using the second-order Newton-Raphson relaxation scheme, depending on convergence rate and the value of the selected iteration error criterion. According to Fig. 1, the upper boundary condition of the model can be implemented as lateral inflow $q(x,t)$, and/or as inflow to the plane from uphill $Q(0,t)$.

Boundary Conditions and Initial Conditions of the Test Scenarios

Four model test scenarios with different upper boundary conditions were selected for comparative model analysis. The lateral boundary condition is—as usual for sheet flow modeling—given by a lateral inflow $q(t)$ to the model domain. Additionally, the incorporation of a time-variable inflow $Q(0,t)$ at the uppermost model boundary at $x = 0$ is possible. To keep brevity, no model results for inflow via the upper boundary are shown. The maximum inflow rates are set to $q(t)_{\max} = 20{,}45{,}90{,}120$ mm/h, linearly rising from zero to the maximum within 10 min and staying constant for the next 39 min (see Table 1 and Fig. 2). The selected inflow rates span a wide range of events, leading to pronounced flow on the plane. For all included models, a zero-flow initial condition was applied. Furthermore, for the numerical models, a zero-depth gradient was used as downstream boundary condition. Infiltration was not taken into account to take care for better model intercomparability. The coupling of a selected infiltration model with the specific surface flow models would have posed a source of uncertainties because the coupling strategies would have differed, e.g., because of different temporal discretization strategies and the nonlinear dependency of surface and subsurface flow. If the portrayal of infiltration is desired, any arbitrary functional relationship describing transient infiltration could be taken into account with the presented analytical ZI approach, which was already shown by Wöhling et al. (2006) and Philipp et al. (2010).

Table 1. Lateral Inflow Rates $q(t)$ to the Model Domain for the Test Scenarios 1, 2, 3, and 4

Time (minutes)	Scenario 1 (millimeters per hour)	Scenario 2 (millimeters per hour)	Scenario 3 (millimeters per hour)	Scenario 4 (millimeters per hour)
0	0.0	0.0	0.0	0.0
1	2.0	4.5	9.0	12.0
2	4.0	9.0	18.0	24.0
3	6.0	13.5	27.0	36.0
4	8.0	18.0	36.0	48.0
5	10.0	22.5	45.0	60.0
6	12.0	27.0	54.0	72.0
7	14.0	31.5	63.0	84.0
8	16.0	26.0	72.0	96.0
9	18.0	40.5	81.0	108.0
10	20.0	45.0	90.0	120.0
—	—	—	—	—
50	20.0	45.0	90.0	120.0

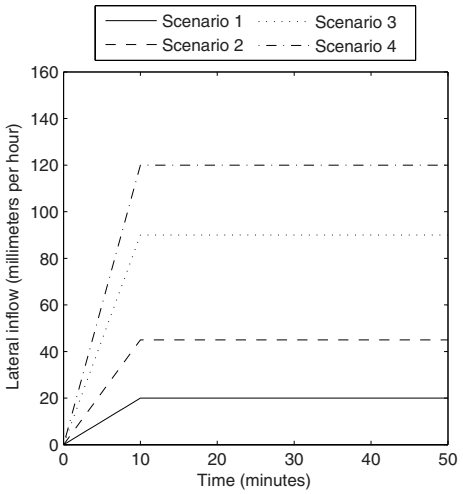

Fig. 2. Lateral inflow rates $q(t)$ to the model domain for the test scenarios 1, 2, 3, and 4

Comparison of Model Results

Mass Balance Check

The fulfillment of mass conservation of the four incorporated models is considered first. For this purpose, the four different lateral inputs of scenarios 1 to 4 are supplied to the synthetic test plane of a specific roughness. A mass conservation check is carried out for every model by comparing the sum of water of the lateral input and the sum of modeled outflow at the plane's lowermost cross-section at $x = 80$ m after 50 min. A variation of Chézy coefficients of $K_C = 2.0, 5.0, 10.0, 20.0$ m$^{1/2}$/s was used to sample a wide range of surface roughness conditions. The temporal and spatial resolution of the numerical models was set to equal values of $\Delta t = 2$ s and $\Delta x = 0.5$ m. The spatial resolution of the analytical model was also set to $\Delta x = 0.5$ m to take care for a certain degree of comparability of the results regarding spatial model resolution. The resulting relative mass balance errors are given in Table 2.

The mass balance comparison unveils that the analytical zero inertia model outperformed the numerical models for most constellations of lateral inflow rates and Chézy friction coefficients. The deviations in the mass balance of the aZI model output amounted to some 0.1% for 14 out of 16 calculation runs and were therewith significantly smaller than for the numerical models in 11 out of 16 cases. For the numerical models, the nKW model outperformed the nHD and nZI models with respect to mass conservation for all simulation runs. The errors of the incorporated numerical models were directly dependent on spatial and temporal resolution of the solution scheme. The deviations of the aZI model from the reference could additionally be improved by tightening the error

Table 2. Comparison of the Relative Mass Conservation of the Numerical Hydrodynamic Model (nHD), Numerical Kinematic Wave Model (nKW), Numerical and Analytical Zero Inertia Models (nZI and aZI) for Different Lateral Inputs to the Synthetic Test Plane after 50 Minutes of Inflow

	K_C[m$^{1/2}$/s]	2.0 (%)	5.0 (%)	10.0 (%)	20.0 (%)
$q(t)_{max}$ =	nHD	−1.43	−1.75	−1.86	−2.29
20 mm/h	nKW	**−0.51**	**−0.56**	−0.58	−0.60
	nZI	−1.43	−1.75	−1.86	−2.30
	aZI	−1.38	−1.11	**−0.49**	**−0.53**
$q(t)_{max}$ =	nHD	−1.32	−1.34	−1.81	−1.79
45 mm/h	nKW	**−0.53**	−0.58	−0.59	**−0.61**
	nZI	−1.32	−1.34	−1.81	−1.80
	aZI	−0.84	**−0.55**	**−0.37**	−0.63
$q(t)_{max}$ =	nHD	−1.25	−1.26	−1.66	−1.30
90 mm/h	nKW	**−0.56**	−0.59	−0.60	−0.61
	nZI	−1.25	−1.26	−1.67	−1.31
	aZI	−0.64	**−0.48**	**−0.52**	**−0.58**
$q(t)_{max}$ =	nHD	−1.24	−1.25	−1.64	−1.46
120 mm/h	nKW	−0.56	−0.59	−0.60	−0.61
	nZI	−1.24	−1.25	−1.65	−1.43
	aZI	**−0.26**	**−0.15**	**−0.18**	**−0.25**

Note: Best results are set in bold.

criterion of the iteration procedure given by Eqs. (13) and (14). The mass balance error decreased with higher total peak inflow for all incorporated models. The mass balance errors of the aZI model were always lowest for moderate friction coefficients of $K_C = 5.0, 10.0$ m$^{1/2}$/s. Overall, the aZI model performed very well compared with the other models.

Results of the Test Scenario Calculations

The aforementioned initial conditions and boundary conditions were applied to the four presented models and the simulated flow hydrographs for the lowermost observation point of the synthetic test plane ($x = 80$ m) were compared. Fig. 3 depicts the resulting hydrographs of the scenario calculations 1, 2, 3, and 4 (maximum inflow rate $q(t)_{max} = 20,45,90,120$ mm/h) for a friction coefficient of $K_C = 5.0$ m$^{1/2}$/s. The results for other friction coefficients ($K_C = 2.0, 10.0, 20.0$ m$^{1/2}$/s) look similar but with decreased/increased dynamics of the rising limb of the simulated flow hydrographs. Table 3 shows the quasi-stationary flow rates $Q(x,t)$ after 50 min at the lowermost cross-section $x = 80$ m for the scenario calculations. The process dynamics of all scenarios are soundly portrayed by the four incorporated models. These observations apply for the whole range of investigated Chézy friction coefficients. Onset and rising limb of the hydrograph and transition to the quasi-stationary peak flow rate are convergent for the investigated models. The calculations for higher Chézy coefficients led to a slightly better agreement of the resulting peak flow rates of the different models.

The analytical zero inertia model nearly matched the stationary peak inflow rates of $q(t)_{max} = 20,45,90,120$ mm/h for all applied Chézy friction coefficients, which is supported by the analytical character of the model. The aZI model performed best for 15 out of 16 herein presented calculations. The quality of the aZI

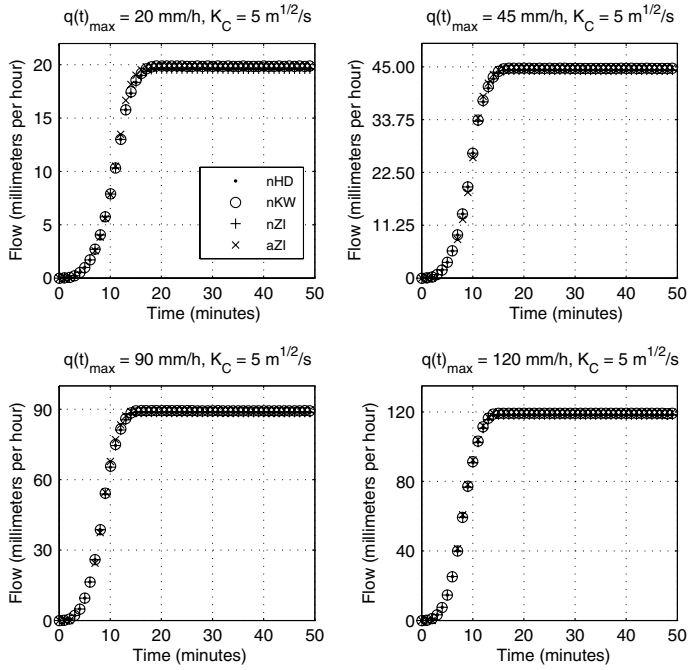

Fig. 3. Flow hydrograph comparison for lateral input scenarios 1, 2, 3, and 4 (maximum inflow rate $q(t)_{max} = 20$; 45; 90; 120 mm/h) and Chézy friction coefficient of $K_C = 5.0$ m$^{1/2}$/s at location $x = 80$ m of the synthetic test plane; simulation results provided by numerical full hydrodynamic model (nHD), numerical kinematic wave model (nKW), and numerical and analytical zero inertia models (nZI and aZI)

Table 3. Comparison of Absolute and Relative Quasi-Stationary Flow Rates (Millimeters per Hour) at the Lowermost Cross-Section after 50 Minutes $Q(x = 80\ \text{m},\ t = 50\ \text{min})$ for Scenario Calculations 1, 2, 3, and 4

	$K_C[\text{m}^{1/2}/\text{s}]$	2.0	5.0	10.0	20.0
$q(t)_{\max} = 20$ mm/h	nHD	19.6664 (−1.67)	19.6142 (−1.93)	19.5944 (−2.03)	19.5086 (−2.46)
	nKW	19.8535 (**−0.73**)	19.8358 (−0.82)	19.8471 (−0.76)	19.8231 (−0.88)
	nZI	19.6664 (−1.67)	19.6141 (−1.93)	19.5940 (−2.03)	19.5079 (−2.46)
	aZI	19.7730 (−1.14)	19.8923 (**−0.54**)	19.9350 (**−0.33**)	19.9283 (**−0.36**)
$q(t)_{\max} = 45$ mm/h	nHD	44.3164 (−1.52)	44,3303 (−1.49)	44,1184 (−1.96)	44,1370 (−1.92)
	nKW	44.6670 (−0.74)	44,6942 (−0, 68)	44,5782 (−0, 94)	44,4173 (−1, 29)
	nZI	44.3162 (−1.52)	44,3296 (−1, 49)	44,1168 (−1, 96)	44,1332 (−1, 93)
	aZI	44.6850 (**−0.70**)	44.8425 (**−0.35**)	44.8650 (**−0.30**)	44.7975 (**−0.45**)
$q(t)_{\max} = 90$ mm/h	nHD	88.7156 (−1.43)	88.7314 (−1.41)	88.3846 (−1.79)	88.7334 (−1.41)
	nKW	89.3272 (−0.75)	89.3021 (−0.78)	89.3449 (−0.73)	89.2886 (−0.79)
	nZI	88.7151 (−1.43)	88.7295 (−1.41)	88.3800 (−1.80)	88.7219 (−1.42)
	aZI	89.4375 (**−0.63**)	89.7075 (**−0.33**)	89.6625 (**−0.38**)	89.4825 (**−0.58**)
$q(t)_{\max} = 120$ mm/h	nHD	118.2978 (−1.42)	118.3182 (−1.40)	117.8628 (−1.78)	118.0799 (−1.60)
	nKW	119.0986 (−0.75)	119.0993 (−0.75)	118.9665 (−0.86)	119.1663 (−0.69)
	nZI	118.2970 (−1.42)	118.3152 (−1.40)	117.8555 (−1.79)	118.1176 (−1.57)
	aZI	119.4300 (**−0.47**)	119.7225 (**−0.23**)	119.6100 (**−0.33**)	119.4525 (**−0.46**)

Note: The relative deviations from the maximum lateral inflow to the test plane $q(t)_{\max}$ are given in parentheses. Best results are set in bold.

results could be even improved by tightening the convergence criterion of the incorporated iterative solution procedure that led to higher computational effort. The aZI model showed the lowest peak flow errors for moderate Chézy coefficients. Peak flow errors of the aZI model decreased with increasing peak flow rates. For the numerical models, the nKW model performed best in matching quasi-stationary peak flow rates. The respective relative errors of the nKW model were always lower than the errors of the nHD and the nZI model. Furthermore, the errors of the nHD and nZI model were nearly equal for the specific simulations. Like for the aZI model, peak flow errors of the numerical models decreased with increasing peak flow rates.

Computation Time Requirements

A comparison of CPU time requirements for the calculations of the aforementioned test scenarios (four different boundary conditions with four different friction coefficients) was conducted. The numerical models were all implemented in FORTRAN language and compiled with the same compiler. The analytical zero inertia model was implemented and executed in the MATLAB environment. A 1.6 GHz machine with 2 GB of memory was used for computation. The CPU time of each model for all 16 model setups were averaged and normalized by the mean CPU time requirement of the analytical ZI model:

$$\text{CPU time factor} = \frac{\text{CPU time}_{\text{nHD,nKW,nZI}}}{\text{CPU time}_{\text{aZI}}} \tag{16}$$

The mean CPU time and CPU time factors for the four different models are given in Table 4.

As expected, CPU time increased with the complexity of the governing flow equations of each model. The flow simulations with the nHD model required the highest CPU time, followed by the nZI and the nKW model. The aZI model exhibited the lowest CPU time requirements. CPU time is primarily required for the iterative solution of the system in Eqs. (13) and (14), which needed typically fewer than 20 iteration loops for yielding convergence. Tightening the iteration criterion led to slightly better model results but higher CPU time. It has to be mentioned that the nHD, nKW, and the nZI code were used as compiled executable code, whereas the aZI code was executed in the MATLAB interpreter environment. It is assumed that a compiled version of the aZI code would outperform the other investigated models by far, considering CPU time requirements.

Table 4. Comparison of Average Central Processing Unit (CPU) Time Requirements of the Full Hydrodynamic Model (nHD), Kinematic Wave Model (nKW), Numerical Zero Inertia Model (nZI), and Analytical Zero Inertia Model (aZI)

Model	Code execution	Spatial resolution Δx (meters)	Temporal resolution Δt	Averaged CPU time (second)	CPU time factor
nHD	Compiled	0.5	2 s	9.56	1.40
nKW	Compiled	0.5	2 s	6.92	1.01
nZI	Compiled	0.5	2 s	8.97	1.31
aZI	Interpreted	0.5	Adaptive	6.83	1.00

Discussion and Conclusions

The presented analytical zero inertia model showed a highly satisfactory performance for modeling typical scenarios of sheet flow on a synthetic plane, charged by time-variable rainfall events. In a comparative analysis the aZI model delivered mostly better results than the commonly used numerical approaches in terms of an adequate mass balance and matching peak runoff rates. Furthermore, the aZI model showed a convergent solution for the process dynamics of the flow compared with the numerical solutions. At the same time, the aZI model demanded less CPU time than the employed numerical solution schemes.

The mass balance error of the aZI model for the 16 simulation runs amounted −0.15 to −1.38%, which made the model superior for 11 out of 16 runs regarding mass balance errors. The mass balance errors of the numerical models for all simulation runs spanned 1.24 to −2.29% (nHD), −0.51 to −0.61% (nKW), and −1.24 to −2.30% (nZI). The errors of the aZI model for the portrayal of peak inflow rates were again comparatively small with −0.23 to

−1.14%. The nHD model (−1.40 to −2.46%), nKW model (−0.68 to −1.29%), and nZI model (−1.40 to −2.46%) showed larger relative errors, related to peak inflow rates. The aZI model met the peak flow rates best for 15 out of 16 simulations. The very exact match of the aZI model of mass balance and peak inflow rate is supported by the analytical character of the model.

The aZI model demanded the lowest computation times of all investigated models. Although, CPU time requirements of the aZI model were only slightly lower than those of the nKW model for the flow calculations on the investigated simple geometry. The nHD model demanded the highest CPU times that were factor 1.4 higher than for the aZI model. The benefit of lower CPU time of the aZI model will very well improve spatially distributed surface flow modeling on catchment scale. At the same time, the aZI model is free of numerical inconveniences, like discretization errors, phase errors, and convergence problems, which often endanger the solution of numerical schemes, particularly regarding weak process dynamics of typical sheet flow phenomena. To delimit such errors, the authors of this study had to chose a relatively fine spatial and temporal resolution of the employed numerical solution schemes which led to higher CPU times. Furthermore, as shown by Wöhling et al. (2004; 2006) and Philipp et al. (2010), the straightforward coupling of the surface flow model with any arbitrary infiltration model is easy because of the analytical character of the surface flow model.

Consequently, the proposed analytical zero inertia model can represent a valuable element in a boundary condition coupled, cell-wise surface runoff modeling environment because it is (1) accurate, (2) fast in terms of low computational demand, and (3) robust for a wide range of process dynamics. The authors are working on an implementation of the proposed model in a rainfall runoff modeling framework. For spatially distributed hydrological modeling, the aZI model can potentially improve the portrayal of overland flow in terms of reduction of errors and total model execution times.

Appendix

Using a continuous formulation, Eq. (15) can be written as

$$h(x,t) = h_0\sqrt{1-\frac{x}{x_{\text{tip}}}} \tag{17}$$

where both h_0 and x_{tip} depend on time. Differentiating Eq. (17) with respect to t therefore yields

$$\frac{\partial h}{\partial t} = \frac{dh_0}{dt}\sqrt{1-\frac{x}{x_{\text{tip}}}} + \frac{h_0}{2\sqrt{1-\frac{x}{x_{\text{tip}}}}}\frac{x}{x_{\text{tip}}^2}u_{\text{tip}} \tag{18}$$

This result can be inserted for the first integrand in Eq. (10)

$$\int_0^x \frac{\partial h}{\partial t}(\xi,t)d\xi = \frac{dh_0}{dt}\int_0^x\sqrt{1-\frac{\xi}{x_{\text{tip}}}}d\xi + \frac{h_0 u_{\text{tip}}}{2x_{\text{tip}}^2}\int_0^x\frac{\xi}{\sqrt{1-\frac{\xi}{x_{\text{tip}}}}}d\xi \tag{19}$$

Both integrals on the right-hand side of Eq. (19) can be explicitly evaluated (e.g., Bronstein and Semendjajev 1966) and the resulting expression reads

$$\begin{aligned}\left\{\int_0^x \frac{\partial h}{\partial t}(\xi,t)d\xi = \right.& -\frac{2}{3}x_{\text{tip}}\frac{dh_0}{dt}\left[\left(1-\frac{x}{x_{\text{tip}}}\right)^{3/2}-1\right]\\ &-\frac{1}{3}u_{\text{tip}}h_0\left[\left(2+\frac{x}{x_{\text{tip}}}\right)\sqrt{1-\frac{x}{x_{\text{tip}}}}-2\right]\\ =&\frac{2}{3}\frac{d}{dt}(x_{\text{tip}}h_0)-\frac{2}{3}x_{\text{tip}}\frac{dh_0}{dt}\left(1-\frac{x}{x_{\text{tip}}}\right)^{3/2}\\ &\left.-\frac{1}{3}u_{\text{tip}}h_0\left(2+\frac{x}{x_{\text{tip}}}\right)\sqrt{1-\frac{x}{x_{\text{tip}}}}\right\}\end{aligned} \tag{20}$$

The first term on the right-hand side of Eq. (20) equals $Q_0 - \int_0^{x_{tip}} q(\xi,t)d\xi$, as can be seen from Eq. (12). Consequently, Eq. (10) can be simplified to

$$\begin{aligned}\left[Q(x,t) = \right.&\frac{2}{3}x_{\text{tip}}\frac{dh_0}{dt}\left(1-\frac{x}{x_{\text{tip}}}\right)^{3/2}\\ &\left.+\frac{1}{3}u_{\text{tip}}h_0\left(2+\frac{x}{x_{\text{tip}}}\right)\sqrt{1-\frac{x}{x_{\text{tip}}}}+\int_x^{x_{\text{tip}}}q(\xi,t)d\xi\right]\end{aligned} \tag{21}$$

which yields the discharge per unit width, $Q(x,t)$.

Acknowledgments

Professor Rao S. Govindaraju is acknowledged for the highly fruitful conversation and for providing FORTRAN code for the numerical solution of the flow equations.

References

Bronstein, I. N., and Semendjajev, K. A. (1966). *Taschenbuch der mathematik*, B. G. Teubner Verlagsgesellschaft Vienna, Austria (in German).

Bronstert, A., and Bárdossy, A. (2003). "Uncertainty of runoff modelling at the hillslope scale due to temporal variations of rainfall intensity." *Phys. Chem. Earth.*, 28(6–7), 283–288.

Daluz Vieira, J. H. (1983). "Conditions governing the use of approximations for the saint-venant equations for shallow surface water flow." *J. Hydrol.*, 60(1–4), 43–58.

Di Giammarco, P., and Todini, E., and Lamberti, P. (1995). "A conservative finite elements approach to overland flow: The control volume finite element formulation." *J. Hydrol.*, 175(1–4), 267–297.

Esteves, M., Faucher, X., Galle, S., and Vauclin, M. (2000). "Overland flow and infiltration modelling for small plots during unsteady rain: Numerical versus observed values." *J. Hydrol.*, 228(3–4), 267–291.

Govindaraju, R. S., Jones, S. E., and Kavvas, M. L. (1988). "On the diffusion wave model for overland flow: 1. Solution for steep slopes." *Water Resour. Res.*, 24(5), 734–744.

Govindaraju, R. S., Kavvas, M. L., and Jones, S. E. (1990). "Approximate analytical solutions for overland flows." *Water Resour. Res.*, 26(12), 2903–2912.

Govindaraju, R. S., Kavvas, M. L., and Tayfur, G. (1992). "A simplified model for two-dimensional overland flows." *Adv. Water Resour.*, 15(2), 133–141.

Henderson, F. M., and Wooding, R. A. (1964). "Overland flow and groundwater flow from a steady rainfall of finite duration." *J. Geophys. Res.*, 69(8), 1531–1540.

Hjelmfelt, A. T. (1981). "Overland flow from time-distributed rainfall." *J. Hydraul. Div., Am. Soc. Civ. Eng.*, 107(2), 227–238.

Hjelmfelt, A. T. (1984). "Convolution and the kinematic wave equations." *J. Hydrol.*, 75(1–4), 301–309.

Howes, D. A., Abrahams, A. D., and Pitman, E. B. (2006). "One- and two-dimensional modelling of overland flow in semiarid shrubland, Jornada basin, New Mexico." *Hydrol. Processes*, 20(5), 1027–1046.

Jaber, F. H., and Mohtar, R. H. (2003). "Stability and accuracy of two-dimensional kinematic wave overland flow modeling." *Adv. Water Resour.*, 26(11), 1189–1198.
Lighthill, M. J., and Whitham, G. B. (1955). "On kinematic waves: 1. Flood movement in long rivers." *Proc. Roy. Soc.*, A229(1178), 281–316.
Liu, Q. Q., Chen, L., Li, J. C., and Singh, V. P. (2004). "Two-dimensional kinematic wave model of overland-flow." *J. Hydrol.*, 291(1–2), 28–41.
Morris, E. M., and Woolhiser, D. A. (1980). "Unsteady one-dimensional flow over a plane: Partial equilibrium and recession hydrographs." *Water Resour. Res.*, 16(2), 355–360.
Philipp, A., Schmitz, G. H., and Liedl, R. (2010). "An analytical model of surge flow in non-prismatic permeable channels and its application in arid regions." *J. Hydraul. Eng.*, 136(5), 290–298.
Ross, B. B., Contractor, D. N., and Shanholtz, V. O. (1979). "A finite-element model of overland and channel flow for assessing the hydrologic impact of land-use change." *J. Hydrol.*, 41(1–2), 11–30.
Schmid, B. H. (1986). "Zur mathematischen modellierung der abflussentstehung an hängen." Ph.D. thesis, Vienna Univ. of Technology (in German).
Schmitz, G. H. (1989). "Strömungsvorgänge auf der oberfläche und im bodeninneren beim bewässerungslandbau." *Rep. No. 60*, Wasserbau und Wasserwirtschaft, Graz, Austria.
Schmitz, G. H., Liedl, R., and Volker, R. (2002). "Analytical solution to the zero-inertia problem for surge flow phenomena in non-prismatic channels." *J. Hydraul. Eng.*, 128(6), 604–615.
Schmitz, G. H., and Seus, G. (1990). "Mathematical zero-intertia modeling of surface irrigation: Advance in borders." *J. Irrig. Drain. Eng.*, 116(5), 603–615.
Schmitz, G. H., and Seus, G. (1992). "Mathematical zero-intertia modeling of surface irrigation: Advance in furrows." *J. Irrig. Drain. Eng.*, 118(1), 1–18.
Singh, V. P. (2002). "Is hydrology kinematic?" *Hydrol. Processes*, 16(3), 667–719.
Strelkoff, T. (1970). "Numerical solution of Saint-Venant equations, *J. Hydraul. Div.*, 96(1), 223–252.
Tayfur, G., and Kavvas, M. L. (1998). "Areally-averaged overland flow equations at hillslope scale." *Hydrol. Sci. J.*, 43(3), 361–378.
Tsai, T. L., and Yang, J. C. (2005). "Kinematic wave modeling of overland flow using characteristics method with cubic-spline interpolation." *Adv. Water Resour.*, 28(7), 661–670.
Wöhling, T., Fröhner, A., and Schmitz, G. H. (2006). "Efficient solution of the coupled one-dimensional surface–two-dimensional subsurface flow during furrow irrigation advance." *J. Irrig. Drain. Eng.*, 132(4), 380–388.
Wöhling, T., and Mailhol, J.-C. (2007). "Physically based coupled model for simulating 1D surface–2D subsurface flow and plant water uptake in irrigation furrows. II: Model test and evaluation." *J. Irrig. Drain. Eng.*, 133(6), 548–558.
Wöhling, T., and Schmitz, G. H. (2007). "Physically based coupled model for simulating 1D surface–2D subsurface flow and plant water uptake in irrigation furrows. I: Model development." *J. Irrig. Drain. Eng.*, 133(6), 538–547.
Wöhling, T., Singh, R., and Schmitz, G. H. (2004). Physically based modeling of interacting surface-subsurface flow during furrow irrigation advance." *J. Irrig. Drain. Eng.*, 130(5), 349–356.
Woolhiser, D. A., and Liggett, J. A. (1967). "Unsteady one-dimensional flow over a plane—the rising hydrograph." *Water Resour. Res.*, 3(3), 753–771.
Yen, B. C., and Tsai, C. W.-S. (2001). "On noninertia wave versus diffusion wave in flood routing." *J. Hydrol.*, 244(1–2), 97–104.
Zhang, W., and Cundy, T. W. (1989). "Modeling of two-dimensional overland flow." *Water Resour. Res.*, 25(9), 2019–2035.

Integrated Modeling System for Flash Flood Routing in Ephemeral Rivers under the Influence of Groundwater Recharge Dams

Andy Philipp*† and Jens Grundmann‡

This accepted manuscript is scheduled to appear
in the Journal of Hydraulic Engineering, volume 139, issue 12.

Abstract

Flash floods in ephemeral rivers are characterized by pronounced runoff dynamics, rapidly rising hydrographs, and infiltration through permeable river beds. In numerous countries, this infiltration—which is commonly referred to as transmission loss—is artificially increased by means of dams in order to promote groundwater recharge of local aquifers. However, flow dynamics are significantly altered by dam operation, i.e., initially pronounced process dynamics are reduced and standing/receding wave effects may occur in downstream river sections. For the adequate portrayal of such flow processes, we develop an integrated modeling system for flow routing in ephemeral rivers with groundwater recharge dams. The proposed system is based on a process-oriented description of flow, infiltration, and reservoir evaporation and allows for a robust application under a limited data situation, as usually encountered in arid and semi-arid regions.

Particularly, the proposed framework accounts for (a) the considerable loss of mass and momentum from the weakly dynamic flow downstream of a dam, attributable to transmission losses; (b) the transient character of transmission losses, which are nonlinearly depending on time and changing channel flow conditions; and (c) circumvents any numerical inconveniences associated with the modeling of dam release flow over initially dry beds by employing an analytical solution procedure of the governing flow equations. Following a comprehensive sensitivity analysis, relevant process parameters are estimated and the modeling system is applied for Wadi Ma'awil, Northern Oman. The application demonstrates both the system's accurateness and robustness for flash flood routing under transmission losses along the wadi, where a recharge dam causes strong flow retention. Therefore, the proposed modeling system can aid in deriving potential groundwater recharge rates, which is of high importance for a sound water resources assessment in the study area.

*Research Associate, Chair of Hydrology, Institute of Hydrology and Meteorology, Technische Universität Dresden, Bergstraße 66, 01069 Dresden, Germany

†Desk Officer, Saxon State Office for Environment, Agriculture and Geology, Pillnitzer Platz 3, 01326 Dresden, Saxony, Germany

‡Senior Research Associate, Chair of Hydrology, Institute of Hydrology and Meteorology, Technische Universität Dresden, Bergstraße 66, 01069 Dresden, Germany

Introduction

Ephemeral rivers are common in many dryland regions, e.g., Australia, India, Saudi Arabia, and the Southwestern United States (Schick, 1988; Tooth, 2000). According to the specific regional and climatic conditions, the riverbeds (or wadis) are dry throughout most of the year. Especially in arid regions, convective rainstorms can lead to pronounced runoff events, called flash floods, which typically show a rapidly rising water level. Since there is no direct connection between streamflow and groundwater, a certain amount of runoff infiltrates through the permeable bed. Therefore, surface flow and infiltration are mutually dependent, which demands a coupled process description. Infiltration is often very noticeable and the phenomenon is referred to as transmission loss, although the water is not lost but can recharge the groundwater (Sharma and Murthy, 1994; Shentsis and Rosenthal, 2003; Goodrich et al., 2004). Numerous authors, e.g., Rushton (1997) and Scanlon and Healy (2002) define transmission losses as potential groundwater recharge, whereas actual recharge is potential recharge minus the amount of water which has infiltrated but does not contribute to the groundwater. Furthermore, transmission loss rates may even exceed flow rates, which prevents the infiltrating flow domain from reaching more downstream sections (Tooth, 2000). In general, infiltrating runoff in ephemeral streambeds provides a certain contribution to groundwater recharge, whose quantification is inevitable, e.g., with respect to regional groundwater assessment (Wheater, 2002).

Modeling of flow influenced by transmission losses is challenging. The validity of modeling results mainly depends on the availability of gauging data, which are usually scarce in arid environments (Morin et al., 2009). Therefore, a wide range of concepts was applied for ephemeral flow modeling, depending on the specific and mostly limiting data situation, as well the various aims of the related studies. These concepts include simple regression models (e.g., Sharma and Murthy, 1994; Dunkerley and Brown, 1999), hydrologic routing approaches (e.g., Sharma and Murthy, 1995; Costelloe et al., 2003), and all types of hydrodynamic models (e.g., El-Hames and Richards, 1998; Goodrich et al., 2004; Philipp et al., 2010). However, several studies indicate the need for a hydrodynamic modeling if a detailed prognosis of flood dynamics, the transient extents of the flow domain, and—consequently—transmission losses is desired (e.g., Morita and Yen, 2002; Mudd, 2006).

Hydrodynamic models can be grouped into full hydrodynamic (HD) models (Eagleson, 1970), zero-inertia (ZI) models (Hayami, 1951), and kinematic wave (KW) models (Lighthill and Whitham, 1955). The ZI model keeps the pressure-gradient and momentum-source/sink terms of the full hydrodynamic model but neglects the inertial terms, the KW model neglects all the aforementioned. The KW model is commonly used for hydrodynamic flow routing in ephemeral channels, as shown e.g., by Goodrich et al. (2004), Al-Qurashi et al. (2008), Saber et al. (2009) and Morin et al. (2009), and allows for a robust and reliable model application for slopes >0.001 (Ponce, 1991). Other authors applied ZI models (e.g., Philipp et al., 2010) or HD models (e.g., El-Hames and Richards, 1998; Mudd, 2006).

Most often, the aforementioned routing approaches are treated numerically, which can cause specific problems, ranging from considerable mass balance errors to convergence problems, especially if the flow advance is very dynamic and/or occurs over an initially dry bed (Garcia-Navarro et al., 1999), or process dynamics get very weak (Philipp et al., 2010). This can jeopardize a discrete numerical solution which may not be able to resolve such dynamics under a feasible temporal

and spatial resolution. As a way out, a virtual baseflow rate is often introduced to circumvent numerical issues, which, however, may distort the character of the modeled flow. Like other authors, Schmitz et al. (2002) tried to overcome such problems by employing an analytical solution of the ZI equations in order to avoid numerical errors for dam-break flood modeling, where the flow advance was considered as a free-boundary problem, aiming at accurately capturing the wave tip dynamics.

Together with the aforementioned hydrodynamic routing approaches, transmission losses are often portrayed with simple regression models (e.g., Saber et al., 2009), channel water balance methods (e.g., Goodrich et al., 2004; Al-Qurashi et al., 2008), or constant infiltration rates (e.g., Morin et al., 2009). Nevertheless, infiltration is dependent on infiltration opportunity times and the transient depth of water, resulting in a variably wetted cross-sectional perimeter. A specific water level in the channel further causes a hydrostatic pressure head which—besides gravitation and the matrix potential of the soil—drives infiltration. This is demonstrated e.g., by Parissopoulos and Wheater (1991), who used Richards' equation for describing infiltration processes in permeable channels.

Furthermore, when coupling surface flow and infiltration processes on milder slopes—which might establish a significant loss of mass *and* momentum of the flow—transmission losses should be considered in the momentum equation since they slow down the downstream movement of the infiltrating flow domain. This was done e.g., by Philipp et al. (2010), who used an extended ZI model for modeling advancing open channel flow under infiltration. Mudd (2006) proved the highly nonlinear interdependency of flow and infiltration by means of coupling a HD model with Richards' equation in order to perform a numerical study.

For the coarse upper layers of the thick, unsaturated alluvial soils found in wadi beds, the matrix gradient does not strongly differ from zero and the initial vertical water movement is mainly, but not solely, a consequence of gravitation (Scanlon and Healy, 2002). Moreover, the influence of a transient hydrostatic pressure head on wadi infiltration is assumed to be small (Bouwer, 1982; Haimerl, 2004). Furthermore, infiltration on permeable alluvial material is also driven by macropore flow processes (Beven and Germann, 1982; Wood et al., 1997). Together with the limited data situation in arid areas, the applicability of matrix flow models (i.e., models based on Richards' equation) for the quantification of infiltration is often precluded. The present study, therefore, incorporates an empirical Kostiakov-Lewis model for predicting wadi infiltration.

Improving groundwater recharge is of high importance for a sustainable water resources management in arid and semi-arid areas. For instance, several groundwater recharge dams have been constructed in the wadis of the Sultanate of Oman in order to promote recharge of the coastal aquifers. Such dams retain flood flow and support a decelerated release of water, which leads to higher infiltration opportunity times in the downstream wadi sections (Haimerl, 2004). Furthermore, the dams prevent clogging of the downstream channel reaches by retaining sediment load. Recharge dams decrease runoff dynamics significantly since dam release rates—typically established by culvert release—are low compared to peak inflow rates. Consequently, a sound modeling of ephemeral flow under the influence of recharge dams has to consider the variable runoff dynamics upstream and downstream of the dam, especially if process dynamics get weak and standing/receding wave effects occur.

To tackle the aforementioned problems, we develop an integrated modeling system for ephemeral channel flow, influenced by a groundwater recharge dam. Compared to previous work (e.g., Morin et al., 2009), the modeling system aims at a more process-oriented description of flow and infiltration.

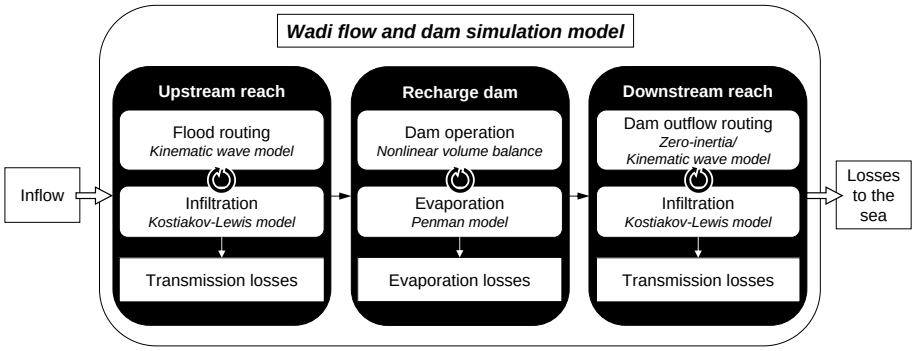

Figure 1: Components of the proposed modeling system.

The proposed modeling system accounts particularly for (a) the considerable loss of momentum from less dynamic flow downstream of a dam, attributable to transmission losses; (b) the transient development of channel infiltration, nonlinearly depending on time and changing channel hydraulics; and (c) circumvents any numerical inconveniences associated with dam release flow routing under pronounced losses by employing an analytical solution procedure of the governing flow equations. The proposed system is applied for Wadi Ma'awil, Northern Oman, where flow is controlled by a large groundwater recharge dam. The application results suggest that the herein presented modeling system can serve as a valuable and robust tool for the quantification of transmission losses within a larger framework for water resources management in arid regions (Grundmann et al., 2012).

The Wadi Flow and Dam Simulation Model

The full modeling system (Fig. 1) incorporates three main elements: each a hydrodynamic model for the upstream and the downstream reaches; as well a dam simulation model with a Penman evaporation component. The hydrodynamic models are each coupled with a Kostiakov-Lewis infiltration model for the quantification of transmission losses which can be parametrized on the basis of infiltrometry data. For the more pronounced flow in the steeper upstream reaches, we implemented a KW model. To accommodate for the more complex character of the flow downstream of the dam, flow advance and recession were treated separately. To circumvent numerical instabilities and to take care for the potentially strong influence of infiltration, a tailor-made analytical ZI model was set up for modeling the advancing flow domain. In turn, flow recession in the downstream reaches—which is not covered by the derived analytical ZI solution—was modeled with the KW equations. The same applies for dam outflow caused by spillway operation. All sub-models are one-dimensional and are coupled horizontally via the flow $Q(t)$.

Flow Routing and Transmission Losses

Kinematic Wave Routing Model

The unsteady flow upstream of the dam is modeled with the KW equations which assume that friction slope equals bed slope. Consequently, the KW model cannot reproduce a depth-discharge hysteresis.

The continuity equation reads

$$\frac{\partial A}{\partial t} + \frac{\partial Q}{\partial x} = -q \tag{1}$$

in which t: time [T]; x: longitudinal space coordinate [L]; $A(x,t)$: wetted cross-sectional area [L^2]; $Q(x,t)$: discharge [$\mathrm{L}^3\mathrm{T}^{-1}$]; $q(x,t)$: volumetric rate of infiltration per unit width [$\mathrm{L}^2\mathrm{T}^{-1}$].

Under the aforementioned restrictions of the kinematic wave assumptions, the corresponding momentum equation reads

$$0 = S_0 - S_\mathrm{f} \tag{2}$$

where S_0: bottom slope [−] and S_f: friction slope [−].

Velocity, slope, and channel roughness are commonly related using a friction law in the form

$$u = K R^\beta S_\mathrm{f}^{\frac{1}{2}} \tag{3}$$

where $u(x,t)$: flow velocity [LT^{-1}]; K: Roughness coefficient [$\mathrm{L}^{1-\beta}\mathrm{T}^{-1}$]; $R(x,t)$: hydraulic radius [L]; β: exponent of the flow formula [−] (e.g., $\beta = \frac{2}{3}$ for the Manning-Strickler law).

Equation (3) is rearranged and inserted into Eq. (2), yielding

$$0 = S_0 - \frac{u^2}{K^2 R^{2\beta}} = S_0 - \frac{Q^2}{K^2 R^{2\beta} A^2} \tag{4}$$

The geometry of the wadi cross sections can be incorporated in the one-dimensional model by means of two profile functions, e.g., relating the wetted cross-sectional area and the hydraulic radius to the water depth:

$$\tilde{A}(x,h) = \int_0^{\tilde{B}(x,h)} \tilde{h}(x,y)\mathrm{d}y \tag{5}$$

$$\tilde{R}(x,h) = \frac{\tilde{A}(x,h)}{\tilde{P}(x,h)} = \frac{\displaystyle\int_0^{\tilde{B}(x,h)} \tilde{h}(x,y)\mathrm{d}y}{\displaystyle\int_0^{\tilde{B}(x,h)} \sqrt{1+\tilde{h}'(x,y)^2}\mathrm{d}y} \tag{6}$$

where y: space coordinate perpendicular to the flow at a specific channel location x [L]; $h(x,y)$: depth of water reaching the cross-sectional coordinate (x,y) [L]; $\tilde{A}(x,h)$: wetted cross-sectional area as a function of water depth [L^2]; $\tilde{B}(x,h)$: flow width in the channel as a function of water depth [L]; $\tilde{R}(x,h)$: hydraulic radius as a function of water depth [L]; and $\tilde{P}(x,y)$: the wetted cross-sectional perimeter [L].

This way, $\tilde{A}$, $\tilde{R}$, and $\tilde{P}$ are biuniquely related via the water depth. Another practice is expressing the water depth and the hydraulic radius in terms of the wetted cross-sectional area, i.e., obtaining $\tilde{h}(x,A)$ and $\tilde{R}(x,A)$ (cf. Eqs. (18) and (19)), which can be achieved by employing the inverse function of $\tilde{A}(x,h)$ and mapping $\tilde{R}(x,h)$ on $\tilde{R}(x,A)$. For formal reasons, the profile-specific functions $\tilde{h}$, $\tilde{B}$, $\tilde{A}$, $\tilde{R}$, and $\tilde{P}$ are distinguished from the spatiotemporal functions of the dependent variables $h(x,t)$, $B(x,t)$, $A(x,t)$, $R(x,t)$, and $P(x,t)$.

Assuming K and S_0 to be constant for a channel element, Eq. (4) is rearranged and differentiated with respect to x, yielding

$$\frac{\partial Q}{\partial x} = K S_0^{\frac{1}{2}} R^{\beta-1}\left(\beta A \frac{\partial R}{\partial x} + R\frac{\partial A}{\partial x}\right) \tag{7}$$

Eq. (7) is inserted into Eq. (1) and the resulting equation is numerically integrated using an explicit Runge-Kutta finite differencing scheme. Despite implicit finite difference schemes feature greater numerical stability and comparably intermediate computational demand (Press et al., 1992), an explicit scheme was chosen since the routing model is intended for the portrayal of highly dynamic, shock-prone flows, as present in sewer networks (Duchesne et al., 2001), associated with dam-break problems (e.g., Garcia-Navarro et al., 1999), or—as applies for this work—flash flood routing (e.g., Mudd, 2006).

The numerical scheme evaluates the solution at specific spatiotemporal points, which are equally spaced with the spatial step Δx and the time step Δt. For explicit schemes, the chosen spatiotemporal discretization has to fulfill the Courant-Friedrichs-Lewy condition (Courant et al., 1928), which relates the spatial and temporal resolution to the maximum process velocity, established by the flow velocity u and wave celerity $c = \sqrt{gh}$:

$$\frac{\Delta x}{\max(u \pm c)} \overset{!}{>} \Delta t \tag{8}$$

The solution of the KW model requires the specification of initial and boundary conditions. The upstream boundary condition at $x = 0$ is the inflow hydrograph

$$Q_0 = Q_0(t) = Q(x = 0, t) \tag{9}$$

and the downstream boundary can be characterized by an advancing wave tip. Therefore, the downstream boundary conditions read

$$A(x_{\text{tip}}, t) = 0 \tag{10}$$

$$u(x_{\text{tip}}, t) = u_{\text{tip}}(t) = \frac{\mathrm{d}x_{\text{tip}}}{\mathrm{d}t} \tag{11}$$

where $x_{\text{tip}}(t)$: location of the advancing wave tip [L] and $u_{\text{tip}}(t)$: velocity of the wave tip [LT^{-1}].

The ideal dry channel initial condition is

$$x_{\text{tip}}(t = 0) = 0 \tag{12}$$

For the numerical KW model, the initial condition is alleviated to prevent numerical issues. A minimum flow $Q(x, t = 0) > 0$ is introduced and the initial values of the other dependent variables are calculated prior the numerical integration, assuming uniform flow conditions. Due to the simplifications inherent to the KW momentum equation (2), the model cannot account for the influence of the dam on the upstream wadi section, which poses no restriction with respect to the pronounced slope of the wadi section upstream of the dam.

Since cross-sectional infiltration is dependent on the wetted perimeter, and vice versa, the flow equation is coupled with the infiltration function by employing a fixed-point iteration scheme in order to carry out an alternating iterative coupling procedure (cf. Morita and Yen, 2002). This means, that the flow equations and the loss relationship are solved separately, but in the same time step. Surface flow and losses are interlinked via infiltration as internal boundary condition. The fulfillment of the continuity equation is used to check for convergence with respect to a specific tolerance criterion.

Zero-Inertia/Kinematic Wave Routing Model

The advancing and infiltrating dam release flow is modeled with the extended ZI equations

$$\frac{\partial A}{\partial t} + \frac{\partial Q}{\partial x} = -q \tag{13}$$

$$\frac{\partial h}{\partial x} = S_0 - S_\mathrm{f} + \frac{qu}{gA} \tag{14}$$

in which $h(x,t)$: water depth [L] and g: acceleration due to Earth's gravity [LT^{-2}]. Compared to Eq. (2), Eq. (14) introduces a non-parallelism of friction slope and bed slope, and accounts for the impact of infiltration on the momentum balance via the qu/gA term.

Using Eq. (3), Eq. (14) can be rewritten to

$$\frac{\partial h}{\partial x} = S_0 - \frac{u^2}{K^2 R^{2\beta}} + \frac{qu}{gA} \tag{15}$$

For the solution of the system (13);(15), Eq. (15) is multiplied at first by $R^{2\beta}$, which yields

$$R^{2\beta}\frac{\partial h}{\partial x} = \left(S_0 + \frac{qu}{gA}\right) R^{2\beta} - \frac{u^2}{K^2} \tag{16}$$

The concept of the proposed analytical solution draws upon that the inflow boundary can be considered as a kind of momentum-representative cross section (Schmitz et al., 2002). The momentum described by the right hand side of Eq. (16)—which equals zero in kinematic wave analysis—is continuously represented by the transient amount of momentum at $x = 0$, the location of the inflow boundary. Thus, the right-hand side of Eq. (16) no longer depends explicitly on x and the equation can be expressed as

$$R^{2\beta}\frac{\partial h}{\partial x} = \left(S_0 + \frac{q_0 u_0}{gA_0}\right) R_0^{2\beta} - \frac{u_0^2}{K^2} = \left(S_0 - \frac{u_0^2}{K^2 R_0^{2\beta}} + \frac{q_0 u_0}{gA_0}\right) R_0^{2\beta} \tag{17}$$

with $A_0 = A_0(t) = A(x = 0, t)$, $R_0 = R_0(t) = R(x = 0, t)$, $u_0 = u_0(t) = u(x = 0, t)$, and $q_0 = q_0(t) = q(x = 0, t)$. The right-hand side of Eq. (17) covers contributions from bottom slope, friction, and infiltration through the channel bed, and may, therefore, be regarded as a measure of the transient momentum at $x = 0$.

The variable cross-sectional geometries are described by the power laws (cf. Schmitz et al., 2002)

$$\tilde{h}(x, A) = h(x, t) = p_1(x) A(x, t)^{p_2} \tag{18}$$

$$\tilde{R}(x, A) = R(x, t) = p_3(x) A(x, t)^{p_4} \tag{19}$$

with $p_1(x)$, p_2, $p_3(x)$, and p_4: geometry parameters for expressing water depth and hydraulic radius of a channel cross section as a function of the wetted cross-sectional area. Nonprismatic irregular cross sections can be closely approximated by adjusting the free parameters $p_1(x)$, p_2, $p_3(x)$, and p_4, as shown by Schmitz et al. (2002).

The system (13);(17) requires initial and boundary conditions. At $x = 0$, the boundary condition is

$$Q_0 = Q_0(t) = Q(x = 0, t) \tag{20}$$

Strongly falling hydrographs cannot be used as upper boundary condition for the analytical ZI model (Schmitz et al., 2002). Therefore, the approach is applicable for gradually varied dam culvert outflow but not for dynamically changing flow hydrographs, as present in the upstream wadi section or downstream of the dam, as a consequence of spillway release.

The following conditions have to be fulfilled at the advancing wave tip

$$A(x_{\mathrm{tip}}, t) = 0 \tag{21}$$

$$u(x_{\mathrm{tip}}, t) = u_{\mathrm{tip}}(t) = \frac{\mathrm{d}x_{\mathrm{tip}}}{\mathrm{d}t} \tag{22}$$

and the initial condition is

$$x_{\mathrm{tip}}(t = 0) = 0 \tag{23}$$

Employing Eqs. (18) and (19), the momentum Eq. (17) can be analytically solved:

$$A(x,t) = p_1(x)^{-\frac{1}{p_2}} \left\{ \left(1 + \frac{2\beta p_4}{p_2}\right) \left(-S_0 + \frac{u_0^2}{K^2 R_0^{2\beta}} - \frac{q_0 u_0}{g A_0}\right) R_0^{2\beta} \int_x^{x_{\mathrm{tip}}(t)} \left(\frac{p_1(\xi)^{\frac{p_4}{p_2}}}{p_3(\xi)}\right)^{2\beta} \mathrm{d}\xi \right\}^{\frac{1}{2\beta p_4 + p_2}} \tag{24}$$

where ξ indicates the integration variable in space.

To preserve the concept of a moving lower boundary condition, the virtual-wave concept of Schmitz and Seus (1992) is applied. This means, that the modeling domain is continuously extended in downstream direction if the advancing wave tip reaches the end of the considered channel reach. With the upstream boundary condition (20), the continuity equation (13) can be directly integrated, yielding the discharge $Q(x,t)$ as

$$Q(x,t) = Q_0(t) - \int_0^{x(t)} \left(\frac{\partial A}{\partial t}(\xi, t) + q(\xi, t)\right) \mathrm{d}\xi \tag{25}$$

where the integrand can be obtained by differentiating Eq. (24) with respect to t. Eqs. (24) and (25) solve the system (13);(17) and also satisfy the boundary conditions (21) and (22). The nonlinear system (24);(25) is solved iteratively. For the detailed solution procedure cf. Philipp et al. (2010). Foremost, this solution soundly accounts for the possibly strong hydraulic feedback between the advancing flow over a dry riverbed and water losses due to infiltration.

During the beginning advance of dam release flow, infiltration quotas are comparably high and the consideration of infiltration in the momentum balance is indicated for an accurate transmission loss modeling. Generally, the advance rate of the wave tip decreases with increasing time and increasing extent of the infiltrating domain, which can lead to standing wave effects. This is the case if infiltration rates equal inflow rates. If dam outflow rates are lower than infiltration rates, the flow domain starts receding in upstream direction. This condition is not covered by the analytical

solution of the ZI equations. When the flow advance ceases, the ZI model results are, therefore, written to the initial condition of a KW model, which covers the recession phase and is set up following the concepts already discussed.

Under spillway release—which is a rare condition for the investigated recharge dam—total dam outflow rates are high compared to culvert outflow alone. This implies a negligible impact of infiltration on flow momentum during spillway operation. Moreover, downstream infiltration rates have already dropped significantly at the time of spillway activation. Furthermore, the spillway outflow features strongly falling hydrographs. We chose, therefore, to route the dam outflow during spillway operation again with a KW model. When the spillway is activated, ZI results are passed to the initial condition of the KW model and vice versa, when the spillway outflow ceases. The such combined downstream hydrodynamic model, consisting of a ZI model and a KW model for routing the advancing/receding culvert outflow and an additional KW model for flow routing during spillway operation, is referred to as ZI/KW model in the following.

Kostiakov-Lewis Infiltration Model

Any arbitrary relationship could be used for the quantification of transmission losses within the proposed modeling framework. Wadi infiltration is not solely a consequence of matrix flow, which omits the application of typical deterministic infiltration models. Furthermore, no soil hydraulic data are available, which would be a precondition for applying, e.g., Green and Amp type models. We assume, therefore, an empirical model to be appropriate in case infiltrometry data are available. Infiltration is portrayed by the empirical Kostiakov-Lewis model (Haverkamp et al., 1988), which reads

$$q_{\mathrm{K}}(x,t) = k_{\mathrm{a}} k_{\mathrm{k}} t^{(k_{\mathrm{a}}-1)} + k_{\mathrm{c}} \tag{26}$$

where q_{K}: infiltration rate per unit area [LT^{-1}]; k_{a}: empirical Kostiakov-Lewis exponent [−]; k_{k}: empirical Kostiakov-Lewis exponent [$\mathrm{LT}^{-k_{\mathrm{a}}}$]; and k_{c}: steady or final infiltration rate [LT^{-1}].

The volumetric cross-sectional infiltration q is calculated by taking into account the wetted cross-sectional perimeter at which infiltration occurs

$$q = q_{\mathrm{K}} P(x,t) \tag{27}$$

and the quantity of total infiltrated water along a channel section can then be calculated by

$$I(x,t) = \int_0^t \int_0^x q(x,t)\mathrm{d}x\,\mathrm{d}t \tag{28}$$

where $I(x,t)$ is the total cumulative infiltration [L^3].

Dam Operation

Nonlinear Dam Retention Model

The dynamic change of the water volume within a retention reservoir under varying inflow conditions can be expressed by the differential storage equation, representing continuity. Sedimentation causes clogging of the reservoir bottom and, consequently, infiltration through the bottom will tend to zero (Haimerl, 2004). Due to the specific cubature of the herein considered reservoir—located in the

coastal plain—the inclined reservoir sides, which are less prone to clogging and, therefore, potentially permeable, make up an only small fraction of the bottom area. For this reason, infiltration losses are neglected in the reservoir balance. The continuity equation of the reservoir reads

$$\frac{\mathrm{d}V}{\mathrm{d}t} = Q_{\mathrm{in}} - Q_{\mathrm{out}} - E \tag{29}$$

where $V(t)$: storage volume [L^3]; $Q_{\mathrm{in}}(t)$: inflow to the reservoir [$\mathrm{L}^3\mathrm{T}^{-1}$]; $Q_{\mathrm{out}}(t)$: total outflow of the reservoir [$\mathrm{L}^3\mathrm{T}^{-1}$]; $E(t)$: evaporation from the reservoir's surface [$\mathrm{L}^3\mathrm{T}^{-1}$].

According to the morphology of the dam site, the storage volume is a function of the water level, $W(t)$ [L]: $V(t) = f(W(t))$. The water surface area of the reservoir, $A_{\mathrm{r}}(t)$ [L^2], can be related to the water level as well: $A_{\mathrm{r}}(t) = f(W(t))$. Furthermore, evaporation is—besides the climatic influence—a function of the evaporating free water surface area: $E(t) = f(A_{\mathrm{r}}(t))$.

$Q_{\mathrm{out}}(t)$ is constituted of the outflow through the dam's culverts, $Q_{\mathrm{out}_{c_i}}(t)$, and—depending on a certain water level which activates the spillway—the outflow over the spillway, $Q_{out_{\mathrm{s}}}(t)$:

$$Q_{\mathrm{out}}(t) = \sum^{i} Q_{\mathrm{out}_{c_i}} + Q_{out_{\mathrm{s}}} \tag{30}$$

where i is the number of culverts [−].

The outflow through the culverts and over the spillway is nonlinearly depending on water depth $W(t)$. Assuming the outflow not to be controlled from downstream, the outflow is modeled with an exponential stage–discharge relationship in the form (Chow, 1959)

$$Q_{\mathrm{out}_{c_i,\mathrm{s}}}(t) = \begin{cases} \alpha_{\mathrm{c}} A_{\mathrm{c}} \left(W - H_{\mathrm{c}_i}\right)^{\frac{1}{2}} & \text{for the culverts} \\ \alpha_{\mathrm{s}} L_{\mathrm{s}} \left(W - H_{\mathrm{s}}\right)^{\frac{3}{2}} & \text{for the spillway} \end{cases} \tag{31}$$

where $\alpha_{\mathrm{c,s}}$: empirical hydraulic discharge coefficient of the culverts and the spillway, respectively [−]; A_{c}: culvert inlet area [L^2]; $H_{\mathrm{c}_i,\mathrm{s}}$: elevation of the culvert inlet axes and the spillway crest, respectively [L]; L_{s}: length of the spillway [L].

For the culverts, Eq. (31) applies for submerged conditions. For part full conditions, further discrimination of the flow situation is needed. According to Chow (1959), free surface flow conditions can be assumed if the water level is lower than 1.2 times the culvert diameter. The free surface flow is assumed to be critical and can be calculated for a circular culvert with the relationship (Vischer and Hager, 1999)

$$Q_{\mathrm{out}_{c_i}}(t) = \left(\frac{3\left(W - \left(H_{\mathrm{c}_i} - \frac{1}{2} D_{\mathrm{c}}\right)\right)}{5 D_{\mathrm{c}}} \right)^{\frac{5}{3}} \left(g D_{\mathrm{c}}^5\right)^{\frac{1}{2}} \tag{32}$$

where D_{c} is the culvert diameter [L].

Defining t_j as a specific point in time and integrating Eq. (29) by applying the trapezoidal rule leads to

$$V(t_j + \Delta\mathrm{t}) = V(t_j) + \frac{\Delta t}{2} \left(Q_{\mathrm{in}}(t_j) + Q_{\mathrm{in}}(t_j + \Delta t) - Q_{\mathrm{out}}(t_j) - Q_{\mathrm{out}}(t_j + \Delta t) - E(t_j) - E(t_j + \Delta t)\right) \tag{33}$$

The system (30);(33) is solved for $V(t_j + \Delta t)$ with a fixed-point iteration scheme. This solution accounts for the nonlinear dependency of dam outflow, evaporation, and water level.

Penman Evaporation Model

For the quantification of transient evaporation from the dam water surface, any arbitrary functional relationship can be included within the proposed modeling framework. To utilize the quite detailed available climate data (cf. subsequent section), evaporation is calculated with the Penman model (Penman, 1948). A potential oasis effect is not taken into account. The Penman model reads

$$E(t) = \frac{sE_G + \gamma + v(e_0 - e)}{s + \gamma} A_\mathrm{r} \tag{34}$$

where $s(T)$: gradient of the saturated water vapor pressure curve [$\mathrm{ML^{-1}T^{-2}\Theta^{-1}}$] with $T(t)$: temperature [Θ]; $E_G(t)$: evaporation equivalent of global radiation $G(t)$ [$\mathrm{LT^{-1}}$]; $\gamma(T)$: psychrometric constant [$\mathrm{ML^{-1}T^{-2}\Theta^{-1}}$]; $v(t)$: wind function, dependent on site conditions and wind speed $w(t)$ [$\mathrm{LT^{-1}}$]; $e_0(t)$: saturated water vapor pressure [$\mathrm{ML^{-1}T^{-2}}$]; $e(t)$: actual water vapor pressure [$\mathrm{ML^{-1}T^{-2}}$]. The parameters of the Penman model can be calculated by obtaining temperature $T(t)$, actual vapor pressure $e(t)$, global radiation $G(t)$, and wind speed $w(t)$ (for details see e.g., Brutsaert, 1982).

Study Area and Data

The study area is located in the Batinah Region, Sultanate of Oman (Fig. 2), and covers two catchments: Wadi Ma'awil (835 $\mathrm{km^2}$) and Wadi Bani Kharus (1,183 $\mathrm{km^2}$), with the focus set on Ma'awil. The catchments are bordered by the Gulf of Oman in the north and the Hajar Mountain Range in the south. Fresh water resources are scarce in the region and the coastal alluvial aquifer is threatened by over-abstraction, and—consequently—saltwater intrusion. The variability of rainfall patterns in space and time is extreme, where relatively wet periods can be followed by extremely dry periods. Both catchments exhibit a groundwater recharge dam. A set of specific data is required for setting up the proposed modeling system. Required input data are: cross-sectional wadi profile parameters; corresponding general slopes; roughness coefficients; parameters of the infiltration model; dam characteristics, including culvert and spillway characteristics; time series of inflow to the model domain; and climate data for evaporation modeling. Table 1 summarizes data requirements and gives information on data assessment for the herein presented application.

Morphological data of the wadis were derived from a digital elevation model (DEM). The ASTER data sets (Abrams, 2000; NASA, 2012) were used. Cross-sectional cut lines were extracted from the DEM, supplemented by superimposed aerial imagery to capture typical flow widths. Figure 3a–b shows plots of the general profile of the main channels of Wadi Ma'awil and Wadi Bani Kharus. Fluvial geomorphology of Wadi Ma'awil and Wadi Bani Kharus features very wide cross-sectional profiles, which change only gradually in downstream direction. The alluvium extends down to −220 m a.s.l. (meters above sea level) in the study area (MAF, 1990).

The general slope of Wadi Ma'awil between Afi gauging station and Ma'awil Dam was estimated to 0.00868 and 0.00375 downstream of the dam. The neighboring Wadi Bani Kharus exhibits a very similar morphology (Fig. 3). Channel slope was estimated to 0.00738 for upper Wadi Bani Kharus

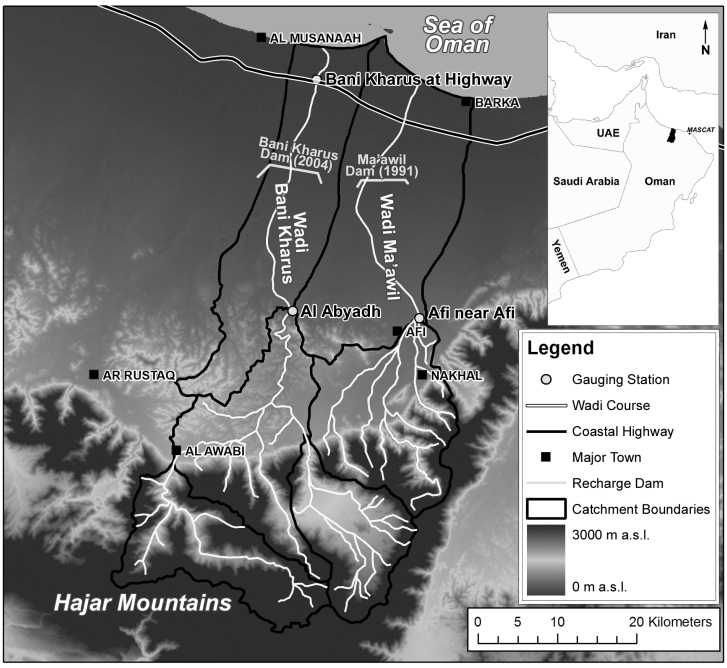

Figure 2: Overview of the study area. Base map created from ASTER GDEM data (NASA, 2012).

Table 1: Required input data for the full modeling system. Parameters indicated with an asterisk were included in the parameter sensitivity analysis.

Data	Parameter(s)	Assessment	Notes
Wadi cross-sectional data	$\tilde{A}(x,h)$, $\tilde{R}(x,h)$; resp. $p_1(x)$, p_2, $p_3(x)$, p_4	Obtained from digital elevation model and aerial imagery	Cross-sectional data included via specific profile functions
Longitudinal profile	${S_0}^*$	Obtained from digital elevation model	Calculated from thalweg of cross sections
Channel roughness	${K_{\mathrm{St}}}^*$	Calibration (based on flow observations)	Initial estimate from field assessment
Infiltration characteristics	${k_{\mathrm{a}}}^*$, ${k_{\mathrm{k}}}^*$, ${k_{\mathrm{c}}}^*$	Calibration (based on observed transmission losses)	Infiltration modeled with Kostiakov-Lewis model
Dam characteristics	$V = f(W)$, $A_{\mathrm{r}} = f(W)$, $\alpha_{\mathrm{c,s}}$, $H_{\mathrm{c}_i,\mathrm{s}}$, L_{s}, D_{c}	Engineering report of the dam	Outflow characteristics determinable a priori
Flow data	$Q(t)$	Obtained at gauging station	Daily and sub-daily values, peak values
Dam water level over time	$W(t)$	Water level recorder	Timely-resolved data available for event 06/06/07
Climate data	$T(t)$, $e(t)$, $G(t)$, $w(t)$	Seeb climate station	Evaporation modeled with Penman model

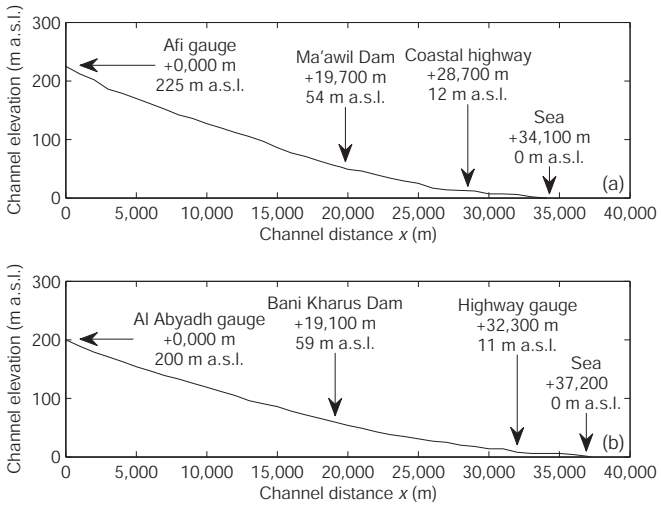

Figure 3: General profile plots. (a) Wadi Ma'awil; (b) Wadi Bani Kharus.

and 0.00326 for the reach below the dam. Infiltrometry measurements were carried out in the area in order to assess suitable dam locations. MAF (1985) performed 60 double-ring infiltrometry tests in the Ma'awil area which delivered mean steady infiltration rates from 0.744 to 4.920 $\mathrm{m \cdot d^{-1}}$ for a four-hour duration (with an overall mean around 2.0 $\mathrm{m \cdot d^{-1}}$). MAF (1990) carried out further infiltrometry tests which suggest that wadi infiltration in Bani Kharus is in the same order of magnitude (0.850 to 15.360 $\mathrm{m \cdot d^{-1}}$; mean value 5.1 $\mathrm{m \cdot d^{-1}}$).

The present study specifically addresses Ma'awil Dam which was constructed in 1991. Table 2 summarizes the main properties of the dam, obtained from the engineering report (MAF, 1989). For Wadi Ma'awil, surface flow data were available for Afi gauging station. Gauging data with a temporal resolution of one hour were available for the years 1984 to 1995 and since 1996 with a resolution of five minutes. Timely-resolved stage recorder data were available for a 2007 event, caused by cyclonic storm Gonu (event 06/06/07). This event led to highest observed peak flow rates (881 $\mathrm{m^3 \cdot s^{-1}}$) and highest flow volumes ($15.156 \cdot 10^6$ $\mathrm{m^3}$) at Afi station. The dam's operational storage capacity was completely filled and the spillway was activated.

There are two gauging stations located along the lower reaches of Wadi Bani Kharus: Al Abyadh and Bani Kharus at Highway. Bani Kharus Dam was constructed as recently as 2004 and, therefore, a significant portion of available flow data were unaffected by dam operation, which allows for a direct estimation of transmission losses. Daily values were available until 1997 and five-minute records were available as recently as 1997, which limits usable data to the years 1997 to 2003. At least gauging data of four events with a temporal resolution of five minutes could be correlated by validating travel times between the two gauges. Additionally, the influence of lateral inflow could be excluded for these events by analyzing event-related rainfall patterns.

Table 3 summarizes the available hydrological information for the two inflow gauges of the considered catchments. It can be seen that the ephemeral character of the flow regime is very pronounced. The information given in Table 3 further illustrates the strong similarities of both catchments which are a consequence of the catchments' neighborship, their similar morphology, geology, and climate. Finally, climate data required for dam evaporation modeling (cf. Table 1)

Table 2: Main properties of Ma'awil Dam.

Property	Value
Dam crest height (m)	8.3
Dam crest length (m)	7,500
Design storage (10^6 m^3)	10
Number of culverts i	10
Culvert diameter D_c (m)	0.8
Culvert inlet area A_c (m^2)	0.50265
Culvert inlet axis elevation H_{c_i} (m a.s.l.)	54.36, 54.07, 54.53, 54.75, 54.07, 54.53, 54.53, 54.53, 54.07, 55.20
Culvert discharge coefficient α_c	2.726
Spillway crest length L_s (m)	4,040
Spillway crest elev. H_s (m a.s.l.)	59
Spillway discharge coefficient α_s	1.350
Design flood (m$^3 \cdot$ s^{-1})	4,000

Table 3: Hydrological information for the inflow gauges of the considered catchments.

	Inflow gauges (catchment)	
	Afi (Ma'awil)	Al Abyadh (Bani Kharus)
Observation period	1984–2007	1981–2007
Days with runoff per year (min–mean–max)	0–14–75	0–16–75
Daily runoff (min–mean–max) (m$^3 \cdot$ s^{-1})	0.000–0.088–175	0.000–0.113–81.2
Mean runoff for all days with runoff (m$^3 \cdot$ s^{-1})	2.254	2.611
Highest observed flood peak with date (m$^3 \cdot$ s^{-1})	881 (06/06/07)	777 (06/06/07)

were taken from Seeb International Airport station, located in the Batinah plain at 8.4 m a.s.l. in a distance of ca. 50 km east of the dam site.

Model Application and Discussion

This section demonstrates the application of the proposed modeling system for a case study under realistic data conditions. A stepwise procedure was carried out. First, a parameter sensitivity analysis was performed in order to identify the sensitivity of process parameters, associated with flow and transmission loss modeling in Wadi Ma'awil. Second, to account for the insufficient data situation, the sensitive parameters were calibrated for a neighboring and morphologically very similar catchment and then transferred to the investigation area. Finally, the full modeling system was used to simulate wadi flow and transmission loss dynamics, influenced by dam operation for extreme event 06/06/07.

Parameter Sensitivity Analysis

For Wadi Ma'awil, a synthetic input hydrograph was routed with the full modeling system under varied parameters and the results were subsequently compared. Each single parameter was altered ±30 % for each model run, whereas the remaining parameters were held to their respective initial values. Sensitivity was checked for parameters of the hydrodynamic and infiltration models (indicated

with an asterisk in Table 1). The dam parameters are assumed to be certain by referring to the construction report of the dam and were, therefore, excluded from the sensitivity analysis.

The initial channel slope was set to a mean value $S_0 = 0.00660$ and initial channel roughness was estimated to $K_{\mathrm{St}} = 30\,\mathrm{m}^{\frac{1}{3}}\cdot\mathrm{s}^{-1}$ during an in-situ assessment of wadi sediments, using tabulated values (Chow, 1959). The steady-state infiltration rate k_{c} was set to an initial value of $2.3148 \cdot 10^{-5}\,\mathrm{m}\cdot\mathrm{s}^{-1}$, which equals $2.0\,\mathrm{m}\cdot\mathrm{d}^{-1}$ and is, therefore, in the range of mean infiltration rates, inferred from the afore discussed infiltrometry data. Since available infiltrometry data comprise only integral infiltration rates, but no temporal information which would allow for the inference of k_{a} and k_{k}, the two Kostiakov-Lewis parameters were taken from a model fitted for infiltrometry tests in Wadi Ahin, located 125 km west of Wadi Ma'awil (Haimerl, 2004; $k_{\mathrm{a}} = 0.8640$ and $k_{\mathrm{k}} = 7.7433 \cdot 10^{-5}\,\mathrm{m}\cdot\mathrm{s}^{-k_{\mathrm{a}}}$).

Spatial and temporal resolution of the upstream KW routing model were set to $\Delta x = 50\,\mathrm{m}$ and $\Delta t = 1\,\mathrm{s}$. The time step of the dam simulation model was set to $\Delta t = 60\,\mathrm{s}$. The combined ZI/KW downstream routing model was discretized with $\Delta x = 100\,\mathrm{m}$ in space and with an adaptive time step for the ZI component and $\Delta t = 1\,\mathrm{s}$ for the KW component, respectively. To suppress numerical oscillations, we ran the upstream KW model with a low virtual baseflow rate of $0.1\,\mathrm{m}^3\cdot\mathrm{s}^{-1}$. Only flow above this level was taken into account for transmission loss modeling.

A synthetic triangular flow hydrograph of a two-hour duration and with a peak value of $200\,\mathrm{m}^3\cdot\mathrm{s}^{-1}$ (peak return period of ca. 2.5 years and a flow volume of $0.720 \cdot 10^6\,\mathrm{m}^3$) was implemented as upper boundary condition at Afi gauging station. The spillway was not activated under the considered inflow. Mean climate data of Seeb station for the month of July were employed for evaporation modeling. Process parameter sensitivity was estimated with respect to flow arrival times, maximum extent of the infiltrating flow domain, transmission losses, and evaporation volumes (Table 4).

All investigated parameters turned out to be sensitive to a certain degree. Channel roughness (Manning-Strickler coefficient K_{St}) had the strongest impact on arrival times, followed by bed slope S_0. Increased slope and decreased channel roughness (higher values of K_{St}) caused a faster advance of the flow. In contrast, the maximum extent of the infiltrating flow was only weakly controlled by channel slope and roughness. Increased slope and decreased roughness led to a slight extension of the infiltrating flow domain. The final position of the flow domain was foremost determined by the parameters of the infiltration model, where k_{a} was dominant. For smaller values of k_{a}, less water infiltrated and the flow persisted over a longer distance, and vice versa. Total transmission losses were strongest influenced by the parameters of the infiltration model. Again, k_{a} showed the highest sensitivity. For k_{a} set to 1.1232 (+30 %), infiltration *increases* from the start. This led to a total consumption of surface flow before Ma'awil Dam was reached. The flow was consumed by infiltration after ca. 2.5 h and reached station +17,100 m for this specific model run.

Although transmission losses and arrival times are comparably variable, evaporation volumes simulated by the dam model only slightly differed for the investigated parameter combinations. Besides the climatic forcing, evaporation is dependent on the development of the dam water level over time. Since outflow rates of the dam are low compared to inflow rates, evaporation is almost completely related to the maximum water level elevation caused by an event, which in turn determines how long the evaporating water table persists.

For the downstream wadi section, all available water infiltrated before reaching the sea for every investigated parameter combination due to slow culvert release. Taking into account the similar dam evaporation of all model runs, higher upstream transmission losses caused lower dam inflows, and, therefore, lower downstream transmission losses. This leads to an only seemingly contradictory

Table 4: Results of the parameter sensitivity analysis of the full modeling system for Wadi Ma'awil under a total inflow of $0.720 \cdot 10^6\,\mathrm{m}^3$.

		Parameter variation (%)	$S_0 = 0.00660$	$K_{\mathrm{St}} = 30\,(\mathrm{m}^{\frac{1}{3}} \cdot \mathrm{s}^{-1})$	$k_{\mathrm{a}} = 0.8640$	$k_{\mathrm{k}} = 7.7433\,(10^{-5}\,\mathrm{m} \cdot \mathrm{s}^{-k_{\mathrm{a}}})$	$k_{\mathrm{c}} = 2.3148\,(10^{-5}\,\mathrm{m} \cdot \mathrm{s}^{-1})$	Mean value
Arrival time		+30	2.1	2.0	∞	2.3	2.3	2.2
at Ma'awil Dam (+19,700 m)		±0	2.3	2.3	2.3	2.3	2.3	2.3
(h)		−30	2.5	2.8	2.2	2.3	2.3	2.4
Maximum extent		+30	24,900	25,200	17,100	23,700	23,800	22,980
of infiltrating flow		±0	24,700	24,700	24,700	24,700	24,700	24,700
(m)		−30	24,300	24,000	31,800	26,200	26,800	26,620
Arrival time at		+30	8.8	11.2	0.1	9.8	9.8	8.0
maximum extent of flow		±0	9.5	9.5	9.5	9.5	9.5	9.5
(days)		−30	8.5	10.2	9.0	9.1	9.9	9.4
	Transmission losses	+30	0.343	0.333	0.719	0.390	0.390	0.435
	Afi–Ma'awil Dam	±0	0.355	0.355	0.355	0.355	0.355	0.355
	($10^6\,\mathrm{m}^3$)	−30	0.374	0.392	0.237	0.319	0.318	0.328
Upstream	Inflow	+30	0.376	0.386	0.000	0.326	0.327	0.283
KW	Ma'awil Dam	±0	0.361	0.361	0.361	0.361	0.361	0.361
model	($10^6\,\mathrm{m}^3$)	−30	0.341	0.323	0.478	0.397	0.398	0.388
	Relative mass	+30	0.194	0.141	0.139	0.488	0.439	0.280
	balance error	±0	0.560	0.560	0.560	0.560	0.560	0.560
	(% of total inflow)	−30	0.680	0.641	0.635	0.489	0.598	0.609
	Evaporation	+30	0.100	0.101	–	0.098	0.098	0.099
	Ma'awil Dam	±0	0.100	0.100	0.100	0.100	0.100	0.100
	($10^6\,\mathrm{m}^3$)	−30	0.099	0.098	0.104	0.101	0.101	0.101
Dam	Outflow	+30	0.269	0.281	–	0.225	0.225	0.250
simulation	Ma'awil Dam	±0	0.257	0.257	0.257	0.257	0.257	0.257
model	($10^6\,\mathrm{m}^3$)	−30	0.238	0.221	0.369	0.292	0.292	0.282
	Relative mass	+30	0.888	0.639	–	0.569	0.549	0.661
	balance error	±0	0.556	0.556	0.556	0.556	0.556	0.556
	(% of total inflow)	−30	0.646	0.706	0.677	0.630	0.563	0.644
	Transmission losses	+30	0.269	0.281	–	0.225	0.225	0.250
	Ma'awil Dam–sea	±0	0.257	0.257	0.257	0.257	0.257	0.257
Down-	($10^6\,\mathrm{m}^3$)	−30	0.238	0.221	0.369	0.292	0.292	0.282
stream	Losses to	+30	0.000	0.000	–	0.000	0.000	0.000
combined	the sea	±0	0.000	0.000	0.000	0.000	0.000	0.000
ZI/KW	($10^6\,\mathrm{m}^3$)	−30	0.000	0.000	0.000	0.000	0.000	0.000
model	Relative mass	+30	0.057	0.058	–	0.067	0.067	0.062
	balance error	±0	0.043	0.043	0.043	0.043	0.043	0.043
	(% of total inflow)	−30	0.042	0.057	0.026	0.095	0.091	0.062
Overall relative error		+30	1.025	0.723	0.139	0.990	1.055	0.786
of full modeling system		±0	1.159	1.159	1.159	1.159	1.159	1.159
(% of total inflow)		−30	1.368	1.290	1.338	1.025	1.252	1.255

influence of parameter variations on transmission losses for the upstream and the downstream wadi sections. The maximum extent of the flow domain was typically reached after a couple of days, which is the case if total infiltration rates equal inflow rates for the wadi downstream of the dam. Generally, higher inflow rates led to a faster advance of the flow. The incorporated ZI/KW model for routing the dam's culvert outflow was capable of accurately portraying such weak process dynamics in the initially dry wadi. This is reflected by the very small mass balance errors.

The overall relative mass balance errors in Table 4 were calculated for every investigated parameter combination by comparing the sum of transmission losses upstream and downstream of the dam, dam evaporation, and losses to the sea against the total inflow. The full model's mean relative mass balance error was ca. 1 % of inflow. Regarding the relative errors of the incorporated sub-models, the downstream ZI/KW model featured the lowest mass balance errors, which is supported by the ZI advance model's analytical character. The errors of the ZI/KW model ranged between 0.026 % and 0.095 % of total inflow. The KW model for the upstream wadi reaches caused mass balance errors between 0.139 % and 0.680 %, which is mainly a consequence of the approximate numerical model solution. The dam simulation model showed slightly higher deviations with mean errors between 0.549 % and 0.888 %. These errors mainly emerged from the iterative solution of the dam retention equation.

Estimation of Process Parameters

For Wadi Ma'awil, dam operation hinders the calibration of process parameters due to the influence of flow retention and dam evaporation. Furthermore, highly resolved data of a downstream gauge are lacking for the pre-dam era (before 1991), which would have facilitated a model calibration based on a sequence of gauges. Theoretically, an inverse reconstruction of event-related dam inflow would be possible on the basis of stage recorder data. Together with an upstream wadi gauge, this data could be used for the calibration of routing and transmission loss parameters. Specifically for Ma'awil dam, such an approach is questionable due to (a) the potentially very dynamic change of dam inflow rates, which is not resolved by the stage recorder; and (b) the uncertain relationship of dam water level and outflow rates under spillway release conditions, caused by the high hydraulic capacity of the spillway.

Therefore, the parameters were calibrated and validated for the westerly adjacent and morphologically similar catchment of Wadi Bani Kharus (cf. Study Area and Data section), using data of the two serial gauges Al Abyadh and Bani Kharus at Highway (Fig. 3b). Then, the validated parameters were transferred to Wadi Ma'awil. The KW routing model was operated for events of the period prior the construction of Bani Kharus Dam (2004), hence these flow data are unaffected by dam operation. As discussed in the Study Area and Data section, valid flow data were available for four events.

The employed KW model was calibrated for event 03/27/97 with respect to channel roughness K_{St} and Kostiakov-Lewis parameters k_{a}, k_{k}, and k_{c}. Regarding flow volumes and peak flow rates, the smallest event was chosen for calibration in order to challenge the model's extrapolation ability in the subsequent validation. Calibration was performed simultaneously for the four considered parameters, using the CMA-ES optimization algorithm (Hansen, 2006). The Nash-Sutcliffe model efficiency coefficient (NSE) (Nash and Sutcliffe, 1970) was used to evaluate model quality. Channel slope and cross-sectional profiles were estimated as outlined before. The spatial and temporal

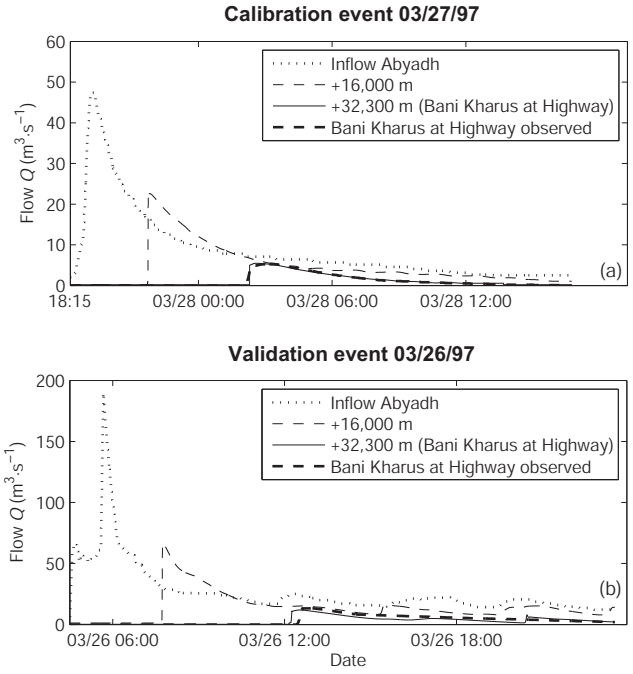

Figure 4: Modeling results of the kinematic wave flood routing model for Wadi Bani Kharus. (a) Calibration event 03/27/97; (b) validation event 03/26/97.

resolution of the routing model were set to $\Delta x = 50\,\mathrm{m}$ and $\Delta t = 1\,\mathrm{s}$. As for the sensitivity analysis, the numerical KW model was charged with a very low initial base flow rate of $0.1\,\mathrm{m}^3 \cdot \mathrm{s}^{-1}$ to impede numerical oscillations.

Roughness and infiltration parameters were calibrated to $K_{\mathrm{St}} = 26.67\,\mathrm{m}^{\frac{1}{3}} \cdot \mathrm{s}^{-1}$, $k_{\mathrm{a}} = 0.5406$, $k_{\mathrm{k}} = 9.9980 \cdot 10^{-4}\,\mathrm{m} \cdot \mathrm{s}^{-k_{\mathrm{a}}}$, and $k_{\mathrm{c}} = 5.5198 \cdot 10^{-7}\,\mathrm{m} \cdot \mathrm{s}^{-1}$. A NSE of 0.9719 indicates a nearly perfect convergence of modeled and gauged flow, which can also be seen from Fig. 4a. Observed transmission losses were slightly underestimated by 0.8 %. Timing and magnitude of the flow were accurately matched.

Validation was carried out for the remaining three events. Results are shown exemplarily for event 03/26/97 in Fig. 4b. A NSE of 0.4373 usually indicates that the model only acceptably simulated the flow observations. Nevertheless, flow volume and peak rate observations at the highway station ($0.2422 \cdot 10^6\,\mathrm{m}^3$ and $13.2\,\mathrm{m}^3 \cdot \mathrm{s}^{-1}$) were adequately met by the model ($0.2089 \cdot 10^6\,\mathrm{m}^3$ and $11.8\,\mathrm{m}^3 \cdot \mathrm{s}^{-1}$). The flow peak time lag between observation and model output was 15 minutes. This shows that the rather low NSE is mainly caused by the phase differences of modeled and observed values. Moreover, the NSE was not calculated over the whole simulation period but only starting from the onset of the flow, whereas including the preceding zero values would have apparently improved the NSE. For flash flood routing under intense transmission losses, such validation results are very encouraging.

For all four investigated validation events, observed transmission losses ranged from 85.0 % to 90.8 % (mean value 87.5 %), whereas modeled transmission losses were between 68.8 % and 88.7 % (mean value 82.9 %). The maximum arrival time prediction error was 15 minutes (mean value 4 minutes). For validation, flow volumes were comparably low and in turn transmission

losses were high, which caused mass balance errors of slightly over 1 %. Nevertheless, the results suggest that the calibrated parameter set is representative for a realistic range of event magnitudes and can, therefore, be transferred to the neighboring catchment of Wadi Ma'awil, for which this parametrization is subsequently validated.

Wadi Flow Routing and Dam Simulation

The presented modeling system was subsequently applied for Wadi Ma'awil, extreme event 06/06/07. Flow observations with a temporal resolution of five minutes were used as upper boundary condition for the upstream KW model. Morphological data were prepared as outlined before. Roughness and infiltration parameters were transferred from Wadi Bani Kharus. Spatial and temporal resolution of the upstream and downstream routing models were set to $\Delta x = 50\,\mathrm{m}$ and $\Delta t = 1\,\mathrm{s}$. An initial flow rate of $0.1\,\mathrm{m}^3 \cdot \mathrm{s}^{-1}$ was applied for the upstream KW model. The temporal resolution was adaptive for the downstream ZI component. Evaporation was calculated using actual climate data of Seeb station. The temporal resolution of the dam simulation model was set to $\Delta t = 60\,\mathrm{s}$.

The results of the upstream hydrodynamic model are shown in Fig. 5a–b. The pronounced dynamics of this event reflect in a surging flow with a modeled arrival time of the strongly rising limb of ca. 1.5 h. Due to generally high flow volumes and low infiltration opportunity times, modeled transmission loss quotas were comparably low for the upper wadi section. The inflow volume to the dam was modeled to $14.299 \cdot 10^6\,\mathrm{m}^3$, which is 94.3 % of total inflow to the model domain ($15.156 \cdot 10^6\,\mathrm{m}^3$). Transmission losses in the upstream section were modeled to $0.813 \cdot 10^6\,\mathrm{m}^3$, which is 5.4 % of total inflow. During the first hours of the simulation, infiltration was limited by available water, which caused slowly rising total infiltration volumes (Fig. 5b).

Figure 5c–d shows the results of the subsequent dam simulation model. For the investigated event, the total outflow of the dam was modeled to $14.166 \cdot 10^6\,\mathrm{m}^3$ (93.5 % of total inflow) and total evaporation to $0.133 \cdot 10^6\,\mathrm{m}^3$ (0.9 % of total inflow). The peak inflow rate of $853\,\mathrm{m}^3 \cdot \mathrm{s}^{-1}$ was retained to $237\,\mathrm{m}^3 \cdot \mathrm{s}^{-1}$ in the dam's outflow (c). Modeled peak water level was 59.11 m, whereas the recorded peak was 59.09 m.

The modeled dam outflow persisted for over eight days. Unfortunately, the available limnigraph data ended before the dam was depleted. Nevertheless, stage recorder data were adequately simulated by the dam model (Fig. 5d). This supports not only the chosen parametrization of the dam model, but foremost the reasonable estimates of inflow volumes and inflow dynamics, delivered by the upstream KW model. These findings effectively validated the routing and infiltration parameters of the upstream KW model, which were calibrated for the neighboring catchment of Wadi Bani Kharus.

Figure 5e–f shows the results of the downstream combined ZI/KW model. Losses to the sea were modeled to $11.762 \cdot 10^6\,\mathrm{m}^3$ (77.6 % of total inflow) and transmission losses to $2.403 \cdot 10^6\,\mathrm{m}^3$ (15.9 % of total inflow). For the investigated extreme event, a significant portion of flow was lost to the sea. However, the initial advance of the flow domain towards the sea is a consequence of culvert release. The sea is reached at ca. 20:00 UTC on 06/06/07 (Fig. 5e). This advance is controlled by the nonlinear interaction of flow dynamics and infiltration, which in turn affects flow volumes and momentum, and could, therefore, be adequately modeled by the proposed analytical ZI model component. Less extreme, more frequent events (e.g., as investigated in the sensitivity analysis) would have featured weaker downstream dynamics, which would have posed a stronger indication

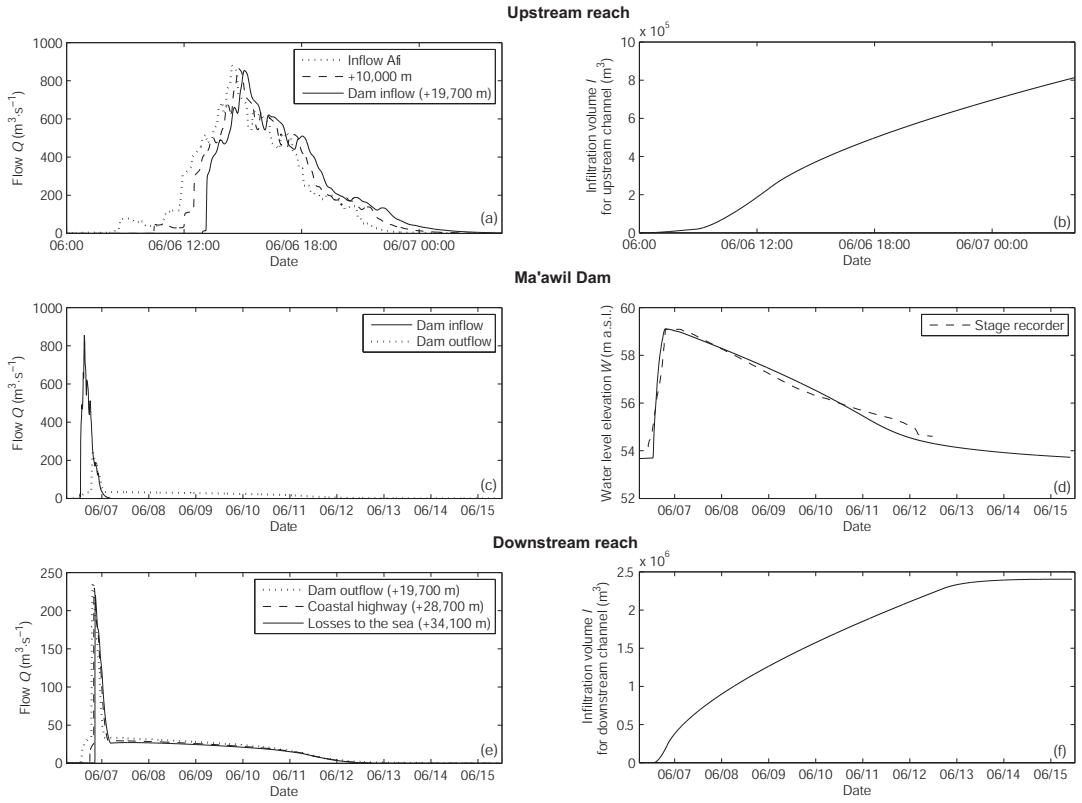

Figure 5: Modeling results for Wadi Ma'awil, event 06/06/07. (a) Flow hydrographs at different upstream channel locations; (b) cumulative infiltration volumes for the upstream reach; (c) dam inflow and outflow; (d) modeled and recorded dam water level; (e) flow hydrographs at different downstream channel locations; (f) cumulative infiltration volumes for the downstream reach.

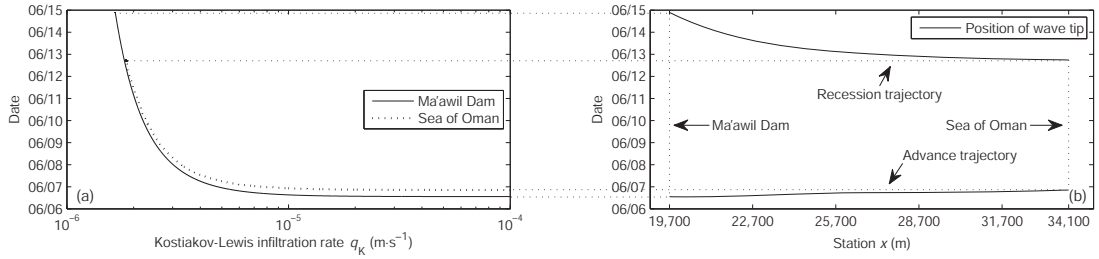

Figure 6: Model results for lower Wadi Ma'awil, event 06/06/07. (a) Infiltration rates over time; (b) advance and recession trajectories.

for the ZI advance model. Nevertheless, the investigated event was chosen due to sufficient data were available.

The spillway was activated between 20:25 UTC on 06/06/07 and 04:15 UTC on 06/07/07, leading to a very dynamic outflow, which was routed with the KW component. The remaining culvert outflow persisted over days and, therefore, established the major portion of transmission losses (ca. 85 %). When inflow rates were lower than infiltration rates, the infiltrating flow domain started receding in upstream direction. Modeled recession began after ca. 6.5 days close to the coast and lasted for two days until infiltration ceased directly below the dam (Fig. 6a and b).

Both the simulated upstream and downstream hydrographs showed a certain steepening tendency. This phenomenon is sometimes referred to as kinematic shock (Lighthill and Whitham, 1955), which is not only a property of the governing equations but can appear physically in ephemeral channels with pronounced slope (Ponce, 1991; Sharma and Murthy, 1995). Additionally, the initially high infiltration rates after the onset of an event amplify the steepening of the hydrographs' rising limb.

Albeit the dynamic character of the investigated event—with spillway operation and losses to the sea—relative errors were lower than for the sensitivity analysis. This is mainly attributable to higher total flow volumes which led to lower transmission loss quotas and, therefore, lower relative mass balance errors. The full model's total mass balance error was estimated to ca. 0.3 % by comparing the inflow volume at Afi to the sum of transmission losses, evaporation losses, and losses to the sea. Although total transmission loss quotas were low compared to the results of the sensitivity analysis (21.3 % of total inflow), absolute infiltrated volumes were high ($3.216 \cdot 10^6\,\mathrm{m}^3$).

Summary and Conclusions

We presented a comprehensive and process-oriented modeling system for ephemeral river flow under the influence of a groundwater recharge dam. A special focus of model development was set on the resolution of intricate process dynamics under significant transmission losses. Flow and infiltration dynamics downstream of the recharge dam were soundly portrayed by implementing an analytical ZI model for the flow advance phase, combined with a numerical KW model for flow recession. The more pronounced flow dynamics in the upstream reaches were modeled with a numerical KW model, where the approach turned out to be an appropriate simplification of the full hydrodynamic process description. Infiltration was captured with a robust Kostiakov-Lewis model. Dam operation was modeled with the nonlinear storage equation. Evaporation from the free water surface was calculated using the Penman model, since daily climate data were available for the investigation area.

Assuming validity of the flow data used for calibration, three important properties of the modeled infiltrating open channel flow were observed. First, the hydrographs tend to steepen in downstream direction, leading to a surging flow. This steepening tendency is amplified by initially high transmission losses. Second, assuming a constant infiltration rate over time—as proposed by numerous authors—will not necessarily lead to a satisfactory portrayal of hydrograph shape under significant transmission losses. Third, mean modeled infiltration rates for typical event durations (hours to days) were in the lower range or lower than suggested by infiltrometry testing (10^{-5} to $10^{-4}\,\mathrm{m \cdot s^{-1}}$). This is covered e.g., by the findings of Wheater (2002), who states that observed transmission losses in ephemeral channels tend to be actually lower than those inferred from infiltrometry tests.

Notwithstanding the fact that the proposed modeling system could be successfully applied for flash flood routing in ephemeral rivers under the influence of groundwater recharge dams, the imponderables of hydraulic modeling in arid environments became very clear. The major problem are the lacking data which strongly limit model calibration and validation. This is due to the rareness of events together with coarse observation networks for precipitation and flow. Additionally, surface and subsurface flow processes are strongly interconnected and very dynamic in space and time. Therefore, all available data should be exploited thoroughly, which might justify the use of empirical modeling approaches, as in the case of the incorporated infiltration model.

As comprehensively reviewed by Tooth (2000), dryland rivers undergo change, even on an event scale. Therefore, some further remarks have to be made on the herein incorporated assumptions that the roughness coefficient, channel morphology, and bottom slope are temporally invariant. Theoretically, an erosion–sedimentation model could be connected with the herein applied methodology in order to describe transient channel morphology, i.e., by accounting for a change in the cross-sectional profile functions. A further concern is posed by the dependency of friction and the suspended load. Despite there are numerous studies on suspended load transport dynamics in ephemeral rivers, the mutual relationship of friction and sediment load often remains unclear beyond lab scale (e.g., Vanoni and Brooks, 1957; Martin-Vide et al., 1999).

Moreover, in the absence of a friction law for unsteady flows, velocity, channel roughness, channel geometry, and friction slope are commonly related using a steady flow formula, e.g., of the Manning-Strickler type. Consequently, friction is portrayed with the help of an effective parameter (i.e., the roughness coefficient) which delivers only a mean and event-specific description of friction. Nevertheless, the herein presented modeling framework is intended to aid as a prognosis tool. Recalling the tremendous uncertainties of the driving rainfall in arid and semiarid regions, the uncertainties and inadequatenesses in the portrayal of ephemeral river morphology and friction are not the major source of the model's predictive uncertainty.

Summing up, the paper focused on model development under the problem-specific conditions which are typical for (semi)arid regions. The herein provided first model application bears an exploratory character. Therefore, further model application is of interest. For instance, the modeling system could be used within a stochastic framework for obtaining, e.g., the expected value of transmission losses as a function of the flood return period. Such calculations could then be repeated assuming the absence of a recharge dam which would deliver the expectable dam efficiency with regard to transmission losses. Moreover, model applications in other regions (e.g., as Australia and the Southwestern US) are proposed to foster further model refinement.

Acknowledgments

The manuscript was prepared within the research project IWAS, funded by the German Federal Ministry of Education and Research (BMBF) under grant №02WM1166. Additionally, we wish to thank the Ministry of Regional Municipalities, Environment and Water Resources of the Sultanate of Oman for supporting the IWAS IWRM project. The ASTER data were obtained through the online Data Pool at the NASA Land Processes Distributed Active Archive Center (LP DAAC), USGS/Earth Resources Observation and Science (EROS) Center, Sioux Falls, South Dakota (https://lpdaac.usgs.gov).

References

Abrams, M. The Advanced Spaceborne Thermal Emission and Reflection Radiometer (ASTER): data products for the high spatial resolution imager on NASA's Terra platform. *International Journal of Remote Sensing*, 21(5): 847–859, 2000.

Al-Qurashi, A., N. McIntyre, H. S. Wheater, and C. Unkrich. Application of the KINEROS2 rainfall–runoff model to an arid catchment in Oman. *Journal of Hydrology*, 355(1–4): 91–105, 2008.

Beven, K. and P. Germann. Macropores and water flow in soils. *Water Resources Research*, 18(5): 1311–1325, 1982.

Bouwer, H. Design considerations for earth linings for seepage control. *Ground Water*, 20(5): 531–537, 1982.

Brutsaert, W. *Evaporation Into the Atmosphere: Theory, History and Applications*. D. Reidel Publishing Company, Dordrecht, 1982.

Chow, V. T. *Open Channel Hydraulics*. McGraw-Hill, New York, 1959.

Costelloe, J. F., R. B. Grayson, R. M. Argent, and T. A. McMahon. Modelling the flow regime of an arid zone floodplain river, Diamantina River, Australia. *Environmental Modelling and Software*, 18(8–9): 693–703, 2003.

Courant, R., K. Friedrichs, and H. Lewy. Über die partiellen Differenzengleichungen der mathematischen Physik. *Mathematische Annalen*, 100(1): 32–74, 1928.

Duchesne, S., A. Mailhot, E. Dequidt, and J.-P. Villeneuve. Mathematical modeling of sewers under surcharge for real time control of combined sewer overflows. *Urban Water*, 3(4): 241–252, 2001.

Dunkerley, D. and K. Brown. Flow behaviour, suspended sediment transport and transmission losses in a small (sub-bank-full) flow event in an Australian desert stream. *Hydrological Processes*, 13(11): 1577–1588, 1999.

Eagleson, P. S. *Dynamic Hydrology*. McGraw-Hill, New York, 1970.

El-Hames, A. S. and K. S. Richards. An integrated, physically based model for arid region flash flood prediction capable of simulating dynamic transmission loss. *Hydrological Processes*, 12(8): 1219–1232, 1998.

Garcia-Navarro, P., A. Fras, and I. Villanueva. Dam-break flow simulation: some results for one-dimensional models of real cases. *Journal of Hydrology*, 216(3–4): 227–247, 1999.

Goodrich, D. C., D. G. Williams, C. L. Unkrich, J. F. Hogan, R. L. Scott, K. R. Hultine, D. Pool, A. L. Coes, and S. Miller. Comparison of methods to estimate ephemeral channel recharge, Walnut Gulch, San Pedro River basin, Arizona. In Phillips, F. M., J. F. Hogan, and B. Scanlon, editors, *Recharge and Vadose Zone Processes: Alluvial Basins of the Southwestern United States*, pages 77–99. American Geophysical Union, Washington DC, 2004.

Grundmann, J., N. Schütze, G. H. Schmitz, and S. R. Al-Shaqsi. Towards an integrated arid zone water management using simulation-based optimisation. *Environmental Earth Sciences*, 65(5): 1381–1394, 2012.

Haimerl, G. *Groundwater Recharge in Wadi Channels Downstream of Dams*. Number 99 in Berichte des Lehrstuhls und der Versuchsanstalt für Wasserbau und Wasserwirtschaft. Technische Universität München, Institut für Wasserwesen, 2004.

Hansen, N. The CMA evolution strategy: a comparing review. In Lozano, J., P. Larranaga, I. Inza, and E. Bengoetxea, editors, *Towards a new evolutionary computation. Advances on estimation of distribution algorithms*, pages 75–102. Springer, 2006.

Haverkamp, R., M. Kutilek, J. Y. Parlange, L. Rendon, and M. Krejca. Infiltration under ponded conditions: 2. infiltration equations tested for parameter time-dependence and predictive use. *Soil Science*, 145(5): 317–329, 1988.

Hayami, S. On the propagation of flood waves. *Bulletin of the Disaster Prevention Research Institute, Kyoto University*, 1(1): 1–16, 1951.

Lighthill, M. J. and G. B. Whitham. On kinematic waves: 1. flood movement in long rivers. *Proceedings of the Royal Society of London*, A229(1178): 281–316, 1955.

MAF. *Infiltrometry Testing in Wadi Ma'awil.* Technical report, Ministry of Agriculture and Fisheries of the Sultanate of Oman, 1985.

MAF. *Groundwater Recharge Schemes for Barka-Rumais Areas: Feasibility Report Engineering and Economics.* Technical report, Ministry of Agriculture and Fisheries of the Sultanate of Oman, 1989.

MAF. *Groundwater Recharge Schemes for Barka-Rumais Areas: Feasibility Report Hydrogeology.* Technical report, Ministry of Agriculture and Fisheries of the Sultanate of Oman, 1990.

Martin-Vide, J. P., D. Niñerola, A. Bateman, A. Navarro, and E. Velasco. Runoff and sediment transport in a torrential ephemeral stream of the Mediterranean coast. *Journal of Hydrology*, 225(3–4): 118–129, 1999.

Morin, E., T. Grodek, O. Dahan, G. Benito, C. Kulls, Y. Jacoby, G. V. Langenhove, M. Seely, and Y. Enzel. Flood routing and alluvial aquifer recharge along the ephemeral arid Kuiseb River, Namibia. *Journal of Hydrology*, 368(1–4): 262–275, 2009.

Morita, M. and B. C. Yen. Modeling of conjunctive two-dimensional surface—three-dimensional subsurface flows. *Journal of Hydraulic Engineering*, 128(2): 184–200, 2002.

Mudd, S. M. Investigation of the hydrodynamics of flash floods in ephemeral channels: scaling analysis and simulation using a shock-capturing flow model incorporating the effects of transmission losses. *Journal of Hydrology*, 324(1–4): 65–79, 2006.

NASA. NASA Land Processes Distributed Active Archive Center (LP DAAC), ASTER GDEM, USGS/Earth Resources Observation and Science (EROS) Center, Sioux Falls, South Dakota (https://lpdaac.usgs.gov). 2012.

Nash, J. E. and J. V. Sutcliffe. River flow forecasting through conceptual models part I—a discussion of principles. *Journal of Hydrology*, 10(3): 282–290, 1970.

Parissopoulos, G. A. and H. S. Wheater. Effects of wadi flood hydrograph characteristics on infiltration. *Journal of Hydrology*, 126(3–4): 247–263, 1991.

Penman, H. L. Natural evaporation from open water, bare soils and grass. *Proceedings of the Royal Society of London*, 193(1032): 120–145, 1948.

Philipp, A., G. H. Schmitz, and R. Liedl. Analytical model of surge flow in nonprismatic permeable channels and its application in arid regions. *Journal of Hydraulic Engineering*, 136(5): 290–298, 2010.

Ponce, V. M. The kinematic wave controversy. *Journal of Hydraulic Engineering*, 117(4): 511–525, 1991.

Press, W. H., S. A. Teukolsky, W. T. Vetterling, and B. P. Flannery. *Numerical Recipes*. Cambridge University Press, New-York, 1992.

Rushton, K. *Recharge of Phreatic Aquifers in (Semi-)Arid Areas*, chapter Recharge from Permanent Water Bodies. A. A. Balkema Publishers, Rotterdam, 1997.

Saber, M., T. Hamaguchi, T. Kojiri, and K. Tanaka. Spatiotemporal runoff features of hydrological modeling in Arabian wadi basins through comparative studies. *Annuals of the Disaster Prevention Research Institute, Kyoto University*, 52(B): 813–830, 2009.

Scanlon, B. R. and R. W. Healy. Choosing appropriate techniques for quantifying groundwater recharge. *Hydrogeology Journal*, 10(1): 18–39, 2002.

Schick, A. P. *Flood Geomorphology*, chapter Hydrologic Aspects of Floods in Extreme Arid Environments, pages 189–203. Wiley Interscience, New York, 1988.

Schmitz, G. H., R. Liedl, and R. Volker. Analytical solution to the zero inertia problem for surge flow phenomena in nonprismatic channels. *Journal of Hydraulic Engineering*, 128(6): 604–615, 2002.

Schmitz, G. H. and G. J. Seus. Mathematical zero-inertia modeling of surface irrigation: advance in furrows. *Journal of Irrigation and Drainage Engineering*, 118(1): 1–18, 1992.

Sharma, K. D. and J. S. R. Murthy. Estimating transmission losses in an arid region—a realistic approach. *Journal of Arid Environments*, 27(2): 107–112, 1994.

Sharma, K. D. and J. S. R. Murthy. Hydrologic routing of flow in arid ephemeral channels. *Journal of Hydraulic Engineering*, 121(6): 466–471, 1995.

Shentsis, I. and E. Rosenthal. Recharge of aquifers by flood events in an arid region. *Hydrological Processes*, 17(4): 695–712, 2003.

Tooth, S. Process, form and change in dryland rivers: a review of recent research. *Earth-Science Reviews*, 51(1–4): 67–107, 2000.

Vanoni, V. A. and N. H. Brooks. *Laboratory Studies of the Roughness and Suspended Load of Alluvial Streams*. Technical Report E-68, California Institute of Technology, Pasadena, 1957. Report to the U. S. Army Corps of Engineers.

Vischer, D. L. and W. H. Hager. *Dam Hydraulics*. John Wiley and Sons, Chichester, 1999.

Wheater, H. S. *Hydrology of Wadi Systems*. UNESCO, Paris, 2002.

Wood, W. W., K. A. Rainwater, and D. B. Thompson. Quantifying macropore recharge: examples from a semi-arid area. *Ground Water*, 35(6): 1097–1106, 1997.

für Kurti und Karlinchen